

HIGH SPATIAL RESOLUTION MULTI-OMIC  
INVESTIGATIONS OF *STAPHYLOCOCCUS AUREUS*  
BIOFILM LAYERS: VISUALIZING DAPTOMYCIN-RESISTANCE

By

Emilio Sanchez Rivera

Dissertation

Submitted to the Faculty of the  
Graduate School of Vanderbilt University  
in partial fulfillment of the requirements

for the degree of

DOCTOR OF PHILOSOPHY

in

Biochemistry

December 17<sup>th</sup>, 2022

Nashville, Tennessee

Approved:

Richard M. Caprioli, Ph.D.

Kevin L. Schey, Ph.D.

Manuel Ascano, Ph.D.

Jeffrey M. Spraggins, Ph.D.

Eric P. Skaar, Ph.D.

## ACKNOWLEDGEMENTS

Nothing worth doing is done in a vacuum, and this dissertation is certainly no exception. As such, I will do my best to thank everyone who has helped along the way. I would like to start by thanking my advisors, Drs. Richard Caprioli, Jeff Spraggins, and Eric Skaar. Richard, you have a unique ability to push people to be the best versions of themselves. You challenged me every day to be a better scientist and a better person, and along the way you showed me where the rocks are. For that, I will be eternally grateful. Jeff, you set the bar for professional and personal mentorship. You always manage to keep things in perspective and have helped me to do that same. Leading by example, you have guided me along my entire graduate career, and that is not something I take for granted. Eric, I'm still not entirely convinced you're human. Despite your absurd level of productivity, you're somehow never too busy to provide guidance and I am very grateful for that. To the rest of my committee, Drs. Kevin Schey and Manny Ascano; I can't thank you enough for helping me find my way towards becoming a true scientist.

I would also like to thank my lab mates, without whom I would never have made it through grad school. I can't express how much your open ears and open hearts have meant to me. In particular, I would like to thank Chris Good for being an unwavering friend. My graduate experience would have been very different without our Chipotle runs and woodworking endeavors. I'm also very grateful to the collaborators I've been lucky enough to work with, Drs. Andy Weiss, Jeff Freiberg, Dustin Klein, Angela Kruse, and Lukasz Migas. Without your help I literally wouldn't have a thesis. Finally, one of the best friends I'll ever have, Kate Djambazova. Without your friendship, generosity, and selflessness, I don't know where or even who I would be today. Our friendship will, in part, define this period of my life and I can't thank you enough for that.

I've also been fortunate enough to have many previous mentors in my life and career that molded me along the way. Dr. Kevin Schey, your mentorship during my time as an MS Core employee is what drove me to pursue science at the highest level. Dr. Wade Calcutt, you've been there to lend advice, an ear, a laugh, or a lawnmower at every point of my time in Nashville, and I am truly proud to call you a mentor and a friend. I

would be remiss if I left out Dr. Antonio Lara. When I met you, I knew I loved science, but you taught me how to channel it. As I advance through my career, using science to help people will be at the forefront of my mind, and I thank you for that. Finally, Dr. and Mrs. McComas, I can't thank you enough. You opened up your house and your lives to me and helped focus my drive. I wouldn't be here today without your guidance and mentorship.

Last and certainly not least, my friends and family. Stephen, knowing we're still best friends even when we haven't spoken for months has helped me more than you'll ever know. To the newest members of my family, my in-laws, your love and support has been invaluable. I'm so grateful to you for everything you've done for us. Tias Rivera and Tio Joven, I can't thank you enough for always being there through thick and thin. Ninos Segura, the sacrifices you make for your kids (including me) is a source of inspiration to me, and I'm forever grateful. Sisters, knowing you're watching drives me every day to set the best example I possibly can, and your unconditional love gives me the strength to get back up when I fall short. Joaquin, "no te dejas" doesn't translate to English, but it's a quality of mine that has gotten me through the tough times, and I got it from you – thanks for that. My parents, Lupe, Pat, and Emilio, I owe you everything. You gave me the tools and set an example for how to use them. Raul, you're the reason I'm here. My original and most important scientific mentor, I can't thank you enough for showing me the way and sharing in my experiences at every step. I guess Pete was on to something. And of course, my wife. Lindsay, you're my best friend, my rock... and my most constructive critic. Not only have you helped me get through every facet of graduate school, but you've given me a life that makes it all worth it. Thank you for sharing my life with me.

## TABLE OF CONTENTS

ACKNOWLEDGMENTS.....	ii
LIST OF TABLES.....	vii
LIST OF FIGURES.....	viii
LIST OF ABBREVIATIONS.....	x
Chapters	
I. Introduction .....	1
a. MALDI Imaging Mass Spectrometry.....	1
i. Overview.....	1
ii. Common Types of Mass Spectrometers Used in MALDI IMS.....	5
1. Time-of-Flight.....	5
2. Fourier Transform – Ion Cyclotron Resonance .....	7
3. Quadrupole – Time-of-Flight .....	10
b. Integrating IMS with Ion mobility .....	12
i. Common Types of Ion Mobility Coupled to IMS.....	13
1. Travelling Wave Ion Mobility Spectrometry .....	13
2. High-Field Asymmetric Waveform Ion Mobility Spectrometry.....	15
3. Drift Tube Ion Mobility Spectrometry .....	15
4. Trapped Ion Mobility Spectrometry .....	16
c. <i>Staphylococcus aureus</i> Biofilms .....	17
i. Impact on Human Health and Antibiotic-Resistance .....	17
ii. Bacterial Biomolecular Drivers of Antibiotic Resistance .....	18
iii. <i>S. aureus</i> Biofilms.....	21
iv. Implementing MALDI IMS for Multi-omic Investigation of <i>S. aureus</i> Biofilms .....	22
II. Considerations for Sample Preparation of <i>S. aureus</i> Biofilms for Multi-Omic Analysis by MALDI IMS .....	23
a. Introduction .....	23
b. Results .....	25
i. Strategies for Preparing <i>S. aureus</i> Biofilms for MALDI IMS Analysis of All Analyte Classes.....	25
1. Biofilm Growth .....	25
2. Embedding.....	26

3. Cryosectioning.....	28
ii. Specific Steps for Analysis of Biofilm Lipids, Peptides or Intact Proteins.....	30
1. Salt Remediation for Lipid Analysis .....	30
2. Exploring Use of Two Dual-Polarity Matrices for Lipid Analysis .....	33
3. Antigen Retrieval for Peptide Analysis .....	36
4. Lipid Remediation for Intact Protein Analysis.....	39
c. Discussion.....	42
d. Methods .....	43
III. Characterization of Instrumental Parameters for Effective MALDI TIMS IMS Analysis of Lipids, Peptides, and Intact Proteins on a timsTOF Pro .....	45
a. Introduction .....	45
b. Results .....	47
Part I.....	47
i. Technological Considerations for Lipid Analysis by MALDI TIMS IMS ...	47
1. Overview .....	47
2. Analysis of Bacterial Lipid Standards.....	48
3. Applying TIMS for Lipid Analysis of <i>S. aureus</i> .....	50
ii. Technological Considerations for Peptide Analysis by MALDI TIMS IMS.....	51
1. Overview .....	51
2. Analysis of Peptide Standards .....	53
3. Endogenous Peptide MALDI IMS of Human Pancreas .....	55
iii. Technological Considerations for Intact Protein Analysis by MALDI TIMS IMS.....	57
1. Overview .....	57
2. Analysis of Intact Protein Standards .....	59
3. Endogenous Intact Protein Investigation of Murine Tissue .....	63
Part II.....	63
i. Multi-omic Heterogeneity Between <i>S. aureus</i> Biofilm Layers is Revealed by MALDI TIMS IMS .....	63
1. Lipids .....	63
2. Tryptic Peptides .....	79
3. Intact Proteins .....	82
c. Discussion.....	84
d. Methods.....	87

IV. Characterizing Lipidomic Distributions in Biofilms of Daptomycin-Susceptible and -Resistant Clinical Isolates of <i>S. aureus</i> .....	93
a. Introduction .....	93
b. Results .....	96
i. Clinical Isolates.....	96
1. Determining Genotypic Contributions to Daptomycin-Resistance ....	96
ii. MALDI TIMS IMS Reveals Basal Lipidomic Differences Between Daptomycin-Resistant and -Susceptible <i>S. aureus</i> Clinical Isolates .....	98
iii. Spatial Investigation of Bacterial Lipidomic Response Within Clinical Isolate Biofilms During Daptomycin Treatment .....	100
1. Measuring Daptomycin Penetration in <i>S. aureus</i> Biofilms .....	100
2. Visualizing the Lipidomic Response to Daptomycin Exposure .....	102
c. Discussion.....	106
d. Methods.....	108
V. Conclusions and Future Directions .....	110
a. Conclusions.....	111
b. Current Limitations and Future Directions .....	115
REFERENCES.....	120

## LIST OF TABLES

Table	Page
3.1 List of tryptic peptides detected by MALDI MS .....	54
3.2 Human tryptic peptide identifications from MALDI IMS experiment.....	57
3.3 Protein standards used for MALDI analysis in figure 3.5 and 3.6.....	63
3.4 Details pertaining to each lipid depicted in Figures 3.10 – 3.17 .....	68
3.5 <i>S. aureus</i> tryptic peptides observed in MALDI IMS experiment .....	82
4.1 Antibiotic susceptibility status for clinical isolates .....	95

## LIST OF FIGURES

Figure	Page
1.1 Schematic of MALDI IMS .....	2
1.2 Overview of imaging mass spectrometry ion sources .....	4
1.3 Schematic depicting a MALDI TOF .....	7
1.4 Schematic depicting an FT-ICR .....	9
1.5 Schematic depicting a MALDI QTOF .....	11
1.6 Overview of ion mobility techniques .....	14
1.7 Schematic depicting lipid structure .....	19
2.1 Comparisons of growth and embedding media .....	27
2.2 Visual assessments of use of Teflon slide and washing.....	28
2.3 Schematic of multi-omic workflow .....	30
2.4 Evaluation of washing on chemical interferences .....	32
2.5 Effect of washing on CL signal .....	33
2.6 Comparison DAN and DHA matrices .....	34
2.7 Evaluation of matrix clusters .....	35
2.8 Tryptic peptide MALDI IMS workflow.....	37
2.9 Effects of antigen retrieval.....	39
2.10 Effects of Carnoy's wash.....	41
3.1 MALDI analysis of lipid standards .....	49
3.2 Effects of TIMS on MALDI IMS of lipids .....	51
3.3 MALDI spectra of trypsin digested BSA and HeLa cell extracts .....	54
3.4 MALDI IMS of a portion of human pancreas collected on the timsTOF Pro .....	56



3.5 MALDI mass spectrum of a protein standard mixture.....	60
3.6 Effects of MALDI source pressure on intact protein analysis .....	62
3.7 Intact protein MALDI IMS of whole-body mouse pup .....	64
3.8 High spatial resolution intact protein MALDI IMS of murine cerebellum .....	65
3.9 k-means clustering performed on IMS.....	66
3.10 High spatial resolution lipid MALDI IMS of <i>S. aureus</i> lipids .....	68
3.11 Bacterial cardiolipin species distribute heterogeneously within biofilm layers ...	70
3.12 MALDI IMS and fluorescence microscopy of biofilm middle layer .....	71
3.13 Ion images of CL(58:0) and CL(65:0) .....	71
3.14 MS/MS of bacterial lipids.....	74
3.15 Comparison of CL abundances between biofilm layers.....	76
3.16 MALDI IMS of CL lipids in USA300 LAC and JE2 .....	77
3.17 Lipid MALDI IMS of anaerobic biofilm .....	79
3.18 MALDI IMS of bacterial tryptic peptides .....	80
3.19 MALDI IMS of bacterial intact proteins .....	83
4.1 Schematic depicting daptomycin-resistance .....	94
4.2 Clinical Isolate Growth Curves .....	96
4.3 Diagram depicting the <i>S. aureus</i> protein MprF .....	97
4.4 Basal lipid MALDI IMS of <i>S. aureus</i> clinical isolates.....	99
4.5 MALDI IMS of laboratory strain of <i>S. aureus</i> exposed to daptomycin .....	101
4.6 MALDI IMS of <i>S. aureus</i> clinical isolates exposed to daptomycin .....	103
4.7 Comparison lysyl-PG distributions between treated and untreated biofilms.....	104
4.8 Assessment of bacterial viability in daptomycin-treated biofilm.....	106

## LIST OF ABBREVIATIONS

ACN: Acetonitrile

AR: Antigen retrieval

BSA: Bovine serum albumin

BHI: Brain-heart infusion

CaCl<sub>2</sub>: Calcium chloride

CAMP: Cationic antimicrobial peptide

cDHA: (E)-4(2,5-dihydroxyphenyl)but-3-en-2-one (2',5'-cDHA)

CMC: Carboxymethylcellulose

CCS: Collision cross-section

CHCA: alpha-cyano-4-hydroxy-cinnamic acid

CID: Collision induced dissociation

CL: Cardiolipin

C: Cytosine

d: Distance

Da: Dalton

DAN: 1,5-diaminonaphthalene

DAP-S: Daptomycin-Susceptible

DAP-R: Daptomycin-resistant

DC: Direct current

DESI: Desorption electrospray ionization

DG: Diacylglycerol

DGDG: digalactosyldiacylglycerol

DHA: 2,5-dihydroxyacetophenone

DNA: Deoxyribonucleic acid

DTIMS: drift tube ion mobility spectrometry

ESI: Electrospray ionization

ECM: Extracellular matrix

EFG: Electric field gradient

FA: Formic acid

FAIMS: High-field asymmetric waveform ion mobility  
FT-ICR: Fourier transform ion cyclotron resonance  
FWHM: Full-width half maximum  
GFP: Green fluorescent protein  
HPLC: High performance liquid chromatography  
Hz: Hertz  
IMS: Imaging mass spectrometry  
IR-MALDIESI: infrared matrix-assisted laser desorption electrospray ionization  
ITO: Indium-tin-oxide  
kDa: Kilodalton  
KE: kinetic Energy  
LAESI: laser-assisted electrospray ionization  
LC: Liquid chromatography  
LC-MS/MS: Liquid chromatography – tandem mass spectrometry  
LESA: Liquid extraction surface analysis  
LMJ-SSP: liquid-microjunction surface sampling probe  
m/z: mass-to-charge  
MALDI: Matrix-assisted laser desorption ionization  
mM: millimolar  
MprF: Multiple peptide resistance factor  
mRNA: messenger ribonucleic acid  
MRSA: Methicillin-resistant *S. aureus*  
MS/MS: Tandem mass spectrometry  
MS: Mass spectrometry  
NaCl: Sodium chloride  
Nd:YAG: Neodymium-doped yttrium  
nm: Nanometer  
OCT: Optimal cutting temperature  
PASEF: Parallel accumulation serial fragmentation  
PC: phosphatidylcholine  
PG: phosphatidylglycerol

pH: -log of H<sup>+</sup> concentration  
PIA: Polysaccharide intercellular adhesin  
PIP: Phosphatidylinositol phosphates  
PSM: Phenol-soluble modulin  
PTM: Post-translational modification  
q: Charge  
QTOF: Quadrupole time-of-flight  
RF: Radio frequency  
RNA: Ribonucleic acid  
S/N: Signal-to-noise  
T: Thymine  
t: Time  
TFA: Trifluoroacetic acid  
TIC: Total ion current  
TIMS: Trapped ion mobility spectrometry  
TOF: Time-of-flight  
TSA: Tryptic soy agar  
TSB: Tryptic soy broth  
TWIMS: Traveling wave ion mobility spectrometry  
UV: Ultraviolet  
UVPD: Ultraviolet photodissociation  
V: Voltage  
V<sub>pp</sub>: Peak to peak voltage  
z: charge  
λ: Wavelength  
μm: micrometer  
WT: Wild-type

## CHAPTER I

### INTRODUCTION

This chapter was in part adapted from *Integrating Ion mobility and Imaging Mass Spectrometry for Comprehensive Analysis of Biological Tissue: A Brief Review and Perspective* with permission from the publishers and co-authors.

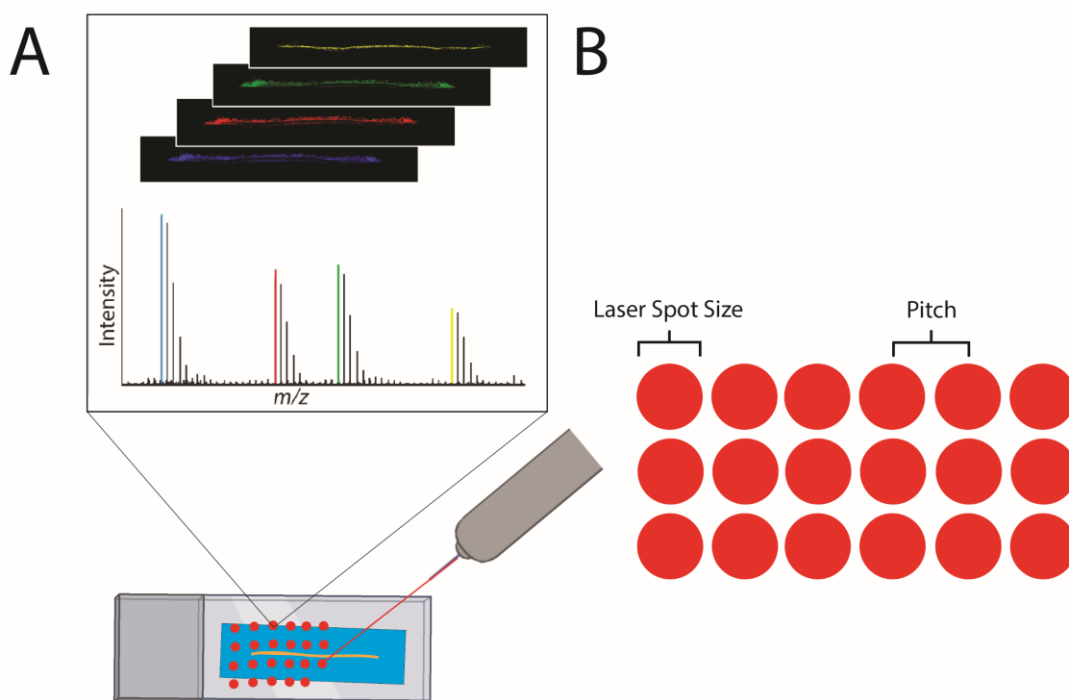
#### **Matrix-Assisted Laser Desorption/Ionization Imaging Mass Spectrometry**

##### *Overview*

At the root of biological discovery lies the need to determine the composition of a given specimen. This fundamental need has given rise to a myriad of analytical tools including various types of microscopy, immunohistochemistry, chromatography, and spectroscopy that provide information about the structural or molecular makeup of a sample. Mass spectrometry (MS) is a powerful tool capable of measuring the mass-to-charge ( $m/z$ ) of a molecule and as such, provides a tool for identifying biomolecules. MS has been heavily relied upon to answer biological inquiries dating back nearly to its' invention. The versatility of MS lends it to coupling with many orthogonal techniques such as chromatography or ion mobility. These powerful technologies have proven themselves invaluable for the molecular investigations of biological samples via bulk digestions or tissue homogenizations but cannot alone provide information about the distributions of the molecules observed within the specimen in question.

To fully characterize the biomolecular underpinnings of processes such as homeostasis and pathogenesis, technologies are necessary that can capture this molecular diversity while maintaining spatial context.<sup>1</sup> One such tool, imaging mass spectrometry (IMS), achieves this by combining the molecular sensitivity and specificity of mass spectrometry with tissue sampling technologies that enable rapid, high spatial resolution imaging. IMS is a label-free technology that provides ion maps that are easily correlated to tissue histology for a diverse array of biological specimens.<sup>2-8</sup> While alternative techniques such as fluorescence-based approaches can provide high

resolution imaging, the number of molecular channels is limited because of excitation and emission overlap between fluorophores.<sup>9</sup> In contrast, other techniques such as Raman or infrared spectroscopy are sensitive to many types of molecular features, but often at the expense of chemical specificity.<sup>10,11</sup> Only IMS offers an untargeted spatial examination of hundreds to thousands of detected molecules in a single experiment. Moreover, IMS provides the analytical flexibility to investigate vastly different classes of biomolecules including small metabolites,<sup>12,13</sup> lipids,<sup>14,15</sup> drugs,<sup>16,17</sup> glycans,<sup>18,19</sup> peptides,<sup>20,21</sup> and proteins.<sup>22,23</sup> Direct sampling of tissues for imaging does, however, introduce challenges of dynamic range, peak capacity, and the ability to structurally identify observed species.



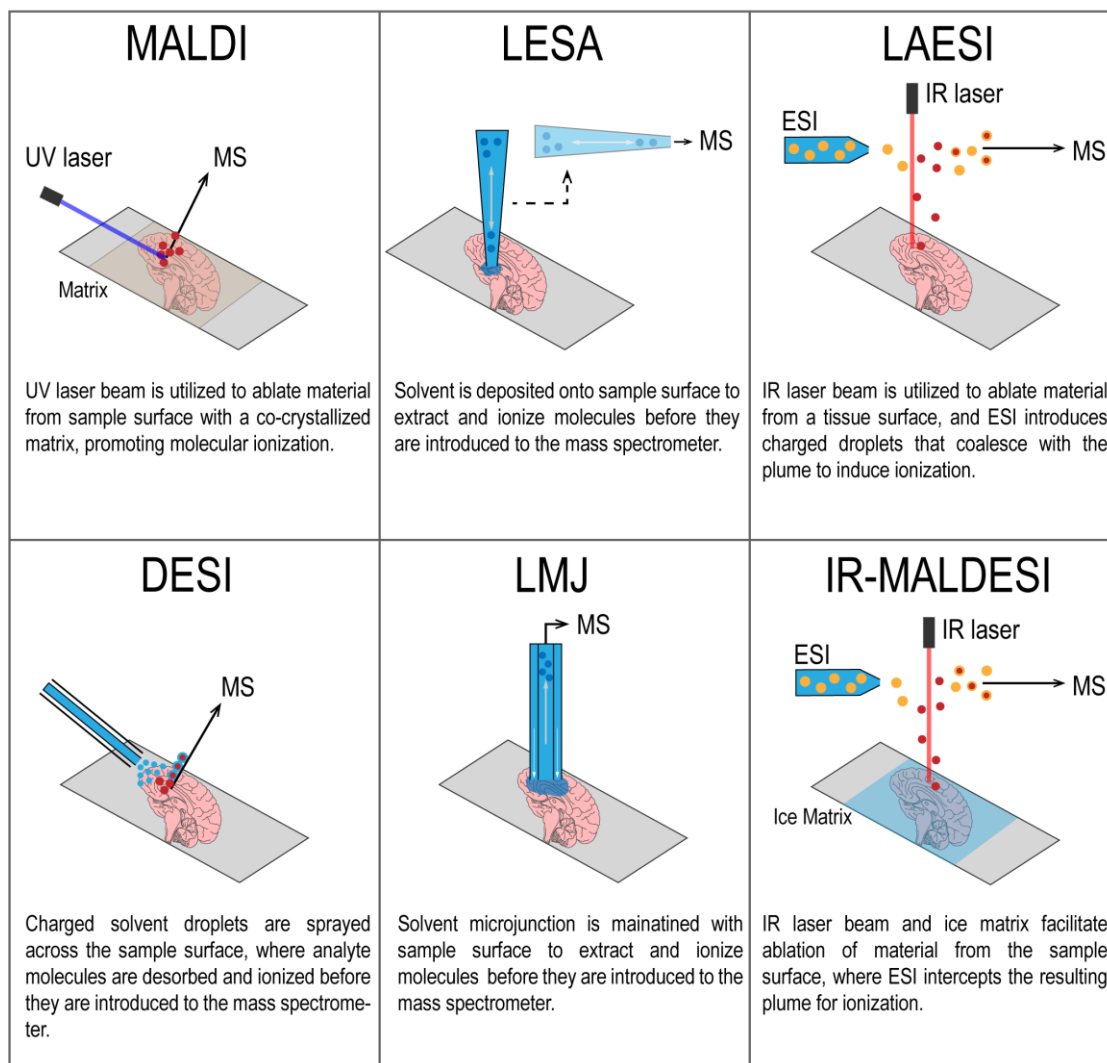
**Figure 1.1:** Schematic depicting the MALDI IMS process. A UV laser is used to ablate the sample at discrete locations (pixels) across an x-y coordinate. Analytes of interest are then measured by their  $m/z$  and an average mass spectrum can be generated from all pixels, where ions can be selected and their intensities plotted as a heatmap (**A**). A schematic describing the laser spot size, and the distance between pixels (**B**).

IMS can be leveraged for the spatial investigation of biomolecules by sampling across a tissue section and collecting mass spectra at discrete locations. The intensity of any molecule detected can then be plotted as a heat map to generate ion images (**Figure 1.1**). Various types of ion sources have been used for IMS including Matrix-assisted laser desorption/ionization (MALDI), liquid extraction surface analysis (LESA), laser-assisted electrospray ionization (LAESI), desorption electrospray ionization (DESI), liquid-microjunction surface sampling probe (LMJ-SSP), and infrared matrix-assisted laser desorption electrospray ionization (IR-MALDIESI) (**Figure 1.2**).

While these other ionization sources have their advantages and therefore warrant mention here, MALDI is the most common and versatile ionization source employed for IMS and will be the focus herein. MALDI is a “soft” ionization technique that relies on the use of small aromatic molecule matrix with which the sample of interest is co-crystallized.<sup>24</sup> A UV laser is then focused onto a discrete position on the sample where the matrix acts to absorb energy from the laser and facilitate the desorption/ionization of analytes from the sample. During this process, the matrix can either donate or abstract a proton from the analyte, generating an analyte ion that can then be directed into the mass spectrometer and detected. MALDI IMS was first introduced by *Caprioli et al.* in 1997, where it was demonstrated that a tissue sample could be sectioned and thaw-mounted onto a conductive microscope slide, followed by coating with a matrix.<sup>2</sup> The MALDI laser could then be used to sample the tissue at discrete positions across an X-Y domain and generate a mass spectrum at each location. Analyte intensities could then be plotted as a heatmap where the intensity of an analyte at each discrete position corresponds to a pixel intensity, generating an ion image. As with any imaging modality, spatial resolution can be modulated in a MALDI IMS experiment by decreasing the distance between pixels (pitch). This is fundamentally limited by the size of ablated material by the laser where the smaller the area, the higher the potential spatial resolution. Increasing the spatial resolution inherently increases the number of pixels collected and can therefore increase data acquisition time and data file size significantly.<sup>25</sup> As the field of IMS advances, the sensitivity of MS is under constant improvement. One such improvement is the integration with various forms of ion mobility. In brief, when coupled to MS, ion

mobility is a technology that provides gas-phase separations of ions based on their size-to-charge ratio prior to mass analysis.<sup>26</sup> This gas-phase separation has been shown to significantly improve the sensitivity and specificity for various analyte classes in an imaging experiment. For these reasons, ion mobility has become a common addition to IMS workflows.<sup>27</sup>

## Imaging Mass Spectrometry



**Figure 1.2: Overview of imaging mass spectrometry ion sources.** Matrix-assisted laser desorption/ionization (A), liquid extraction surface analysis (LESA) (B), laser ablation electrospray ionization (LAESI) (C), desorption electrospray ionization (DESI) (D), liquid microjunction (LMJ) (E), and infrared matrix-assisted laser desorption electrospray ionization (IR-MALDESI) (F).



MALDI IMS has also been leveraged for the spatial molecular investigation of many different biological systems varying from complex mammalian multi-organ systems,<sup>28</sup> to single cells.<sup>29</sup> Among these studies, MALDI IMS has proven effective at mapping the molecular distributions within complex bacterial communities.<sup>30–32</sup> *Staphylococcus aureus* is an important human pathogen and represents a major burden on human health. Importantly, *S. aureus* often develops into three-dimensional multi-cellular communities known as biofilms that aid in its ability to survive under challenging conditions. Further, these biofilms have been observed to develop discrete horizontal layered subpopulations with phenotypic differences.<sup>33,34</sup> Although some studies have previously investigated molecular distributions within *S. aureus* biofilms via MALDI IMS,<sup>35–37</sup> none have applied a multi-omic approach to mapping biomolecular distributions within these horizontal layers. Below is an introduction to different MALDI IMS technologies and the advantages of integration with ion mobility, followed by a discussion about the need for multi-omic spatial investigations of *S. aureus* biofilms horizontal layers.

### *Common Types of Mass Spectrometers Used in MALDI IMS*

#### Time-of-Flight

Time of Flight (TOF) mass spectrometers have been the mass analyzer of choice for MALDI IMS historically, owing to their sensitivity, prevalence, and high mass range relative to other instruments.<sup>38</sup> These instruments are capable of detecting large molecules and have even been shown to be capable of measuring large protein complexes exceeding one megadalton.<sup>39</sup> The simple TOF design is also appealing to researchers making it easier to mend, maintain and modify. MALDI TOF mass spectrometers provide mass detection by accelerating ions via high voltage to an equal kinetic energy, propelling them through a flight tube devoid of electric fields toward a detector at the opposite end (**Figure 1.3A**). This kinetic energy for any given ion is the product of the charge of the ion ( $z$ ) and the voltage ( $V$ ) applied for acceleration. Kinetic energy can then be represented as a function of mass and velocity where ( $m$ ) is the mass and ( $v$ ) is the velocity of an ion, in the equation:

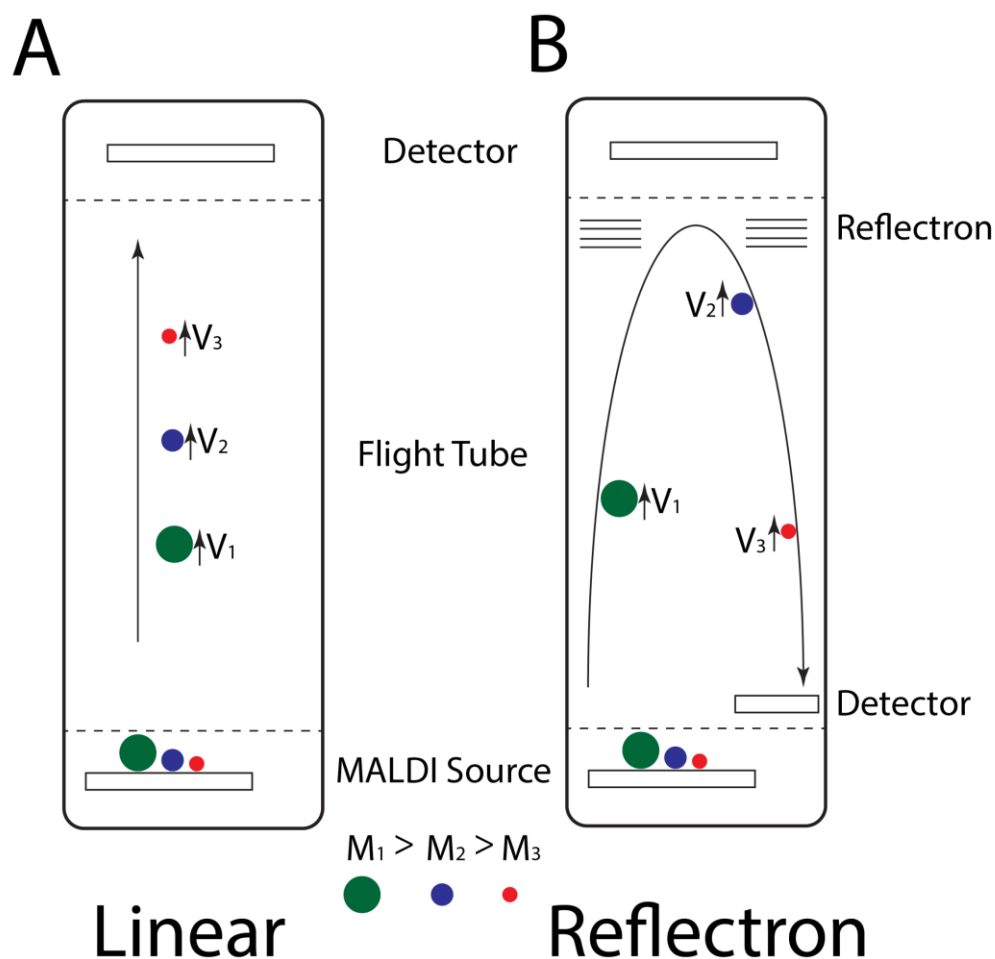
$$KE = zV = \frac{mv^2}{2}$$

Ions traversing this field-free flight tube separate by  $m/z$ , as the time to reach the detector increases with increasing  $m/z$ . By substituting ( $v$ ) for distance ( $d$ ) and time ( $t$ ), the equation can be rearranged to calculate the  $m/z$  of an ion based on the time it takes to traverse the distance of the flight tube:

$$t = d \sqrt{\frac{m}{2zV}}$$

With these known variables in combination with calibration using a sample of known mass, it is possible to calculate the  $m/z$  of a detected ion.

TOF MS provides mass analysis with high speed. Relying only on the time taken by the heaviest ion in the scanned mass range, the duty cycle, or time between individual mass spectra, is usually in the microsecond timescale.<sup>40</sup> In a MALDI IMS experiment, this quality means that the rate of data acquisition is only limited by the rate at which the MALDI process can be performed between pixels. This quality, in combination with the high sensitivity offered by the platform have allowed TOF instruments to achieve high spatial resolution imaging with reasonable acquisition times. The major tradeoff of the TOF is the achievable mass resolution. As resolution in this platform is a function of the distance ( $d$ ) the ions traverse, the resolution a TOF is capable of achieving is limited by the length of the flight tube.<sup>41</sup> This limitation has been addressed through multiple approaches including reflectron TOF instruments where ions are reflected at the end of the flight tube toward a detector on the originating end of the flight tube, effectively doubling the flight distance (**Figure 1.3B**).<sup>42</sup> Despite these improvements, most TOF instruments are limited to modest resolving powers compared to other MS platforms. For example, for higher mass resolving power capabilities, researchers can turn to other instruments such as the Fourier Transform – Ion Cyclotron Resonance MS or Quadrupole – time-of-flight MS.



**Figure 1.3:** A schematic depicting a MALDI TOF with either linear detection (A), or reflectron detection (B). In both cases, MALDI generated ions are accelerated by a high voltage grid into a field-free flight tube where ions separate based on their velocities, which is a function of  $m/z$ . In the linear TOF, ions reach the detector at the end of the flight tube, where the time is measured, allowing for  $m/z$  calculation. In the reflectron TOF, ions are redirected at the end of the flight tube before reaching a detector at the original side of the flight tube, doubling the distance travelled by the ions and allowing them more time to separate prior to detection.

### Fourier Transform – Ion Cyclotron Resonance

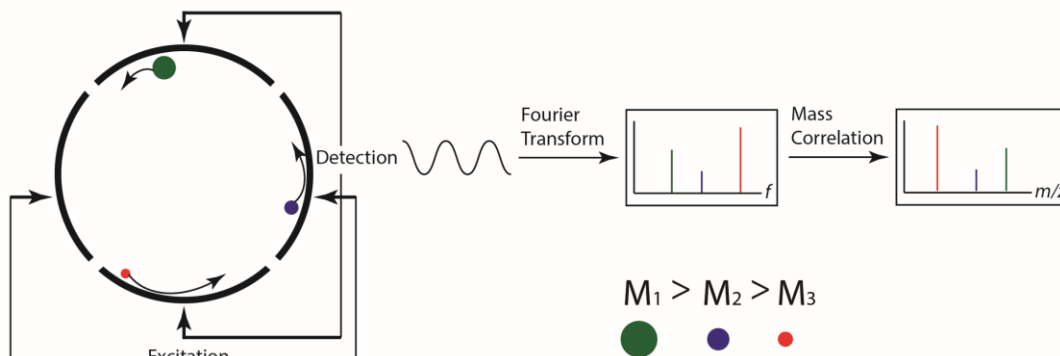
Differing from TOF instruments, Fourier Transform – Ion Cyclotron Resonance (FT-ICR) mass spectrometers offer the highest mass resolving power on any other commercially available instrument platform.<sup>43</sup> Briefly, the FT-ICR functions by first generating ions in the source and directing them through a series of ion optics into an ICR cell at the center of a large super conducting magnet for mass detection.<sup>44</sup> These

ion optics usually include a quadrupole for  $m/z$  isolation and a collision cell for performing collision-induced dissociation (CID) of selected ions, which together allow for MS/MS capabilities. Once contained inside the ICR cell, rotational force (Lorentz force) due to the magnetic field will propel the ions in a circular motion. The radius of this circular motion is a function of both the mass of the ion, as well as the strength of the magnetic field. As a result, ions with higher mass rotate at a lower frequency (cyclotron frequency) than those with lower mass and  $m/z$  can therefore be calculated from the following equation where ( $\nu_c$ ) is the cyclotron frequency, and ( $B$ ) is the field strength of the magnet:

$$\nu_c = \frac{1.535611 \times 10^7 B}{m/z}$$

The ions rotating inside the ICR cell can then be excited by resonant excitation, resulting in an enlargement of the diameter of the trajectory for each ion, pushing them closer to the electrodes on the outside of the cell, and inducing a change in the electrical current at these electrodes. This change in electrical current can then be used to measure the frequencies of each ion inside the cell, generating an image current. Fourier Transform can then be performed to convert these measured frequencies into a mass spectrum (**Figure 1.4**).

## Fourier Transform - Ion Cyclotron Resonance



**Figure 1.4:** A schematic depicting an FT-ICR. Once inside the ICR cell, the cyclotron motion is initiated by the magnetic field. Ions are then excited by two plates on opposite sides of the cell and frequency for each ion is measured by adjacent detection plates. Fourier transform is then performed on these measured frequencies, followed by mass correlation based on a calibration with ions of known mass to determine  $m/z$  for each ion detected.

Although much of the work performed on FT-ICRs has been done via electrospray ionization, FT-ICR's have been readily coupled to other ionization techniques including MALDI, which enables MALDI IMS. The ultra-high mass resolving power of the FT-ICR has lent itself to applications in biology, where individual isotopes of large biomolecules such as intact proteins can be resolved, aiding in precise mass measurement.<sup>45</sup> For lower mass biomolecules such as lipids, the ultra-high mass resolving power of the FT-ICR is capable of resolving two distinct lipid species that may have extremely similar mass (isobars). Each of these qualities has been exploited for use in MALDI IMS, making it a noteworthy instrument platform in the field. However, as with the TOF, there are drawbacks to performing MALDI IMS with an FT-ICR. At the top of this list, is the acquisition time. Unlike the TOF that requires only microseconds to generate a mass spectrum, the detection process for an FT-ICR can routinely take

several seconds to perform.<sup>45</sup> Indeed, the higher the resolving power desired by the user, the longer the time for detection.

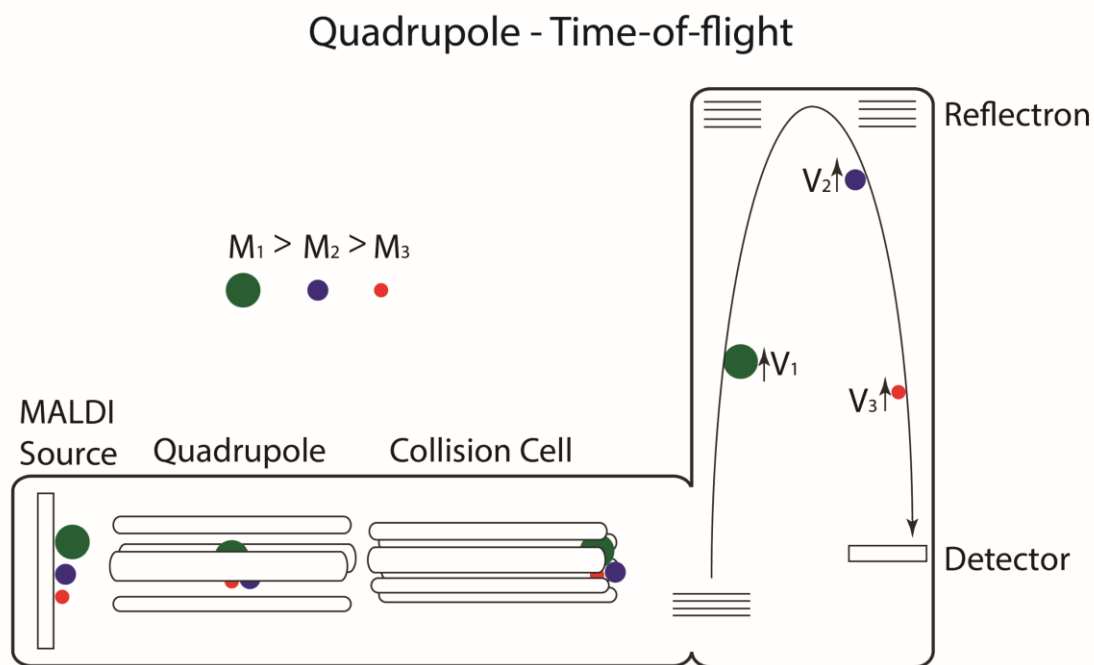
Ultimately, the TOF has strengths where the FT-ICR lacks, such as spatial resolution and speed, and vice versa the FT-ICR provides ultra-high mass resolving power compared to the modest resolving power of the TOF. Analysis by MALDI IMS could therefore benefit from performance on a quadrupole – time-of-flight (QTOF) instrument, which provides some qualities from both the TOF, and the FT-ICR.

### Quadrupole – Time-of-Flight

The Quadrupole – time-of-flight (QTOF) mass spectrometer is a somewhat newer development in the field of MS compared to the TOF and FT-ICR instruments.<sup>46</sup> At its core, the QTOF is simply a TOF instrument with a quadrupole mass filter preceding the TOF (**Figure 1.5**). When used for MALDI IMS, MALDI generated ions are first directed into the quadrupole to which a DC voltage can be applied to select of an  $m/z$  window for passage through to the TOF. The quadrupole can also be operated in a radio frequency-only mode, allowing all ions to pass.<sup>46</sup> Like FT-ICR systems, most current commercial QTOF platforms are also equipped with a collision cell following the quadrupole to allow for CID of selected ions. Of note, commercial QTOF systems are usually reflectron-only TOF systems, where some even have multiple reflectrons at each end of the flight tube, allowing for multiple passes to further increase resolving power. This advancement improves resolving power without sacrificing duty cycle, as most commercial platforms are capable of achieving ~40,000 resolving power within the microsecond time domain.<sup>47</sup> Another major advantage the of the QTOF over the traditional TOF is the uncoupled ion source. Because the MALDI source in a QTOF is not a component of the TOF itself, it does not require high voltage or high vacuum, making the QTOF much more amenable to coupling with various ionization sources.<sup>47</sup>

Since its development, the QTOF has proven itself a highly versatile instrument platform for many LC-based applications including metabolomics,<sup>48,49</sup> lipidomics,<sup>50,51</sup> and proteomics.<sup>52,53</sup> In the field of IMS, various QTOF platforms have been routinely coupled to DESI and MALDI ionization sources.<sup>54,55</sup> Indeed, its use in IMS is on the rise

as it provides a middle ground between speed of analysis and mass resolving power between the TOF and FT-ICR. The speed, mass resolving power, and versatility of the QTOF lend it to coupling with other analytical technologies such as ion mobility.



**Figure 1.5:** Schematic depicting a MALDI QTOF mass spectrometer. MALDI generated ions are accelerated into a quadrupole mass filter capable of selecting ions within a selected mass window or allowing all ions to pass through. Beyond the quadrupole, ions enter the collision cell where CID fragmentation can be performed prior to mass analysis. Either intact molecules or their fragments are then accelerated into the reflectron TOF for mass detection.

## Integrating IMS with Ion Mobility

Traditionally, other mass spectrometry-based techniques rely on orthogonal separation methods such as chromatography or electrophoresis to separate complex mixtures and provide an additional dimension of information such as retention time. However, practical considerations such as throughput and sampling limitations minimize their applicability to most imaging methods. Ion mobility, however, is one technology which offers effective separation within milliseconds,<sup>56</sup> and yields additional mobility information, making it amenable to IMS. While there are many different types of ion mobility, all achieve molecular separation by exposing analytes to opposing forces where a force is applied to analytes in one direction by collisions with an inert gas and in the opposite direction by a voltage gradient (**Figure 1.6**). Molecules are differentially affected based on their apparent size and charge.<sup>57</sup> Differences between molecular size-to-charge ratio determine mobility and cause molecules to exit from the ion mobility cell at differing times, referred to as the drift or arrival time.<sup>58,59</sup> Akin to retention times in chromatography, these arrival times can often distinguish molecules of similar mass. Moreover, ion mobility can be used to calculate the collision cross section (CCS), 3-dimensional surface area of an ion, which provides additional structural information for a given molecule.<sup>60-62</sup> This structural characterization has proven valuable for various analyses in its own right, including estimation of a molecule's binding affinity<sup>63</sup> or prediction of blood-brain barrier permeation.<sup>64</sup> Ion mobility has effectively analyzed a wide range of analyte classes without the need for dramatic changes to the system like switching mobile or stationary phases in chromatography. Not only is ion mobility capable of separating discrete analyte classes, but it is often used to distinguish both isobaric<sup>65,66,67</sup> and isomeric<sup>68,69,70</sup> species. Ion mobility comes in several forms, each alike in gas-phase separation, but distinct in design and performance. The separating power of ion mobility has major implications for coupling to imaging mass spectrometry where analyses are often hindered by spectral complexity. Moreover, use of ion mobility for discrimination of ions with similar or equal  $m/z$  could prove invaluable for direct tissue analysis where even the most powerful mass spectrometers cannot distinguish structural isomers with mass resolving power alone.



For these reasons, ion mobility is often integrated with imaging mass spectrometry and provides efficient separation after ionization, but before mass analysis. When these two technologies are coupled, ion mobility has been demonstrated to provide a variety of functions such as basic separation of analytes from chemical noise for increased signal-to-noise (S/N).<sup>54,66,71</sup> In addition, as the resolving power of ion mobility techniques continues to improve, applications of ion mobility-IMS is evolving to discriminate biomolecules closer in  $m/z$  without the need for ultra-high mass resolving power mass spectrometers. Coupling of ion mobility with IMS stands to propel the field toward a deeper understanding of the molecular intricacies within spatially and chemically complex biological systems.

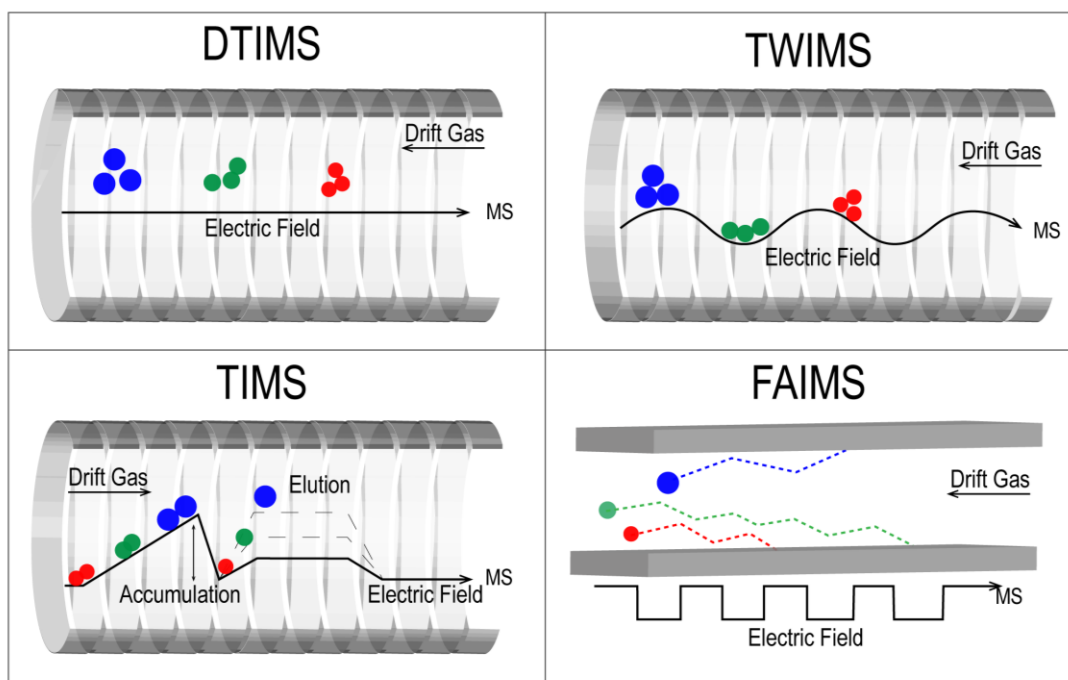
### *Common Types of Ion Mobility Coupled to IMS*

#### Traveling Wave Ion Mobility Spectrometry

Traveling wave ion mobility spectrometry (TWIMS) is perhaps the most common form of ion mobility coupled with imaging mass spectrometry. Briefly, TWIMS achieves gas-phase separation by transmitting ions into a cell lined with a series of ring electrodes where they are radially confined with an RF voltage (**Figure 1.6**), and ion propulsion is achieved by applying an additional DC voltage to a pair of adjacent ring electrodes. This voltage is then pulsed down the length of the TWIMS cell, creating a travelling electric field wave that ions 'ride' through an inert gas, such as nitrogen.<sup>72,73</sup> Differential propulsion of ions through this gas leads to separation as a function of effective size, shape, and charge. Similar to mass spectrometry, ion mobility performance is often measured in terms of resolving power, but it is important to note that these values are often calculated differently across ion mobility methods. As such, care should be taken when making inter-platform comparisons as elegantly discussed in a review by May and McLean<sup>74</sup> and later addressed by Dodds et al.<sup>61</sup> Here, a CCS-based calculation (CCS/CCS) will be used that allows for cross-platform comparisons whenever possible. TWIMS commonly yields a resolving power of  $\sim 40$  (CCS/ $\Delta$ CCS),<sup>61</sup> which is sufficient for resolving many isobaric ion species<sup>66,75</sup> and some isomeric ions, often with the aid of chemical derivatization<sup>76</sup> or metal adduction.<sup>77,78</sup> CCS values for a

myriad of analyte classes are also frequently calculated using TWIMS-based analyses, leading to the curation of several databases for species such as proteins and steroids.<sup>60,79</sup> Despite being newer than some other ion mobility techniques, utilization of TWIMS already extends across many analytical disciplines. Upon commercialization, TWIMS has also been incorporated into many imaging mass spectrometry workflows for increasing the chemical information obtained from a pixel and applied to various analyte classes in an imaging context.<sup>54,80,81</sup> For example, TWIMS has been coupled to many imaging mass spectrometry ion sources including MALDI,<sup>66,82–86</sup> DESI,<sup>54,80,86,87</sup> LAESI,<sup>88,89</sup> and LESA<sup>71,90–92</sup> (**Figure 1.2**). For detailed descriptions of these ionization sources, see these recent reviews.<sup>93–95</sup>

## Ion Mobility Spectrometry



**Figure 1.6:** Overview of ion mobility techniques. Drift tube ion mobility spectrometry (DTIMS) (A), travelling wave ion mobility spectrometry (TWIMS) (B), trapped ion mobility spectrometry (TIMS) (C), and high-field asymmetric waveform ion mobility (FAIMS) (D).

### High-Field Asymmetric Waveform Ion Mobility

High-field asymmetric waveform ion mobility (FAIMS), also known as differential mobility separation, is another form of ion mobility commonly exploited for use in IMS. FAIMS achieves gas-phase separation of ions at atmospheric pressure based on their mobility prior to entering the mass spectrometer.<sup>96–98</sup> FAIMS functions by applying a dispersion field, a high frequency asymmetric waveform of alternating low and high fields, perpendicular to the ion trajectory through the device (**Figure 1.6**). This alternating dispersion field causes ions to oscillate through a buffer gas, usually nitrogen or helium, causing deviation from their initial trajectory as a function of their respective mobilities through bombarding gas. This deviation ultimately leads to neutralization upon collision with the electrode wall. Selective ion transmission is made possible by the superimposition of a secondary DC field known as the compensation voltage which acts to correct the deviation of ions within a select mobility window, allowing transmission of ions with specific mobilities. Unlike other ion mobility methods, FAIMS is not usually used to provide orthogonal information such as drift time or CCS but to increase signal-to-noise, sensitivity, and dynamic range.<sup>97</sup> Since FAIMS operates at atmospheric pressure, it has not yet been coupled with sub-atmospheric IMS ion sources, such as mid-low pressure MALDI sources. While modifications to recently developed atmospheric MALDI sources could make MALDI-FAIMS possible, it has not yet been reported. For this reason, all examples of FAIMS applied to IMS to date have been conducted with ambient ion sources such as DESI and LESA.

### Drift Tube Ion Mobility Spectrometry

The design of drift tube ion mobility spectrometry (DTIMS) is rooted in the early days of ion mobility, making it perhaps the simplest modern form of these gas-phase separation technologies. DTIMS functions by transmitting ions through an inert gas within a drift tube comprised of stacked ring electrodes. Ions are driven through the cell by a uniform electric field where they collide with drift gas (**Figure 1.6**). Ions with a larger CCS encounter more drift gas molecules compared to ions with a smaller CCS, allowing for ion separation as a function of mobility.<sup>74</sup> The simplistic design of DTIMS does not, however, equate to low performance as DTIMS can routinely achieve

moderate-high resolving power ( $\sim 60$  (CCS/ $\Delta$ CCS)<sup>74,99</sup> and produces consistent CCS measurements.<sup>62</sup> DTIMS also readily couples to MS and is very commonly used to provide analyte separation for increased peak capacity and reduced spectral complexity.<sup>100–102</sup> Moreover, DTIMS has proven invaluable for offering orthogonal information about analytes in a MS experiment, being a primary technology used to measure absolute CCS.<sup>74,103</sup> Stow and coworkers recently demonstrated the robustness of DTIMS for measuring CCS values in an interlaboratory study where they reported a relative standard deviation of 0.29%.<sup>62</sup> This level of robustness has also been exploited by several groups to compile DTIMS CCS databases.<sup>104–107</sup> Despite its clear utility and popularity in other MS fields, a limited number of examples of DTIMS-IMS experiments have been reported within recent years. This could be partially explained by the early success of the commercialized TWIMS QTOF mass spectrometer discussed above; as it was offered with a variety of sources and provided researchers with an ‘out-of-the-box’ ion mobility-IMS system. Likewise, custom integration of DTIMS with modern IMS platforms poses many challenges such as instrument synchronization, and communication.<sup>108</sup> Whatever the reason, only a select few groups have reported DTIMS-IMS, but its significance warrants discussion here.

### Trapped Ion Mobility Spectrometry

Trapped ion mobility spectrometry (TIMS) is a high resolving power ion mobility technology introduced by Fernandez-Lima and coworkers in 2011.<sup>57</sup> TIMS separations are carried out in the first vacuum stage of a mass spectrometer consisting of an augmented ion funnel with an entrance funnel, TIMS tunnel, and exit funnel (**Figure 1.6**).<sup>57,26</sup> In brief, ions are accumulated in the device, where analytes with differing mobilities are trapped and separated by opposing forces. Moving forward through the funnel, ions are propelled by a carrier gas. In the opposite direction, force is applied to the ions using an axial electric field gradient. To elute trapped ions, the electric field gradient is gradually reduced/scanned resulting in transmission of ions with ascending mobilities. Note, this is reverse from most other ion mobility techniques which transmit ions based on descending mobility, accomplished by applying a forward force using an electric field and collisions with the gas counteracts this forward motion. The scan rate

of a TIMS experiment is defined by the scan time (ms) and voltage range, which correspond to user-defined mobility values. Scan rates dictate the separation resolution, with slower scan rates resulting in higher resolutions. To date, resolving power of >300 for singly charged species and >200 for doubly charged species have been reported.<sup>109</sup>

For IMS applications, TIMS was first introduced in a MALDI QTOF platform in 2019 by Spraggins and coworkers.<sup>67</sup> MALDI TIMS IMS studies have successfully demonstrated enhanced data quality over images collected with TIMS disabled.<sup>67</sup> Specifically, TIMS separations greatly increase the peak capacity of an IMS experiment, as reported by Neumann et al., who detected >900 more spectral features by utilizing TIMS in comparison to QTOF-only mode when analyzing metabolites within human kidney tissue.<sup>110</sup> In addition, TIMS successfully resolved matrix peaks from metabolite signal and demonstrated the separation of both isobaric and isomeric metabolites with distinct spatial localizations within human kidney tissue.<sup>110</sup> TIMS has also been utilized in spatial interrogation of lipids.

Since TIMS is a relatively new introduction to the field of imaging mass spectrometry, it has only been integrated with MALDI and more recently LESA.<sup>111,112</sup> Previous reports have also shown TIMS to be a powerful tool for structural investigation of proteins and peptides, suggesting its implementation for investigation of these analyte classes in an imaging context is possible.

## ***Staphylococcus aureus* Biofilms**

### *Impact on Human Health and Antibiotic-Resistance*

*Staphylococcus aureus* is a Gram-positive opportunistic pathogen responsible for over 10,000 deaths and 320,000 hospitalizations per year in the United States, and is categorized as a threat level serious by the Centers for Disease Control.<sup>113</sup> The immense impact *S. aureus* has on human health is due in part to its prevalence in the human population, with approximately one out of every three Americans colonized by this pathogen.<sup>114,115</sup> Furthermore, the ubiquitous nature of *S. aureus* helps make it a leading cause of endocarditis, bacteremia, and soft-tissue infections, as well as one of

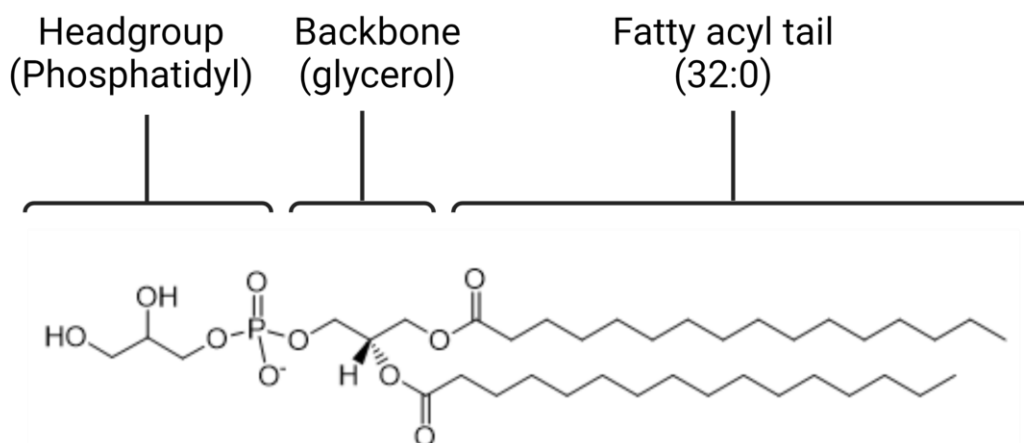
the most common causes of healthcare-associated infections.<sup>116,117</sup> With such high case volumes, the threat to human health posed by this bacterium is imminent. Even more concerning than the prevalence of *S. aureus* is its propensity for developing resistance to various antibiotics. *S. aureus* resistance to common antibiotics such as  $\beta$ -lactams<sup>118</sup> have been readily observed in the clinic. Indeed, these antibiotic-resistant infections are all the more alarming when compared to the slowing rate of novel antibiotics to combat infection.<sup>119</sup> Of the few antibiotics introduced to treat *S. aureus* infections in the past 20 years, daptomycin has offered a last-line option for multidrug-resistant *S. aureus* infections, owing to a mechanism of action that differs from other more common antibiotics.<sup>120,121</sup> In cases of multidrug-resistant infections, clinicians over the past 10 years have often turned to daptomycin for effective treatment. However, daptomycin-resistance is now also being observed in the clinic.<sup>120,122</sup> Uncovering the molecular drivers of daptomycin-resistance in *S. aureus* could lead to new therapeutic strategies and help alleviate the burden posed by this human pathogen.

### *Bacterial Biomolecular Drivers of Antibiotic-Resistance*

Lipids are fundamental building blocks of life as primary constituents of cell membranes.<sup>123</sup> Consisting of a headgroup, a backbone, and fatty acyl tails (**Figure 1.7**), lipids can expand a diverse range of chemical structures. Lipids are categorized by their backbone and headgroup, e.g. phosphatidylcholine (PC), or phosphatidylglycerol (PG), etc, and are further specified by their fatty acyl tail composition. Naming convention for lipids consists of their class, followed by the number of combined carbons in their fatty acyl tails, ending with the combined number of double bonds between carbons in the fatty acyl tails, e.g. PG(32:0) (**Figure 1.7**).<sup>124</sup>

In *S. aureus*, lipids play many important roles ranging from membrane composition to evasion of the host immune response.<sup>125–127</sup> Bacterial metabolic processes, stress response, and virulence factor production can be affected by changes in lipid composition.<sup>128,129</sup> Additionally, changes in the *S. aureus* lipidome correlate with resistance to common antibiotics,<sup>127,130–133</sup> further asserting the importance of

understanding the role of lipids in bacterial infection. The *S. aureus* lipidome consists primarily of phospholipids including phosphatidylglycerols (PG), phosphatidylinositol phosphates (PIP), cardiolipins (CL), and lysyl-PG,<sup>128,130,134–136</sup> each with distinct roles in bacterial functions including stress responses and virulence.<sup>129,137</sup> In particular, lysyl-PG lipids have been implicated in *S. aureus* resistance to multiple antibiotics including daptomycin.<sup>130,135</sup>



**Figure 1.7.** Schematic depicting an exemplary lipid, phosphatidylglycerol (32:0) is comprised of a head group, backbone, and fatty acyl tails, demonstrating the basic structure of lipids.

Specifically, one proposed mechanism of daptomycin-resistance in *S. aureus* is electrostatic repulsion of the positively charged daptomycin complex.<sup>126</sup> Increased turnover of positively charged lysyl-PG lipids synthesized from PG lipids, for example, would lead to a net increase in charge of the bacterial membrane, electrostatically repelling the positively-charged daptomycin complex and contributing to daptomycin-resistance. Others have investigated alterations in the bacterial lipidome of daptomycin-resistant *S. aureus* to uncover changes in the abundances of the products of PG, CL and lysyl-PG lipids.<sup>130,135</sup> Specifically, a decrease in PG content and a concomitant increase in lysyl-PG lipid content has been associated with daptomycin-resistance.<sup>138</sup> The association of daptomycin-resistance with changing CL abundance have been less concrete as changes of CL abundance are not always observed.<sup>139</sup> Despite *S. aureus*

being the most common pathogen in biofilm-related infections,<sup>140</sup> all previous studies have focused on investigating molecular changes that take place with daptomycin-resistance in planktonic bacteria and not within the context of a biofilm. Additionally, no studies have investigated how lipid species change when daptomycin-resistant bacteria are actually exposed to the antibiotic.

Proteins, another class of biomolecules, are major drivers of biological processes. Part of the central dogma of biology, where DNA is transcribed into mRNA, followed by translation into proteins, these biomolecules are responsible for carrying out a myriad of highly diverse functions.<sup>141</sup> The importance of proteins in a biological system cannot be overstated, as they play roles in vital bacterial processes varying from DNA replication to combating host immune responses.<sup>142,143</sup> Bacterial enzymes can also be responsible for catalyzing specific biological reactions, such as the metabolism of certain molecules like lipids. Because of this relationship between enzymes and the reactions they catalyze, it is possible to study a biological question by investigating the enzyme itself, or the substrates and products of the reaction catalyzed by that enzyme.

Unsurprisingly, proteins are often important to bacterial resistance to antibiotics. Many enzymes have been shown to have altered expression or turnover in instances of antibiotic resistance.<sup>144,145</sup> In particular, a mutation in the gene encoding for a specific protein can result in the incorporation of a different amino acid at a certain position within the primary structure of a protein. This different amino acid could lead to a change in the catalytic activity of the protein.<sup>146,147</sup> A 'gain-of-function mutation' is a mutation that results in a protein that is more catalytically active than the WT protein, and these mutations can lead to increased resistance to antibiotics in bacteria.<sup>148</sup> Daptomycin-resistance in *S. aureus* has been associated with mutations in genes encoding various enzymes involved in lipid synthesis including *pgsA*, *cls2*, and *mprF*.<sup>133,149,150</sup> These findings indicate that changes in lipid content may be the primary drivers of daptomycin-resistance.

Similar to lipidomic studies, the direct analysis of bacterial proteins is usually performed through LC-MS/MS based approaches where proteins are first extracted from bacteria prior to bottom-up proteomics.<sup>151</sup> Data produced from these experiments can be highly informative, often detecting hundreds to thousands of proteins, with the



ability to compare relative abundances of proteins between samples.<sup>152</sup> While these LC-MS/MS studies for both lipidomics and proteomics have been able to provide a great deal of molecular information regarding bacteria during planktonic growth, they are limited in their ability to unlock the intricacies of bacteria when they exist in a community, such as a biofilm.

### *S. aureus* Biofilms

Part of the success of *S. aureus* as a pathogen is due to its ability to form biofilms, complex, three-dimensional bacterial communities that adhere to a surface such as surgical prosthetics or biological tissue in infection.<sup>153</sup> As a result, *S. aureus* is the leading pathogen in biofilm-related infections.<sup>140</sup> Biofilm development leads to changes in bacterial characteristics compared to planktonic bacteria that provide a survival advantage. These changes include increased stress tolerance and altered gene regulation,<sup>33,154–156</sup> and can involve changes in the bacterial lipidome.<sup>157</sup> Biofilms are complex, three-dimensional bacterial communities that adhere to a surface such as surgical prosthetics or biological tissue in infection.<sup>158,159</sup> *S. aureus* biofilms are also associated with a thick milieu of peptides, proteins, carbohydrates, and extracellular DNA within a sticky substance called polysaccharide intercellular adhesin (PIA).<sup>160,161</sup> This milieu is known as the extracellular matrix (ECM) and is a hallmark of the *S. aureus* biofilm and contributes to many of the characteristic attributes of biofilms such as increased stress tolerance.<sup>162</sup> While biofilms can exist as polymicrobial communities containing *S. aureus* with other microbes, *S. aureus* infections are usually monomicrobial,<sup>163</sup> asserting the need to study these biofilms in the absence of other microbes. In some cases, external stimuli such as nutrient gradients have been observed to cause spatially discrete molecular striations within biofilms.<sup>32,34,37</sup> Bacteria within these communities display heterogeneous behavior, and *S. aureus* biofilms can also develop spatially discrete horizontal layers comprised of bacteria in different phenotypic states in the absence of obvious external stimuli. Indeed, Moormeier *et al.*

posited that there may exist a mechanism of biofilm structure formation involving metabolic differentiation of cells leading to metabolically distinct subpopulations within an *S. aureus* biofilm.<sup>164</sup> In particular, *S. aureus* biofilms have been observed to form in distinct horizontal layers with different expression levels of certain proteins.<sup>33</sup> This suggests that these horizontal biofilm layers are acting as discrete subpopulations, which may also differ in their molecular profiles. It is possible that focused molecular distributions to specific horizontal biofilm layers may lead to an ability of the biofilm to exhibit unique molecular responses to different stimuli such as an interface with air, or nutrient source. If these layers are molecularly distinct, this spatial specificity in molecular distributions may contribute to the survival advantage observed in *S. aureus* biofilms compared to planktonic culture. Understanding how important biomolecules distribute within these horizontal biofilm layers could lead to new insights for combating *S. aureus* biofilm infections.

#### *Implementing MALDI IMS for Multi-omic Investigation of S. aureus Biofilms*

Many previous studies have used extracts from cultured bacteria to investigate the molecular profile of *S. aureus* for research interests ranging from membrane rigidity to antibiotic resistance.<sup>130,135,165,166</sup> These approaches provide quantitation of the overall content, but come at the expense of spatial information that is especially important in biofilm formation. The ability to interrogate molecular distributions within bacterial communities by MALDI IMS has been previously demonstrated for a wide range of microbial molecules including phenol-soluble modulins,<sup>35,167,168</sup> metabolites,<sup>34,35,37,169–174</sup> oligosaccharides<sup>175</sup> and some lipids.<sup>36,169,170,175,176</sup> However, in monomicrobial *S. aureus* biofilms, no multi-omic studies have been performed. A study of this nature would offer insight to the basal phenotypic state of bacterial molecular distributions. In addition, most prior examples of MALDI IMS of microbial molecules have been performed by sampling the top of the biofilm, investigating molecular distributions on the surface of the biofilm. While informative, this approach does not capture any potential molecular heterogeneity that would correspond with oxygen, nutrient, and pH gradients. To map molecular distributions that may be the result of these stimuli, a cross-section of a

biofilm must be investigated. A few examples of biofilm cross-sections have been demonstrated for the investigation of microbial metabolites within the cross-sectional depth of the biofilm,<sup>34,37</sup> but none have investigated *S. aureus* molecular distributions within horizontal biofilm layers.

One challenge posed by microbial imaging is the small size of an individual bacterium. Most MALDI IMS studies of bacterial communities have been performed at spatial resolutions > 50  $\mu\text{m}$ , with rare exceptions.<sup>36,177</sup> Because these *S. aureus* biofilms are only hundreds of micrometers thick, higher spatial resolutions are necessary to effectively investigate inter-layer variations. To this end, the work herein sought to demonstrate a high spatial resolution, multi-omic investigation of a bacterial biofilm to enable visualization of multicellular biofilm layers. While high spatial resolution is achievable, it is often at the expense of sensitivity. However, through the implementation of TIMS for increased sensitivity, high spatial resolution MALDI IMS of cross-sections was achieved. This spatial investigation of lipids and proteins within *S. aureus* biofilms uncovered distinct, horizontal layers with stark inter-layer heterogeneity at the lipidomic and proteomic levels.

## CHAPTER II

### CONSIDERATIONS FOR SAMPLE PREPARATION OF *S. AUREUS* BIOFILMS FOR MULTI-OMIC ANALYSIS BY MALDI IMS

This chapter was in part adapted from *Imaging Mass Spectrometry Reveals Complex Lipid Distributions Across Staphylococcus aureus Biofilm Layers* with permission from the publishers and co-authors.

#### Introduction

Multi-omic analysis consists of the investigation of two or more analyte classes within the same biological system. By interrogating multiple molecular facets of a

particular question, these types of studies have been demonstrated to yield more impactful findings than investigating any one molecular class alone. The most common “omics” performed via MS are metabolomics, lipidomics and proteomics.<sup>178</sup> MS is a powerful technology capable of investigating each of these classes of biomolecules with unparalleled sensitivity and specificity, however each class requires different preparation techniques for proper analysis owing to their differences in chemical composition. For example, when performing traditional LC-based omics where extractions are necessary for analysis of biomolecules, many classes of lipids that are less polar, require more non-polar solvents for proper extraction from tissue.<sup>179</sup> Conversely, small, polar metabolites generally require polar extraction solvents, and may even require derivatization for effective chromatography.<sup>180</sup>

Sample preparation for IMS is not exempt from these analyte class-dependent requirements, and distinct methodologies must be considered for multi-omic investigations. For effective MALDI IMS of certain analyte classes, specific sample preparation steps can be taken to improve sensitivity. These steps can include selection of MALDI matrix or additional reagents such as an enzyme for generating the target analyte. For example, a protein-cleaving enzyme such as trypsin can be applied directly to tissue for digesting endogenous proteins into tryptic peptides, making them detectable by MALDI MS.

Besides improving signal for detection of specific analyte classes, another challenge associated with MS analysis is chemical interferences. In LC-based experiments, a common approach is to perform an extraction of the specific analytes of interest for analysis, leaving behind all unwanted potential interferences. MALDI IMS is performed directly on tissue, making any extractions of specific analytes impossible. It is therefore necessary to consider alternative strategies for remediating chemical interferences. Here, any undesired ion detected in an IMS experiment can be considered an interference. Spectral interferences are often highly abundant molecules that impede the ability to detect lower abundant analytes of interest. This can result from a wide range of exogenous molecules such as excessive salts in a sample that ionize preferentially leading to decreased sensitivity for analytes. Not all spectral interferences are exogenous to the sample being analyzed, however. Classes of biomolecules that

are not the intended target of the experiment can also be considered interferences. For example, highly abundant endogenous lipids can generate spectral interferences when performing IMS of intact proteins.

Although these strategies may enhance the ability to detect certain analytes, they may come at the expense of damaging the specimen being investigated. With the ultimate goal of applying these sample preparation strategies for multi-omic investigations of *S. aureus* biofilms, some more general components of the sample preparation workflow must also be defined. As a result, variables affecting the spatial fidelity of downstream MALDI IMS analyses of *S. aureus* biofilms such as growth media for biofilm thickness and embedding strategies for retaining structural integrity throughout the sample preparation process were also investigated herein. Taken together, many specific considerations must be made for the multi-omic spatial investigation of any biological specimen including *S. aureus* biofilms.

The experiments below outline the specific requirements determined herein for growing and preparing *S. aureus* biofilms for multi-omic analysis by MALDI IMS. Beginning with general steps for growing, embedding, and cryosectioning biofilms which are applicable to IMS of any analyte class. Next, specific details for analysis of lipids, peptides, and intact proteins are discussed.

## Results

### *Strategies for Preparing S. aureus Biofilms for MALDI IMS Analysis of All Analyte Classes*

#### Biofilm Growth

It is noteworthy that *S. aureus* biofilms are comprised of bacteria bound to one another via a soft extracellular matrix.<sup>164</sup> Manipulating *S. aureus* biofilms without damaging their structure presents a significant challenge for preparing them for downstream IMS. To this end, a polycarbonate filter disc with a 0.1  $\mu\text{m}$  pore size was used to provide a structural scaffolding on which the biofilm can grow. In all experiments

below, the filter disc was placed on the media and bacterial liquid culture was pipetted onto the disc filter and incubated to allow for biofilm development.

Many types of bacterial growth media including tryptic soy agar (TSA) and brain-heart infusion (BHI) offer *S. aureus* the necessary nutrients for growth. Each medium contains different combinations of nutrients, often leading to different strains of bacteria growing preferentially on specific media. Previous studies reported that *S. aureus* biofilms grew efficiently on BHI, or TSA with 3% NaCl and 0.5% dextrose added.<sup>181</sup> Here, the optimal growth medium for growing USA300 LAC *S. aureus* as a biofilm was assessed. To do this, *S. aureus* biofilms were grown on different media for equal time periods and biofilm thickness was measured.

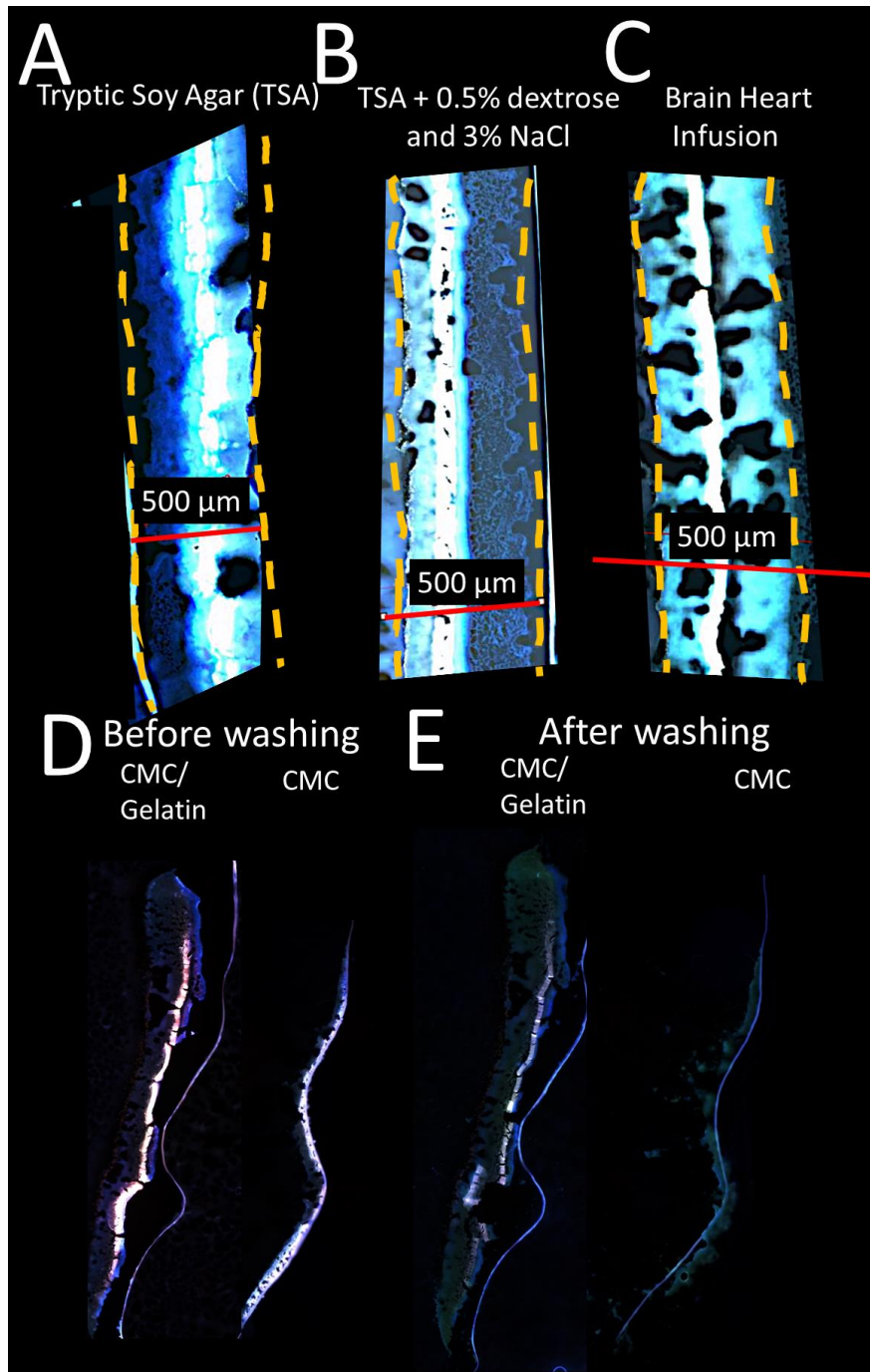
*S. aureus* biofilms grown on TSA, BHI and TSA with added NaCl and dextrose were embedded, cryosectioned, and thaw-mounted on microscope slides. Each sample was then subjected to autofluorescence microscopy where biofilm thickness could be assessed. BHI was found to generate the thinnest biofilms overall, with an average thickness of less than 500  $\mu\text{m}$ . In addition, no measurable difference was observed in thickness between biofilms grown on TSA alone or TSA with added NaCl and dextrose (**Figure 2.1A - C**). For these reasons, all future experiments were performed by growing biofilms on TSA alone.

### Embedding

Unlike other bacterial species such as *P. aeruginosa*, *S. aureus* biofilms grown *in vitro* often lack structural rigidity, making it challenging to retain their morphology during IMS sample preparation. For these reasons, it is necessary to embed the biofilm in some form of matrix to provide additional rigidity and aid the biofilm structure to survive the remainder of sample preparation for MALDI IMS. Traditional embedding materials, such as optimal cutting temperature (OCT), interfere with MALDI IMS analysis by introducing severe spectral interferences. As a result, two different embedding materials were assessed for optimal structure retention of *S. aureus* biofilms.

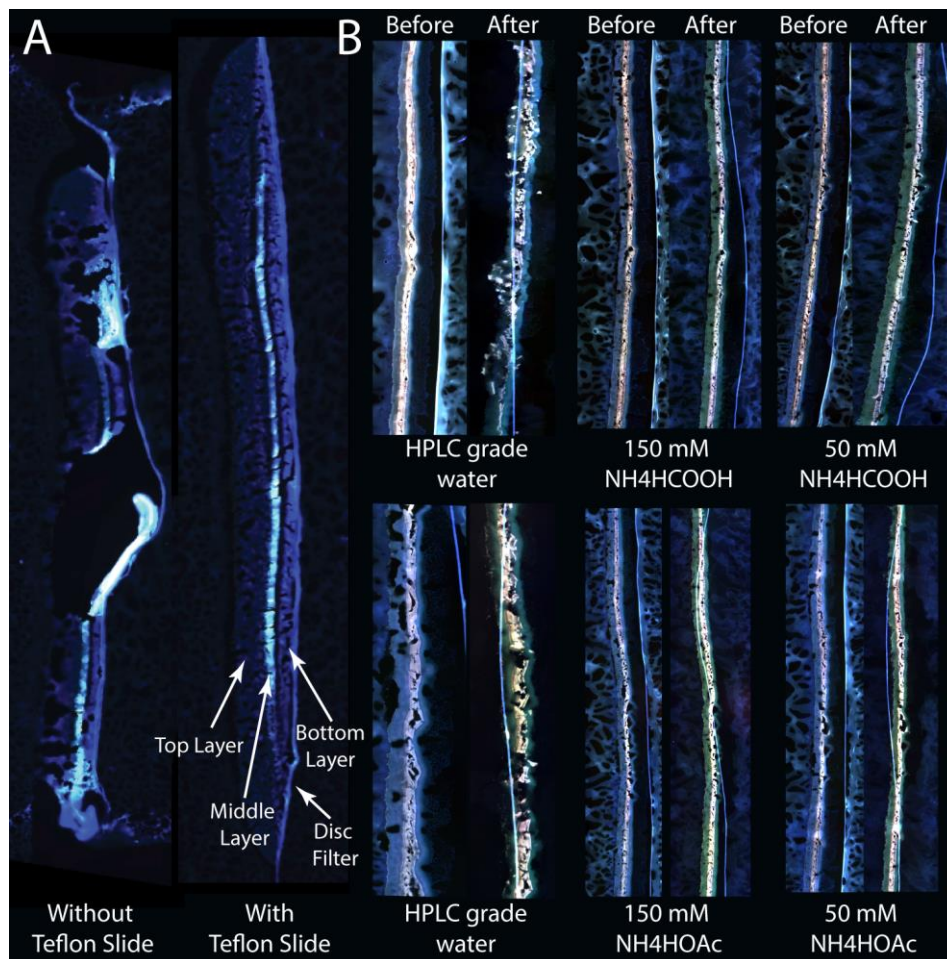
Carboxymethylcellulose (CMC) and a mixture of CMC and gelatin (5% and 10% w/w, respectively) were selected for investigation. Both of these embedding materials have a history of being used for tissue embedding and have shown great promise for

application in MALDI IMS because they do not ionize and therefore do not generate spectral interferences.<sup>182</sup>



**Figure 2.1.** Autofluorescence microscopy of *S. aureus* biofilm structures for comparison of the effects of various growth media, TSA (A), TSA + 0.5% dextrose and 3% NaCl (B), and BHI (C) on biofilm thickness, and a comparison of different embedding materials for *S. aureus* biofilms including a mixture of CMC/gelatin and CMC alone before (D) and after washing (E).

Similar to the assessment of growth media, biofilms were embedded in each embedding material, cryosectioned, and thaw-mounted on a microscope slide. Autofluorescence again provided an assessment of biofilm structure retention. Although both embedding materials provided sound structural support for the biofilms during the cryosectioning process, the ultimate structure retention provided by the CMC/gelatin mixture was superior to the CMC alone (**Figure 2.1D - E**). Moreover, the CMC/gelatin mixture provided a much smoother cut during cryosectioning, leading to reduced risk of biofilm tearing. Thus, all subsequent experiments were performed by embedding the biofilms in the CMC/gelatin.

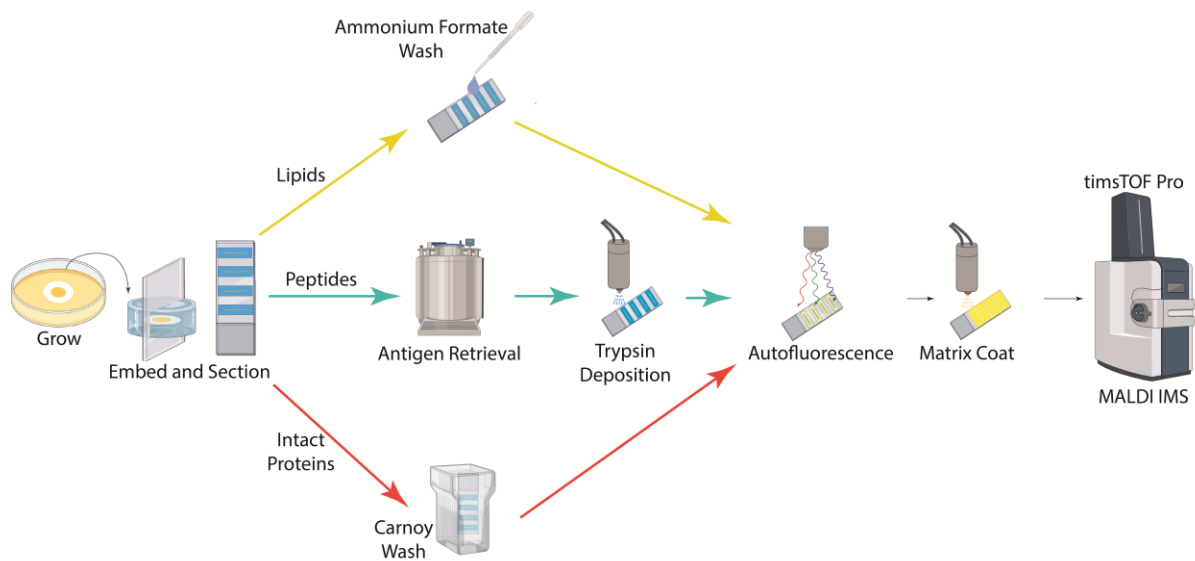


**Figure 2.2.** Autofluorescence of an *S. aureus* biofilm without, and with even adherence provided by the Teflon-coated slide, showing reduced shriveling of the biofilm with the Teflon-coated slide (**A**); Autofluorescence before and after washing with HPLC grade water, 150 mM and 50 mM ammonium formate ( $\text{NH}_4\text{HCOOH}$ ) and ammonium acetate ( $\text{NH}_4\text{OAc}$ ) (**B**).



## Cryosectioning

Although the success of cryosectioning is highly dependent on the preceding embedding step, several details specific to the *S. aureus* biofilm cryosectioning process were noted. In particular, thaw-mounting the biofilms to a microscope slide presented a significant challenge. Traditional cryosectioning methods simply require that the sample be placed on the microscope slide after which heat is applied from the bottom of the slide to induce thawing of the sample. This thawing adheres the sample to the surface of the microscope slide which can then be further processed for MALDI IMS. Inadvertent uneven heat application during this process can, however, lead to temperature differentials between different locations on the microscope slide. These temperature differentials may not have an effect when thaw-mounting mammalian tissue due to its inherent structural integrity, but *S. aureus* biofilms lack this structural integrity. As a result, these temperature differentials from thaw-mounting were found to lead to significant tearing of the biofilm (**Figure 2.2A**). To combat this, a Teflon-coated microscope slide was used to press down on the biofilm section, sandwiching the sample between the microscope slide and the Teflon-coated slide. This led to an even adherence of the biofilm to the microscope slide prior to thaw-mounting, allowing for a more even distribution of heat during the thaw-mounting process. This even adherence of the biofilm circumvents biofilm tearing, therefore aiding in the retention of biofilm morphology with discrete layers (**Figure 2.2**). Following this process of thaw mounting, workflows can diverge with specific steps for multi-omic analysis. (**Figure 2.3**).



**Figure 2.3.** Multi-omic MALDI IMS workflow for *S. aureus* biofilms, beginning with growing, embedding and cryosectioning for MALDI IMS of any of the three analyte classes discussed. Following cryosectioning, the workflow diverges for lipids, peptides, or intact proteins.

### *Specific Steps for Analysis of Biofilm Lipids, Peptides, or Intact Proteins*

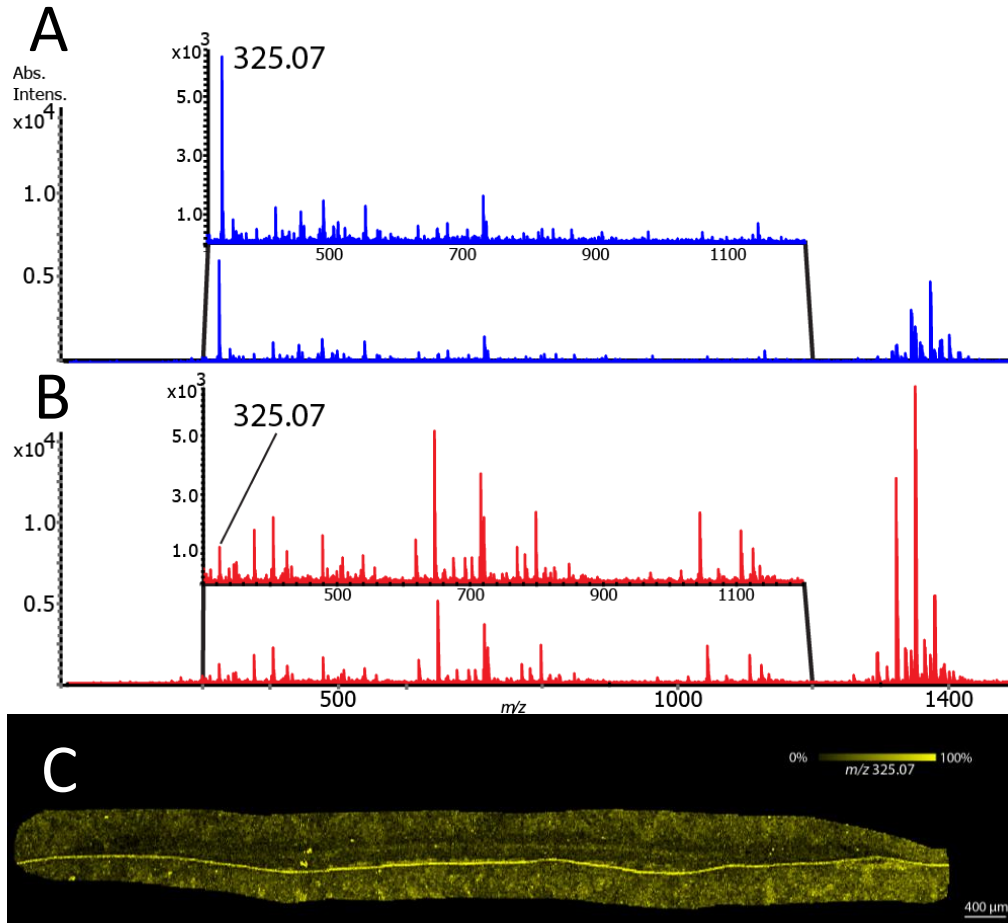
#### Salt Remediation for Lipid Analysis

As discussed above, spectral interferences from exogenous molecules such as salts can cause significant losses in analyte sensitivity. Salts such as sodium chloride are required for bacterial growth and are common additives in media. TSA ingredients include 12.5% (w/w) NaCl, leading to a significant challenge for downstream MS. A common method for combatting salt-induced spectral interferences is the addition of a washing step. Following thaw-mounting, washing the sample with a solvent in which the exogenous salts are soluble can significantly reduce spectral interferences. Another consideration, however, is the tonicity of the solvent used. Washing with a solvent that is isotonic to the bacterial cell is necessary as highly hypertonic or hypotonic solvents can lead to lysing of the bacterial cells, causing structural damage to the biofilm. For these reasons, use of various solvents were explored for their abilities to reduce

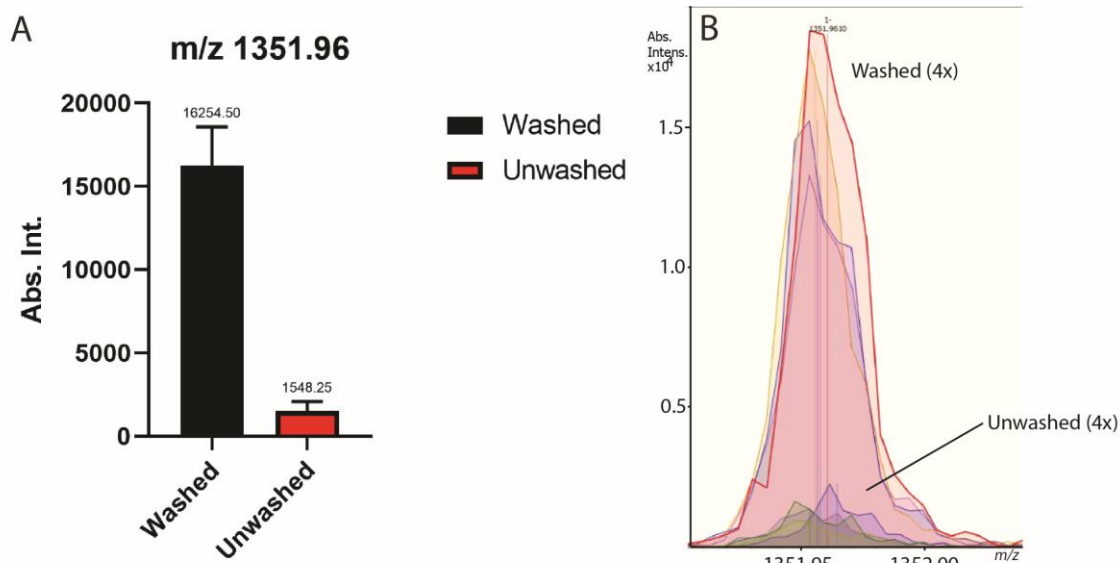
spectral interferences and enhance analyte signal without causing structural damage to the biofilm.

HPLC grade water and both 50 mM and 150 mM solutions of ammonium formate and ammonium acetate were assessed for removing the salt and other additives present in growth media. Sample loss resulting from each wash procedure was determined by autofluorescence microscopy by comparing before and after wash images. Of all the washes, 150 mM ammonium formate minimally perturbed sample morphology (**Figure 2.2B**), while water caused the most damage.

Furthermore, it was determined that washing with 150 mM ammonium formate yielded increased lipid signal for lipid species above  $m/z$  300, especially enhancing CL lipid signal (**Figure 2.4A – B**) compared to unwashed samples. For example, CL(64:0) displayed a more than ten-fold enhancement after washing when analyzed in quadruplicate (**Figure 2.5A – B**). The identity of the predominant peak measured at  $m/z$  325.07 in the unwashed samples is unknown, however it was determined to localize to the matrix around the biofilm and primarily to the filter disc. It is likely a chemical interference from the bacterial culture or sample preparation process being remediated by the washing step (**Figure 2.4C**).



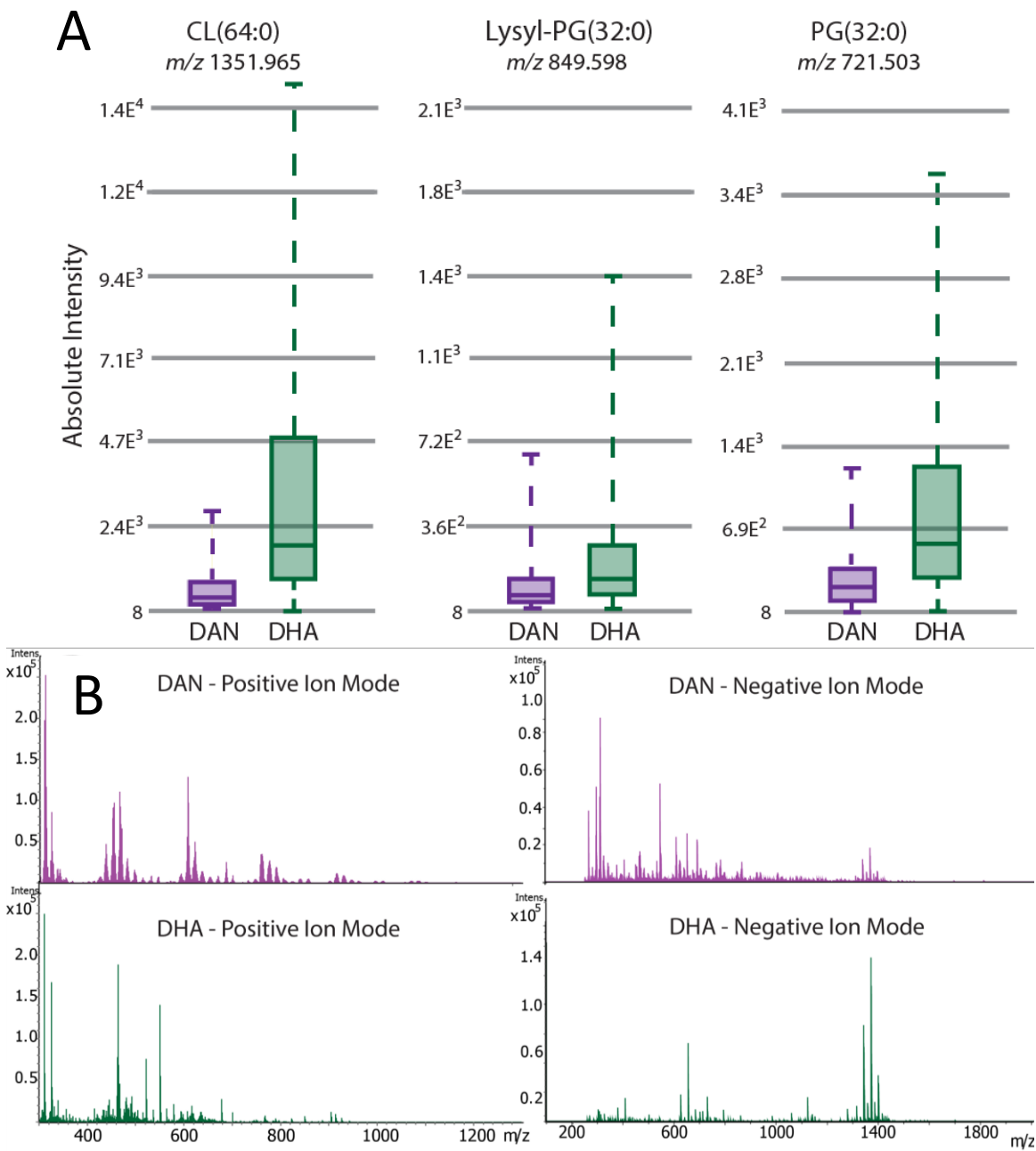
**Figure 2.4.** Mass spectra before (A), and after (B) washing show that washing also enhances signal of lipids, while reducing signal of chemical noise. Ion image of  $m/z$  325.07, showing localization to the filter disc and matrix around the biofilm (C).



**Figure 2.5.** Comparison of signal intensity measured for CL(64:0) at  $m/z$  1351.96 between washed and unwashed samples where four biofilm serial sections were analyzed for each group. A bar graph demonstrates a difference of over 10-fold between washed and unwashed sample means ( $p = 0.0006$ ) (A) and the resulting spectra for each replicate zoomed in on  $m/z$  1351.96, where each replicate peak can be seen (B).

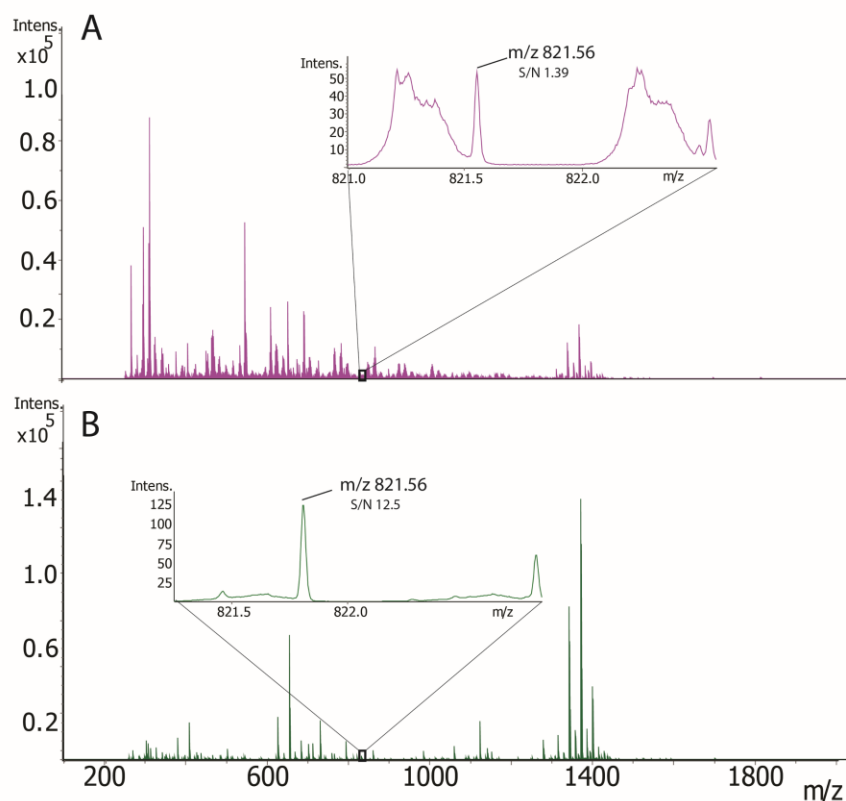
### Exploring Use of Two Dual-Polarity Matrices for Lipid Analysis

There are many MALDI matrices from which to choose when performing a MALDI IMS experiment. Each matrix offers an array of advantages such as ionization of certain classes of analytes, or effectiveness of ionizing in both negative and positive ionization modes. Disadvantages must also be considered such as in-source fragmentation and propensity for creating matrix-clusters.



**Figure 2.6.** Averaged mass spectra of positive and negative-ion mode MALDI analysis of *S. aureus* biofilms with DAN matrix (purple) and DHA matrix (green) demonstrating matrix clusters throughout the spectrum when DAN was used; **(A)**, Signal intensity box plots of CL(64:0), lysyl-PG(31:0) and PG(32:0) compare DHA and DAN matrices, demonstrating higher signal intensity for each lipid with DHA **(B)**.

For lipid analysis of *S. aureus* biofilms, both 2',6'-Dihydroxyacetophenone (DHA), and 1',5'-Diaminonaphthalene (DAN) matrices were assessed as they enable dual polarity imaging, thereby increasing the number and type of lipid species that can be detected. For effective comparison, MALDI analysis was performed on a *S. aureus* biofilm and PG(32:0), lysyl-PG(31:0) and CL(64:0) lipids were selected as representative of three unique and biologically important lipid classes. Absolute signal intensity for each of these lipids was compared for both MALDI matrices and in each case, DHA provided higher signal intensity than DAN (**Figure 2.6A**). Moreover, DAN matrix clusters were detected across the measured  $m/z$  range in both polarities (**Figure 2.6B**), increasing overall background signal and conflating with lipid species. For example, lysyl-PG(30:0) was detected with an interfering and overlapping ion using DAN, but fully resolved using DHA (**Figure 2.7A - B**).



**Figure 2.7.** Averaged mass spectra of negative-ion mode MALDI analysis of *S. aureus* biofilms with DAN matrix (purple) and DHA matrix (green) with spectra zoomed in on lysyl-PG(30:0) ( $m/z$  821.56) demonstrates spectral interferences around the peak of interest and low S/N in the data acquired with DAN (**A**), and no such interfering peaks in the data acquired with DHA (**B**).

To assess the effect of this on downstream lipid identifications, a LipidMAPS search of these datasets was performed comparing DAN and DHA where the number of annotated peaks using DHA was 388 compared to only 185 when DAN was used. Ultimately, DHA proved to be the superior matrix for this application by providing higher signal intensity for analytes of interest, without generating interfering ion clusters that cause challenges for identifying lipids and was therefore selected for all future experiments. With the establishment of optimal MALDI matrix for MALDI IMS analysis of *S. aureus* biofilms, all steps of the sample preparation process for lipid analysis were defined (**Figure 2.3**).

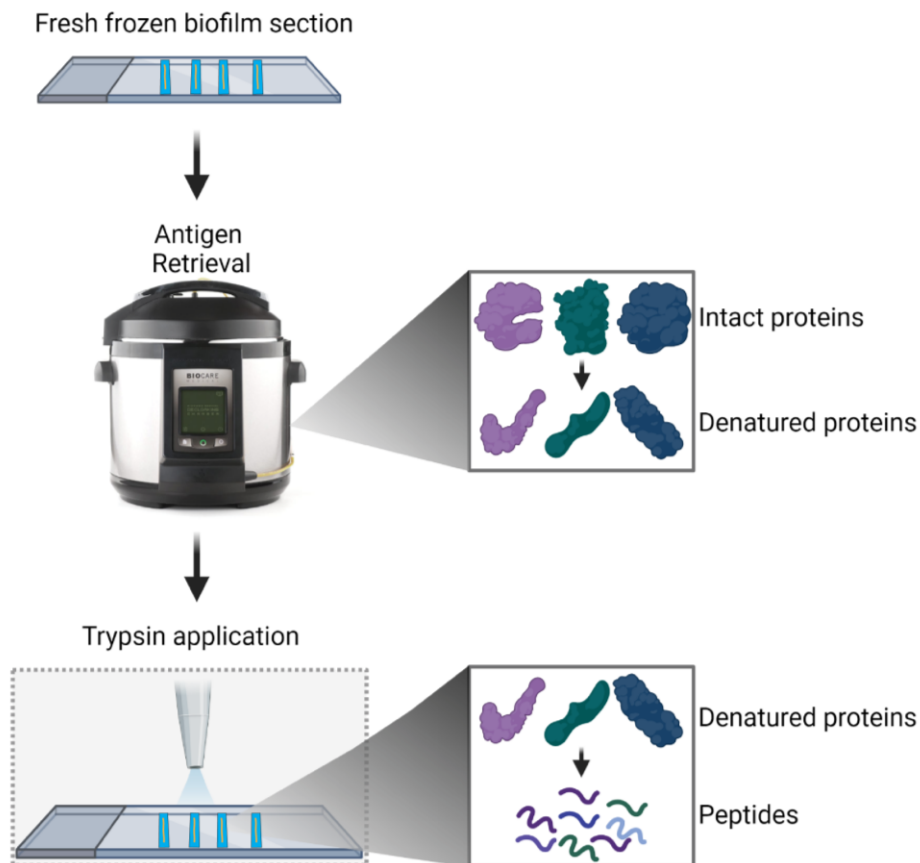
### Antigen Retrieval for Peptide Analysis

MALDI IMS of peptides relies upon many of the same principles utilized by traditional LC-based proteomics. Endogenous proteins are enzymatically digested into peptides for detection by MS, and detection of peptides with specific amino acid sequences can be linked back to a particular protein. Trypsin, the most common enzyme used for protein digests, cleaves proteins on the c-terminal side of lysine and arginine residues, and therefore requires access to as much of the protein sequence as possible. In traditional proteomics, proteins are extracted from a sample and maintained in solution during digestion, making access to the protein sequence easier to achieve than doing so directly on tissue. In an IMS experiment, trypsin can be applied by robotic sprayer directly onto the specimen for on-tissue digestion of endogenous proteins.

Historically, detecting proteins directly from tissue has presented many challenges. In particular, techniques for spatial investigation such as antibody-based methods like immunohistochemistry rely on access to binding sites on the endogenous protein within the tissue section.<sup>183</sup> These binding sites can be inaccessible while proteins are in their native state, decreasing sensitivity. One technique developed to address this challenge is antigen retrieval. This process consists of submerging the tissue section into a pH-balanced solution and applying heat. This heat acts to effectively denature the proteins within the tissue section, thereby rendering all binding sites on the protein accessible for downstream detection. For MALDI IMS of peptides, these principles can be exploited to provide accessibility to protein sequences for



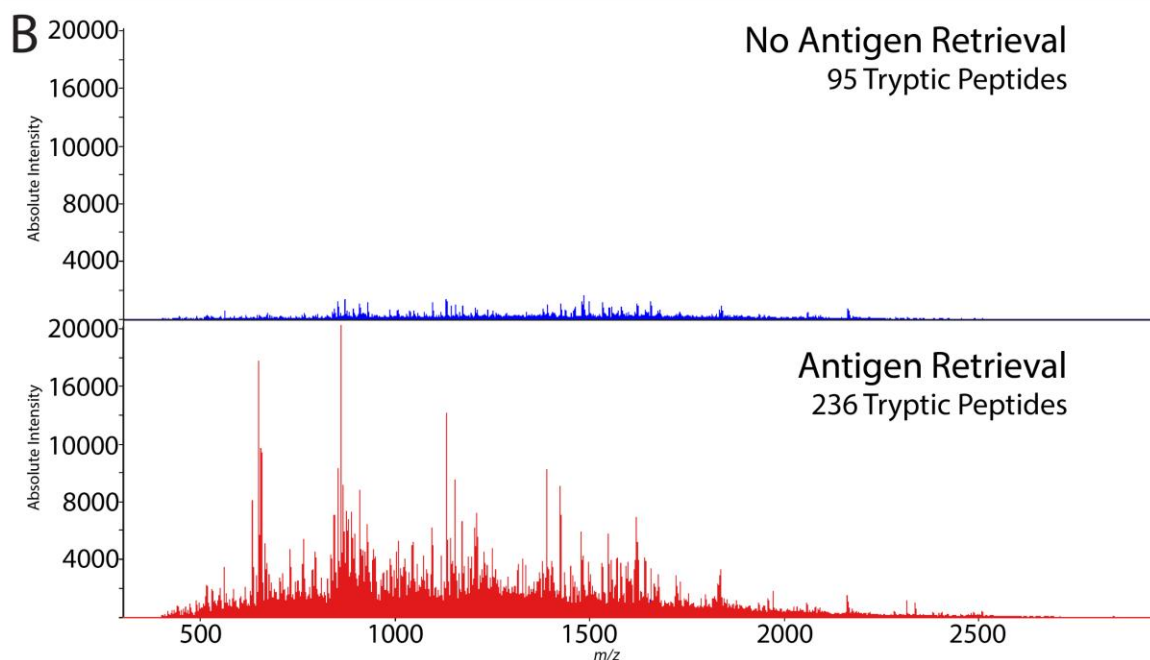
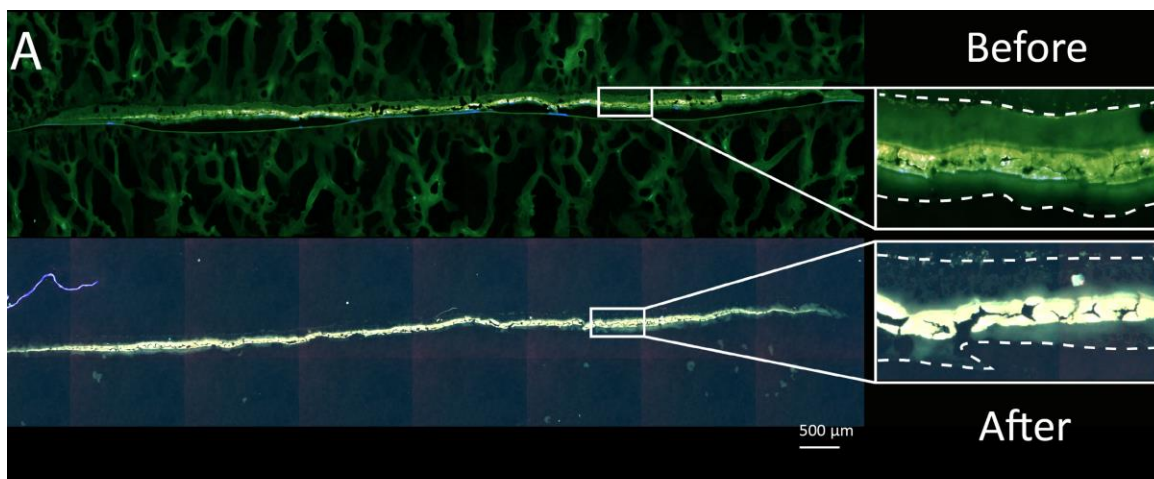
trypsin when applied directly on tissue. As a result, the workflow for MALDI IMS of tryptic peptides consists of mounting the sample onto a microscope slide, followed by antigen retrieval, trypsin application and overnight incubation before matrix application and data collection (**Figure 2.8**).



**Figure 2.8.** Sample preparation workflow for preparing *S. aureus* biofilms for on-biofilm trypsin digestions followed by downstream MALDI IMS of tryptic peptides.

Prior to spectral comparisons, it was important to assess the impact of antigen retrieval on the structural integrity of the biofilm sections. To do this, autofluorescence of biofilm sections was collected prior to performing antigen retrieval to establish the initial structure. Antigen retrieval was then performed and autofluorescence collected again to assess structural loss of the biofilm compared to the initial micrograph (**Figure 2.9A**).

Although some deterioration of the biofilm was noted, the overall loss was determined to be acceptable as bacterial autofluorescence signal was still observed at all locations within these biofilms. Antigen retrieval was therefore investigated further for its effect on MALDI detection of tryptic peptides. To probe the effectiveness of antigen retrieval for peptide MALDI IMS on *S. aureus* biofilms, two serial sections of a biofilm were prepared concurrently with only one being subjected to antigen retrieval prior to trypsin application. Following an overnight incubation for tryptic digestion and application of alpha-cyano-4-hydroxy-cinnamic acid (CHCA) matrix, mass spectra were collected by MALDI from both biofilms for spectral comparison. Here at least 236 peptides were detected from the biofilm that did receive antigen retrieval, where only 95 were detected from the biofilm that did not receive antigen retrieval (**Figure 2.9B**). This experiment demonstrates the necessity for performing this step on *S. aureus* biofilms for effective peptide analysis by MALDI. These data signified an established workflow for preparing *S. aureus* biofilms for analysis by MALDI, and downstream MALDI IMS could be attempted.



**Figure 2.9.** Effects of antigen retrieval on an *S. aureus* biofilm. Autofluorescence performed on the same biofilm section before and after antigen retrieval reveal some loss of biofilm structure as a result of AR; **(A)** and spectral comparisons of serial sections of *S. aureus* biofilms with (red) and without (blue) antigen retrieval demonstrating a substantial difference in the number of detected tryptic peptides **(B)**.

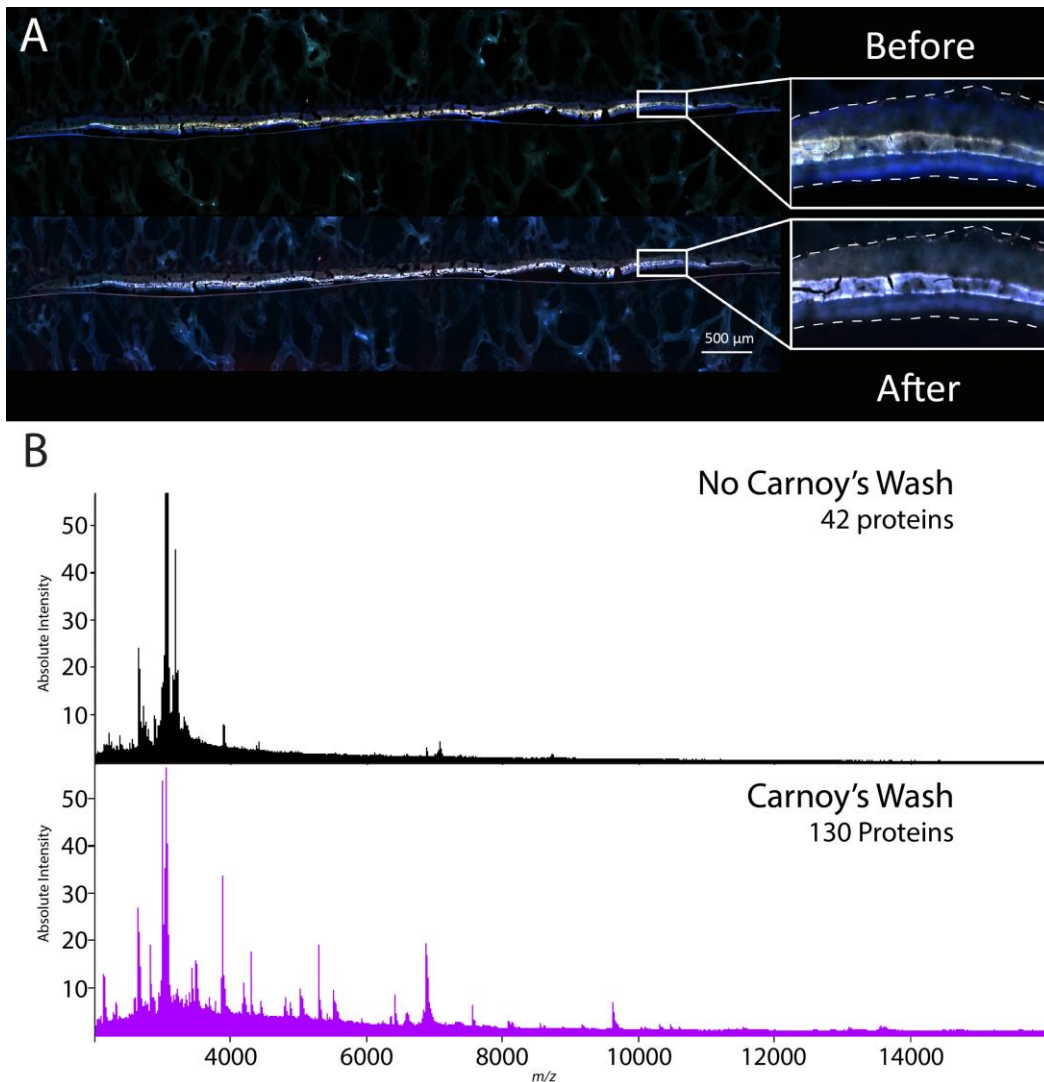
### Lipid Remediation for Intact Protein Analysis

Intact proteins present many of their own unique challenges for analysis by MALDI IMS. Transmission of high mass protein ions is difficult to achieve in many MALDI IMS platforms, and often requires instrument modifications such as lower radio

frequencies applied to ion optics, or significant alterations to MALDI source pressure. In addition, MALDI traditionally provides ionization of only singly charged ions, limiting the mass range of detectable proteins. This is in contrast to electrospray ionization which offers higher charge states, acting to lower the  $m/z$  of a high mass protein ion. Sensitivity can also be hampered by the lower natural abundance of proteins in a tissue section compared to other analyte classes such as lipids. Because endogenous lipid species are more abundant than proteins within a tissue section, and ionize with high efficiency by MALDI, they often act as spectral interferences during MALDI IMS analysis of intact proteins. Steps can be taken to remediate these interferences. For example, washing the sample with a solvent in which lipids are soluble and proteins are not can remove the undesired interferences, yielding higher sensitivity for the target analytes. Here, a Carnoy's wash containing chloroform was investigated for its effect on eliminating bacterial lipids from *S. aureus* biofilms for enhanced sensitivity of intact proteins by MALDI IMS.

*S. aureus* biofilms were grown, embedded, and cryosectioned as described above and two serial sections were prepared concurrently with only one receiving a Carnoy's wash. Prior to spectral comparisons, it was important to assess the impact the Carnoy's wash had on the structural integrity of the biofilm sections. To do this, autofluorescence of biofilm sections was collected prior to the Carnoy's wash to establish the initial structure. Autofluorescence collected following the Carnoy's wash revealed almost no loss of biofilm structure with only slight cracking of the middle layer, presumably due to dehydration from the organic solvents (**Figure 2.10A**). *S. aureus* biofilms were then coated with (E)-4(2,5-dihydroxyphenyl)but-3-en-2-one (2,5-cDHA) MALDI matrix and mass spectra were collected of both samples for comparison. The biofilm subjected to a Carnoy's wash yielded a rich spectrum of bacterial 130 proteins ranging from  $m/z$  2,000 – 17,000. In contrast, the sample that did not receive the Carnoy's wash yielded detection of only 42 proteins (**Figure 2.20B**). It is to be noted here, that although there are no spectral interferences detected at this mass range, the reduced sensitivity for intact proteins in this experiment is likely due to the intense presence of bacterial lipid species that are below the  $m/z$  2,000 lower mass limit leading to ionization of the endogenous lipids rather than intact proteins. Although these

preferentially ionized lipids are not within the  $m/z$  range of data acquisition, they still act as severe interferences and must therefore be removed for all future MALDI IMS analyses of intact proteins within *S. aureus* biofilms. With these results in hand, the specific sample preparation steps for MALDI analysis of intact proteins in *S. aureus* biofilms were determined, and MALDI IMS could be attempted as demonstrated in Chapter III.



**Figure 2.10.** Effects of's wash on an *S. aureus* biofilm. Autofluorescence performed on the same biofilm section before and after the wash reveal almost no loss of biofilm structure; (**A**) and spectral comparisons of serial sections of *S. aureus* biofilms with (purple) and without (black) a Carnoy's wash demonstrating a substantial difference in the number of detected intact proteins (**B**).

## Discussion

Performing multi-omic analysis of *S. aureus* biofilms by MALDI IMS presents an array of challenges for any class of analytes, from growing the biofilm, to embedding and cryosectioning. From there, analyte-specific challenges necessitate specific steps for effective measurement. For lipids, washing with ammonium formate to remediate residual salt from bacterial growth media proved critical, increasing CL signal by as much as tenfold while decreasing interfering ions in the low mass range. While this analysis could be performed without the washing step, the 150 mM ammonium formate yielded a higher sensitivity for bacterial lipid species, potentially providing greater molecular insight to the experiment. Further, DHA and DAN MALDI matrices were compared for bacterial lipid signal of *S. aureus* biofilms. DAN was found to produce matrix clusters in both positive and negative polarities that led to more convoluted spectra and decreased confidence in lipid identification. DHA provided intense lipid signal, and did not produce significant spectral interferences, and was consequently selected as the optimal MALDI matrix for *S. aureus* biofilm lipid analysis.

Performing antigen retrieval prior to MALDI IMS proved imperative for investigating peptides, where significantly more peptides were observed from *S. aureus* biofilms when antigen retrieval was performed. This is likely due to the denaturing of bacterial proteins as a direct result of antigen retrieval,<sup>184</sup> providing trypsin with access to the primary structure of proteins for an efficient digestion. Another possible explanation for this difference is that antigen retrieval acted to lyse the bacterial cell wall, providing trypsin with access to penetrate the thick cell wall of the gram-positive *S. aureus* bacteria and reach endogenous proteins more efficiently. Antigen retrieval proved imperative for peptide analysis of *S. aureus* biofilms by MALDI, affording future steps to be taken towards spatial analysis of tryptic peptides by MALDI IMS.

Finally, a Carnoy's wash containing chloroform was found to be necessary for obtaining signal of intact proteins from *S. aureus* biofilms by MALDI IMS. The non-polar washing step acted to remediate bacterial lipids from the biofilm sample, eliminating spectral interferences and greatly improving the sensitivity for intact proteins. Importantly, this washing step exploited chemical characteristics of chloroform to

dissolve and remove lipids while leaving the water-soluble proteins largely unperturbed. Although each of the aforementioned specific requirements for investigating individual analyte classes cannot be performed on a single biofilm section, they can be performed on serial sections of a biofilm, allowing for downstream multi-omic, spatial investigations of these bacterial communities.

## Methods

### Lipids

2',6'-Dihydroxyacetophenone (DHA), 1',5'-Diaminonaphthalene (DAN), ammonium formate, ammonium acetate, and poly-L-lysine solution were purchased from Sigma-Aldrich Chemical Co. (St. Louis, MO, USA). HPLC-grade acetonitrile, methanol, and gelatin powder were purchased from Fisher Scientific (Pittsburgh, PA, USA). Carboxymethylcellulose (CMC) was purchased from PM MP Biomedicals (Salon, OH). Tryptic soy agar (TSA) and tryptic soy broth (TSB) were purchased from Becton, (Dickinson, Franklin Lakes, NJ) and all lab plasticware was from USA Scientific (Ocala, FL) or Corning (Corning, NY). Filter discs were Whatman Nuclepore (0.1  $\mu\text{m}$  pore size) acquired from Millipore Sigma (Burlington, MA).

*S. aureus* bacterial cultures and biofilm growth. *S. aureus* USA300 LAC was streaked on TSA and incubated at 37°C. Single colonies were picked and used to inoculate 5 mL of TSB in 15 mL polypropylene tubes. Tubes were agitated for 16 hr at 37°C. Twenty microliters were then pipetted onto filter discs on TSA plates and incubated at 37°C for a total of 72 h. During this time, filter discs were transferred to fresh TSA plates every 24 h. After 72 h growth, *S. aureus* biofilms were embedded in a CMC/gelatin mix and frozen at -80°C, cryosectioned to a 10  $\mu\text{m}$  thickness using a CM3050 S cryostat (Leica Biosystems, Wetzlar, Germany), and thaw-mounted onto conductive indium tin oxide coated glass slides (Delta Technologies, Loveland, CO, USA) coated with poly-L-lysine. Washing was performed using an eyedropper 3X for 30 s and dried in a vacuum desiccator. Autofluorescence microscopy images were acquired using EGFP, DAPI, and DsRed filters on a Zeiss AxioScan.Z1 slide scanner (Carl Zeiss Microscopy GmbH, Oberkochen, Germany) before matrix application. Briefly, 150 mg of DHA was dissolved in 10 mL of a methanol/acetonitrile/water

(80:10:10) solution and applied to a density of 2.08  $\mu\text{g}/\text{mm}^2$  by an M5 TM sprayer (HTX Technologies, Chapel Hill, NC). DAN was applied similarly by dissolving 100 mg into acetonitrile/water (90:10) and spraying to a density of 1.67  $\mu\text{g}/\text{mm}^2$ .

### Peptides

Alpha-cyano-4-hydroxy-cinnamic acid (CHCA) matrix, ammonium formate, ammonium acetate, and trifluoroacetic acid (TFA) were purchased from Sigma-Aldrich Chemical Co. (St. Louis, MO, USA). Trypsin was purchased from Promega (Madison, WI).

*S. aureus* biofilms were grown, embedded, and cryosectioned as described above. Following thaw-mounting, antigen retrieval was performed. Those samples undergoing antigen retrieval were submerged in a solution of tris base (pH 9) and placed in a decloaking chamber for 20 min at 90° C, followed by a 10 min cooldown. Samples were then rinsed with milli-Q water. Enzyme application was performed by spraying 400 $\mu\text{L}$  of trypsin in ammonium bicarbonate and 40% acetonitrile using an HTX sprayer. Biofilm sections were digested in a humidity oven at 100% humidity and 37° C for 16 hours. CHCA matrix was applied at a concentration of 5mg/mL in 90% acetonitrile with 0.1% TFA for 6 passes using a TM Sprayer (HTX Technologies, LLC, Chapel Hill, NC).

### Intact proteins

(E)-4(2,5-dihydroxyphenyl)but-3-en-2-one (2',5'-cDHA) was synthesized in-house. Indium-tin-oxide (ITO)-coated microscope slides were purchased from Delta Technologies (Loveland, CO). Agilent Tuning mix was purchased from Agilent (Santa Clara, CA). Water, chloroform, acetonitrile, ethyl acetate, acetic acid and formic acid were purchased from Fisher Scientific (Waltham, MA).

Biofilms were grown, embedded and cryosectioned as described above. For those biofilms receiving a Carnoy's wash, following thaw-mounting, *S. aureus* biofilms were subjected in sequence to a submersion in 70% ethanol, 90% ethanol, 95% ethanol, and 100% ethanol for 30 s each. Next, samples were submerged in Carnoy's solution containing chloroform and methanol (6:3) for 3 min, followed by 90% ethanol,



and finally pure water for 30 s each. After drying, all samples were coated with cHDA matrix following a previously published method.<sup>185</sup> Briefly, a 3 mg/mL solution of cHDA dissolved in ethyl acetate and toluene (1:1) was applied, followed by a second application of 9 mg/mL solution dissolved in ACN/H<sub>2</sub>O (3:7) with 1% TFA and 0.5% ammonium hydroxide, each using a TM Sprayer (HTX Technologies, LLC, Chapel Hill, NC). Tissues were rehydrated by suspending samples over 1 mL of 50 mM acetic acid for 3 min at 37° C.

## **CHAPTER III**

### **CHARACTERIZATION OF INSTRUMENTAL PARAMETERS FOR EFFECTIVE MALDI IMS ANALYSIS OF LIPIDS, PEPTIDES, AND INTACT PROTEINS ON A TIMSTOF PRO**

#### **Introduction**

With the advent of the timsTOF Pro, biomolecular analyses can be performed with previously unmet speed, mass resolving power, and added TIMS dimension for increased sensitivity and specificity. As described in detail in Chapter I, these qualities make the timsTOF uniquely suited for complimentary analyses of different analyte classes such as lipids, tryptic peptides, and intact proteins. Several liquid chromatography-based omic analyses on the timsTOF Pro have been previously reported,<sup>151,186</sup> taking advantage of these analytical characteristics, but do not provide spatial information. Because integration of the timsTOF Pro with MALDI for imaging capabilities was only developed recently, these analytical advantages have not yet been applied to a spatial, multi-omic study. Specific instrumental strategies for such a workflow have not yet been defined and are therefore explored herein. The work outlined below provides specific information regarding the optimization and validation of the timsTOF Pro for MALDI IMS analyses of bacterial lipids, tryptic peptides, and intact

proteins. These strategies were then applied to the spatial, multi-omic investigation of *S. aureus* biofilm layers.

Characterization of this instrument platform affords the complimentary spatial analysis of lipids, tryptic peptides, and intact proteins on a single platform. Although the instrumental methodologies curated here were ultimately applied to the investigation of *S. aureus* biofilms, they demonstrate the full extent of the capabilities of the timsTOF Pro for spatially aware multi-omic investigations. The work herein has the potential to be applied toward any biological question for which MALDI IMS can be informative, with unparalleled speed, mass resolving power, and spatial resolution and is therefore of great value to the IMS community.

For each class of analytes investigated, systematic studies were performed beginning with the MALDI analysis of commercially available standards, followed by MALDI IMS examples on control tissue in Part I of this chapter. In Part II, these methodologies were then applied towards the spatial investigation of horizontal layers within *S. aureus* biofilms. Beyond specific sample preparation strategies described in Chapter II, each of the analyte classes also require unique instrumental parameters to be optimized for effective analysis. Perhaps most obviously, differences in mass range between these analyte classes represents a major challenge for multi-omic analyses on a single platform. Most endogenous lipids are detected between  $m/z$  ~500 – 1500, whereas tryptic peptides range from  $m/z$  ~500 to often in excess of  $m/z$  3000. Finally, intact proteins are large macromolecules with high molecular weights that can exceed 3 million Da.<sup>187</sup> While QTOF mass spectrometers are capable of detecting ions up to or exceeding  $m/z$  20,000, instrumental parameters must be optimized for effective ion transmission at each mass range. Specifically, based on principles covered in Chapter I, high mass molecules require more time to reach components of the instrument, making timing of any electric potentials critical for each mass range. Similarly, transmission of larger molecules has been shown to require lower pressures to achieve effective transmission through the mass spectrometer.<sup>188</sup> Beyond mass spectrometric parameters, the implementation of TIMS in these analyses provides many analytical advantages, but further narrows the range of ion transmission for a given experiment.

Each of these challenges for effective analysis of lipids, tryptic peptides, and intact proteins by MALDI TIMS IMS is addressed in the work described herein.

## Results

### Part I

#### *Technological Considerations for Lipid Analysis by MALDI TIMS IMS*

##### Overview

Lipids represent a vital class of biomolecules in biology with roles ranging from energy storage<sup>189</sup> to signaling<sup>190</sup> and various classes of lipids can be found in nearly all facets of life. In *S. aureus* biology, lipids are responsible for membrane composition to evasion of the host immune response,<sup>125–127</sup> among many other processes. In eukaryotic multi-cellular organisms, many lipids are associated with specific cell types, resulting in spatially discrete localizations. Bacterial biofilms are also multi-cellular and have been demonstrated to contain bacteria that are in different phenotypic states with different biomolecular profiles.<sup>34</sup> Advances in LC-MS/MS strategies over the past three decades have provided robust analysis options for lipids from gross extractions. While these options often provide high dimensionality with various types of chromatography and routine MS/MS for obtaining fragmentation, they do not provide spatial information. Recent developments in the field of MALDI IMS have afforded next-generation spatial exploration of different biomolecules, improving data quality. One of these advancements, as described in detail in Chapter I, is the integration of MALDI IMS with various forms of ion mobility.<sup>27</sup> In particular, the advent of the timsTOF Pro by Bruker Daltonics is the first commercial mass spectrometer coupled with trapped ion mobility spectrometry (TIMS).<sup>55</sup>

Prior to its integration with MALDI, the timsTOF Pro had been in production for several years with only electrospray ionization (ESI) offered for LC-MS/MS workflows.<sup>26,191</sup> During this time, it was proven as a robust instrument for proteomic and

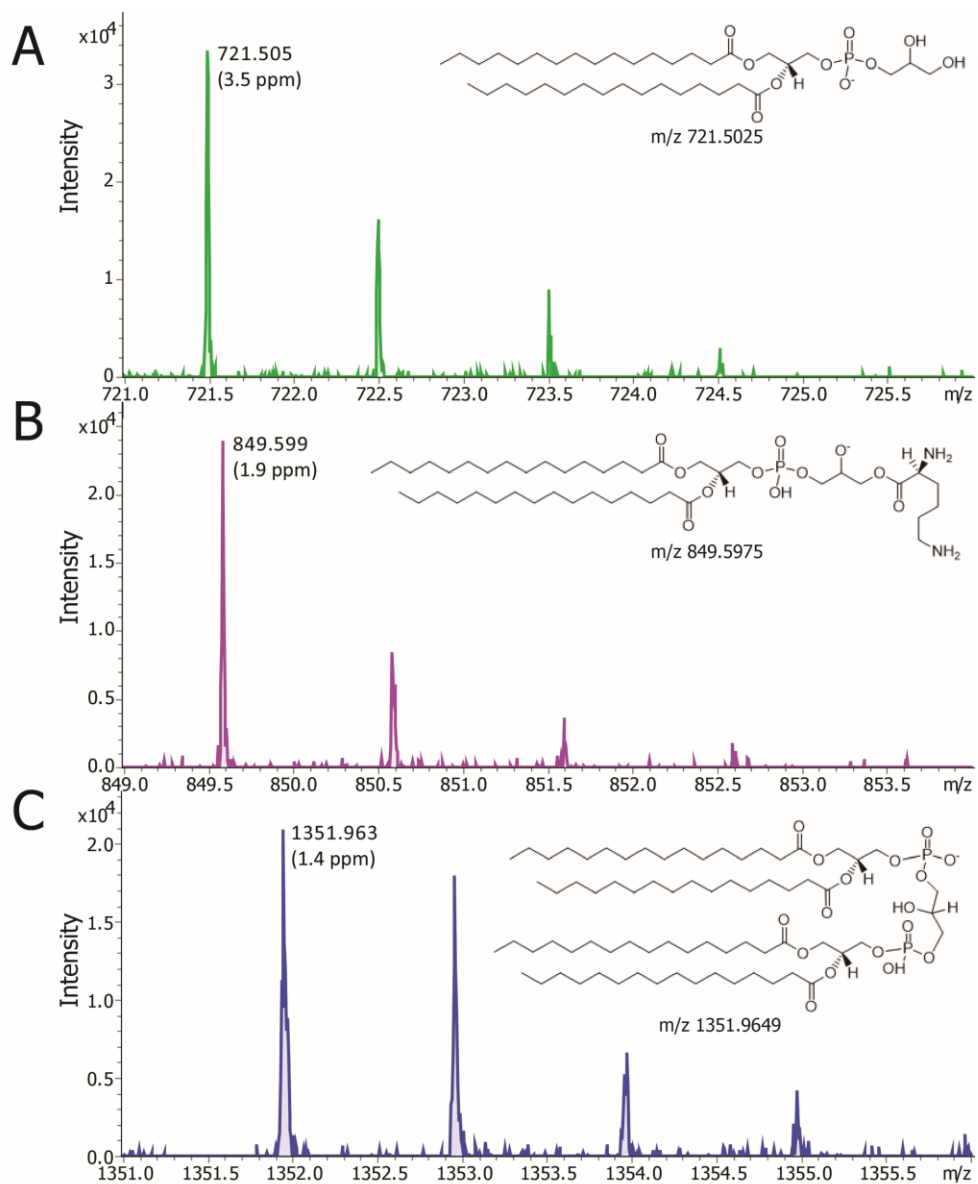
lipidomic studies with the orthogonal dimensionality of TIMS providing increased sensitivity and peak capacity.<sup>192</sup> Ultimately, efforts to equip the timsTOF Pro with a MALDI source capable of performing high quality IMS experiments were led by the Caprioli laboratory.<sup>55</sup> The resultant instrument is a platform capable of high spatial resolution MALDI IMS (5-10  $\mu\text{m}$ ) on a QTOF MS that provides  $\sim 40,000$  resolving power across the entire mass range, coupled to TIMS for added sensitivity and peak capacity in an IMS experiment. These qualities make it ideally suited for high spatial resolution MALDI IMS investigations of *S. aureus* biofilm cross-sections.

### Analysis of Bacterial Lipid Standards

As described above, previously published work by Spraggins *et al.* demonstrated the capabilities of the timsTOF Pro for MALDI IMS analyses of lipids directly from mammalian tissue.<sup>55</sup> Before performing MALDI IMS on *S. aureus* biofilms, it was prudent to assess the instrument for the detection of bacterial lipids using commercially available standards. Three representative lipid species from the most common lipid classes in *S. aureus*,<sup>193</sup> (PG(32:0), lysyl-PG(32:0), CL(64:0)) were selected for standard analysis. These lipid standards were not only selected for their predominance in *S. aureus*, but because they all share the same fatty acyl tail length of 16:0. In fact in *S. aureus*, PG(32:0) is the substrate used to synthesize both lysyl-PG(32:0) and CL(64:0) through enzymatic reactions.<sup>137,194</sup> By separately mixing each of these standards with DHA matrix, MALDI investigations revealed sensitive detection of each standard (**Figure 3.1A – C**). Specifically, PG(32:0) was detected with a S/N of 29.5 at  $m/z$  721.505 and low mass error compared to theoretical (3.5 ppm) (**Figure 3.1A**). Similarly, lysyl-PG(32:0) and CL(64:0) were detected with S/N of 40.5 and 23.9, and mass errors of 1.9 and 1.4, respectively (**Figure 3.1B – C**).

In addition to the mass spectral data collected for each of these bacterial lipid standards, the TIMS dimension was also applied for increased sensitivity. Overall, these results clearly demonstrated the capability of the timsTOF Pro to analyze relevant bacterial lipids by MALDI with high sensitivity and low mass error. These results, in combination with the work published by Spraggins *et al.*, demonstrated that the timsTOF Pro is capable of high-performance MALDI IMS of lipids directly from tissue, as

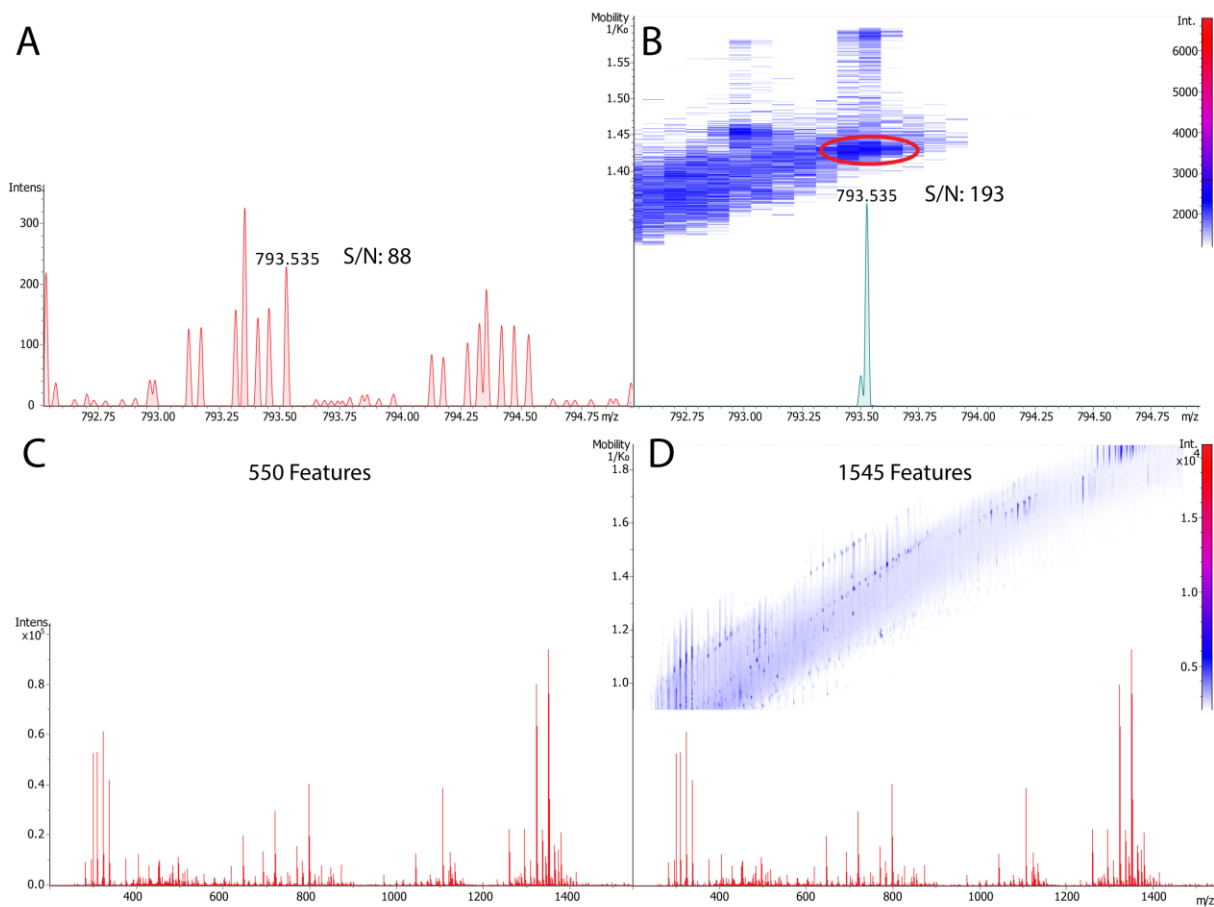
well as sensitive detection of bacterial lipid species. Now fully validated for *S. aureus* biofilm MALDI IMS, imaging of biofilm cross-sections could be performed.



**Figure 3.1.** MALDI spectra and structures of PG(32:0) (A), lysyl-PG(32:0) (B) and CL(64:0) (C).

### Applying TIMS for Lipid Analysis of *S. aureus*

The combination of qualities offered by a QTOF MS platform and those offered by TIMS, made it a clear choice for performing the spatial investigations herein. The contributions of TIMS were first assessed by comparing peak capacity and signal-to-noise (S/N) with, and without TIMS separation implemented in an imaging experiment. Specifically, a MALDI experiment was performed on an *S. aureus* biofilm to compare data quality with and without TIMS. Without considering the TIMS dimension, detection of 550 features was achieved (**Figure 3.2C**). Low signal intensity for various lipids such as lysyl-PG species was observed with relatively low S/N. Considering the TIMS dimension however, S/N was increased for most detected lipid species. For example, lysyl-PG(28:0) ( $m/z$  793.535) was detected with a S/N of 88 (**Figure 3.2A**), but by excluding noise at ion mobility values other than the lipid of interest, S/N was found to be improved by more than two-fold (S/N 193, **Figure 3.2B**). Furthermore, when the TIMS dimension was considered for the dataset as a whole, ion mobility separation revealed ~1,000 additional detected features (1,545), likely consisting of isobars, isomers, and conformers of detected analytes (**Figure 3.2D**). Chemical specificity was also enhanced by TIMS, and many ions of interest were observed with notable peak tailing in the TIMS dimension, which could be due to slight separation of additional confounding species from the ion of interest at similar  $m/z$ . By selecting a narrow window around the peak of interest, extraneous species were excluded to enhance chemical specificity. As a result, all analyses herein were performed with TIMS to reduce the overall spectral noise and increase chemical specificity.



**Figure 3.2.** Averaged mass spectrum of a negative-ion mode IMS experiment of *S. aureus* biofilm, zoomed in to range  $m/z$  792.5 – 795.0 showing lysyl-PG(28:0) with a S/N of 88 without the TIMS dimension considered (A), and S/N of 193 when the TIMS dimension is considered (B). Averaged mass spectrum of the same negative-ion mode IMS experiment as above with 550 features detected when no TIMS was considered (C), and 1,545 features when TIMS was considered (D).

### *Technological Considerations for Peptide Analysis by MALDI TIMS IMS*

#### Overview

Proteins are responsible for an enormous variety of biological processes in all organisms. Advancements in the field of proteomics have expanded the ability to measure changes in protein abundance, modification, and conformation. Development, environment, and disease have profound and nuanced impacts on the proteome of cells

and tissues. Pancreatic beta cells are responsible for insulin production but become dysfunctional and die during diabetes progression.<sup>195</sup> Beta cells are found within islets that are distributed among exocrine, ductal, and vascular tissues.

While studies of homogenized tissue or dissociated cells are invaluable, spatial proteomics approaches can complement the former by isolating specific anatomical structures within complex tissues such as the pancreas.<sup>196</sup> Some spatial proteomic workflows target a specific tissue region of interest for digestion and identify peptides in the resulting sample using liquid chromatography tandem mass spectrometry (LC-MS/MS). One such technology is micro-liquid extraction surface analysis (microLESA) which deposits a drop of trypsin approximately 110µm in diameter on a specific tissue coordinate, performs an on-tissue digestion, and uses a surface extraction to collect peptides from the digested region.<sup>197</sup> Another technology with a similar goal is laser capture microdissection (LCM) which uses a cutting laser to excise a specific tissue region for tryptic digestion. For each of these methods, specific tissue regions must be selected, and the sample preparation time is extended compared to homogenate analysis.

MALDI IMS is a powerful approach to generate spatially resolved proteomics data. Peptide imaging specifically allows for analysis of tryptic peptides representing the entire theoretical proteome that can be directly related to a precursor protein. In contrast, intact protein imaging is often limited by transmission of high mass ions. Performing concomitant MALDI IMS and LC-MS/MS provides in situ information about complex samples that would otherwise be lost during tissue homogenization and can be used to complement one another.

In IMS experiments, peptides are detected and assigned putative identifications by their intact mass, and peptide detection relies heavily on the resolution of the mass spectrometer. TIMS provides gas-phase separation of ions prior to mass analysis which can afford distinction of isobaric molecules and increase sensitivity.<sup>55</sup> In addition, this separation results in increased peak capacity and the addition of an orthogonal mobility measurement ( $1/K_0$ ) which could be used for increasing confidence in peptide identification. As such, the timsTOF Pro is ideally suited for the detection of peptides because they are very complex molecules that can adopt conformers or closely related



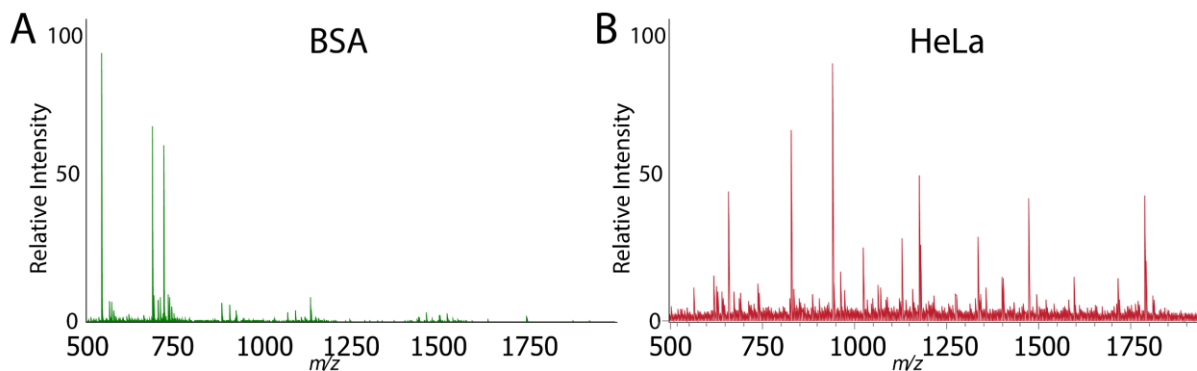
isoforms with similar masses but different biological functions. Herein the utility of the timsTOF for peptide MALDI IMS is demonstrated beginning with MALDI analysis of peptide standards, followed by MALDI IMS of human tissue as a proof-of-concept. Finally, these methodologies were applied to spatial investigation of horizontal layer heterogeneity within *S. aureus* biofilms.

### Analysis of Peptide Standards

To validate the timsTOF Pro for effective analysis of peptides by MALDI IMS, a simple peptide mixture was analyzed first. Bovine serum albumin (BSA) was chosen for this initial analysis due to its longstanding use in traditional bottom-up proteomics as a quality control standard.<sup>198</sup> Following tuning for increased mass range for tryptic peptides, MALDI analysis of BSA was performed by mixing the digested BSA standard with CHCA matrix and applied to a MALDI target. Here, at least 11 tryptic peptides from this single protein were detected with S/N > 3, demonstrating good coverage of tryptic peptides from a simple standard (**Figure 3.3A and Table 3.1**). In addition, the QTOF design of the instrument provided a resolution of 40,000 across the entire mass range and a mass error of < 5 ppm for each tryptic peptide detected, exhibiting the high mass accuracy of the timsTOF Pro platform (**Table 3.1**). These results confirmed the capabilities of the timsTOF for tryptic peptide analysis by MALDI in a simple sample matrix.

Sequence	Theoretical $m/z$	Measured $m/z$	ppm error
HLVDEPQNLIK	1305.7161	1305.711	3.91
DLGEEHFK	974.4577	974.456	1.74
YLVEIAR	927.4934	927.489	4.74
AEFVEVTK	922.488	922.485	3.25
DDSPDLPK	886.4152	886.411	4.74
AWSVAR	689.3729	689.371	2.76
IETMR	649.3338	649.336	-3.39
CASIQK	649.3338	649.336	-3.39
VASLR	545.3405	545.34	0.92
FWGK	537.282	537.282	0.00
FGER	508.2514	508.252	-1.18

**Table 3.1.** List of tryptic peptides detected by MALDI MS on the timsTOF Pro from BSA standard.



**Figure 3.3.** MALDI spectra of trypsin digested BSA, demonstrating detection of numerous peptides (**A**), and trypsin digested protein extracts from HeLa cells demonstrating coverage of over 95 tryptic peptides across the mass range with high S/N (**B**).

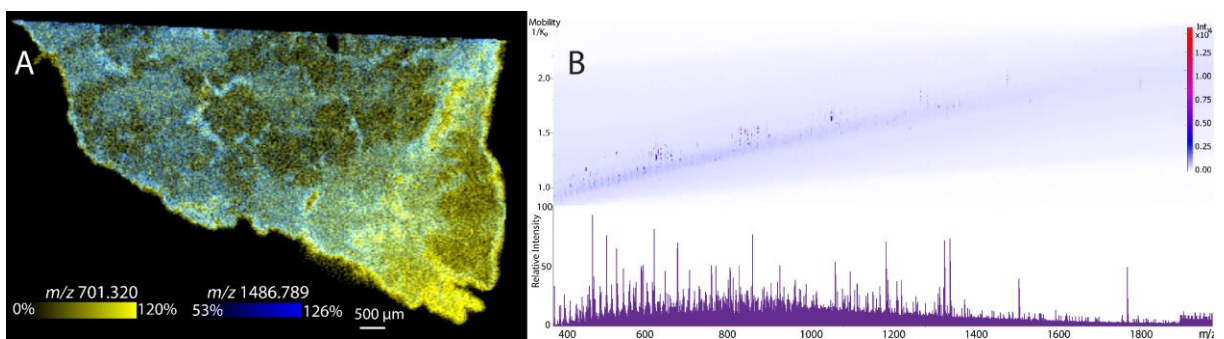
For a more complex sample mixture more akin to what would be observed in a tryptic peptide MALDI IMS experiment of biological tissue, HeLa cells were prepared for bottom-up proteomics with a protein extraction and subsequent trypsin digestion. Also a common QC sample for traditional bottom-up proteomics,<sup>198</sup> this sample matrix was selected because robust tryptic digestion has been characterized in these cells and can therefore be compared against LC-MS/MS data. MALDI analysis of these samples resulted in coverage of over 95 tryptic peptides ranging from  $m/z$  500 - 1800 (**Figure 3.3B**). Similar to the results shown with lipids, the effect of TIMS enhanced the overall peak capacity of these experiments, yielding ~threefold more detected tryptic peptides when the TIMS dimension was considered compared to when it was not. In alignment with observations made in the BSA standard, the high mass accuracy of these tryptic peptides in this complex sample was displayed with each detected peptide measured within 5 ppm of its theoretical  $m/z$ . Taken together, these results demonstrated that the timsTOF Pro was capable of effective MALDI analysis of tryptic peptides from single protein digests as well as complex cell sample digestions with high S/N, mass accuracy, and peptide coverage. Prior to performing MALDI IMS of tryptic peptides on an *S. aureus* biofilm, however, it was necessary to further validate these capabilities in an IMS experiment using better characterized biological tissue.

### Endogenous Peptide MALDI IMS of Human Pancreas

Human pancreas has been studied previously via MALDI IMS for investigation of tryptic peptides using other instrument platforms,<sup>196</sup> making it an ideal candidate tissue with which to validate the timsTOF Pro for MALDI IMS of tryptic peptides. The pancreas is responsible for regulating blood glucose levels by secreting insulin or glucagon in a healthy model. With this important role in blood glucose homeostasis, the pancreas is a major target of investigation in diseases such as diabetes.<sup>199</sup> The pancreas is a complex organ comprised mostly of exocrine tissue with dispersed pockets of endocrine cells known as islets. These islets are comprised largely of  $\alpha$ -cells and  $\beta$ -cells that are responsible for producing glucagon and insulin, respectively.<sup>200</sup> Therefore, spatial investigation by MALDI IMS of pancreas islets could provide insight to the molecular underpinnings of diseases such as diabetes in specific cell-types within the islet.

Validating the timsTOF Pro for MALDI IMS of tryptic peptides in this tissue-type could provide a platform for such spatial investigations.

Human pancreas samples were prepared for tryptic peptide analysis by MALDI IMS including sectioning, antigen retrieval, trypsin application and digestion, and CHCA matrix deposition. Using instrumental methods developed for MALDI analysis of BSA and HeLa cell digests, a region of the pancreas tissue section was imaged. Importantly, these data were also collected with the orthogonal dimension of TIMS to increase sensitivity and peak capacity, resulting in the detection of 375 endogenous peptides. These data represent the first example of tryptic peptide IMS by the timsTOF Pro and exhibit high spatial fidelity for peptide signals within human pancreas (**Figure 3.4**). A common challenge posed by IMS of tryptic peptides, however, is identifying detected peptides and correlating them back to the protein from which they originated. To aid in this process, serial sections of the pancreas tissue were subjected to traditional bottom-up proteomics by LC-MS/MS. This resulted in a database of detected endogenous proteins known to exist within the sample for the MALDI IMS data to be compared against.



**Figure 3.4.** MALDI IMS of a portion of human pancreas collected on the timsTOF Pro. Overlaid ion images of peptides detected at  $m/z$  701.320 (yellow) and 1486.789 (blue) found to localize to exocrine and endocrine tissue, respectively. Averaged spectrum from the MALDI IMS experiment with TIMS heatmap above, demonstrating orthogonal  $1/k_0$  measurement for every peptide detected.

**Glucagon**

sequence	Theoretical m/z	Measured m/z	ppm error
RAQDFVQWLMNTKR	1792.9275	1828.016	-2.588
RHSQGTFTSDYSK	1513.703	1513.7	-1.982
YLDSRR	809.4264	809.424	-2.965
NRNNIA	701.3689	701.367	-2.709

**Table 3.2.** Human tryptic peptide identifications from glucagon in a MALDI IMS experiment, each confirmed to be present in the sample by concurrent LC-MS/MS based bottom-up proteomics.

A process known as tryptic peptide ‘fingerprinting’<sup>201</sup> was then performed, where the detection of multiple unique tryptic peptides originating from the same endogenous protein are used to formulate potential protein identifications. These fingerprinted proteins could then be compared to the database generated by bottom-up proteomics. For example, as described above, glucagon was expected to be observed in high levels in the human pancreas. After confirming the presence of glucagon within the LC-MS/MS database, an *in-silico* digested was performed of the amino acid sequence and peptides interrogated within the MALDI IMS data. Here, four unique peptides were detected in the imaging experiment with mass errors of <3 ppm (**Table3.2**). These experiments served as an example of the capability of the timsTOF Pro to provide a rich spectrum of tryptic peptides in a MALDI IMS experiment. It further indicated that mass fingerprinting in combination with LC-MS/MS based bottom-up proteomics could provide confident identifications of endogenous proteins in this manner.

### *Technological Considerations for Intact Protein Analysis by MALDI TIMS IMS*

#### Overview

Proteins can be analyzed either intact or as peptides generated after on-tissue digestion.<sup>202–204</sup> While on-tissue digestion strategies expand the range of detectable proteins, biologically relevant proteoform information (e.g., post translational modifications, protein sequence truncations, point mutations, etc.) is potentially

lost.<sup>205,206</sup> This makes it prudent to perform complimentary analysis of intact proteins. Here, proteoform information is preserved during intact protein analysis; however, a more limited mass range of detectable proteins is expected with this approach.

Intact protein MALDI IMS experiments are typically performed using TOF mass spectrometers owing to their theoretically unlimited  $m/z$  range and high sensitivity. Novel sample preparation techniques and high mass detectors on TOF instruments have enabled detection of proteins  $\geq 50$  kDa using TOF platforms.<sup>207–209</sup> Lui *et al.* recently reported the use of caffeic acid to detect intact proteins from tissue at  $m/z$   $\sim 190,000$ .<sup>209</sup> In addition, advances in MALDI-TOF instrumentation and laser optics have enabled rapid acquisition of spectra from increasingly small sampling regions<sup>23,185,210,211</sup>; ion images acquired at a rate of up to 30 pixels/sec with a spatial resolution of 5  $\mu\text{m}$ , have been reported.<sup>185</sup> However, during tissue analysis, the limited resolving power of TOF instruments, especially with detection in linear-mode, results in convoluted spectra from which few accurate protein and proteoform intact masses can be determined. Implementation of MALDI on FT-ICR and Orbitrap mass spectrometers has enabled high resolution and high mass accuracy measurements for both intact endogenous proteins from tissue and protein standards.<sup>22,23,188,205,212–214</sup> Historically, FT-ICR and Orbitrap instruments have had lower and narrower  $m/z$  ranges in comparison to TOF mass spectrometers, which has restricted intact protein analysis by MALDI on high resolution instruments. Strategies to overcome  $m/z$  range limitations have included manipulation of instrument source pressure and tuning of ion optics for increased ion transmission efficiency<sup>188</sup>, and use of novel matrices to achieve higher charge state ions<sup>214</sup>. The advent of an extended  $m/z$  range Orbitrap mass spectrometer with an upper range limit of  $m/z$  80,000 also holds promise for intact protein IMS experiments.<sup>215,216</sup> While the mass spectral characteristics of FT-ICR and Orbitrap mass analyzers are attractive, it is crucial to consider the inverse relationship between  $m/z$  and resolving power when performing MALDI IMS on FT-MS systems.<sup>217</sup> To achieve resolving powers capable of providing isotopic resolution at high  $m/z$  values, increasingly long scan times (i.e., time-domain transient lengths of  $\gg 1\text{s}$ ) are required.<sup>188</sup> During a MALDI IMS experiment, where tens to hundreds of thousands of spectra are collected, data acquisition times can exceed 24 hours. To mitigate the time

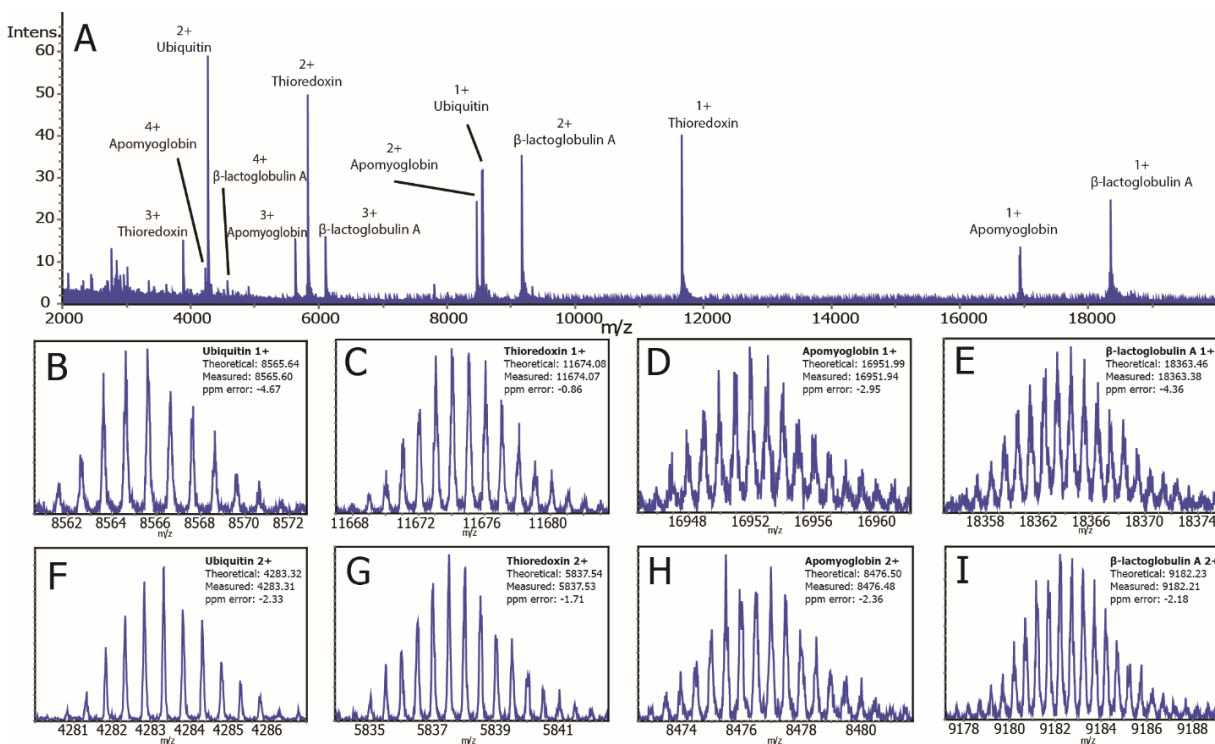
cost associated with MALDI IMS on FT-MS instruments, experiments are often conducted at spatial resolutions  $\geq 75 \mu\text{m}$  or lower mass resolving powers.<sup>188</sup> Computational approaches are also being developed to improve protein imaging performance. Image fusion workflows combining data sets from MALDI-TOF and MALDI FT-ICR mass spectrometers have been developed to capitalize on the benefits of each instrument, for example.<sup>218</sup>

The future of intact protein IMS relies on the development of instrumentation that combines speed, high spatial resolution, and high spectral resolution. Hybrid Quadrupole-TOF (QTOF) mass spectrometers have the potential to unite the benefits of each of the aforementioned platforms. Unlike FT-MS systems where instrument resolving power decreases with increasing  $m/z$ , TOF and QTOF mass spectrometers have relatively constant resolving powers across the  $m/z$  range. Therefore, increased instrument scan times are not required to achieve high mass resolution at high  $m/z$ . A recently introduced QTOF mass spectrometer equipped with MALDI source and trapped ion mobility spectrometry (TIMS) was shown to provide rapid spectral acquisition rates ( $\geq 20 \text{ Hz}$ ), high spatial resolution ( $10 \mu\text{m}$ ), and spectral resolution greater than 40,000 for lipid imaging.<sup>55</sup> The present work demonstrates the advantages of using this mass spectrometer in QTOF-mode for rapid MALDI IMS of isotopically resolved proteins at high spatial resolution beginning with intact protein standards, followed by application of MALDI IMS on various murine tissues.

### Analysis of Intact Protein Standards

MALDI has been previously utilized on the timsTOF Pro for the analysis of metabolites<sup>219</sup>, lipids<sup>55</sup>, and glycans<sup>220</sup>, where the highest upper  $m/z$  limit used for any published study to date has been  $m/z$  4,000. Fernandez-Lima and coworkers recently reported scanning up to  $m/z$  19,000 on modified timsTOF Pro and demonstrated instrument calibration using electrosprayed oligomers from Agilent Tuning mix calibration standard.<sup>221</sup> While instrument calibration is therefore feasible at high  $m/z$  values with ions generated via ESI, the feasibility of high  $m/z$  calibration was assessed here via MALDI-generated ions of red phosphorous. The pre-pulse storage and ion transfer time were adjusted to 50 and 300  $\mu\text{s}$ , respectively, to allow for transmission of

higher  $m/z$  ions. Ions were detected up to  $m/z \sim 17,000$ , confirming that red phosphorus ions cover a wide  $m/z$  range and can be used as a suitable calibration standard for this platform.



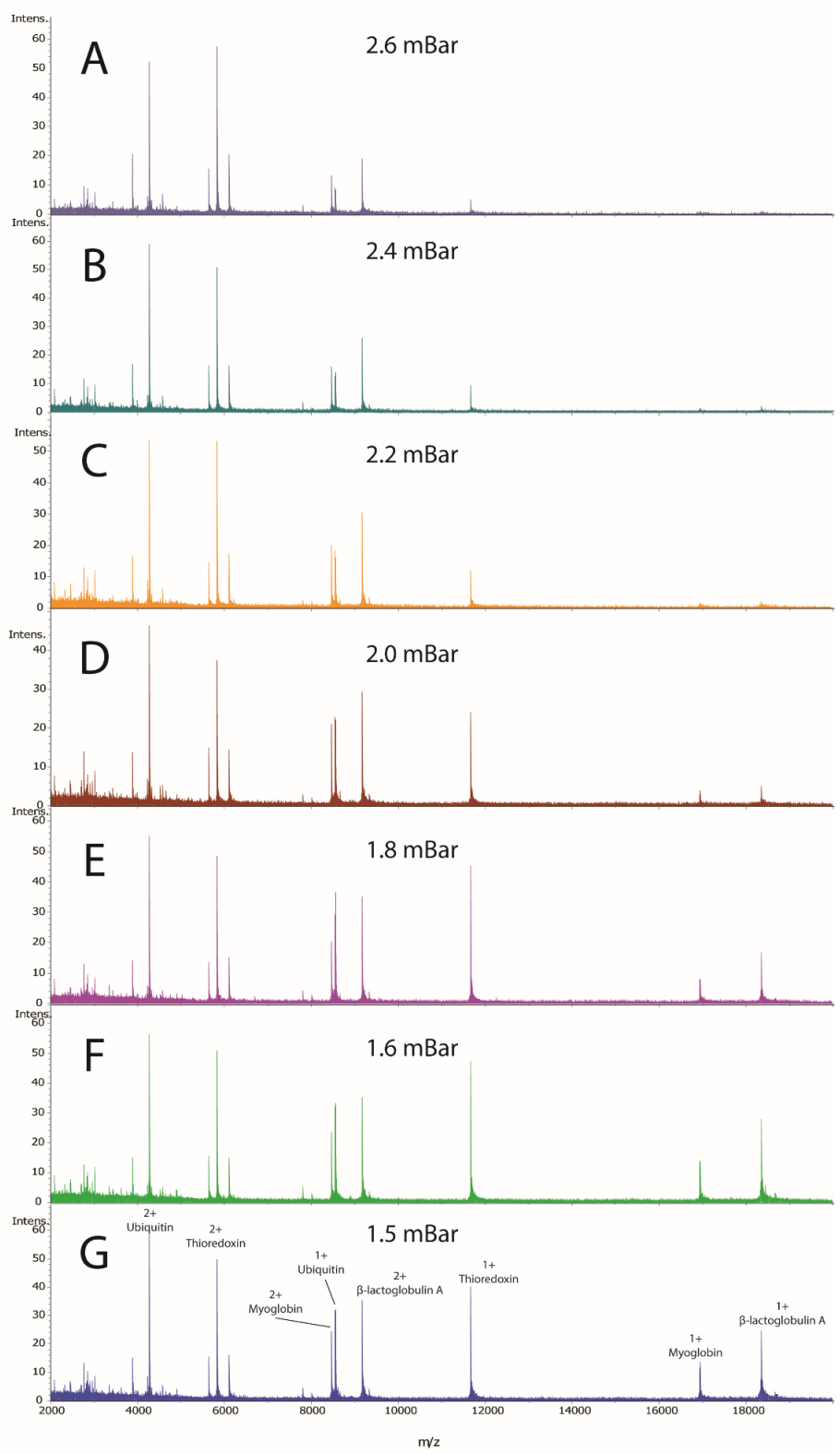
**Figure 3.5.** MALDI mass spectrum of a protein standard mixture composed of ubiquitin (8.6 kDa), thioredoxin (11.6 kDa), apomyoglobin (16.9 kDa), and  $\beta$ -lactoglobulin (18.3 kDa) (A) with expanded insets of the  $[M+H]^+$  (B-E) and  $[M+2H]^{2+}$  (F-I) charge states. A range of charge states are detected for each protein, and all protein ions in the  $[M+H]^+$  and  $[M+2H]^{2+}$  can be isotopically resolved.

To assess instrument performance for intact proteins, MALDI spectra were collected for a protein mixture containing ubiquitin, thioredoxin, apomyoglobin, and  $\beta$ -lactoglobulin with a range of  $m/z$  2,000 - 20,000 (Figure 3.5, Figure 3.6, and Table



**3.3).** Data represented in **Figures 3.5** and **3.6** are averages of 50 spectra. A range of charge states are observed for each protein, including the  $[M+H]^+$  charge state of  $\beta$ -lactoglobulin detected at over  $m/z$  18,000. Like previous work conducted by Prentice *et al.* on a MALDI FT-ICR mass spectrometer, the influence of instrument source pressure on protein charge state intensities was evaluated by adjusting the TIMS tunnel pressure<sup>188</sup> (Determined by the TIMS Tunnel In Pressure instrument reading, **Figure 3.6**).

For ease of spectral comparison, the spectrum from **Figure 3.6G** showing the MALDI mass spectrum at a TIMS tunnel pressure of 1.5 mBar is included in **Figure 3.5** as **Figure 3.5A**. Similar to the results reported by Prentice *et al.* for decreasing ion funnel pressure, reducing TIMS tunnel pressure increases higher  $m/z$  ion intensity. For example, at a TIMS tunnel pressure of 2.6 mBar, which is considered the normal operating pressure for typical proteomic and lipidomic workflows, the  $[M+H]^+$  charge states of apomyoglobin and  $\beta$ -lactoglobulin at  $m/z$  16,000 and  $m/z$  18,000, respectively, are nearly indistinguishable from the instrument noise. With decreasing TIMS tunnel pressure, a gradual increase in signal intensity is observed for singly charged ions. Consequently, all QTOF-only experiments were conducted at 1.5 mBar, the lowest TIMS tunnel pressure setting. **Figures 3.5B – I** contain a series of expanded spectra for the  $[M+H]^+$  and  $[M+2H]^{2+}$  charge states of each protein in the protein standard mixture. Protein signals are isotopically resolved for all charge states, as expected for a constant instrument resolving power of  $\sim 40,000$  across the  $m/z$  range. In addition, calculated ppm error values for the most intense isotopes of the  $[M+H]^+$  and  $[M+2H]^{2+}$  ions for each protein are below 5 ppm. (Sequences for protein standards are provided in **Table 3.4**.) Notably, this data is comparable to that which has been collected on an FT-ICR mass spectrometer.<sup>188</sup>



**Figure 3.6.** MALDI spectra of the protein standard mixture at a TIMS Tunnel In pressure of 2.6 mBar (A), 2.4 mBar (B), 2.2 mBar (C), 2.0 mBar (D), 1.8 mBar (E), 1.6 mBar (F), and 1.6 mBar (G). Reducing the TIMS Tunnel In pressure increases the intensities of lower charge state ions.

Protein Name	Vendor/ Catalog #	UniProt Accession #	Molecular Formula	Monoisotopic Mass (Da)	Protein Sequence
Ubiquitin	Sigma/U6253	P0CG522	C <sub>378</sub> H <sub>629</sub> N <sub>105</sub> O <sub>118</sub> S <sub>1</sub>	8559.62	01 MQIFVKTLTGKTTITLEVEPS 20 21 DTIENVKAKIQDKEGIPPDQ 40 41 QRLIFAGKQLEDGRTLSDYN 60 61 IQKESTLHLVLRIRGG
Thioredoxin	Sigma/T0910	P0AA25	C <sub>528</sub> H <sub>836</sub> N <sub>132</sub> O <sub>159</sub> S <sub>3</sub>	11,666.06	01 <span style="background-color: red;">R</span> SDKI IHLTDDSFDTDLVKA 20 21 DGAILVDFWAEW <span style="background-color: yellow;">C</span> GF <span style="background-color: yellow;">C</span> KMIA 40 41 PILDEIADEYQGKLTVAKLN 60 61 IDQNPGTAPKYGIRGIPTLL 80 81 LFKNGEVAATKVGALSKGQL 100 101 KEFLDANLA
Apomyoglobin	Sigma/M5696	P68082	C <sub>774</sub> H <sub>1221</sub> N <sub>211</sub> O <sub>219</sub> S <sub>3</sub>	16940.96	01 <span style="background-color: red;">R</span> GLSDGEWQQVNLNVWGKVEA 20 21 DIAGHGQEVLRIRLFTGHPET 40 41 LEKFDKFKHLKTEAEMKASE 60 61 DLKKHGTVVLTAALGGILKKK 80 81 GHHEAELKPLAQSHATKHKI 100 101 PIKYLEFISDAI IHVLHSHK 120 121 PGDFGADAQGAMTKALELFR 140 141 NDIAAKYKELGFQG
β-lactoglobulin A	Sigma/L7880	B5B0DA	C <sub>821</sub> H <sub>1322</sub> N <sub>206</sub> O <sub>250</sub> S <sub>9</sub>	18,351.42	01 <span style="background-color: red;">MKQLLALALTCGAQA</span> LIVT 20 21 QTMKGLDIQKVAGTWYSLAM 40 41 AASDISLLDAQSAPLRVYVE 60 61 ELKPTPEGDLEILLQKWEND 80 81 <span style="background-color: yellow;">E</span> CAQKKIAEKTKIPAVFKI 100 101 DALNENKVLVLDTDYKKYLL 120 121 <span style="background-color: yellow;">F</span> MENSAEPEQSLV <span style="background-color: yellow;">C</span> QCLVR 140 141 TPEVDDEALEKFDKALKALP 160 161 MHIRLSFNPTQLEE <span style="background-color: yellow;">Q</span> CHI

**Table 3.3.** Protein standards used for MALDI analysis in figure 3.5 and 3.6.

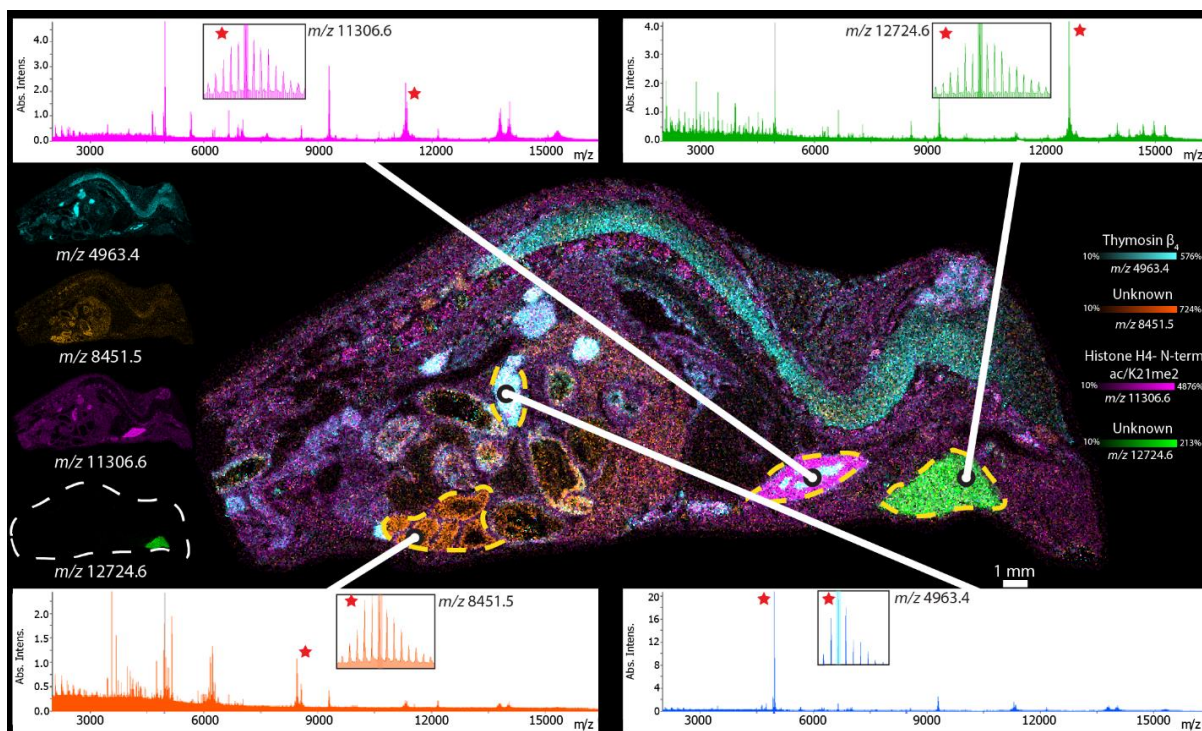
<sup>1</sup>Cysteine residues highlighted in yellow are disulfide bound.

<sup>2</sup>Amino acids highlighted in red are not included in the molecular formulas or the monoisotopic masses and are not part of the detected protein ions.

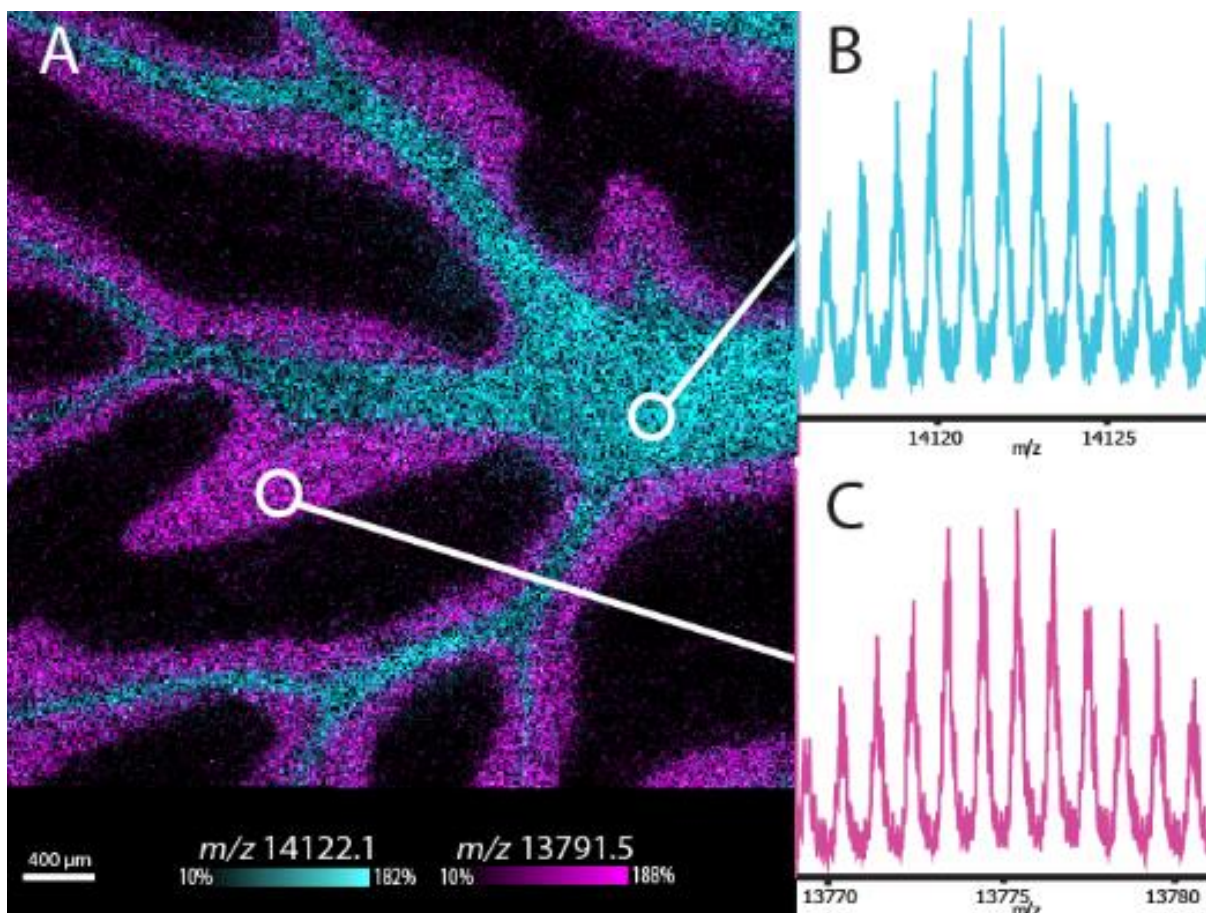
### Endogenous Intact Protein MALDI IMS of Murine Tissues

The high mass resolution, accurate mass MALDI spectra collected for protein standards confirms the suitability of the timsTOF Pro for intact protein analysis. Using the same method, protein IMS was performed on a tissue section of a whole-body mouse pup with a spatial resolution of 50 μm. **Figure 3.7** depicts individual and overlaid ion images for  $m/z$  4,963.4,  $m/z$  8,451.5,  $m/z$  11,306.6, and  $m/z$  12,724.6. Ion images are generated from the most intense individual peak from each isotope distribution. Averaged mass spectra extracted from specific anatomical features (outlined with dotted yellow lines) are shown in **Figures 3.7**. Insets within **Figures 3.7** show expanded spectra for each imaged  $m/z$  value and confirm baseline isotopic resolution was achieved across the measured  $m/z$  range. The ions of  $m/z$  4,963.4 and  $m/z$  11,306.6 were identified as thymosin-B4 and histone H4 based on mass accuracy.

Previous work conducted on the timsTOF Pro has demonstrated that lipid imaging can be conducted with a spatial resolution of 10  $\mu\text{m}$ .<sup>55</sup> To evaluate the potential for imaging of intact proteins at 10  $\mu\text{m}$ , protein IMS was performed on an axial rat brain tissue section (**Figure 3.8**). Overlaid ion images of  $m/z$  13,701.6 and  $m/z$  14,112.1 localizing to the granule cell layer and white matter, respectively, confirm that 10  $\mu\text{m}$  protein IMS data can be collected on the timsTOF Pro. To compensate for the lower signal intensities that result from sampling smaller areas, ion images here were generated from entire isotope distributions. The ion image in **Figure 38A** contains 178,590 pixels and took 5 hours to collect, corresponding to a scan rate of  $\sim 10$  pixels per second. For comparison, to theoretically collect  $\sim 178,000$  pixels on an 15 T FT-ICR mass spectrometer with a spectral resolving power of 40,000 at  $m/z \sim 14,000$  would take approximately 145 hours, respectively. Collection of MALDI IMS data on a QTOF mass spectrometer therefore provides a significant data collection time savings without sacrificing instrument resolving power.



**Figure 3.7.** Intact protein IMS performed on a mouse pup tissue. Individual and overlaid ion images of  $m/z$  4,963.4,  $m/z$  8,451.5,  $m/z$  11,306.6 and  $m/z$  12,724.6 show distinct localization of proteins to anatomical features. Averaged mass spectra are shown for regions surrounded by a dotted yellow line. Peaks used to generate ion images are labeled with a red star and expanded insets are used to show protein ions with resolved isotope distributions.



**Figure 3.8.** Ten micron protein IMS of rat brain tissue. Overlaid ion images of  $m/z$  14,122.1 and  $m/z$  13,791.5 show that high spatial resolution is possible on the timsTOF Pro (**A**). Expanded mass spectra of protein isotope distributions (**B and C**) confirm that high spatial resolution can be performed without compromising mass spectral resolution. Mass spectra are averages generated from regions of interest drawn within each morphological structure (7914 spectra for A and 9507 pixels for B).

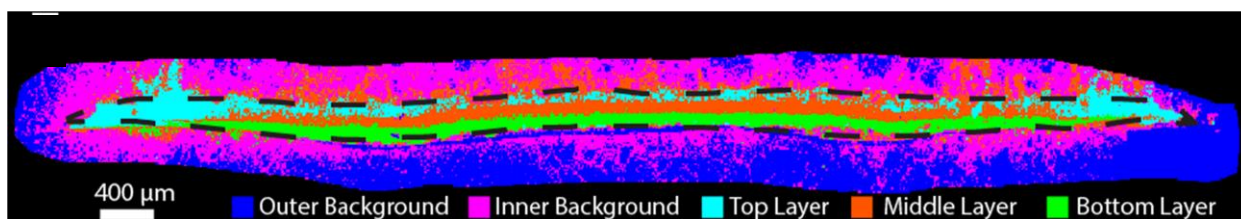


## Part II

### *Multi-omic Heterogeneity Between S. aureus Biofilm Layers is Revealed by MALDI TIMS IMS*

#### Lipids

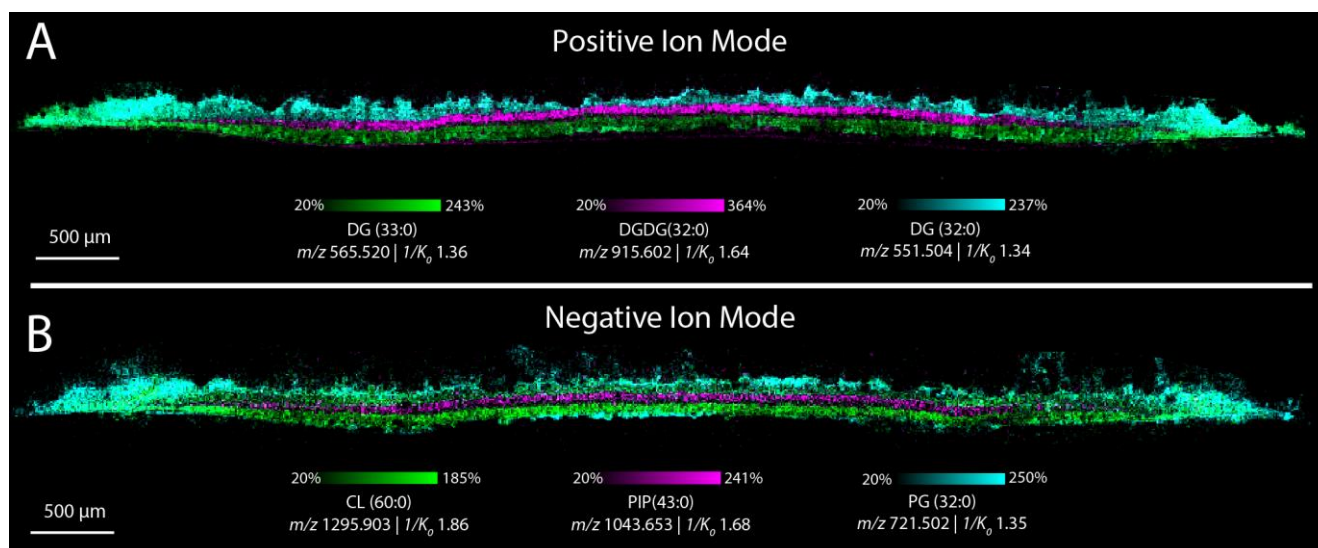
With the goal of visualizing lipidomically distinct layers within the biofilms, methods developed in Chapters II and III were applied for 10  $\mu\text{m}$  spatial resolution IMS of bacterial lipids within an *S. aureus* biofilm. Segmentation by *k*-means clustering was first performed on these data (**Figure 3.9**). This analysis provided an unsupervised approach for clustering pixels whose molecular profiles are similar and then segmenting the imaging data by color coding each pixel by its cluster membership. Using 5 clusters ( $k=5$ ), the matrix background was found to cluster into two classes (outer and inner background, outside dotted line, **Figure 3.9**). This independent clustering of outer and inner background was attributed to slight delocalization of bacterial molecules or whole bacteria around the main structure of the biofilm. Interestingly, three distinct layers within the biofilm were observed to cluster independently, suggesting that the lipidomic profiles differ significantly in these distinct regions.



**Figure 3.9.** *k*-means clustering performed on IMS. data of a biofilm demonstrates biofilm layers cluster independently.

Overall, both odd-chain and even-chain PG, Lysyl-PG and CL were detected, as well as phosphatidylcholine (PC), phosphatidylinositol-phosphate (PIP), diacylglycerols (DG) and digalactosyldiacylglycerols (DGDG), underscoring the sensitivity of the

method. In all cases, detected lipids were detected as the  $[M+H]^+$  or  $[M-H]^-$  in positive and negative ion modes, respectively. The spatial and molecular specificity of IMS uncovered three discrete layers within the biofilm. While layers are known to exist, these results are among the first to visualize this gross structural information on the lipidomic level. As an example, DG(33:0) ( $m/z$  565.520,  $1/K_0$  1.36), DG(32:0) ( $m/z$  551.504,  $1/K_0$  1.34), and DGDG(32:0) ( $m/z$  915.602,  $1/K_0$  1.64) localize to the bottom, top and middle layers, respectively (**Figure 3.10A**). Notably, DG(32:0) and DG(33:0) localize to opposite layers of the biofilm, despite differing only by the addition of a single methyl group on the acyl chain, signifying that lipid localization is not based solely on lipid class. Similar trends were observed in other classes of bacterial lipids such as cardiolipins, as discussed below. Discrete localizations of lipids were found in specific biofilm layers in negative ion mode. For example, CL(60:0) ( $m/z$  1295.903,  $1/K_0$  1.86), PIP(43:0) ( $m/z$  1043.653,  $1/K_0$  1.68), and PG(32:0) ( $m/z$  647.466,  $1/K_0$  1.44) localized to the bottom, middle and top layers, respectively (**Figure 3.10B**). All ions depicted were putatively identified by accurate mass measurement and MS/MS fragmentation where possible (**Table 3.4** and **Figure 3.14**).



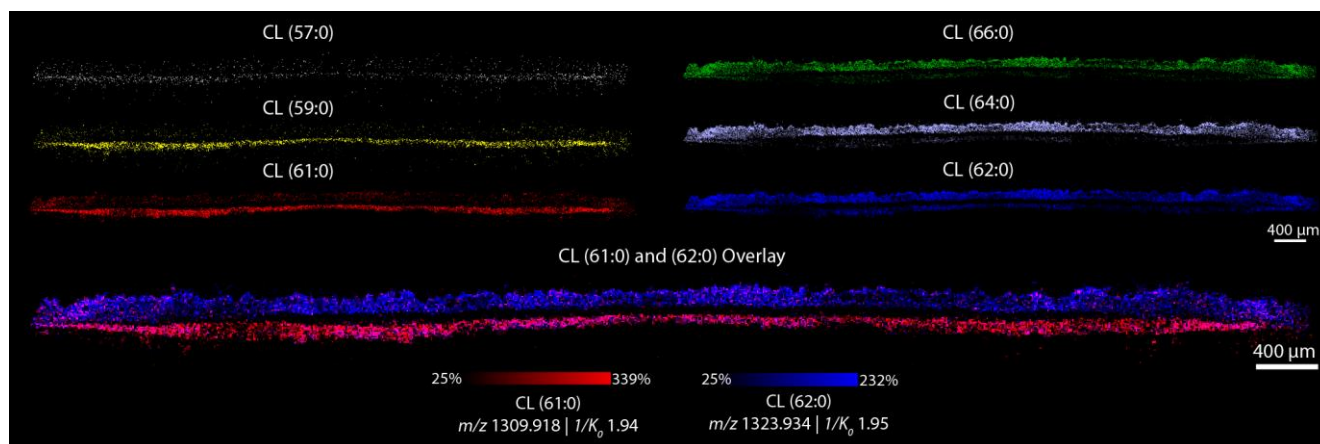
**Figure 3.10.** High spatial resolution IMS (10  $\mu\text{m}$ ) collected of a cross-section of a *S. aureus* biofilm in positive ion mode (A) and negative ion mode (B) showing delineation of three distinct layers. DG(33:0) ( $m/z$  565.520,  $1/K_0$  1.36, 1.77 ppm error) (and CL(60:0) ( $m/z$  1295.903,  $1/K_0$  1.86, 0.46 ppm error) appear to localize primarily to the bottom layer, while DGDG(32:0) ( $m/z$  915.64,  $1/K_0$  1.637, 0.55 ppm error) and PIP(43:0) ( $m/z$  1043.653,  $1/K_0$  1.68, 3.83 ppm error) localize to the middle layer. Finally, DG(32:0) ( $m/z$  551.504,  $1/K_0$  1.34, 1.09 ppm error) and PG(32:0) ( $m/z$  721.502,  $1/K_0$  1.35, 0.14 ppm error) are more abundant in the top layer.

ID	Observed $m/z$	Adduct	Theoretical $m/z$	ppm Error	$1/K_0$	MS/MS
DG(33:0)	565.52	$[\text{M}+\text{H}-\text{H}_2\text{O}]^+$	565.519	1.77	1.36	N
DGDG(32:0)	915.602	$[\text{M}+\text{Na}]^+$	915.6015	0.55	1.64	N
DG(32:0)	551.504	$[\text{M}+\text{H}-\text{H}_2\text{O}]^+$	551.5034	1.09	1.34	N
CL(60:0)	1295.903	$[\text{M}-\text{H}]^-$	1295.9024	0.46	1.86	Y
PIP(43:0)	1043.653	$[\text{M}-\text{H}]^-$	1043.657	3.83	1.68	N
PG(32:0)	721.5026	$[\text{M}-\text{H}]^-$	721.5025	0.14	1.35	Y
CL(57:0)	1253.853	$[\text{M}-\text{H}]^-$	1253.8554	1.91	1.88	N
CL(59:0)	1281.887	$[\text{M}-\text{H}]^-$	1281.8866	0.31	1.91	Y
CL(61:0)	1309.918	$[\text{M}-\text{H}]^-$	1309.9188	0.61	1.94	Y
CL(62:0)	1323.934	$[\text{M}-\text{H}]^-$	1323.9337	0.23	1.95	Y
CL(64:0)	1351.965	$[\text{M}-\text{H}]^-$	1351.965	0	1.98	Y
CL(66:0)	1379.996	$[\text{M}-\text{H}]^-$	1379.9963	0.22	2.01	Y

**Table 3.4:** Details pertaining to each lipid depicted in **Figures 3.10 – 3.17**.

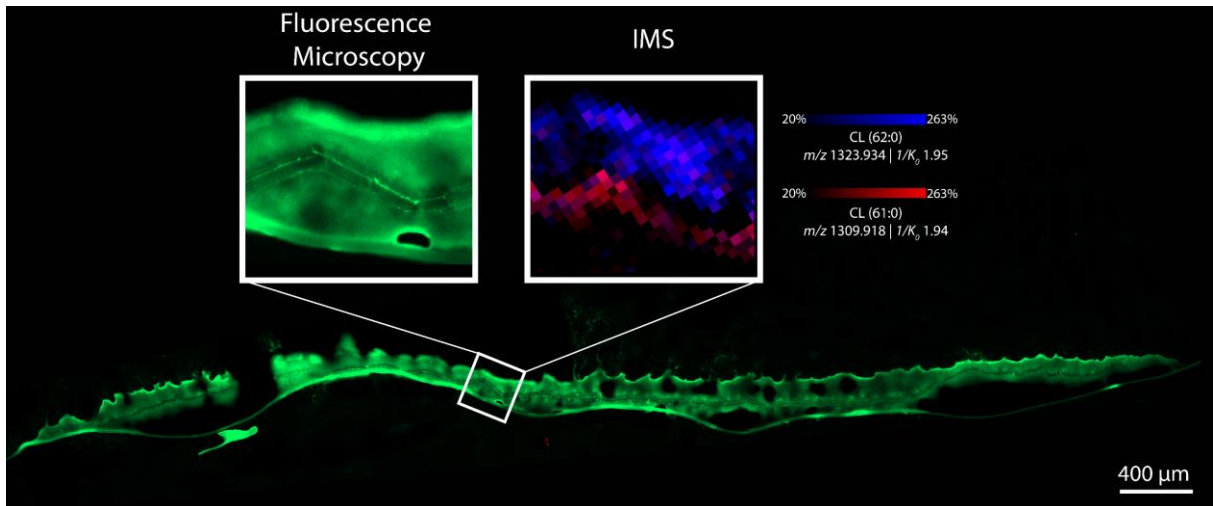


More lipid classes ionize in negative ion mode, leading to the higher diversity of lipids detected. At least five lipid classes were detected in negative ion mode with most ions localizing primarily to a single layer. The lipidomic profile within each of these regions is distinct, and the delineation between each region is visually clear. These results coincide with other work on *Bacillus subtilis* that demonstrated bacteria in different phenotypic states in varying locations within a biofilm,<sup>31,34</sup> and suggest that *S. aureus* biofilm layers also act as discrete communities with a complex system of lipid distribution between them. Again, spatial heterogeneity was found for lipids from within the same class, such as CL(57:0), CL(59:0) and CL(61:0) ( $m/z$  1253.853,  $1/K_0$  1.88,  $m/z$  1281.887,  $1/K_0$  1.91, and  $m/z$  1309.918,  $1/K_0$  1.94) that are all observed primarily in the bottom layer of the biofilm (**Figure 3.11**). Conversely, CL(62:0), CL(64:0) and CL(66:0) ( $m/z$  1323.934,  $1/K_0$  1.95,  $m/z$  1351.965,  $1/K_0$  1.98 and  $m/z$  1379.996,  $1/K_0$  2.01) were all observed primarily in the top layer of the biofilm. All CL lipids were confidently identified by MS/MS (**Figure 3.14**) (except CL(57:0) due to low signal intensity). If these spatial differences were only observed between different classes of lipid such as PG and CL lipids, this phenomenon might have been the result of different growth phases between top and bottom layers. PG lipids are the predominant species in growing *S. aureus*, switching to CL lipids in the stationary phase.<sup>194,222</sup> However, there are no known functional differences for species within the cardiolipin class, potentially suggesting distinct functions of CL species within a spatial context.

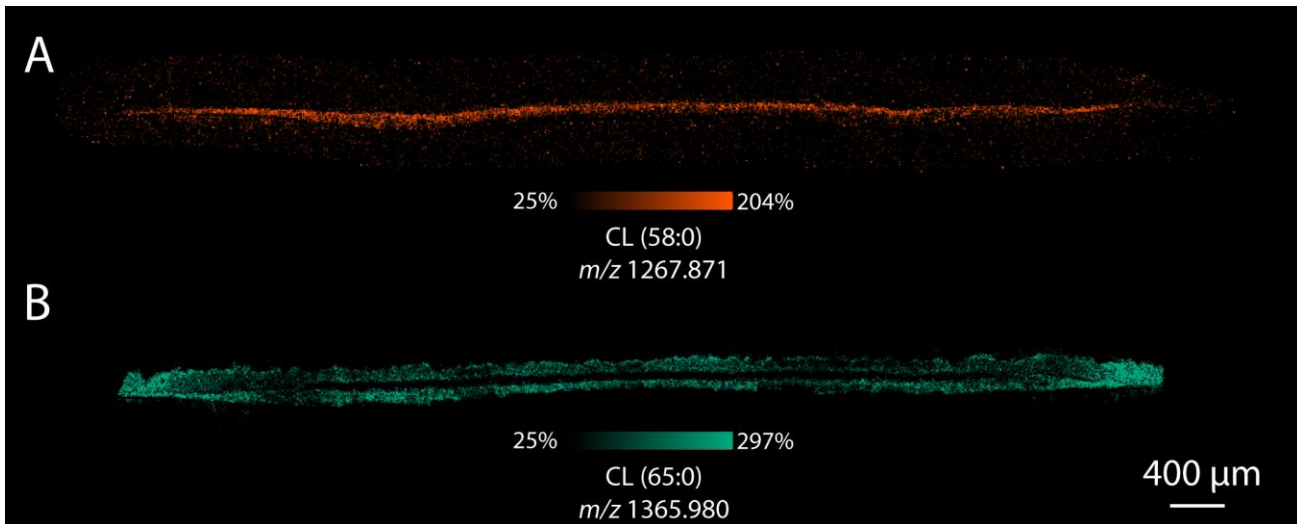


**Figure 3.11.** Bacterial cardiolipin species distribute heterogeneously within biofilm layers. CL(57:0), CL(59:0) and CL(61:0) distribute primarily to the bottom layer, despite being from the same lipid class. Similarly, CL(62:0), CL(64:0) and CL(66:0) distribute primarily to the top layer of the biofilm. An overlay of CL(61:0) and CL(62:0) clearly demonstrates the delineation.

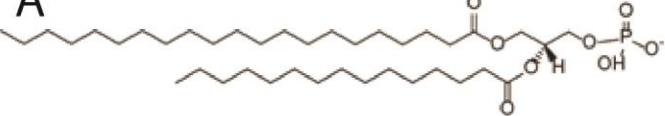
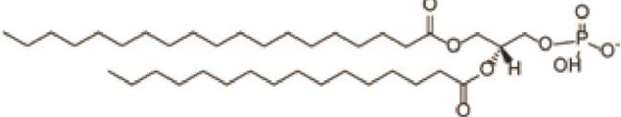



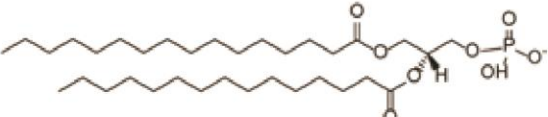
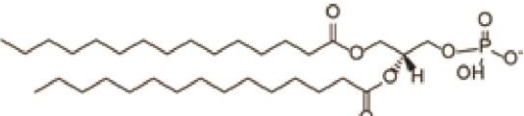
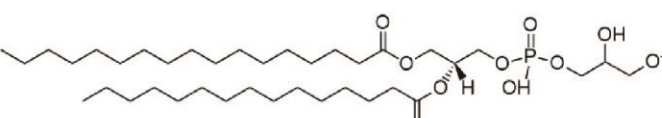




Interestingly, CL signal was below the limit of detection in the middle layer of the biofilm. To determine if this is due to a difference in the cell density in that layer, a biofilm was grown with a strain of USA300 LAC that was genetically modified to constitutively express green fluorescent protein (GFP). Fluorescence microscopy and MALDI TIMS IMS were then collected on the same cross-section and found lower GFP signal in the middle layer by fluorescence microscopy, and corresponding absence of CL signal in the same region by MALDI TIMS IMS (**Figure 3.12**). These results suggest that the absence of CL signal observed in the middle layer may be due to fewer bacteria present in that region of the biofilm. Most odd-chain CL lipids localize primarily to the bottom layer of the biofilm, and even-chain CL lipids are more abundant in the top layer (**Figure 3.11**). However, the trend did not hold in every case in that CL(58:0) and CL(60:0) were observed primarily in the bottom layer of the biofilm (**Figure 3.10** and **Figure 3.13A**). Cardiolipin chain length does not fully explain the separation observed between biofilm layers. Although it appears that longer chain length cardiolipins localize to the top layer and shorter chain length to the bottom, several cardiolipins with longer acyl chain length than 61:0 such as 65:0 have very similar abundances between top and bottom layers (**Figure 3.13B**). While the biological drivers of these observations are still unclear, these results show that CL lipids differing by only one methyl group have starkly different localizations within the microbial community and further underscores the complexity of the lipid distribution patterns between layers within *S. aureus* biofilms.

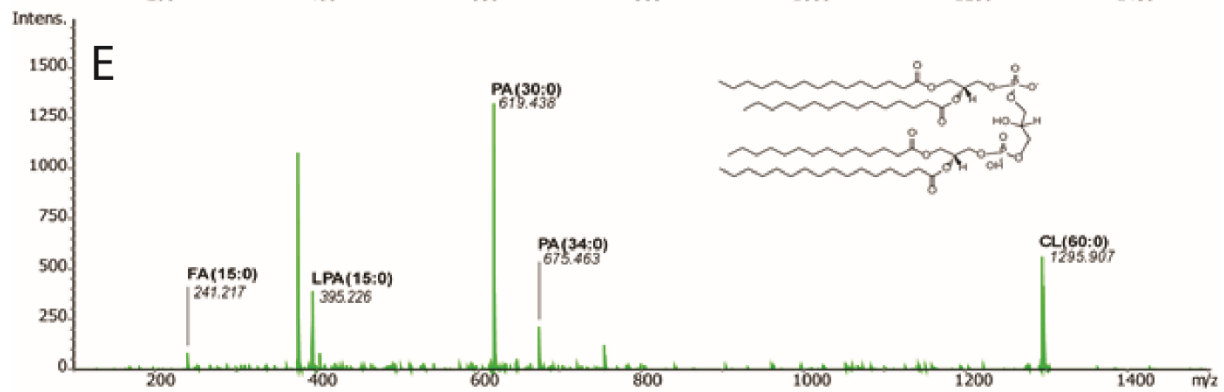
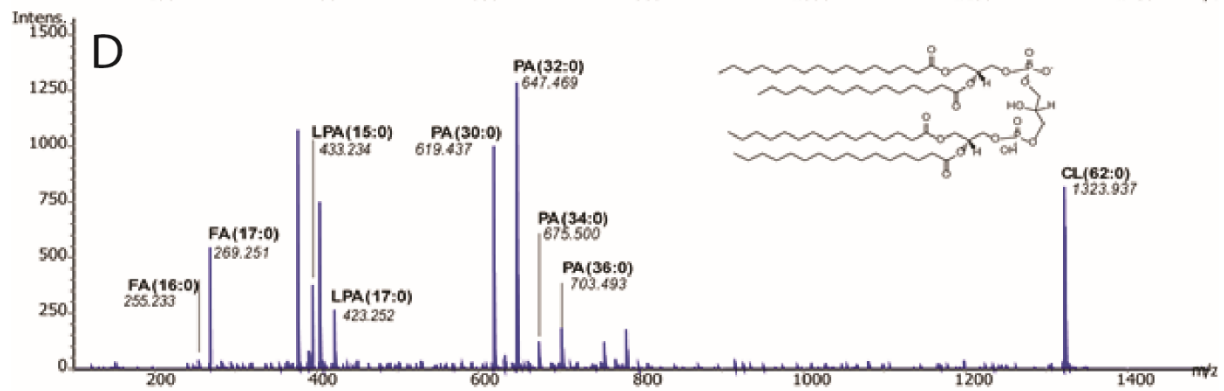
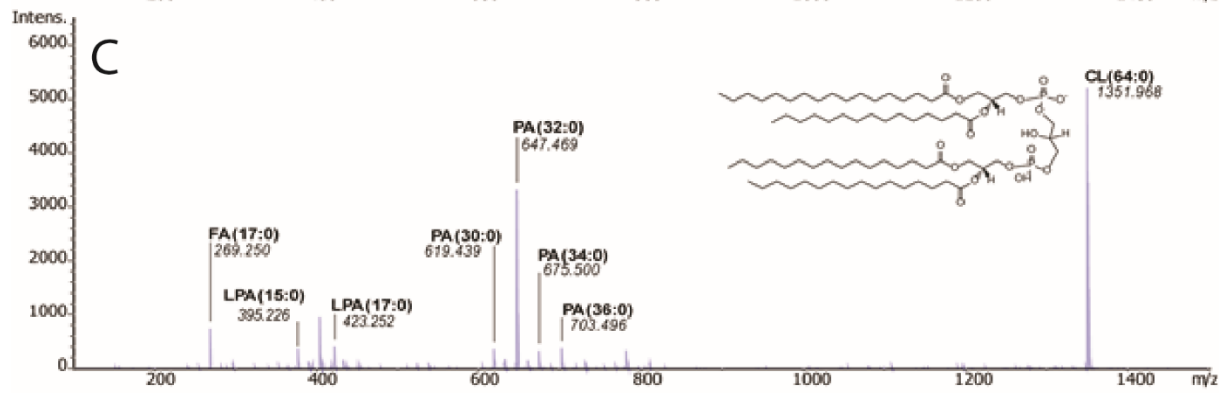
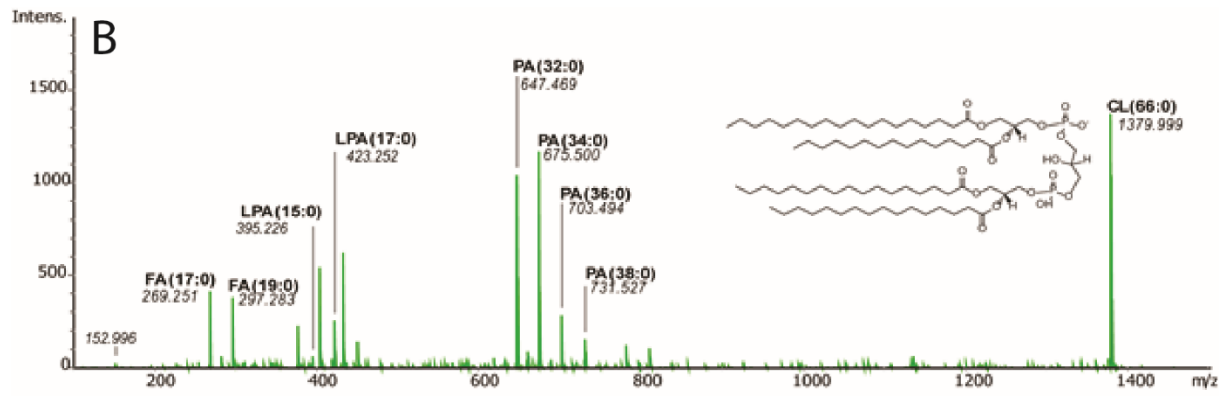


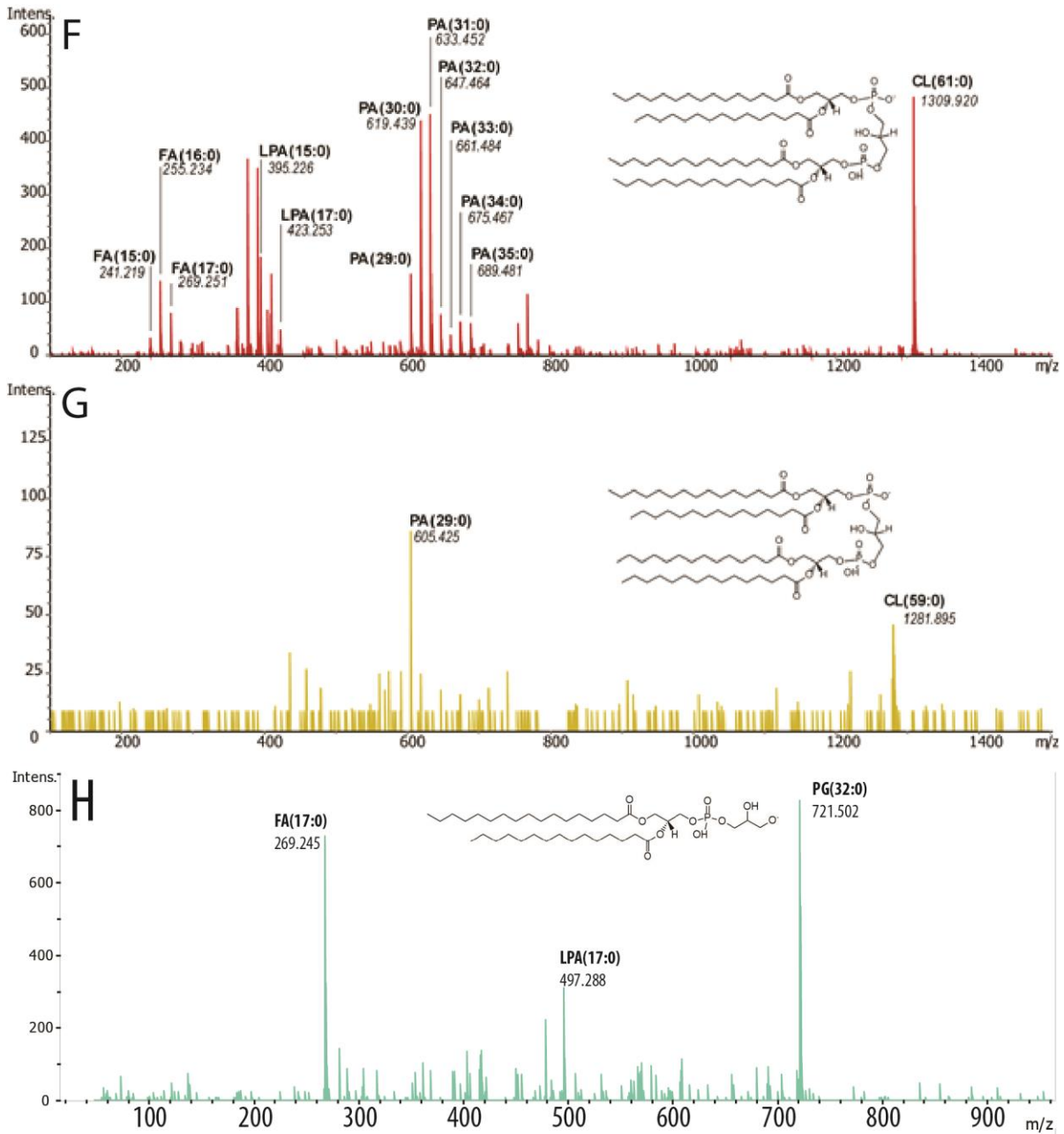
**Figure 3.12.** Fluorescence microscopy of an *S. aureus* biofilm grown with a strain of USA300 LAC that was genetically modified to constitutively express green fluorescent protein (GFP). Lower GFP signal in the middle layer of the biofilm suggests fewer bacteria in this region of the cross-section, and this corresponds with the absence of CL signal observed in the middle layer of the biofilms.



**Figure 3.13.** Ion image of CL(58:0) demonstrates that despite being an even-chain CL lipid it localizes primarily to the bottom layer of the biofilm (A), and CL(65:0) demonstrates that some cardiolipins have very similar abundance between top and bottom layers (B).

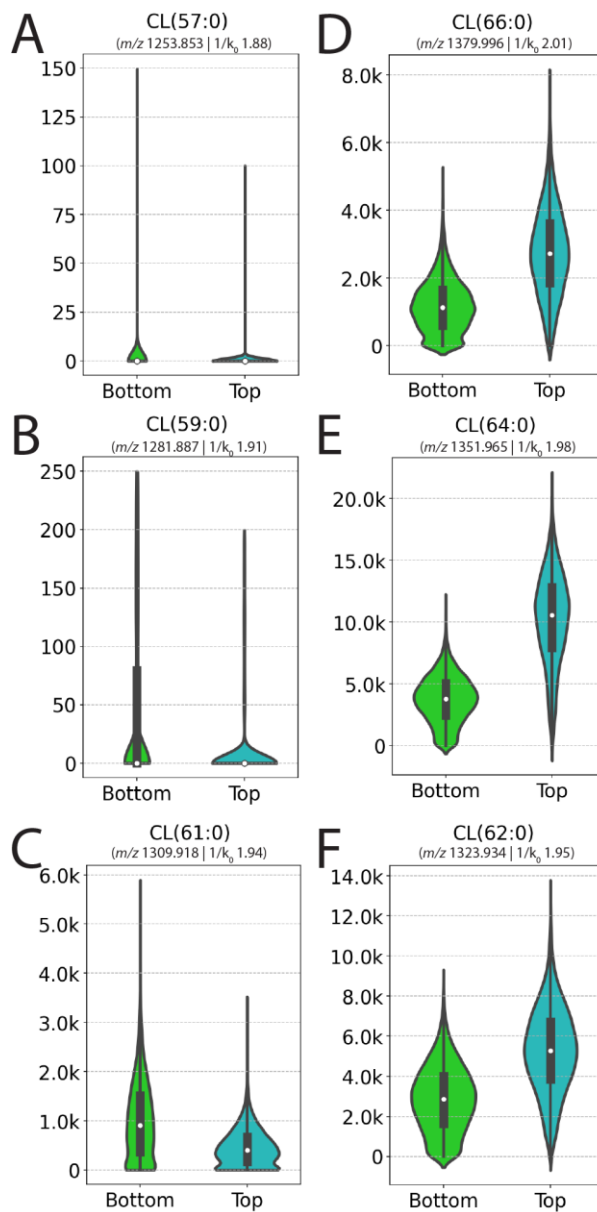
A	Structure		Theoretical $m/z$
		PA(36:0)	703.5283
		PA(35:0)	689.5126
		PA(34:0)	675.4970
		PA(33:0)	661.4813
		PA(32:0)	647.4657
		PA(31:0)	633.4500
		PA(30:0)	619.4344
		PG(32:0)	721.5025
		FA(15:0)	241.2173
		FA(16:0)	255.2329
		FA(17:0)	269.2486
		FA(18:0)	283.2642





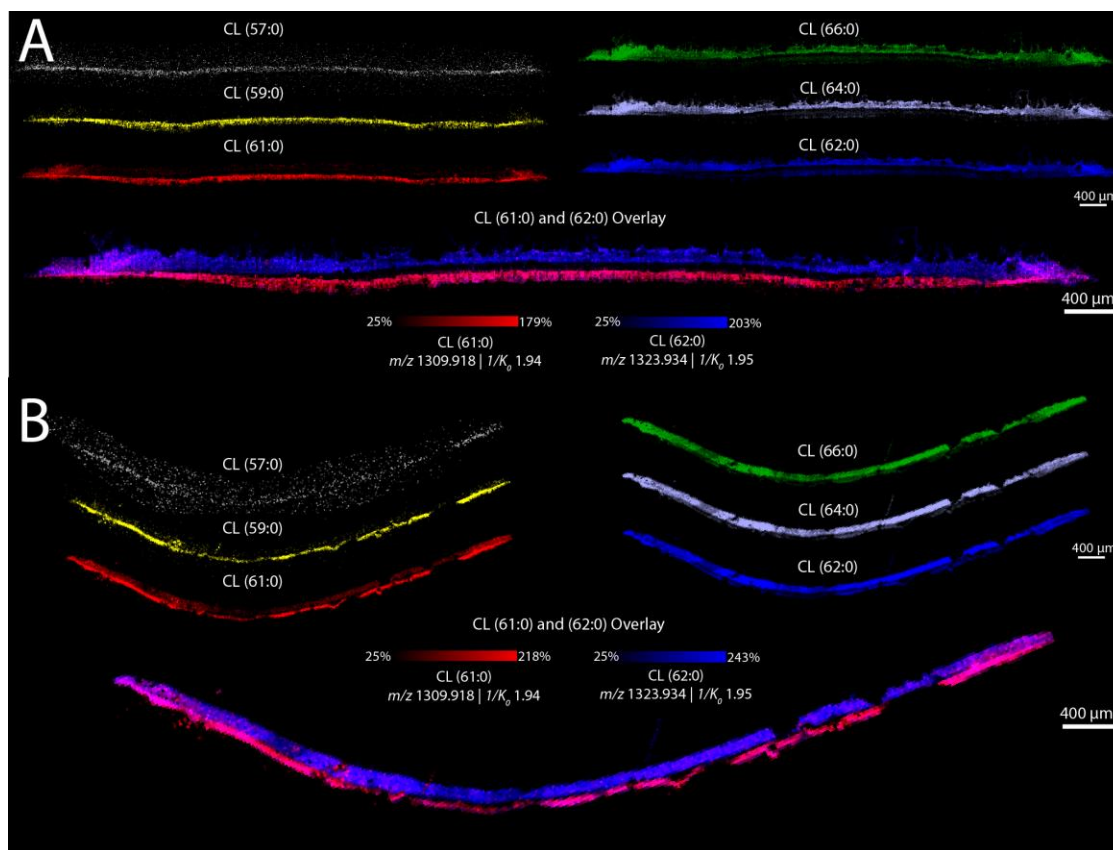
**Figure 3.14.** Representative chemical structures of CL lipids (A) MS/MS for CL(66:0) (B), CL(64:0) (C), CL(62:0) (D), CL(60:0) (E), CL(61:0) (F), CL(59:0) (G) and PG(32:0) (H). Chemical structures shown above are not confirmed, but only representative structures based on  $m/z$ .

To further assess the heterogeneity of lipidomic profiles between biofilm layers, relative comparisons of lipid abundances were made between them. By acquiring IMS of a biofilm in triplicate, spectra were extracted from regions of interest of top and bottom layers. After selecting ion mobility ( $1/K_0$ ) windows to remove chemical noise and any extraneous species, mean signal intensities for each CL species shown in the ion images above were compared (**Figure 3.15**). Here, CL(57:0) CL(59:0) and CL(61:0) were 3.7, 6.3, and 2.3-fold more intense in the bottom layer than in the top layer (**Figure 3.15A – C**). In contrast, CL(62:0), CL(64:0), and CL(66:0), which primarily localize to the top layer, demonstrated a 1.8, 2.6, and 2.2-fold difference between layers (**Figure 3.15D – F**). The means for these six ions were significantly different ( $n=3$ ,  $p<0.03$ ) between the top and the bottom layers. In addition to the quantitative analysis performed in technical triplicate, we confirmed that these trends are consistent in biological replicate (USA300 LAC) as well as a different isolate of USA300 (JE2), (**Figure 3.16A – B**). Although this analysis is an example that analyzes only one class of bacterial lipid species, it demonstrates that the lipidomic differences between biofilm layers are significant and further supports that they are molecularly distinct.



**Figure 3.15.** *S. aureus* biofilms exhibit lipidomic heterogeneity between layers. Violin plots generated from one of three replicate images show that CL(57:0), CL(59:0) and CL(61:0) are more abundant in the spectrum extracted from the bottom layer (green) when compared to the top layer (cyan) (A - C), and that CL(62:0), CL(64:0) and CL(66:0) are more abundant in the top layer compared to the bottom (D - F).

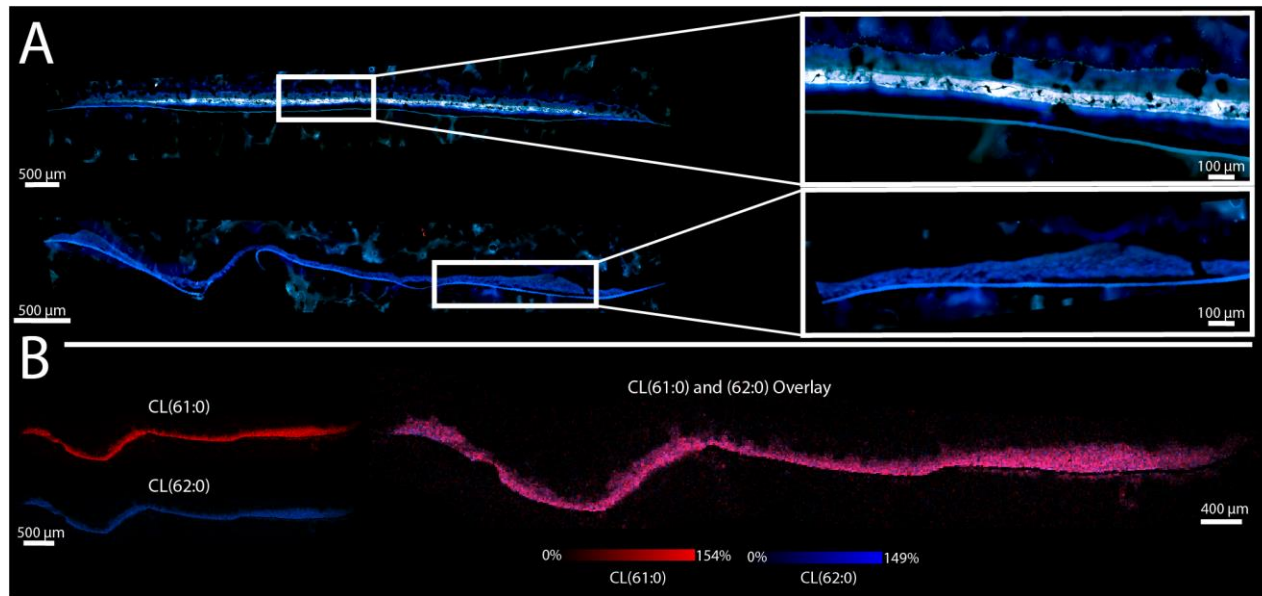




**Figure 3.16.** Biological replicates of *S. aureus* biofilms grown with USA300 LAC (A) and USA300 JE2 (B), demonstrating that the trends seen in cardiolipin distributions hold across not only a biological replicate, but a different strain of USA300 as well.

This pronounced molecular heterogeneity between *S. aureus* biofilm layers led to probing the biological drivers of this phenomenon. Notably, *S. aureus* is a facultative anaerobe with the ability to survive in both aerobic and anaerobic conditions.<sup>223</sup> *S. aureus* growth under anaerobic conditions leads to significant differences in fatty acid content. Specifically, anaerobic metabolism results in a shift from long to short iso-branched fatty acids.<sup>224</sup> Changes in fatty acids, a major building block of lipids, could result in a shift in lipid content. Hypothesizing that these layered subpopulations experience different amounts of accessible oxygen, resultant shifts in fatty acid content

could explain differences in CL lipid content between them. The role of oxygen in the spatial distributions of lipids in biofilms grown under anaerobic conditions was then compared to those grown under atmospheric conditions for the same duration. Autofluorescence of an anaerobic biofilm revealed considerably thinner single-layered biofilms, rather than three distinct layers observed in aerobic biofilms (**Figure 3.17A**). IMS data and *k*-means clustering revealed no discernable layers clustered separately. Instead, the entire biofilm clustered together, further suggesting the existence of a single layer. The absence of layers indicates that oxygen may be necessary to induce *S. aureus* biofilm layer generation that could have implications for biofilm growth in environments of varying oxygen availability. In particular, if the layers observed in aerobic biofilms are the result of waves of bacterial detachment, a known step of the *S. aureus* biofilm generation process,<sup>164,225</sup> these results suggest that oxygen may be required for biofilm detachment. These findings also align with the hypothesis that there may exist a mechanism of biofilm structure formation involving metabolic differentiation of cells leading to metabolically distinct subpopulations within an *S. aureus* biofilm.<sup>164</sup> If this process depends on the presence of oxygen, this could lead to a lack of bacterial differentiation and subsequent absence of biofilm layers. In addition to the loss of layered subpopulations, homogeneous lipid distributions spanning the cross-section of the anaerobic biofilm were observed. For example, when comparing ion images of CL(61:0) and CL(62:0), both species appear to share the same spatial distribution across the entire biofilm (**Figure 3.17B**). This is in contrast to that of the aerobic biofilm where these lipid species demonstrated distinct localizations to discrete biofilm layers (**Figure 3.10**). All CL species in the anaerobic biofilm were also observed, indicating that oxygen is not necessary for the production of these lipid species. However, this does not rule out that an oxygen gradient could be contributing to heterogeneity of lipid abundances between biofilm layers in aerobic biofilms.

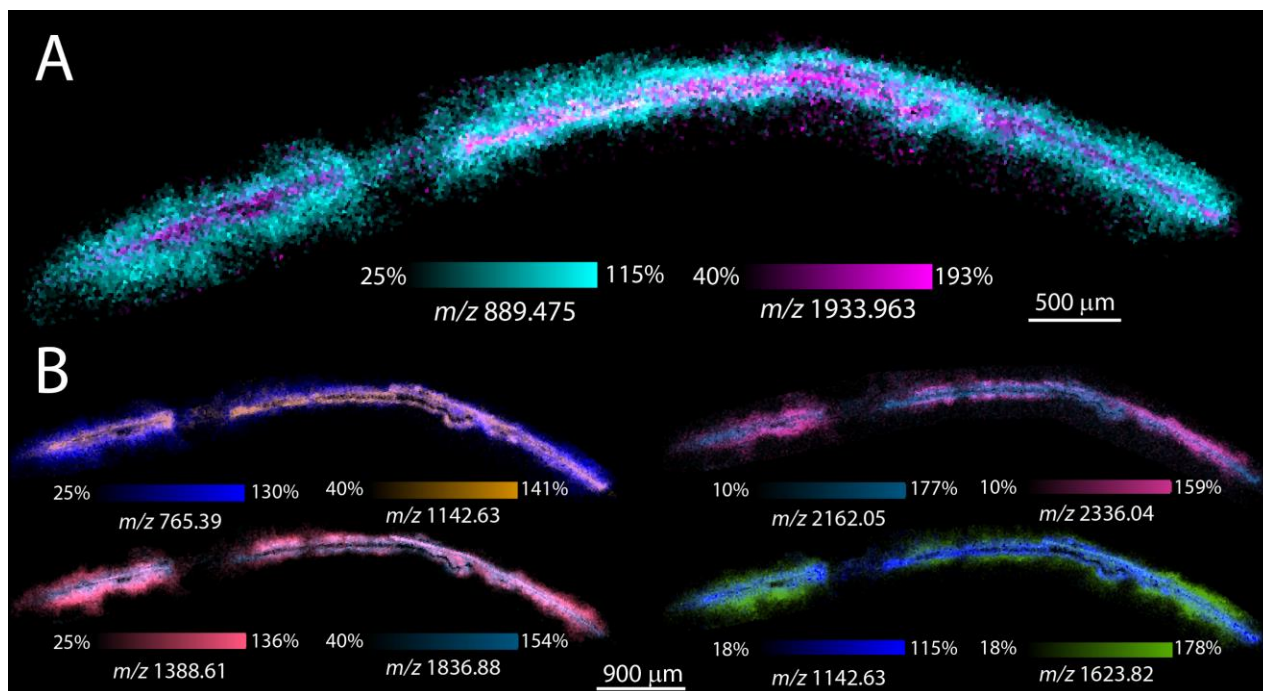


**Figure 3.17.** *S. aureus* biofilms grown under anaerobic conditions generate thinner biofilms (bottom) comprised of a single layer compared to those grown under aerobic conditions (top) (A). IMS of a biofilm grown under anaerobic conditions reveals homogenous distribution of CL(61:0) and CL(62:0) (B) which have different distributions in biofilms grown under aerobic conditions.

### Tryptic Peptides

After demonstrating the molecular heterogeneity that exists between biofilm layers at the lipidomic level, tryptic peptides distributions were assessed. An *S. aureus* biofilm was prepared for analysis of tryptic peptides as described in Chapter II and analyzed by MALDI IMS for tryptic peptides using instrumental methods developed for MALDI IMS of human pancreas as described above. In these data, over 200 peptides were detected ranging from  $m/z$  500 – 2,500 within a single biofilm, underscoring the sensitivity of the timsTOF Pro for bacterial tryptic peptides. These results did have a moderately high baseline ( $\sim 1 \times 10^3$ ) which may have been the result of the sample preparation process with residual chemical noise from the bacterial culture. However, this baseline did not seem to hinder the detection of tryptic peptides. Also likely the result of the sample preparation process, especially during antigen retrieval and trypsin

application, some peptide delocalization was observed. Unfortunately, this delocalization makes delineation between distinct biofilm layers less clear but does not altogether hinder the ability to discern peptide distributions. Like lipids, most detected peptides were found to have specific localizations to certain layers (**Figure 3.18**). For example, as shown in **Figure 3.18A**, a peptide measured at  $m/z$  889.475 appeared to localize to both the top and bottom layers, where another peptide measured at  $m/z$  1933.963 appeared to localize primarily to the middle layer. These distributions were not unique to these peptides however, with many different combinations of peptide signals displaying similar localizations.



**Figure 3.18.** MALDI IMS of bacterial tryptic peptides. Ion image overlay of peptides identified to be from Coenzyme A Disulfide Reductase ( $m/z$  889.475) and Fructose-1,6-Bisphosphatase ( $m/z$  1933.963), demonstrating distinct localization to the bottom/top and middle layers, respectively (**A**), and several other ion image overlays demonstrating that many other observed peptides exhibit localization to distinct layers in the biofilm (**B**).

As with any protein imaging by MALDI IMS, identifying the proteins from which these tryptic peptides originate is a major challenge. To ascertain the identities of tryptic peptides detected, *S. aureus* biofilms were prepared for traditional bottom-up proteomics to create a database of observed proteins as described above for human pancreas. Here, over 760 unique proteins were confidently identified by detection of at

least two unique peptides each, producing a robust database of the proteins known to exist in this biofilm model. Just as performed with the human pancreas, peptides detected in the IMS experiments could then be compared against the database for more confident identification. For example, the peptide detected at  $m/z$  1933.963 was putatively identified as originating from the *S. aureus* protein Fructose-1,6-bisphosphatase. In addition to this peptide, four other unique peptides were detected within 5 ppm of theoretical  $m/z$  and identified as originating from this protein (**Table 3.5**). Next, a cross-comparison to the bottom-up proteomics database confirmed that this protein was observed in high abundance in these biofilms. Using the same workflow, the other peptide shown in **Figure 3.18A** was identified as *S. aureus* Coenzyme A Disulfide Reductase (**Table 3.5**). Because these data were collected in an imaging experiment, the distributions of these proteins can also be assessed. Fructose-1,6-bisphosphatase is involved in *S. aureus* carbohydrate metabolism and does not require aerobic conditions for catalytic activity.<sup>226</sup> Its localization to the middle layer of the biofilm, where oxygen levels are presumably low, may indicate that at least some facets of *S. aureus* biofilm carbohydrate metabolism takes place in the hypoxic environment of this middle layer. Conversely, Coenzyme A disulfide reductase is involved in energy storage<sup>227</sup> and is associated with oxidative stress.<sup>228</sup> This role may drive its localization to the outer two layers of the biofilm which are presumably more oxygenated. Although further experiments would need to be performed to confirm these hypotheses, these peptides serve as examples of the capabilities of this methodology. In summary, this workflow allows for mapping the spatial distributions of bacterial proteins and leverages the coverage of tryptic peptides offered by the timsTOF Pro. Combined with bottom-up proteomics, this workflow can provide robust protein identification in a MALDI IMS experiment.

#### Coenzyme A disulfide reductase

sequence	Theoretical m/z	Measured m/z	ppm error
IVVVGAVAGGATCASQIRR	1828.022	1828.016	-3.282
GFIPVNDK	889.478	889.475	-3.373
FYDR	600.278	600.278	0.000
RLDK	531.325	531.324	-1.882
LDRK	531.325	531.324	-1.882
AAAVGK	516.314	516.315	1.937

#### Fructose 1,6 bisphosphatase

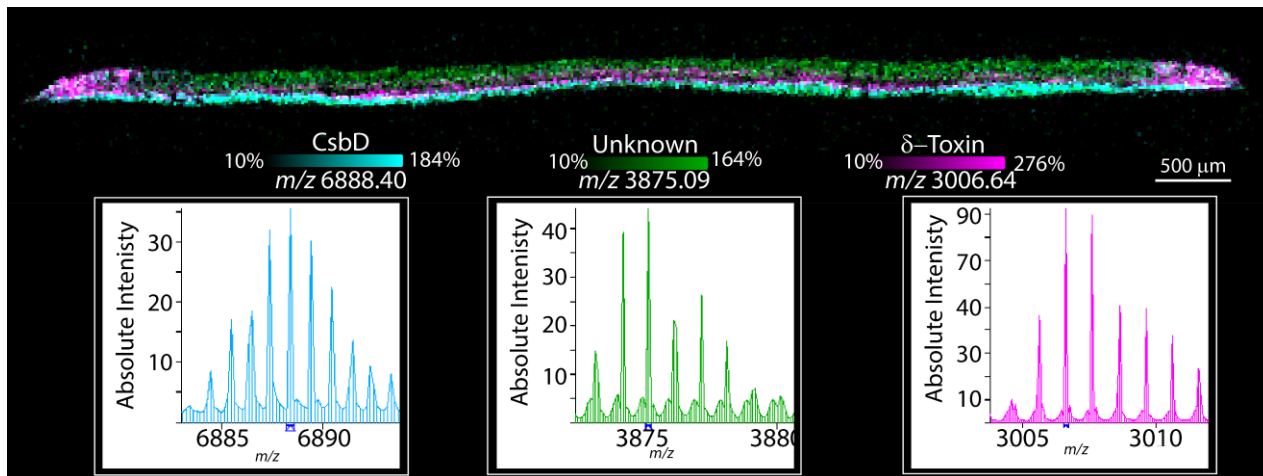
sequence	Theoretical m/z	Measured m/z	ppm error
YYDADNPAFKPKK	1556.774	1556.775	0.642
NPYYHLREDVNMVRK	1933.97	1933.963	-3.619
RVVDK	616.377	616.376	-1.622
LRK	416.298	416.298	0.000
KIR	416.298	416.298	0.000

**Table 3.5.** *S. aureus* tryptic peptides observed in MALDI IMS experiment, where five unique peptides were detected for each protein. The presence of both proteins was confirmed in the *S. aureus* biofilm by concurrent LC-MS/MS based bottom-up proteomics.

### Intact Proteins

Following instrumental validation of the timsTOF Pro for MALDI IMS of intact proteins, the methodologies described in Part I were applied to the spatial investigation of intact proteins in *S. aureus* biofilms. Biofilm cross-sections were prepared as described in Chapter II and subjected to 20  $\mu\text{m}$  spatial resolution MALDI IMS. Here, at least 130 proteins were observed, including signal from intact proteins up to  $m/z$  ~16,000. Just as observed with the distributions of lipids and tryptic peptides, nearly all detected intact bacterial proteins localized primarily to one biofilm layer or another. Much like the distributions of lipids, these data also demonstrate the clear delineation

between the three *S. aureus* biofilm layers. For example, proteins detected at  $m/z$  6888.40,  $m/z$  3875.09, and  $m/z$  3006.64 clearly localized to the bottom, top, and middle layers of the biofilm (**Figure 3.19A**).



**Figure 3.19.** MALDI IMS of bacterial intact proteins. Ion image overlay of proteins identified as Csbd ( $m/z$  6888.40, cyan), unknown ( $m/z$  3875.09 green), and  $\delta$ -Toxin ( $m/z$  3006.64, pink) with each of their measured isotope envelopes, demonstrating that intact proteins also localize to distinct biofilm layers, and that each protein was measured with high S/N and baseline resolution.

Protein identification in an IMS experiment, especially in the case of intact proteins with only a single  $m/z$  measurement, is always a significant challenge. In addition, with chemical changes like post-translational modifications or oxidation, multiple proteoforms for a given endogenous protein are possible, further confounding the identification process. Of the detected protein signatures in these data, only two of the proteins were confidently identified as Csbd ( $m/z$  6888.40) and  $\delta$ -toxin ( $m/z$  3006.64) from previous work by Cassat *et al.*<sup>229</sup> The exact function of Csbd is unknown, but structurally similar proteins have been shown to be involved in stress response, particularly in metal starvation in *S. aureus*.<sup>230,231</sup> Observing this protein in high abundance may indicate that the community is metal starved under these growth

conditions. In addition, the specific distribution of this protein to the bottom layer of the biofilm (**Figure 3.19A**) may further suggest that the communal response to metal starvation is localized to the layer of the biofilm that has access to metals from the agar.

The other identified protein in these data,  $\delta$ -toxin, is in a class of molecules produced by *S. aureus* known as phenol-soluble modulins (PSM).<sup>232</sup> This particular PSM is an important virulence factor for *S. aureus*, whose role is to lyse host cells in an *S. aureus* infection.<sup>232</sup> Observing it in high abundance is no surprise, as  $\delta$ -toxin is one of the molecular hallmarks of *S. aureus*, however its distribution to the middle layer (**Figure 3.19A**) is more confounding. Interestingly, however, is that it is not only localized to the middle layer but was also observed in higher abundance at both edges of the biofilm (**Figure 3.19A**). This phenomenon has also been observed in other studies where MALDI IMS was performed on *S. aureus* colonies from above, rather than cross-sections as investigated herein. In those studies, some PSM's were observed to localize near the outer edge, creating a 'ring' around the bacterial colony.<sup>168</sup> The proposed cause of these distributions is the release of the PSM's into the surrounding area by the *S. aureus* colony, coinciding with the role of  $\delta$ -toxin as a virulence factor meant to be released by the colony for host cell lysis. The study herein revealed that this PSM localizes not only to the edge of the biofilm, but to the middle layer within the biofilm cross-section as well. These findings underscore the importance of the methodologies curated herein for cross-sectional spatial investigations of an *S. aureus* biofilm, to reveal distributions that would not be visible by MALDI IMS investigations performed from above.

## Discussion

The analytical flexibility of the methodologies described herein allowed for a multi-omic investigation of *S. aureus* biofilm cross-sections to reveal stark heterogeneity in the molecular profiles of horizontal biofilm layers. Validating the timsTOF Pro for the effective analysis of bacterial lipids, tryptic peptides, and intact proteins allowed for each



of these analyte classes to be spatially interrogated within *S. aureus* biofilm layers. Prior to MALDI IMS of *S. aureus* biofilm lipids, MALDI analysis of three common commercially available *S. aureus* lipid standards demonstrated high sensitivity and low mass error for detection of bacterial lipids. The implementation of gas-phase separation by TIMS also contributed to increasing both the S/N and the overall peak capacity in 10  $\mu\text{m}$  spatial resolution IMS. Discrete, lipidomically distinct layered subpopulations were revealed by IMS of bacterial lipids in both positive and negative polarities facilitated by the methodologies developed herein. Not only were different lipids observed to localize primarily to discrete layers, but lipids from within the same class, in many cases only differing by one methyl group on the acyl chain, were observed to localize primarily to different layers. Relative quantitation from extracted mass spectra of discrete layers afforded inter-layer comparison of individual lipid abundances and demonstrated differences in select CL lipid species between layers. Further, these findings suggest that individual CL's that have historically been thought to contribute cooperatively toward certain functions, could be playing distinct biological roles. Following the CL study, it was determined that *S. aureus* biofilms grown under anaerobic conditions developed thinner biofilms comprised of a single layer compared to thicker biofilms comprised of three layers when grown under aerobic conditions. This suggests that the generation of multiple layers in *S. aureus* biofilms may require aerobic growth conditions. IMS of these anaerobic biofilms revealed that the lipids analyzed in this work localized homogeneously throughout the anaerobic biofilm. Although further analyses are required to fully understand the significance of lipid distributions within *S. aureus* biofilms, this work using IMS technology demonstrates significant lipidomic heterogeneity between biofilm layers.

Prior to imaging *S. aureus* biofilms, the timsTOF Pro was validated for MALDI analysis of tryptic peptides using trypsin-digested BSA protein and HeLa cell extracts. This instrumental validation along with the implementation of TIMS separation resulted in effective coverage and S/N of tryptic peptides in the BSA standard with at least 11 tryptic peptides detected with a S/N of  $> 3$ . MALDI analysis of HeLa cell protein digests further demonstrated the ability of the timsTOF Pro to obtain effective coverage of tryptic peptides from endogenous proteins in a complex sample matrix. Finally, effective

spatial investigation of tryptic peptides in a MALDI IMS experiment was demonstrated on human pancreas leading to the detection of over 375 tryptic peptides and high spatial fidelity. The sensitivity of this method for tryptic peptides was further underscored by the detection of five unique peptides to confidently identify endogenous proteins. These efforts to validate the instrument combined with the specifications determined in Chapter II for preparing *S. aureus* biofilms for tryptic peptide analysis led to the discovery of similar heterogeneity between horizontal biofilm layers where bacterial proteins were also identified using mass finger printing. Despite some delocalization of tryptic peptides, a common phenomenon known to occur in tryptic peptide imaging, clear localization of most peptide signals was observed to distinct layers within the biofilm. Future work to minimize this delocalization could include changes to the process such as performing the antigen retrieval process in conditions of high humidity, rather than full submersion of the sample.

Finally, MALDI IMS of intact proteins was demonstrated for the first time using a timsTOF Pro. This work demonstrates that untargeted protein IMS performed on a QTOF mass spectrometer enables rapid, high spatial resolution imaging without sacrificing spectral resolving power. In summary, the reduced data acquisition time afforded by performing protein MALDI IMS on a QTOF mass spectrometer lowers the barrier to routine collection of high spectral resolution protein IMS data. Following method development using protein standards and proof-of-concept IMS experiments on murine tissue, this methodology was applied toward the spatial interrogation of bacterial proteins in a biofilm cross-section. These results uncovered clear heterogeneity between biofilm layers, demonstrating that many proteins localized primarily to one horizontal biofilm layer. CsbD and  $\delta$ -toxin were observed to localize primarily to the bottom and middle layers, respectively, with  $\delta$ -toxin exhibiting a unique distribution to the outer edges of the biofilm. These results were in agreement with previous observations made by other investigators performing MALDI IMS from above an *S. aureus* colony. Taken together, the work herein successfully characterized the timsTOF Pro for high spatial resolution, multi-omic investigations by MALDI IMS and demonstrated its utility for spatial investigations to discover stark heterogeneity between horizontal *S. aureus* biofilm layers at the lipidomic and proteomic levels.

## Methods

### Lipids

#### *Materials*

2',5'-Dihydroxyacetophenone (DHA), 1',5'-Diaminonaphthalene (DAN), ammonium formate, ammonium acetate, and poly-L-lysine solution were purchased from Sigma-Aldrich Chemical Co. (St. Louis, MO, USA). HPLC-grade acetonitrile, methanol, and gelatin powder were purchased from Fisher Scientific (Pittsburgh, PA, USA). Carboxymethylcellulose (CMC) was purchased from PM MP Biomedicals (Salon, OH). Tryptic soy agar (TSA) and tryptic soy broth (TSB) were purchased from Becton, (Dickinson, Franklin Lakes, NJ) and all lab plasticware was from USA Scientific (Ocala, FL) or Corning (Corning, NY). Whatman Nucleopore polycarbonate filter discs (0.1  $\mu$ m pore size) were acquired from Millipore Sigma (Burlington, MA).

#### *Sample Preparation*

*S. aureus* bacterial cultures and biofilm growth. *S. aureus* strains USA300 LAC<sup>233</sup> or USA300 LAC modified to constitutively express GFP<sup>197</sup> were streaked on TSA and incubated at 37°C. Single colonies were picked and used to inoculate 5 mL of TSB in 15 mL polypropylene tubes. Tubes were agitated for 16 hr at 37°C. Twenty microliters of the resulting stationary phase culture were then pipetted onto filter discs on TSA plates and incubated at 37°C for a total of 72 hrs. During this time, filter discs were transferred to fresh TSA plates every 24 hrs. Biofilm transfers were performed using antiseptic technique with disinfected forceps to grasp the edge of the filter disc, with care to maintain the biofilm in a horizontal orientation, and to not make contact with the biofilm. In order to measure *S. aureus* biofilm growth over time CFU counts were obtained every 24 hrs after inoculation. To measure CFUs at the appropriate time points individual filter discs containing biofilms were placed into 1.5 mL Navy Eppendorf Bead Lysis Kit tubes containing 1 mL of Phosphate Buffered Saline and homogenized at 4° C for three successive 4 minute cycles using a Bullet Blender Tissue Homogenizer (Next Advance, Inc. Troy, NY) on the maximum speed. Serial dilutions of the homogenates were plated on TSA to determine CFUs.

Anaerobic biofilms were grown by inoculating filters discs as described above and then placing the petri dishes containing the filter discs in a 37°C incubator housed inside an anaerobic chamber (Coy Lab Products, Inc. Grass Lake, MI) filled with a mixture of 90% nitrogen, 5% hydrogen, 5% carbon dioxide. Filter discs were transferred every 24 hrs to fresh TSA plates that had been allowed to equilibrate to the anaerobic chamber for at least 24 hrs prior to transfer.

After 72 hrs growth, *S. aureus* biofilms were embedded in a CMC/gelatin mix and frozen at -80°C. Samples were then cryosectioned to a 10 µm thickness using a CM3050 S cryostat (Leica Biosystems, Wetzlar, Germany), and biofilm sections were then transferred to a conductive indium tin oxide (ITO) coated glass slide (Delta Technologies, Loveland, CO, USA) coated with poly-L-lysine. A Teflon-coated slide was used to press down on top of the biofilm section, sandwiching it between the ITO slide and the Teflon-coated slide, resulting in even adherence of the section to the ITO slide. Sections were then thaw-mounted as normal. Washing was performed using an eyedropper 3X for 30 s and dried in a vacuum desiccator. Autofluorescence and fluorescence microscopy images were acquired using EGFP filter when imaging only GFP, or EGFP, DAPI, and DsRed filters for autofluorescence on a Zeiss AxioScan.Z1 slide scanner (Carl Zeiss Microscopy GmbH, Oberkochen, Germany) before matrix application. Briefly, 150 mg of DHA was dissolved in 10 mL of a methanol/acetonitrile/water (80:10:10) solution and applied to a density of 2.08 µg/mm<sup>2</sup> by an M5 TM sprayer (HTX Technologies, Chapel Hill, NC). DAN was applied similarly by dissolving 100 mg into acetonitrile/water (90:10) and spraying to a density of 1.67 µg/mm<sup>2</sup>.

### *Imaging Mass Spectrometry*

All experiments were performed on a prototype timsTOF fleX mass spectrometer (Bruker Daltonik, Bremen, Germany).<sup>67</sup> Images were acquired in TIMS mode of operation with an ion transfer time of 110 µs and a prepulse storage time of 5 µs. Biofilm imaging data were collected using the Bruker Smartbeam 3D laser capable of

steering the laser beam to ablate an adjustable square area, termed beam scanning. The beam scan was set to 6 x 6  $\mu\text{m}$  with a pitch of 10  $\mu\text{m}$  using 70 shots per pixel and 59% laser power. Positive and negative ionization mode data were collected on biofilm serial sections scanning from  $m/z$  300 – 1,300 and  $m/z$  100 – 2000, respectively. The TIMS EFG scan time was set to 500 ms, with a tunnel-in pressure of 2.1 mbar and reduced mobility ( $1/K_0$ ) range of 0.8–2.2 (V·s)/ $\text{cm}^2$ . TIMS imaging data were visualized via SCiLS Lab (Bruker Daltonik, Bremen, Germany) where hotspot removal was applied. In brief, each signal intensity scale is normalized to the maximum intensity detected for a given ion and the color map is extended for enhanced perception of texture and dynamic range. k-means clustering was also performed in SCiLS using TIC normalization,  $k=5$  and a correlation distance metric. Lipid identifications were determined with high mass accuracy and LIPIDMAPS lipidomics gateway (lipidmaps.org)<sup>234,235</sup> and confirmed by MS/MS fragmentation where possible. Experiments for lipid abundance comparisons were run in technical triplicate and violin plots were generated using in-house developed software capable of considering both  $m/z$  and TIMS dimensions of the data.

### *Data processing*

The data were exported into a custom binary format optimized for storage and speed of analysis of the ion mobility-IMS data. Each frame/pixel contains  $10^4$ - $10^6$  centroid peaks that span the acquisition range of  $m/z$  100 – 2000 with 443,878 and 3,818 bins in the MS and ion mobility dimensions, respectively. The individual centroid peaks were inserted at their correct bin position along the MS and ion mobility dimensions and missing values were set to zero. Data was mass aligned using 7 automatically selected  $m/z$  features and mass calibrated to several known standard molecules. The datasets were also ion mobility aligned to remove any drift time shift acquired throughout the experiment. Ion mobility-aware ion images were extracted using a  $\pm 3$  ppm mass window around each studied mass to produce a matrix of *the number of pixels \* the number of ion mobility bins*. Such images can be used to create an ion image (summing all mobility information into a single vector), a subset of mobility bins can be selected (e.g. to select one or multiple conformations) or all pixels can be

summed to produce an extracted ion mobilogram (XIM). In all cases, ion mobility images are normalized using the total ion current (TIC) normalization.

### *Statistics*

The XIM was fitted with a Gaussian curve to determine the full-width half maximum (FWHM) of the single conformation of the ion. The FWHM boundaries were used to select a subset of ion mobility bins within the ion mobility image and the 2D matrix was summed along the ion mobility dimension to produce a vector of intensities. The *top* and *bottom* masks were used to sub-select a set of pixels in the vector of intensities; each subset of pixels was then collected into a table and padded with NaNs to make sure the two vectors were identical in size and shape. Padding was necessary due to slight differences in the number of pixels in the *top* and *bottom* layer masks. All statistics were computed while excluding NaNs using the *pandas* python package while the violin plots were generated using the *seaborn* visualisation library.

### Tryptic Peptides

#### *Materials*

Alpha-cyano-4-hydroxy-cinnamic acid (CHCA) matrix, ammonium formate, ammonium acetate, and trifluoroacetic acid (TFA) were purchased from Sigma-Aldrich Chemical Co. (St. Louis, MO, USA). Trypsin was purchased from Promega (Madison, WI).

#### *Standard Preparation*

To assess instrument sensitivity and resolution, peptide standards were manually spotted on a target plate with equal volumes 5mg/mL  $\alpha$ -Cyano-4-hydroxycinnamic acid (CHCA) in 90% acetonitrile containing 0.1% trifluoroacetic acid (TFA). Digested Bovine Serum Albumin (BSA) (Pierce) was analyzed at 100 femtomolar. Digested HeLa cell lysate (Pierce) was analyzed at 250 ng/uL.

### *Sample Preparation*

Tissue or biofilm were sprayed with 400uL of trypsin in ammonium bicarbonate containing 0.025% proteaseMax surfactant and 40% acetonitrile using an HDX sprayer. Tissue sections were digested in a humidity oven at 100% humidity and 37° C for 16 hours. CHCA matrix was applied at a concentration of 5mg/mL in 90% acetonitrile with 0.1% TFA for 6 passes.

### *MALDI IMS*

All experiments were performed on a prototype timsTOF fleX mass spectrometer (Bruker Daltonik, Bremen, Germany).<sup>67</sup> Images were acquired in TIMS mode of operation with an ion transfer time of 130  $\mu$ s and a prepulse storage time of 6  $\mu$ s. The beam scan was set to 26 x 26  $\mu$ m with a pitch of 30  $\mu$ m using 250 shots per pixel and 62% laser power. Positive ionization mode data were collected on human pancreas and biofilm sections scanning from  $m/z$  300 – 2500. The TIMS EFG scan time was set to 500 ms, with a tunnel-in pressure of 2.2 mbar and reduced mobility ( $1/K_0$ ) range of 0.8–2.4 (V·s)/cm<sup>2</sup>. TIMS imaging data were visualized via SCiLS Lab (Bruker Daltonik, Bremen, Germany) where hotspot removal was applied.

### Intact Proteins

#### *Materials*

2,5-dihydroxyacetophenone (DHA) matrix, red phosphorus, and the protein standards ubiquitin (8.6 kDa), thioredoxin (11.6 kDa), apomyoglobin (16.9 kDa), and  $\beta$ -lactoglobulin (18.3 kDa), toluene, and ammonium hydroxide were purchased from Sigma-Aldrich (St. Louis, MO). (E)-4(2,5-dihydroxyphenyl)but-3-en-2-one (2,5-cDHA) was synthesized in-house. Tissues were purchased from BioIVT (Westbury, NY). Indium-tin-oxide (ITO)-coated microscope slides were purchased from Delta Technologies (Loveland, CO). Agilent Tuning mix was purchased from Agilent (Santa Clara, CA). Water, chloroform, acetonitrile, ethyl acetate, acetic acid and formic acid were purchased from Fisher Scientific (Waltham, MA). Rat brain tissue was purchased from Pel-Freeze Biologicals (Rogers, AR) and stored at –80 °C until analysis.

### *Sample preparation*

For protein standard analysis, a mixture of protein standards [ubiquitin (2 pmol/uL), apomyoglobin (4 pmol/uL), thioredoxin (6 pmol/uL),  $\beta$ -lactoglobulin (8 pmol/uL)] in water were combined 1:1 with 15 mg/mL DHA in ACN/H<sub>2</sub>O (90:10) with 0.1% formic acid. A series of 1  $\mu$ L aliquots were deposited on to a MTP AnchorChip MALDI target (Bruker Daltonik, Bremen, Germany) and dried. For imaging experiments, all tissues were sectioned using a CM3050S cryostat from Leica Microsystems (GmbH, Wetzlar, Germany) and thaw-mounted on ITO slides. Rat brain tissues were sectioned at 10  $\mu$ m thickness. A one-week-old C57BL/6 control mouse pup was snap-frozen at  $-80^{\circ}\text{C}$ , shaved over dry ice, and cryosectioned at a 20  $\mu$ m thickness. Tissues were coated with cHDA matrix following a previously published method.<sup>185</sup> Briefly, a 3 mg/mL solution of cDHA dissolved in ethyl acetate and toluene (1:1) was applied, followed by a second application of 9 mg/mL solution dissolved in ACN/H<sub>2</sub>O (3:7) with 1% TFA and 0.5% ammonium hydroxide, each using a TM Sprayer (HTX Technologies, LLC, Chapel Hill, NC). Tissues were rehydrated by suspending samples over 1 mL of 50 mM acetic acid for 3 min at 37 $^{\circ}$  C.

### *Mass Spectrometry*

All experiments were conducted in positive ion mode on a prototype timsTOF Pro mass spectrometer (Bruker Daltonik, Bremen, Germany) equipped with a SmartBeam 3D 10 kHz frequency tripled Nd:YAG laser (355 nm) operated with beam scanning on. Spectra of spotted protein standards in both "QTOF"-mode, where no ion mobility separation was performed, and TIMS-mode were acquired with a pixel size of 50  $\mu$ m x 50  $\mu$ m with 1000 laser shots per pixel. IMS of the whole-body mouse pup was also performed at pixel size of 50  $\mu$ m with 1000 laser shots per pixel, and IMS of the rat brain tissue section was performed with a pixel size of 10  $\mu$ m with 750 laser shots per pixel. For optimal transmission of protein ions, the following instrument parameters were used: ion transfer time = 300  $\mu$ s; pre-pulse storage = 50  $\mu$ s; collision RF = 4000 V; collision energy = 10 eV; ion energy in the quadrupole = 5 eV; TIMS Funnel 1 RF = 500 Vpp; TIMS Funnel 2 RF = 475 Vpp. Bruker Data Analysis software and SCiLS Lab



Version 2020 (Bruker Daltonics, Bremen, Germany) were used to analyze data and generate ion images.

## CHAPTER IV

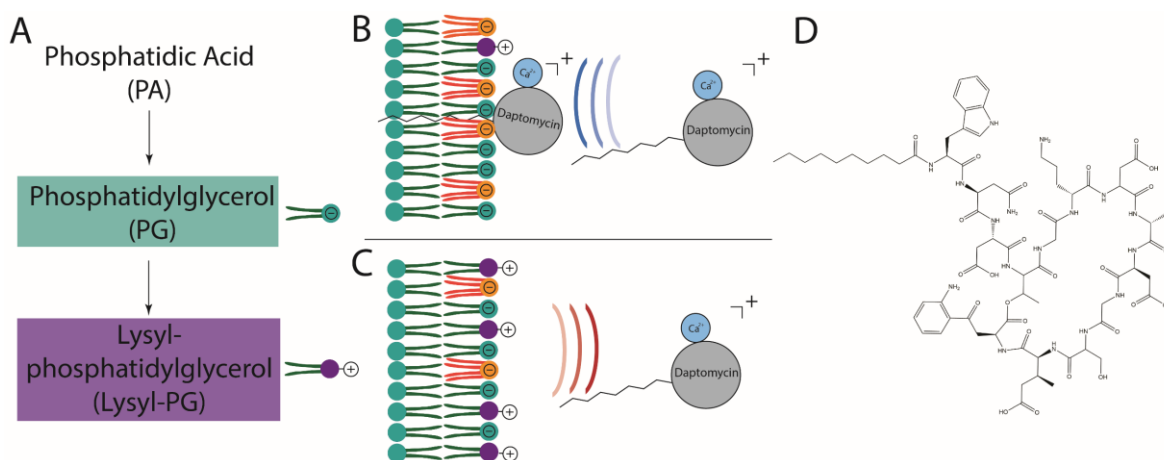
### CHARACTERIZING LIPIDOMIC DISTRIBUTIONS IN BIOFILMS OF DAPTOMYCIN-SUSCEPTIBLE AND -RESISTANT CLINICAL ISOLATES OF *S. AUREUS*

#### Introduction

In addition to methicillin, *S. aureus* often develops resistance to other common antibiotics including penicillin, vancomycin, and linezolid.<sup>236,237</sup> Since its introduction in 2003, daptomycin has also become a common antibiotic for treating gram-positive infections.<sup>238</sup> In a class of antibiotics of its own, daptomycin quickly rose near the top of the list of antibiotics for clinicians to treat multi-drug resistant infections. Daptomycin is considered to be a “last-line” antibiotic commonly used to treat multi-drug resistant infections, particularly in cases of bacteremia.<sup>121</sup> However, recently, even resistance to daptomycin has been observed in the clinic,<sup>121</sup> jeopardizing the efficacy of this important antibiotic. Understanding the biological drivers of daptomycin-resistance in *S. aureus* is critical to developing strategies for retaining its efficacy. Daptomycin is a cyclic lipopeptide containing an acyl chain comprised of nine carbons (**Figure 4.1D**). Upon administration of the antibiotic, daptomycin forms a positive charged complex with endogenous  $\text{Ca}^{2+}$ .<sup>239</sup> This positively charged complex is subsequently attracted to the negatively charged bacterial membrane consisting primarily of negatively charged PG lipids (**Figure 4.1B**).<sup>240</sup> Intercalation of the daptomycin acyl chain into the bacterial membrane causes membrane leakage and ultimately cell death.<sup>241</sup>

As briefly described in Chapter I, a proposed mechanism of daptomycin-resistance in *S. aureus* is electrostatic repulsion.<sup>126</sup> Specifically, increased turnover of positively charged lysyl-PG lipids synthesized from PG lipids (**Figure 4.1A**) leads to a net increase in charge of the bacterial membrane, electrostatically repelling the

daptomycin complex and contributing to daptomycin-resistance (**Figure 4.1C**). Numerous studies have investigated changes in lipid abundance in planktonic *S. aureus* where lysyl-PG lipids have been consistently observed to increase, dependent on various mutations in enzymes related to lipid metabolism.<sup>121</sup> However, these studies have not yet been expanded to interrogate how these daptomycin-resistant strains of *S. aureus* respond to daptomycin treatment. Furthermore, despite *S. aureus* being the most common pathogen in biofilm-related infections,<sup>140</sup> previous studies have focused on investigating molecular changes that take place with daptomycin-resistance in planktonic bacteria and not within the context of a biofilm. The studies described below aimed to elucidate the bacterial response to daptomycin treatment in a daptomycin-resistant *S. aureus* model, and to do this within the context of a biofilm to gain insight to the spatial dimension of this response.



**Figure 4.1.** Daptomycin-resistance in *S. aureus* is associated with lysyl-PG lipids (purple), which are synthesized from PG lipids (turquoise) via a single pathway (**A**). A schematic depicting the mechanism of action for daptomycin, where a positively charged complex is formed with  $\text{Ca}^{2+}$  and is consequently attracted to the WT *S. aureus* membrane where negatively charged PG lipids are the predominant lipid constituent (**B**). Conversely, increased turnover of PG to positively charged lysyl-PG lipids in a daptomycin-resistant *S. aureus* membrane leads to electrostatic repulsion of the daptomycin complex (**C**). The chemical structure of daptomycin (**D**).

To probe the biological drivers of daptomycin-resistance in an *S. aureus* biofilm, two isogenic clinical isolates were interrogated herein. These isolates consisted of one

daptomycin-susceptible clinical isolate (DAP-S), and one daptomycin-resistant isolate (DAP-R), both taken from the same patient. Briefly, these isogenic strains were isolated from a single patient presenting with endocarditis, where an isolate was taken prior to daptomycin treatment and determined to be susceptible to the antibiotic. Daptomycin treatment failed for this patient, leading to a persistent infection and a second isolate was taken that was determined to be resistant to daptomycin (**Table 4.1**). Importantly, only daptomycin-resistance was incurred, retaining its susceptibility for all other antibiotics screened. Biofilms grown with these clinical isolates therefore provide an opportunity to investigate the genotypic and phenotypic changes that may contribute to daptomycin-resistance in a in a real-world infection, while accounting for as many variables as possible in this context. Moreover, by performing these studies in biofilms rather than planktonic bacteria, the important spatial context of these molecular changes could be explored.

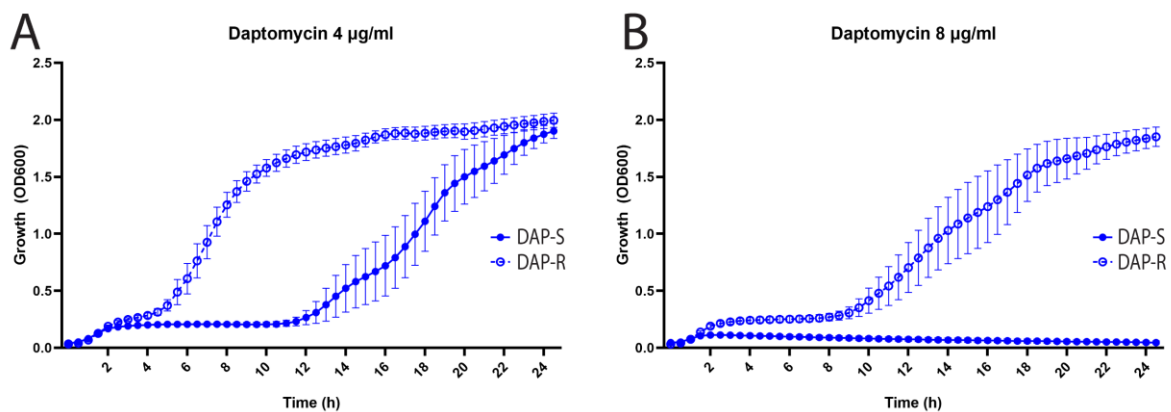
Antibiotic	Isolate 1		Isolate 2	
	MIC ( $\mu\text{g/mL}$ )	Status	MIC ( $\mu\text{g/mL}$ )	Status
Ceftaroline	1	Susceptible	0.5	Susceptible
Clindamycin	$\leq 0.5$	Susceptible	$\leq 0.5$	Susceptible
Daptomycin	$\leq 0.5$	Susceptible	4	<b>Resistant</b>
Doxycycline	$\leq 0.5$	Susceptible	$\leq 0.5$	Susceptible
Erythromycin	$> 4$	<b>Resistant</b>	$> 4$	<b>Resistant</b>
Gentamicin	$\leq 1$	Susceptible	2	Susceptible
Linezolid	$< 1/4$	Susceptible	$\leq 1$	Susceptible
Oxacillin	$> 4$	<b>Resistant</b>	4	<b>Resistant</b>
Penicillin G	$> 1$	<b>Resistant</b>	$> 1$	<b>Resistant</b>
Rifampin	$\leq 0.25$	Susceptible <sup>1</sup>	$\leq 0.25$	Susceptible <sup>1</sup>
Vancomycin	1	Susceptible	2	Susceptible

**Table 4.1.** Antibiotic susceptibility status for both clinical isolates showing that Isolate 1 was susceptible with a minimum inhibitory concentration (MIC) that is below the breakpoint for daptomycin (1  $\mu\text{g/mL}$ ) of  $< 0.5$  and Isolate 2 was resistant with an MIC of 4.

## Results

### *Clinical Isolates*

Prior to performing MALDI IMS on these clinical isolates, it was necessary to validate the daptomycin-resistance phenotype. To do this, growth curves were performed with both clinical isolates grown in varying concentrations of daptomycin (4 and 8  $\mu\text{g}/\text{mL}$ ). In all experiments where antibiotic was present, a clear growth defect was observed in the DAP-S isolate compared to the DAP-R isolate (**Figure 4.2A – B**). These data were consistent with the resistance phenotypes observed in the clinic and confirmed these isolates as daptomycin-susceptible and -resistant.

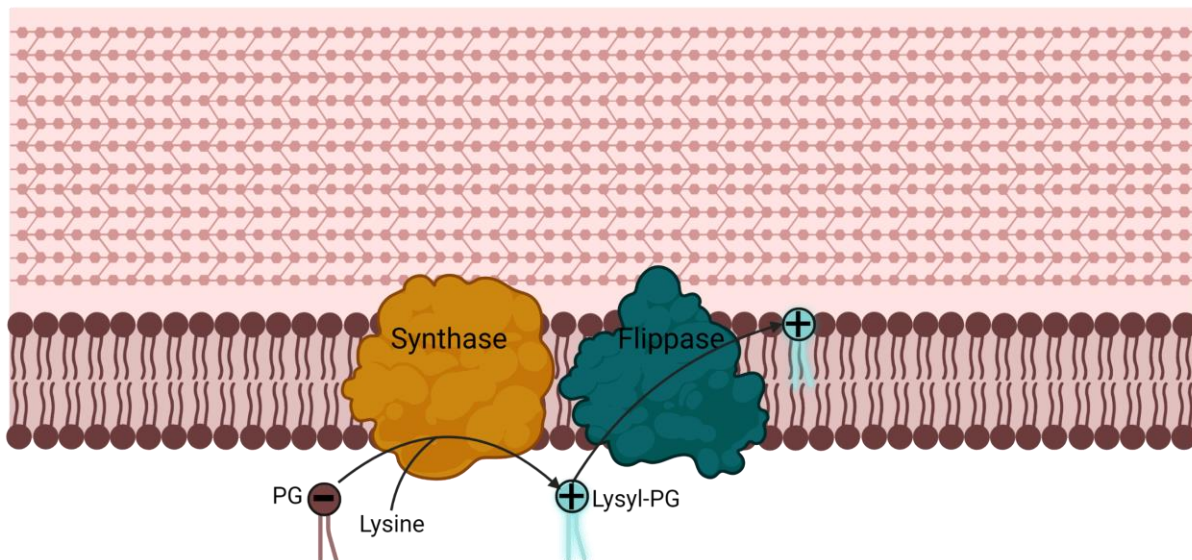


**Figure 4.2.** Growth curves of both *S. aureus* clinical isolates performed in biological triplicate at 4  $\mu\text{g}/\text{mL}$  daptomycin (**A**) and 8  $\mu\text{g}/\text{mL}$  daptomycin (**B**) showing effective growth at both concentrations of antibiotic in the DAP-R isolate, and a clear growth defect in the DAP-S isolate.

### Determining Genotypic Contributions to Daptomycin-resistance

To determine the genotypic drivers of daptomycin-resistance in this model, each clinical isolate was subjected to whole-genome sequencing and compared for mutations that may lead to phenotypic differences in daptomycin-susceptibility. Of particular interest to the phenotype, a mutation from T  $\rightarrow$  C at position 53,411 was found to lead to an amino acid change from leucine to serine at position 341 (L341S) in the gene

*mprF*. This gene encodes the protein MprF (multiple peptide resistance factor) that is responsible for the production of lysyl-PG lipids in *S. aureus*.<sup>242</sup> In brief, MprF is a heterodimer transmembrane protein that uses bacterial phosphatidylglycerol (PG) lipids as a substrate and modifies the lipid headgroup with a lysine moiety. In a two-step process, the synthase domain of MprF first modifies PG lipids in the cytosol after which the flippase domain transports newly synthesized lysyl-PG lipids to the outer leaflet of the membrane (**Figure 4.3**).<sup>243</sup> Importantly, these lysyl-PG lipids are positively charged and have been demonstrated to repel cationic antimicrobial peptides (CAMPs) during infection.<sup>244</sup> A mutation in *mprF* leading to increased lysyl-PG content would act to increase the net charge of the bacterial membrane and this L341S mutation in *mprF* has been observed in the literature previously in association with daptomycin-resistance.<sup>245,246</sup>



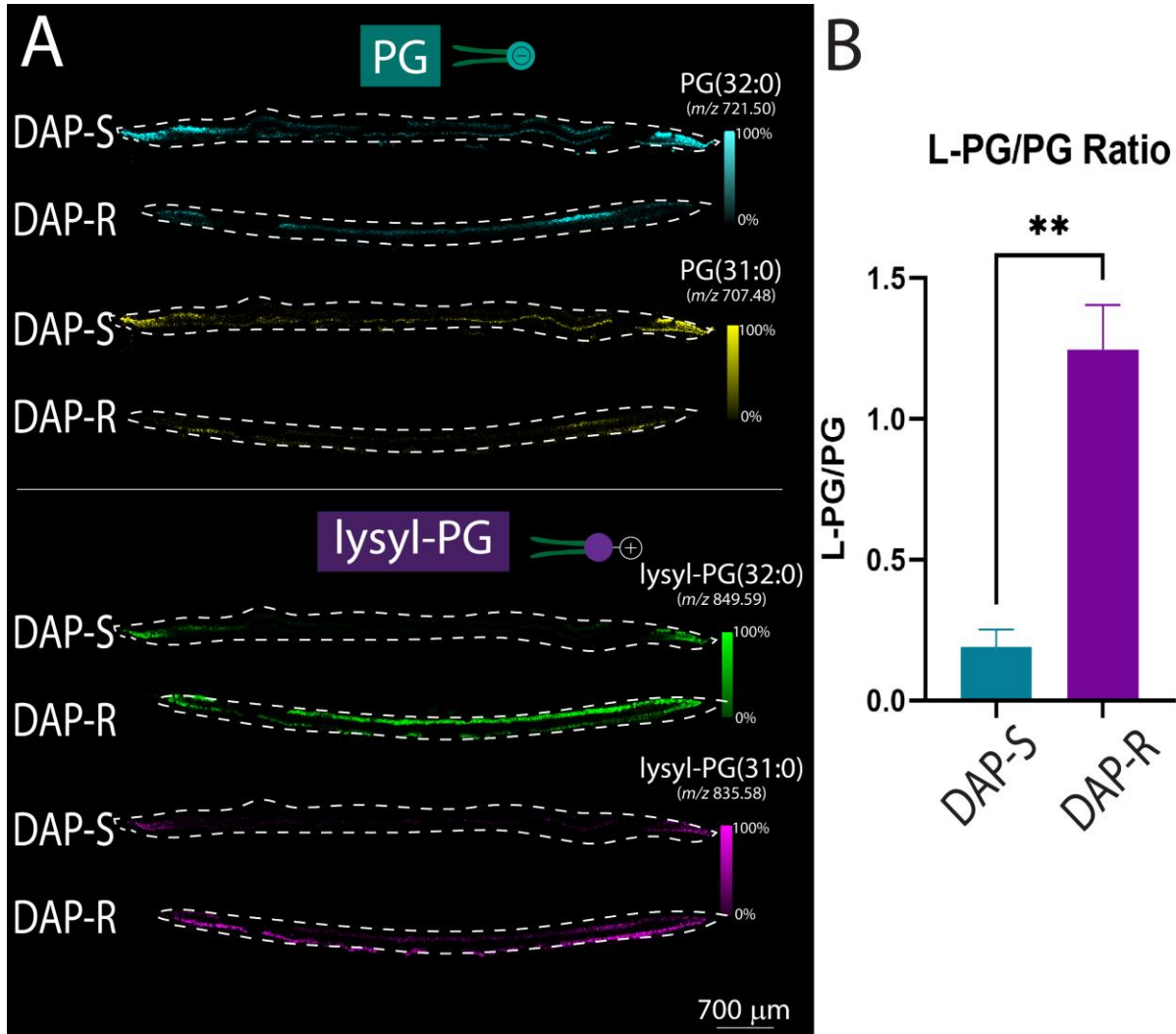
**Figure 4.3.** Diagram depicting the *S. aureus* protein MprF. The synthase domain first binds negatively charged PG lipids with lysine to synthesize a lysyl-PG lipid. The flippase domain then flips the new lysyl-PG lipid to the outer leaflet of the bacterial membrane, increasing the net charge of the membrane.

Because the L341S mutation in MprF has been reported in association with daptomycin-resistance,<sup>245,247</sup> investigating molecular changes associated with this mutation became the primary point of research interest. Unfortunately, MprF has a molecular weight of 97 kDa<sup>243</sup> and is therefore outside of the routine detectable mass range for intact protein IMS. Similarly, tryptic peptides of MprF were not detected in either the MALDI IMS of tryptic peptides, nor in the traditional bottom-up proteomics performed on *S. aureus* biofilms. As such, direct analysis of MprF by MALDI IMS was not feasible. However, as described in Chapters II and III, analysis of the substrate and product of MprF, PG and lysyl-PG lipids species by MALDI IMS was highly achievable. Moreover, because previous studies have found changes in the bacterial lipidome to be associated with daptomycin-resistance, these lipid species became the primary target of investigation for daptomycin-resistance in this model.

*MALDI TIMS IMS Reveals Basal Lipidomic Differences Between Daptomycin-Resistant and -Susceptible S. aureus Clinical Isolates*

To investigate the abundances and distributions of PG and lysyl-PG lipids within the DAP-S and DAP-R clinical isolates, 10  $\mu\text{m}$  spatial resolution imaging mass spectrometry was performed on biofilms grown with each isolate under basal conditions (i.e. without antibiotic). Two representative PG species, PG(32:0) and PG(31:0) detected at  $m/z$  721.50 and  $m/z$  707.48 respectively, were chosen as the representative lipids as substrates of MprF. These lipids exhibited subtle changes in abundance and distribution between the DAP-S and DAP-R clinical isolates. Both species were detected in higher abundance in the DAP-S biofilm, with localization primarily at the periphery of the biofilm (**Figure 4.4A**). In contrast, the abundances of both PG's were lower in the DAP-R biofilm, and the distributions appeared more broadly across the biofilm in both cases (**Figure 4.4A**). Interestingly, the opposite trends were noted in the representative products of MprF, lysyl-PG(32:0) and lysyl-PG(31:0). These species exhibited a concomitant increase in abundance in the DAP-R isolate. Taken together,

these results coincide with a model in which the L341S mutation observed in the DAP-R clinical isolate leads to a gain-of-function phenotype in MprF, resulting in an increase in turnover of PG to lysyl-PG lipids species, contributing to the resistance phenotype.



**Figure 4.4.** MALDI IMS data of both *S. aureus* clinical isolates grown without daptomycin exposure. Ion images of PG(32:0) (cyan) and PG(31:0) (yellow) showing higher levels in the DAP-S isolate and lysyl-PG(32:0) (green) and lysyl-PG(31:0) (pink) showing the opposite trend (A) Ratios of lysyl-PG/PG are higher in the DAP-R isolate (purple) than the DAP-S (turquoise) with values of 1.25 and 0.19, respectively (B).

This turnover was monitored by measuring the ratio of lysyl-PG to PG species in each biofilm. When compared in a triplicate experiment, the ratio of lysyl-PG(32:0) to PG(32:0) was found to be 0.19 in the DAP-S biofilm, and 1.25 in the DAP-R biofilm. Furthermore, these results were found to be significant by a paired t test, with a p-value of 0.003 (**Figure 4.4B**). First, these results confirm that the turnover of PG to lysyl-PG lipids in the DAP-R biofilm is higher than that of the DAP-S. In addition, with a mean value >1 (1.25) in the DAP-R biofilm, the ratio of lysyl-PG to PG indicates that this isolate has higher amounts of these lysylated lipids than the unmodified species. This observation demonstrated that even when grown in the absence of daptomycin pressure, this bacterial community is prepared at the lipidomic level for daptomycin exposure.

### *Spatial Investigation of Bacterial Lipidomic Response Within Clinical Isolate Biofilms During Daptomycin Treatment*

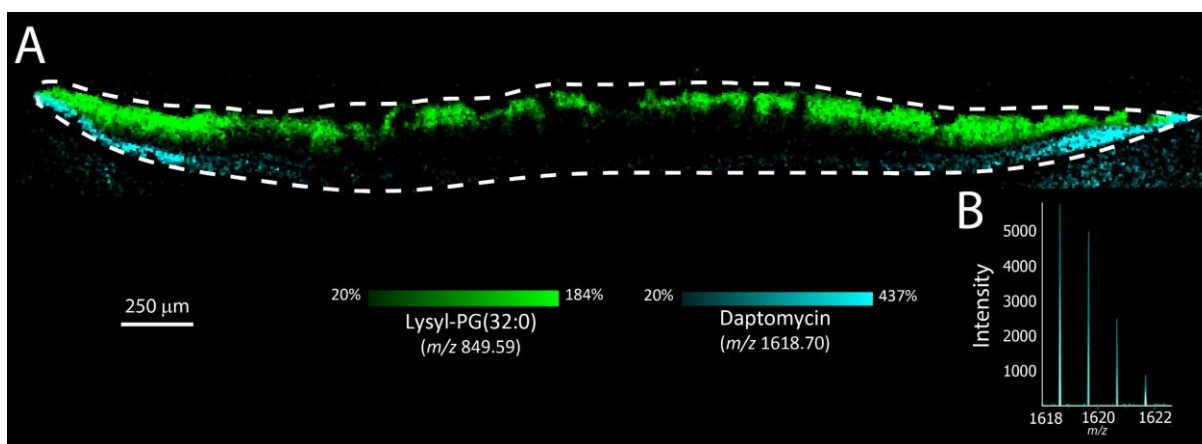
#### Measuring Daptomycin Penetration in *S. aureus* Biofilms

In addition to monitoring changes in the bacterial lipidome, it was important to investigate the distribution of the antibiotic itself. Monitoring the penetration of daptomycin into the biofilm would enable the mapping of lipids to be related back to the antibiotic distribution for additional context into the biofilm spatial response. Untargeted analysis by MALDI IMS has the power to afford the spatial investigation of both the antibiotic, and the lipids thought to play a role in its resistance in the same experiment. To validate the instrument for antibiotic detection, a daptomycin standard was first analyzed by MALDI MS on the timsTOF Pro. Based on the molecular weight of daptomycin, detection of the antibiotic at  $m/z$  1618.70 was expected. Beyond simply increasing the scanned mass range of the mass spectrometer to include the mass of daptomycin, it was determined that optimizing the instrument, including the 'transfer time' and 'pre-pulse storage' was necessary for effective detection of the antibiotic. By



optimizing these instrument parameters, signal at  $m/z$  1618.70 corresponding to the  $[M-H]^-$  of daptomycin was detected with S/N over 500 (**Figure 4.5B**).

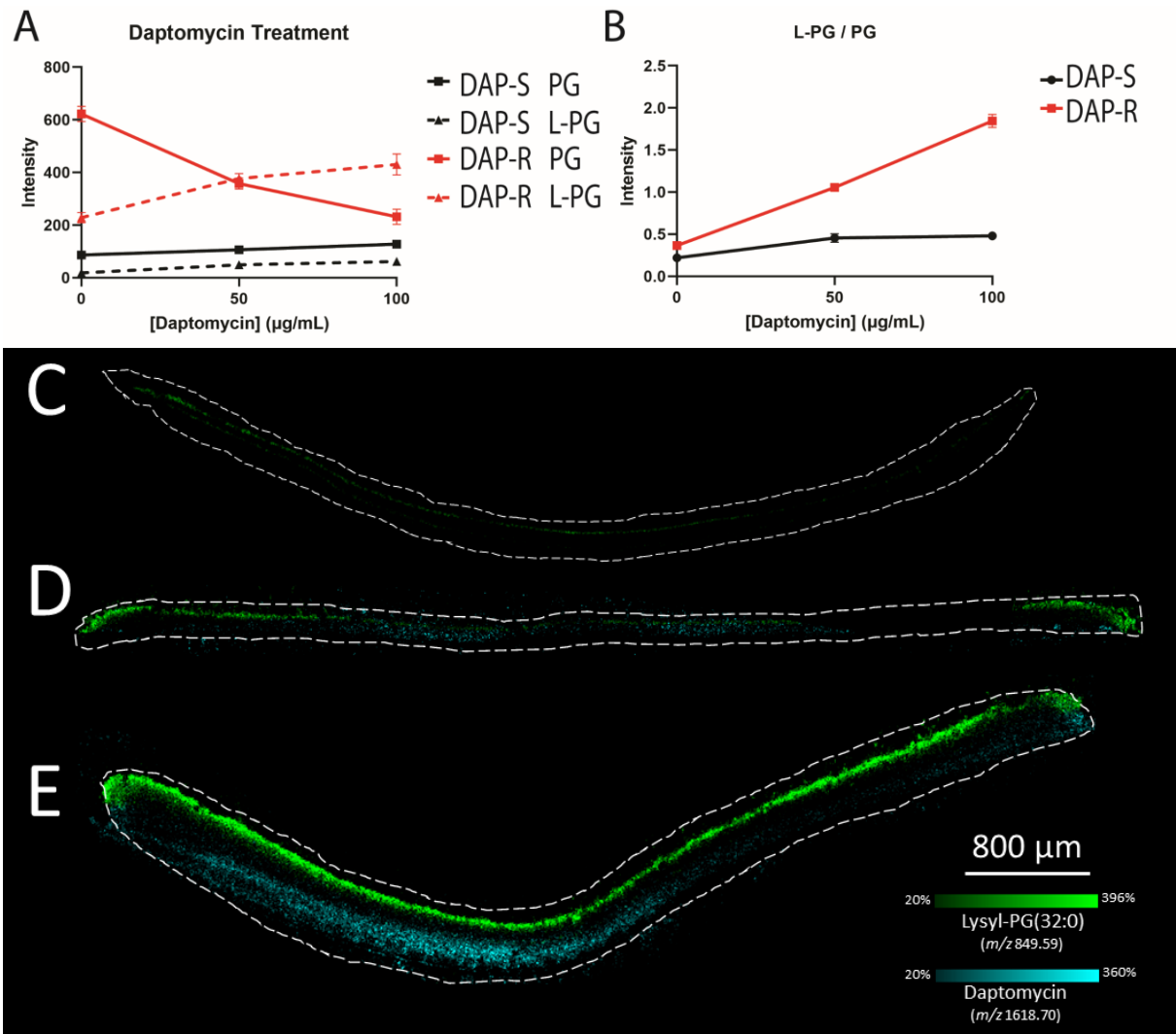
Next, a biofilm was grown with a laboratory strain of *S. aureus* and exposed to daptomycin treatment by introducing the antibiotic at a concentration of 100  $\mu\text{g/mL}$  to the growth media. The biofilm was then prepared as described in Chapter II and 10  $\mu\text{m}$  spatial resolution MALDI IMS was performed in the lipid mass range with modifications made to the instrument method for simultaneous detection of bacterial lipids and antibiotic. Here, daptomycin was observed to penetrate the biofilm (**Figure 4.5A**). In particular, daptomycin appeared to localize to the polar ends of the biofilm, perhaps localizing to the newly replicated bacteria at the periphery. Interestingly, when compared to the localization of lysyl-PG lipids, no co-localization was observed, raising questions about the spatial distributions of lysyl-PG lipids in relation to the antibiotic. Although these experiments were performed with a laboratory strain of *S. aureus*, this experiment demonstrated the feasibility of mapping both lipid and daptomycin distributions in an *S. aureus* biofilm.



**Figure 4.5.** MALDI IMS of a laboratory strain of *S. aureus* exposed to 100  $\mu\text{g/mL}$  daptomycin where the penetration of antibiotic is mapped (cyan) and compared to lysyl-PG(32:0) (green) (**A**). MALDI analysis of a daptomycin standard showing S/N of over 500 (**B**).

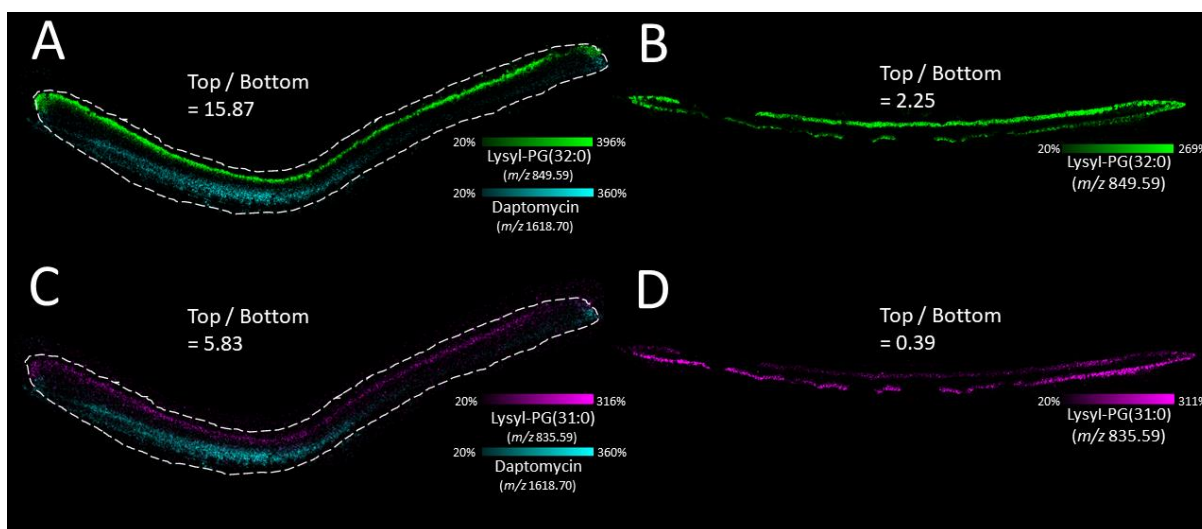
## Visualizing the Lipidomic Response to Daptomycin Exposure

To investigate the lipidomic response to daptomycin exposure in the DAP-S and DAP-R clinical isolates, biofilms grown with each isolate were first allowed to develop on TSA for 72 hrs. Following development, biofilms grown with each isolate were transferred to media containing three clinically relevant concentrations of daptomycin (0, 50, and 100  $\mu\text{g}/\text{mL}$ )<sup>248,249</sup> for an additional 24 hrs. Performed in triplicate, these biofilms were then prepared as described in Chapter II and analyzed by MALDI TIMS IMS using an instrumental method tuned for simultaneous detection of bacterial lipids and daptomycin. Having determined the primary target analytes as PG and lysyl-PG lipids, the abundances of PG(32:0) and lysyl-PG(32:0) were again selected as representative ions and compared between clinical isolates as a function of daptomycin concentration. In the DAP-S isolate, abundances of PG(32:0) and lysyl-PG(32:0) did not change dramatically regardless of daptomycin concentration (**Figure 4.6A**). In contrast, a significant response was observed in the DAP-R biofilm with a dose-dependent decrease in PG, and a concomitant dose-dependent increase in lysyl-PG (**Figure 4.6A**). Moreover, the abundances of lysyl-PG increased to levels greater than PG in the DAP-R isolate. Because measuring the substrate, PG(32:0) and the product, lysyl-PG(32:0) is a measure of MprF activity, the ratio of lysyl-PG was again calculated (**Figure 4.6B**). Here, the ratio of lysyl-PG(32:0) to PG(32:0) did not indicate a dramatic response by MprF in the DAP-S biofilm. A slight increase from 0.22 to 0.46 was observed in the ratio between biofilms grown in 0 and 50  $\mu\text{g}/\text{mL}$ , with no change at 100  $\mu\text{g}/\text{mL}$  (**Figure 4.6B**). These results suggest that the bacteria were not able to alter their membrane composition through increased lysyl-PG production in response to daptomycin exposure in the DAP-S biofilm by MprF activity. The same ratio in the DAP-R biofilm, however, exhibited a stark dose-dependent change, increasing from 0.37 in the biofilm grown without antibiotic, to 1.06 and finally 1.85 in the biofilms exposed to 50 and 100  $\mu\text{g}/\text{mL}$ , respectively (**Figure 4.6B**). This dramatic increase in the ratio of lysyl-PG to PG demonstrates the dose-dependent response by MprF in the DAP-R biofilm. Taken together, the ratios between DAP-S and DAP-R biofilms show that a dose-dependent response was only observed in the DAP-R biofilm.



**Figure 4.6.** MALDI IMS of *S. aureus* biofilms grown with DAP-S and DAP-R clinical isolates exposed to 0, 50, and 100 µg/mL of daptomycin. Abundances of PG and lysyl-PG lipid species show no substantial changes in response to antibiotic in the DAP-S isolate, but a substantial change in the DAP-R isolate (**A**). As a result, the ratio of lysyl-PG/PG does not change substantially in the DAP-S isolate but does demonstrate a dose-dependent response in the DAP-R isolate (**B**). Ion image overlays of daptomycin penetration (cyan) and lysyl-PG(32:0) (green) in the DAP-R biofilm exposed to 0 µg/mL daptomycin (**C**), 50 µg/mL daptomycin (**D**), and 100 µg/mL daptomycin (**E**).

In addition to monitoring the gross lipidomic response by the DAP-R biofilm, MALDI IMS afforded spatial information about the lipidome during daptomycin exposure. Moreover, tuning of the instrument as described above allowed for mapping of the daptomycin penetration into each biofilm, and further afforded the ability to relate daptomycin distributions to the lysyl-PG lipids thought to be electrostatically repelling the antibiotic. In ion images of lysyl-PG(32:0), the dose-dependent response by the DAP-R biofilms is visually clear, with increasing lysyl-PG signal between biofilms exposed to 0, 50 and 100  $\mu\text{g}/\text{mL}$  of daptomycin (**Figure 4.6C – E**). As expected, abundance and penetration of daptomycin increased in each of these biofilms, confirming that increased dose of antibiotic leads to higher levels inside the biofilm (**Figure 4.6C – E**). Interestingly, despite the hypothesis that lysyl-PG lipids are acting to electrostatically repel daptomycin, these molecules did not co-localize with one another. Because daptomycin was introduced to the biofilm from the agar below, it was detected primarily in the bottom layer of the biofilm. However, lysyl-PG(32:0) was detected almost exclusively in the top layer of the biofilm, with no co-localization between them.

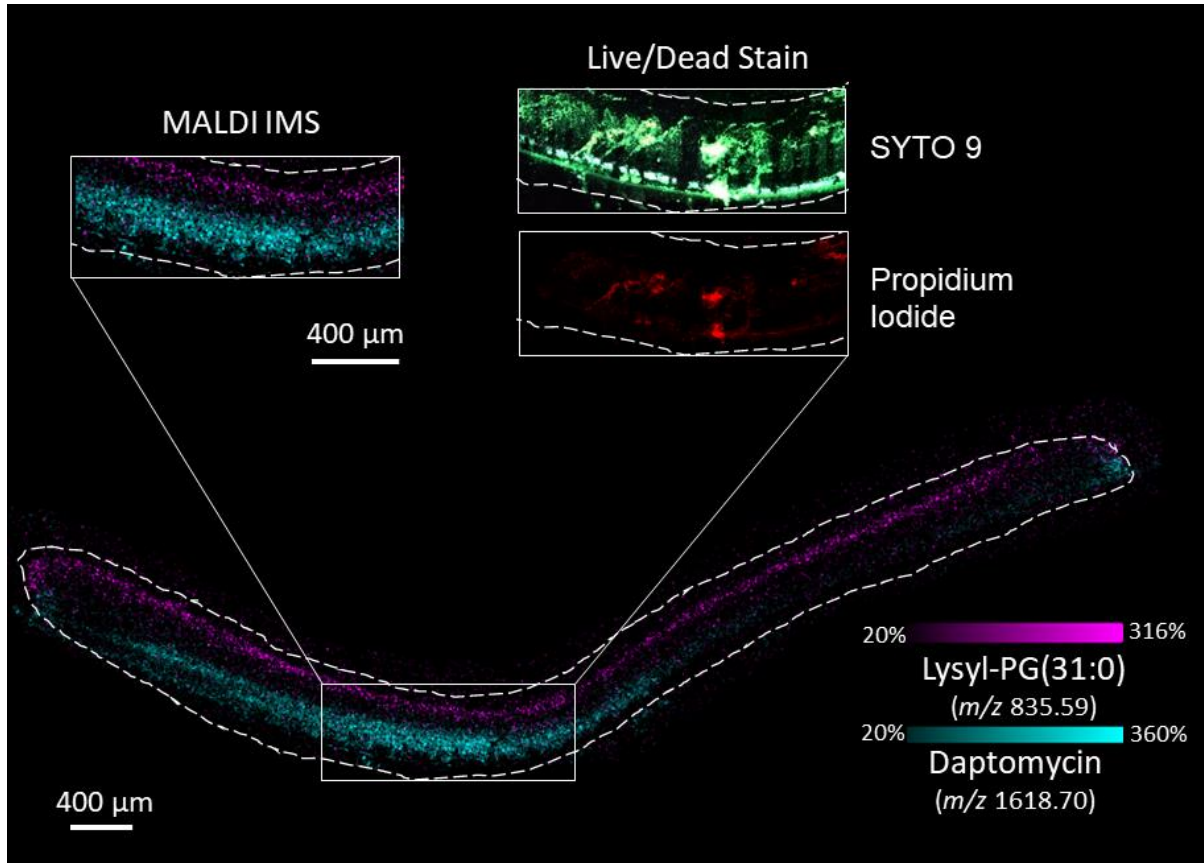


**Figure 4.7.** MALDI IMS of DAP-R clinical isolate showing daptomycin penetration (cyan), lysyl-PG(32:0) (green) and lysyl-PG(31:0). In the biofilm exposed to 100  $\mu\text{g}/\text{mL}$  daptomycin, lysyl-PG(32:0) is observed more abundantly in the top layer of the biofilm with a ratio of top/bottom = 15.87 (**A**), which coincides with its distribution in the untreated biofilm with a ratio of 2.25 (**B**). Conversely, lysyl-PG(31:0) is observed more abundantly in the top layer of the treated biofilm with a ratio of 5.83 (**C**), which does not coincide with its localization in the untreated biofilm where it has a ratio of 0.39 (**D**).

While potentially interesting that lysyl-PG(32:0) did not co-localize with the antibiotic within the treated biofilm, the distribution of this lipid was observed in the top layer of the untreated biofilm (**Figure 4.7B**). For this reason, it was unclear if the biological driver of this distribution was the presence of the antibiotic or the inherent localization of this particular lysyl-PG to the top layer. Lysyl-PG(31:0), however, was observed to inherently localize primarily to the bottom layer in the untreated biofilm without antibiotic stress (**Figure 4.7D**). To assess the localizations of these lipids, the ratios of abundance between top and bottom biofilm layers in the untreated biofilm were calculated. For lysyl-PG(32:0) the ratio of top/bottom was 2.25, whereas lysyl-PG(31:0) was 0.39. These results demonstrate that lysyl-PG(32:0) was detected with more than double the abundance in the top layer compared to the bottom, and that lysyl-PG(31:0) displayed the opposite trend. Conversely, in the biofilm exposed to 100  $\mu\text{g/mL}$ , the distribution of lysyl-PG(31:0) was primarily in the top layer, and the top/bottom ratio was calculated to be 5.83 (**Figure 4.7C**). These results demonstrate that lysyl-PG(31:0) localized primarily in the bottom layer of the untreated biofilm in the absence of antibiotic stress, and switched to the top layer in response to daptomycin penetration.

One potential explanation for this phenomenon was that the bacteria in the bottom layer of the biofilm were dead or metabolically inhibited by the presence of daptomycin and therefore not able to synthesize lysyl-PG species. However, this explanation was not likely as lipids other than lysyl-PG's were still observed to co-localize with the antibiotic penetration, indicating viability of these bacteria. To directly assess the viability of these bacteria, live/dead staining was performed on these biofilms using SYTO 9® and propidium iodide. SYTO 9® is a cell permeable nucleic acid stain and therefore stains any cells green, regardless of viability and propidium iodide is impermeable to cells with intact membranes and therefore should only stain dead cells red. A serial section of the DAP-R biofilm that was exposed to 100  $\mu\text{g/mL}$  daptomycin was prepared and stained. These data clearly demonstrated a lack of propidium iodide signal in the region of the biofilm with the most antibiotic penetration (**Figure 4.8**), suggesting that the bacteria colocalizing with daptomycin were viable. These results further indicated that the switching of lysyl-PG(31:0) localization from the bottom layer in the untreated biofilm to the top layer in the treated biofilm is not the result of cell death

in the bottom layer of the biofilm. As such, it remains likely that this change in lysyl-PG distribution is a component of the coordinated biofilm response to daptomycin treatment.



**Figure 4.8.** MALDI IMS and live/dead staining of DAP-R clinical isolate of *S. aureus* where all bacteria regardless of viability were stained green by SYTO 9®. Conversely, propidium iodide was used to stain only dead bacteria red, as it cannot penetrate intact bacterial membranes. These results show that the bacteria that colocalize with daptomycin penetration (cyan) are still viable and therefore capable of producing lysyl-PG(31:0).

## Discussion

By implementing specific strategies for MALDI IMS of bacterial lipids developed in Chapters II and III in combination with whole-genome sequencing, distinct genotypic and phenotypic differences were observed as a function of daptomycin-resistance in *S.*

*aureus* biofilms. In particular, these studies demonstrated differences between biofilms grown with isogenic DAP-S and DAP-R clinical isolates where isolates were taken from a single patient before and after development of daptomycin-resistance. First, whole-genome sequencing revealed a point mutation between the isolates resulting in an amino acid change from leucine to serine at position 341 within *mprF*. This and other mutations in *mprF* have been observed previously are thought to be a “gain-of-function” mutation.<sup>247</sup> Because *mprF* encodes for the enzyme that is responsible for producing lysyl-PG lipid species that are associated with daptomycin-resistance in *S. aureus*, investigations of these lipid species were performed. Ten  $\mu\text{m}$  spatial resolution MALDI IMS revealed that even in the absence of daptomycin, basal levels of lysyl-PG(31:0) and lysyl-PG(32:0) were higher in the DAP-R biofilm compared to the DAP-S biofilm. These results signify that the DAP-R biofilms were molecularly “primed” for combatting daptomycin treatment without external stimulation. In addition, these findings are in agreement with the previous findings that the L341S mutation is a gain-of-function mutation, leading to increased levels of lysyl-PG species. Furthermore, when these biofilms were exposed to daptomycin treatment at various concentrations, a dose-dependent lipidomic response was observed. The DAP-R biofilm exhibited increasing levels of lysyl-PG species as daptomycin concentration increased. Conversely, a concomitant decrease in PG species of the same fatty acyl tail composition was observed, suggesting that MprF was indeed increasing turnover of PG to lysyl-PG species in a dose-dependent manner. These results mark the first known example of a dose-dependent lipidomic response to daptomycin treatment in *S. aureus* biofilms and provide insight to the daptomycin resistance phenotype.

The methodologies developed herein also afforded the spatial mapping of daptomycin penetration into an *S. aureus* biofilm, allowing the comparison of distributions between daptomycin and the lysyl-PG lipids thought to be repelling it. Here, it was determined that lysyl-PG species did not co-localize with the mapped distributions of daptomycin. In fact, in these treated biofilms, lysyl-PG lipids such as lysyl-PG(31:0) changed localization from the bottom to top layer of the biofilm, no longer localizing in the region where daptomycin was observed. This discovery demonstrates that the lipidomic response to daptomycin treatment in *S. aureus* biofilms is spatially discrete,

and that these lipid species associated with repelling the antibiotic are primarily localized to bacteria that did not experience daptomycin penetration. While the biological drivers of this phenomenon are not readily obvious, it is possible that the biofilm acts as a community against the antibiotic. In this model, the biofilm may be presenting behavior similar to multicellular organs in higher organisms that induce apoptosis to preserve healthy cells.<sup>250</sup> Although further work is necessary to probe this model, it is possible that these microbial communities have a coordinated system for spatially combatting external threats such as antibiotics, which could have major implications for the way *S. aureus* biofilms are treated. Ultimately, the work detailed above uncovered genotypic and phenotypic alterations between DAP-S and DAP-R clinical isolates of *S. aureus* that afford resistance to the antibiotic. Specifically, these studies revealed a dose-dependent, spatially discrete biofilm response to daptomycin only in the DAP-R biofilms. The methodologies developed in Chapter II and III afforded a robust workflow for spatially investigating these biofilms, and without the label-free, untargeted, spatial analyses provided by MALDI IMS, these localized biofilm responses observed herein would not have been uncovered.

## Methods

### *Materials*

2',5'-Dihydroxyacetophenone (DHA), 1',5'-Diaminonaphthalene (DAN), ammonium formate, ammonium acetate, poly-L-lysine solution, and calcium chloride were purchased from Sigma-Aldrich Chemical Co. (St. Louis, MO, USA). HPLC-grade acetonitrile, methanol, gelatin powder, daptomycin standard and Molecular Probes Prolong Diamond Antifade Mountant were purchased from Fisher Scientific (Pittsburgh, PA, USA). Carboxymethylcellulose (CMC) was purchased from PM MP Biomedicals (Salon, OH). Tryptic soy agar (TSA) and tryptic soy broth (TSB) were purchased from Becton, (Dickinson, Franklin Lakes, NJ) and all lab plasticware was from USA Scientific (Ocala, FL) or Corning (Corning, NY). Whatman Nucleopore polycarbonate filter discs (0.1 um pore size) were acquired from Millipore Sigma (Burlington, MA). and stored at -



20° C before being introduced to petri dishes. Tris-buffered saline (TBS) was acquired from Corning (Corning, NY).

### *Sample Preparation*

*S. aureus* bacterial cultures and biofilm were grown and processed as described in Chapter II prior to antibiotic treatment. Following 72 hrs of initial development, each biofilm was transferred to a new petri dish with agar containing TSA with added daptomycin (0, 50 or 100 µg/mL) and 50 µg/mL CaCl<sub>2</sub> to aid in daptomycin efficacy.<sup>245,251</sup> The daptomycin and CaCl<sub>2</sub> were introduced to smaller volumes of liquid TSA (100 mL) via sterile syringe and polycarbonate filter at the appropriate concentration to produce desired final concentration of daptomycin in the total volume of TSA prior to introducing the media to the petri dish.

### *Imaging Mass Spectrometry*

All experiments were performed on a prototype timsTOF Pro mass spectrometer (Bruker Daltonik, Bremen, Germany)<sup>67</sup> as described in Chapter III with slight variations for simultaneous detection of daptomycin and bacterial lipids. Images were acquired in TIMS mode of operation with an ion transfer time of 120 µs and a prepulse storage time of 7 µs. Images were acquired with a modified mass range *m/z* 100 – 2000.

### *Live/Dead Staining*

*S. aureus* biofilm viability was assessed using the Filmtracer™ LIVE/DEAD™ Biofilm Viability Kit (ThermoFisher Scientific, Waltham, MA). In brief, serial sections of the same biofilms exposed to varying concentrations of daptomycin were stained with a mixture of Cyto 9 and propidium iodide (1:1) as outlined in the provided protocol. These stains were allowed to incubate for 30 minutes in the dark followed by washing. Rather than using pure water to wash the excess stain as suggested by the protocol, TBS was used to reduce cell lysis and loss of biofilm structure. Diamond Antifade was applied and sample was cover slipped and allowed to dry for 24 hrs. Fluorescence imaging was performed using EGFP and DsRed filters for on a Zeiss AxioScan.Z1 slide scanner (Carl Zeiss Microscopy GmbH, Oberkochen, Germany).

## CHAPTER V

### CONCLUSIONS AND FUTURE DIRECTIONS

#### Overview

With the growing threat of antibiotic resistance in *S. aureus* infections, particularly for the last-line antibiotic daptomycin, understanding the molecular changes that contribute towards resistance phenotypes is crucial. The field of “spatial omics” is a promising area of research that offers potential for mapping various classes of biomolecules. In the work detailed herein, both sample preparation and instrumental parameters were developed for effective multi-omic investigations of *S. aureus* biofilm cross-sections. First, steps for growing, embedding, and cryosectioning *S. aureus* biofilms were described for any class of analyte, followed by specific details for preparing these biofilms for analysis of either lipids, tryptic peptides, or intact proteins by MALDI IMS. The determination of these sample preparation protocols afforded spatial investigations for any of these analyte classes that can be applied on any IMS platform. Next, detection of each analyte class was validated on a timsTOF Pro by optimizing instrumental parameters, demonstrating a single MALDI IMS platform for effective spatial multi-omic analysis on various murine and human tissue types. The development of these workflows next led to the discovery of multi-omic heterogeneity between horizontal *S. aureus* biofilm layers. Finally, these workflows were applied toward the spatial investigation of lipid distributions within biofilms grown with daptomycin-susceptible and -resistant clinical isolates of *S. aureus*. This work resulted in the discovery of a basal lipidomic difference in distribution and abundance between daptomycin-susceptible and -resistant isolates. When used to study the effects of daptomycin treatment in these isolates, MALDI IMS revealed a dose-dependent lipidomic response to the antibiotic only in the -resistant biofilms. In this chapter, the findings herein will be discussed followed by current limitations of the technology and directions for future study.

## Conclusions

### *Preparing S. aureus biofilms for multi-omic analysis*

The field of multi-omics is growing at a high pace, with increasing interest in investigating multiple analyte classes in a single sample. Major strides have been made in recent years for these multi-omic studies using LC-MS/MS where multiple extractions can be performed for downstream analysis of each analyte class.<sup>252</sup> Such extractions are not possible for spatially aware methodologies such as MALDI IMS performed directly on tissue, making these multi-omic spatial investigations challenging. Analyte-specific challenges necessitate specific steps for effective measurement.

In Chapter II, it was determined that washing biofilm samples with ammonium formate at a concentration that was isotonic to the bacteria effectively remediated residual chemical interferences from bacterial growth media. This washing step increased CL signal by as much as tenfold while decreasing interfering ions in the low mass range. Different MALDI matrices including DHA and DAN were also compared for bacterial lipid signal of *S. aureus* biofilms where DHA provided intense lipid signal, and did not produce significant spectral interferences, and was consequently selected as the optimal MALDI matrix for *S. aureus* biofilm lipid analysis.

Preparing *S. aureus* biofilms for spatial investigation of proteins was demonstrated via two separate methods. First, tryptic digestion was assessed where the importance of performing antigen retrieval prior to MALDI IMS for this sample type was revealed, increasing the number of detected tryptic peptides by more than twofold. It is possible that in addition to denaturing the endogenous bacterial proteins, this improvement was due to lysing of the thick bacterial cell wall, allowing trypsin to more effectively penetrate into the bacteria. While antigen retrieval was determined to increase the sensitivity for tryptic peptides in MALDI IMS of *S. aureus* biofilms, it came at the expense of peptide delocalization. This phenomenon is likely due to the fact that proteins and peptides are water-soluble, and the submergence of the sample for the antigen retrieval process leads to delocalization.

For intact protein analysis of *S. aureus* biofilms by MALDI IMS, it was determined that a Carnoy's wash was necessary to obtain optimal signal of intact proteins. By removing bacterial lipid species that act as spectral interferences, this non-polar washing step improved the sensitivity for intact proteins by more than twofold. Furthermore, a visual investigation of the structural integrity of the biofilm by autofluorescence determined that almost no damage was incurred during the process, underscoring the feasibility of this wash for intact protein analysis of *S. aureus* biofilms.

*Characterization of Instrumental Parameters for Effective MALDI TIMS IMS Analysis of Lipids, Peptides, and Intact Proteins on a timsTOF Pro*

As the field of “spatial omics” grows, the improvement of instrumental methodologies for high spatial resolution MALDI IMS investigation of lipids, tryptic peptides, and intact proteins is necessary. The ability to perform these types of multi-omic investigations in a spatial context has been somewhat limited in part due to the lack of MALDI IMS instrumentation capable of optimal analyses of each analyte class. Where TOF MS often provides high spatial resolution and speed, it often does not provide the necessary mass resolving power, in particular for obtaining baseline resolution of individual isotope within a single protein spectral envelope. Conversely, while the FT-ICR MS is capable ultra-high mass resolving powers, commercially available options require exceedingly long acquisition times, and do not provide high spatial resolutions. In Chapter III, instrumental considerations were described for the effective analysis of lipids, tryptic peptides, and intact proteins on a timsTOF Pro, for simultaneous high spatial resolution, mass resolving power, and speed.

For lipids, MALDI analysis on the timsTOF Pro demonstrated high sensitivity and low mass error of bacterial lipids. Furthermore, the orthogonal gas-phase separation by TIMS led to an increase in both S/N and the overall peak capacity performing 10  $\mu\text{m}$  spatial resolution IMS. Using these developed instrumental methods, high spatial resolution MALDI IMS led to the discovery of discrete, molecularly distinct horizontal layered subpopulations within *S. aureus* biofilm cross-sections. Comparisons of

individual lipid abundances between biofilm layers by relative quantitation demonstrated differences in select CL lipid species between layers, possibly indicating distinct biological roles for these distinct CL species. In addition, investigations of *S. aureus* biofilms grown under anaerobic conditions revealed thinner biofilms comprised of a single layer with homogenous lipid distributions, suggesting that aerobic growth conditions may be required for generation of multiple layers in *S. aureus* biofilms.

Validation of the timsTOF Pro for tryptic peptides using trypsin digested BSA protein and HeLa cell extracts resulted in at least 11 tryptic peptides detected with a S/N of > 3 via MALDI analysis of the BSA standard. Likewise, over 200 tryptic peptides were detected when these instrumental methods were applied for MALDI IMS of tryptic peptides in human pancreas with as many as five unique peptides detected for a single protein. Overall, this work provided validation of tryptic peptide analysis by MALDI IMS on a timsTOF Pro. Combined with the details outlined in Chapter II for preparing *S. aureus* biofilms for tryptic peptide analysis, heterogeneity between horizontal biofilm layers was also observed at the proteomic level.

By first optimizing the MALDI source pressure, the mass range for intact proteins was extended to nearly  $m/z$  20,000 on the timsTOF Pro. The versatility of this instrument was exploited here to demonstrate that untargeted protein IMS on this platform provided rapid, high spatial resolution imaging without sacrificing spectral resolving power. When these methodologies were applied toward the spatial interrogation of bacterial proteins in an *S. aureus* biofilm cross-section, clear heterogeneity between biofilm layers was again uncovered.

*Characterizing lipidomic distributions in biofilms of daptomycin-susceptible and -resistant clinical isolates of S. aureus*

Finally, in Chapter IV high spatial resolution MALDI IMS was used to examine biological drivers of daptomycin resistance in *S. aureus* biofilms. Specific strategies for MALDI IMS of bacterial lipids developed in Chapters II and III provided an approach for the simultaneous mapping of bacterial lipids, and antibiotic penetration. While other approaches such as the use of a fluorescently labeled antibiotic have been used to

measure antibiotic penetration into a biofilm,<sup>253</sup> it remains unknown if such labels affect the penetration of the antibiotic into *S. aureus* biofilms. The MALDI IMS performed herein provided a technology capable of label-free analysis of antibiotic penetration into a biofilm, ensuring that penetration is not hampered by a fluorescent label. In addition, this technology was shown to provide concurrent untargeted analysis of bacterial lipids, allowing their distributions to be compared to that of the antibiotic penetration in a single experiment. In doing so, these studies found differences between biofilms grown with daptomycin-susceptible or daptomycin-resistant clinical isolates of *S. aureus*. Specifically, the discovery of increased basal levels of lysyl-PG lipid species in the daptomycin-resistant biofilm compared to its -susceptible counterpart was observed. By growing these biofilms in the presence of varying concentrations of daptomycin, a dose-dependent, spatially discrete lipidomic response by the daptomycin-resistant biofilm was also noted. Increasing levels of lysyl-PG lipids and localizations of these lipids did not overlap with antibiotic penetration, possibly indicative of a coordinated, communal response by the biofilm to preserve bacteria without antibiotic penetration.

Indeed, biofilms are known to employ a form of signaling system using secreted signaling molecules in a process called quorum-sensing,<sup>254</sup> which has been shown to act as a spatially localized form of intercellular communication to regulate biofilm behaviors such as population density,<sup>255</sup> virulence,<sup>256</sup> and even antimicrobial resistance.<sup>257</sup> It is interesting to speculate on whether this may be driving a coordinated, communal response within an *S. aureus* biofilm that focuses on protecting the bacteria in the regions of the biofilm that have not yet been exposed to antibiotics. One intriguing possibility is that the Agr quorum-sensing system may be involved in a spatially localized biofilm response to daptomycin. Interestingly, in one study by Pader *et al.*, deletion of Agr, led to enhanced *S. aureus* survival during daptomycin treatment of planktonic bacteria.<sup>258</sup> The authors concluded that Agr-mediated secretion of phenol soluble modulins was likely inhibiting the interaction of daptomycin with shed bacterial phospholipids, allowing it to intercalate in bacterial membranes. This work demonstrates that Agr-mediated quorum sensing plays a role in daptomycin-resistance but has not been investigated in a biofilm model. It is therefore possible that quorum-sensing may be affecting lysyl-PG localization within an *S. aureus* biofilm under daptomycin stress.

## Current Limitations and Future Directions

### *Sample Preparation*

Although these results demonstrated a new approach for preparing *S. aureus* biofilms for MALDI IMS, these methodologies do have some distinct limitations. Peptide delocalization presents a major limitation for performing high spatial resolution tryptic peptide MALDI IMS of *S. aureus* biofilms regardless of instrument platform. Future work to minimize the amount of water used in the antigen retrieval process could be investigated to address this issue. For example, performing antigen retrieval under conditions of 100% humidity may provide enough moisture for the antigen retrieval process, without leading to analyte delocalization. Another potential area of exploration is the implementation of enzymatic lysis of bacterial cells. If the antigen retrieval-mediated enhancement of tryptic peptide signal is, in fact due to lysis of bacteria, enzymatic lysis may also be beneficial. The application of lysostaphin, an enzyme capable of degrading the cell wall of *S. aureus* prior to trypsin digestion, may further contribute to improved access of trypsin to endogenous bacterial proteins. Indeed, lysostaphin is commonly applied to *S. aureus* for permeabilization for fluorescence-based techniques,<sup>259</sup> and such a step may benefit on-biofilm tryptic digestion.

While the Carnoy's wash was effective at increasing the overall number of detectable proteins, improvements can still be made. For example, one area of investigation that is largely understudied is the effect of protein denaturation on the desorption/ionization process in MALDI. Protein denaturation could provide certain amino acids within the protein greater access to proton donors, leading to increased ionization efficiency. As antigen retrieval is thought to cause protein denaturation, it may be a possible avenue for increasing protein ionization efficiency. However, this may come at the expense of protein delocalization as it does for tryptic peptide MALDI IMS.

## Instrumentation

Although the work presented in Chapter II represents one of the highest spatial resolution (10  $\mu\text{m}$ ) investigations of bacterial biofilms to date, *S. aureus* bacteria are  $<1$   $\mu\text{m}$  in diameter.<sup>260</sup> Spatial investigations of these microbial communities could benefit from improved spatial resolution. Dreisewerd and coworkers among others have previously reported MALDI IMS experiments with spatial resolutions of 1  $\mu\text{m}$  for lipid analysis on murine tissue.<sup>261,262</sup> Here, the group leveraged the high spatial resolution capabilities of transmission geometry where the MALDI laser is positioned behind the sample for improved laser focus, in combination with increased sensitivity provided by a secondary laser known as MALDI-2. Future work to implement these technologies on the timsTOF Pro could afford single-cell resolution of *S. aureus* bacteria within a biofilm to investigate the molecular delineations between biofilm layers.

A major focus of the work herein is the analytical flexibility of the timsTOF Pro for spatial multi-omic investigations, however there are certain instrumental limitations that must still be overcome. One such limitation stems from the immaturity of the field of TIMS. Despite capabilities of robustly measuring  $1/K_0$  with resolving powers exceeding 200,<sup>263,264</sup> the approaches for calibrating the ion mobility dimension in a MALDI experiment are still undefined.<sup>265</sup> As a result, calculated CCS measurements from MALDI TIMS experiments are often a point of discussion and represent a need in the field. Future work to validate the calibration of  $1/K_0$  from TIMS experiments stands to provide an orthogonal measurement for identifying species in a MALDI IMS experiment. One possible solution is the homogenous application of an exogenous internal standard to the sample. Guo *et al.* recently demonstrated that an internal standard could be applied to a sample for DESI IMS analysis,<sup>266</sup> and the application of a standard with known CCS could provide a signal for ion mobility calibration throughout an IMS experiment. Once CCS values can be calculated reliably from a MALDI experiment; the addition of these values to lipidomic and proteomic (peptide and intact protein) databases will be paramount. Efforts are already underway for including CCS values for biomolecules in databases from ESI experiments,<sup>60,267,268</sup> and the addition of MALDI-



derived measurements for these biomolecular classes into databases could significantly increase the confidence of identifications in an imaging experiment.

Another area of research that is in need of advancement is the addition of MS/MS fragmentation for IMS experiments. The molecular identifications made herein were made possible by off-line fragmentation performed on serial sections for lipids and mass fingerprinting for tryptic peptides. However, this work could have benefitted significantly from fragmentation information within an imaging experiment. MS/MS imaging has been demonstrated previously,<sup>269,270</sup> but is not currently a popular area of research interest in spite of the obvious advantages it stands to provide. However, one example of ongoing work in this area by Colley *et al.*, is aiming to implement parallel accumulation serial fragmentation (PASEF), a TIMS-based method for data-independent acquisition MS/MS in a MALDI IMS experiment that will soon provide fragmentation in an IMS experiment for increased identifying power.<sup>271</sup>

While MS/MS imaging could be highly informative for lipids and tryptic peptides, it would still present challenges for identifying intact proteins. To achieve informative fragmentation and robust identification from a MALDI IMS experiment, two instrument attributes would need to be considered: 1) the upper  $m/z$  limit for ion isolation and 2) the available ion activation methods. Currently, the upper limit for ion isolation on the timsTOF Pro is  $m/z \sim 3,000$ . Adjustment of ion optic and quadrupole RF frequencies has the potential to extend the upper  $m/z$  limit of ion isolation. After ion isolation, production of informative fragment ions during MS/MS is crucial to analyte identification. Low-energy collisional activation, the only available ion activation on the timsTOF Pro, yields few informative fragment ions for low-charge state ions. Alternative ion activation methods, including ultraviolet photodissociation (UVPD), have previously been shown to provide increased protein sequence coverage for singly-charged ions generated by MALDI.<sup>212</sup> In addition, UVPD was recently implemented on a timsTOF equipped with an electrospray source for dissociation of peptides and proteins.<sup>272</sup> Future implementation of UVPD on a MALDI QTOF mass spectrometer may provide benefits for *in situ* protein identification, which is powerful for untargeted, discovery-based analysis.

## *Investigations of daptomycin-resistance in S. aureus biofilms*

The application of the methodologies curated herein led to a robust methodology for multi-omic spatial investigations of *S. aureus* biofilms, that when applied to interrogate daptomycin resistance, uncovered a spatially discrete biofilm response. Orthogonal data demonstrated that the shift in lysyl-PG(31:0) distribution from bottom to top biofilm layers was likely the result of a coordinated communal response, and not the result of dying bacteria. However, if this change in lipid distribution is a coordinated response, its biological drivers remain unexplained. To confirm that the distributions of lysyl-PG's change in response to daptomycin, one potential experiment would be to treat the biofilms with antibiotic from above, rather than from the media below as done here. In this experiment, distributional shifts in the opposite direction would be expected.

While the L341S mutation observed is likely contributing to the daptomycin-resistance phenotype, it does not exclude that levels of MprF are also increasing in the biofilm regions where the lysyl-PG response is observed. Orthogonal techniques such as spatial transcriptomics or another form of spatially targeted proteomics, e.g. LESA, could also be implemented for uncovering the causative agents of the spatially discrete biofilm response observed here. These experiments would also be untargeted and could uncover unknown spatially discrete alterations in the transcript or proteome that may also confer daptomycin-resistance in a biofilm. Finally, high spatial resolution MALDI IMS of *S. aureus* biofilms grown with Agr mutants could shine light on the spatial role played by Agr in daptomycin-resistance and determine if lysyl-PG localization is affected by quorum-sensing.

## Concluding Remarks

As the field continues to evolve, coupling of MALDI IMS with other technologies such as ion mobility will likely take hold as the new standard. Hybrid instruments such as the timsTOF Pro will represent a new generation of instrumentation. As such, work like that presented herein will be required for benchmarking these instruments for analysis of different analyte classes. This growth, however, will not come without challenges, including the robustness of CCS calculations from TIMS measurements for more confident analyte identification. The field of MALDI TIMS IMS is still in its infancy and as the technology continues to improve, so too will the strategies for increasing robustness in CCS calculation. In addition, TIMS has been readily demonstrated to separate closely isobaric or even isomeric molecules in a MALDI IMS experiment.<sup>55,263</sup> As the field moves forward, distinguishing biomolecules with similar or identical  $m/z$  in a single MALDI IMS experiment will become increasingly feasible, significantly broadening the range of identifiable species. Finally, as these technologies take hold, new computational requirements for effective data analysis will have to be met. The construction of some computational pipelines is already underway, and this area of research will only become increasingly critical.

## References

- (1) Norris, J. L.; Caprioli, R. M. Analysis of Tissue Specimens by Matrix-Assisted Laser Desorption/ Ionization Imaging Mass Spectrometry in Biological and Clinical Research. <https://doi.org/10.1021/cr3004295>.
- (2) Caprioli, R. M.; Farmer, T. B.; Gile, J. Molecular Imaging of Biological Samples: Localization of Peptides and Proteins Using MALDI-TOF MS. *Anal. Chem.* **1997**, *69* (23), 4751–4760. <https://doi.org/10.1021/ac970888i>.
- (3) Wiseman, J. M.; Puolitaival, S. M.; Takáts, Z.; Cooks, R. G.; Caprioli, R. M. Mass Spectrometric Profiling of Intact Biological Tissue by Using Desorption Electrospray Ionization. *Angew. Chemie Int. Ed.* **2005**, *44* (43), 7094–7097. <https://doi.org/10.1002/anie.200502362>.
- (4) Ifa, D. R.; Wiseman, J. M.; Song, Q.; Cooks, R. G. Development of Capabilities for Imaging Mass Spectrometry under Ambient Conditions with Desorption Electrospray Ionization (DESI). *Int. J. Mass Spectrom.* **2007**, *259* (1–3), 8–15. <https://doi.org/10.1016/j.ijms.2006.08.003>.
- (5) Robichaud, G.; Barry, J. A.; Garrard, K. P.; Muddiman, D. C. Infrared Matrix-Assisted Laser Desorption Electrospray Ionization (IR-MALDESI) Imaging Source Coupled to a FT-ICR Mass Spectrometer. *J. Am. Soc. Mass Spectrom* **2013**, *24*, 92–100. <https://doi.org/10.1007/s13361-012-0505-9>.
- (6) Nemes, P.; Barton, A. A.; Li, Y.; Vertes, A. Ambient Molecular Imaging and Depth Profiling of Live Tissue by Infrared Laser Ablation Electrospray Ionization Mass Spectrometry. *Anal. Chem.* **2008**, *80* (12), 4575–4582. <https://doi.org/10.1021/ac8004082>.

- (7) Eikel, D.; Vavrek, M.; Smith, S.; Bason, C.; Yeh, S.; Korfmacher, W. A.; Henion, J. D. Liquid Extraction Surface Analysis Mass Spectrometry (LESA-MS) as a Novel Profiling Tool for Drug Distribution and Metabolism Analysis: The Terfenadine Example. *Rapid Commun. Mass Spectrom.* **2011**, *25* (23), 3587–3596. <https://doi.org/10.1002/rcm.5274>.
- (8) Laskin, J.; Heath, B. S.; Roach, P. J.; Cazares, L.; Semmes, O. J. Tissue Imaging Using Nanospray Desorption Electrospray Ionization Mass Spectrometry. *Anal. Chem.* **2012**, *84* (1), 141–148. <https://doi.org/10.1021/ac2021322>.
- (9) Du, Z.; Lin, J.-R.; Rashid, R.; Maliga, Z.; Wang, S.; Aster, J. C.; Izar, B.; Sorger, P. K.; Santagata, S. Qualifying Antibodies for Image-Based Immune Profiling and Multiplexed Tissue Imaging. *Nat. Protoc.* <https://doi.org/10.1038/s41596-019-0206-y>.
- (10) Neumann, E. K.; Comi, T. J.; Spegazzini, N.; Mitchell, J. W.; Rubakhin, S. S.; Gillette, M. U.; Bhargava, R.; Sweedler, J. V. Multimodal Chemical Analysis of the Brain by High Mass Resolution Mass Spectrometry and Infrared Spectroscopic Imaging. *Anal. Chem.* **2018**, *90* (19), 11572–11580. <https://doi.org/10.1021/acs.analchem.8b02913>.
- (11) Baker, M. J.; Trevisan, J.; Bassan, P.; Bhargava, R.; Butler, H. J.; Dorling, K. M.; Fielden, P. R.; Fogarty, S. W.; Fullwood, N. J.; Heys, K. A.; et al. Using Fourier Transform IR Spectroscopy to Analyze Biological Materials. *Nat. Protoc.* **2014**, *9* (8), 1771–1791. <https://doi.org/10.1038/nprot.2014.110>.
- (12) Mulder, I. A.; Esteve, C.; Wermer, J. H.; Hoehn, M.; Tolner, E. A.; Van Den Maagdenberg, A. M. J. M.; McDonnell, L. A.; McDonnell, L. Funnel-Freezing

- versus Heat-Stabilization for the Visualization of Metabolites by Mass Spectrometry Imaging in a Mouse Stroke Model. *Proteomics* **2016**, *16*, 1652–1659. <https://doi.org/10.1002/pmic.201500402>.
- (13) Manier, M. L.; Spraggins, J. M.; Reyzer, M. L.; Norris, J. L.; Caprioli, R. M. A Derivatization and Validation Strategy for Determining the Spatial Localization of Endogenous Amine Metabolites in Tissues Using MALDI Imaging Mass Spectrometry. *J. Mass Spectrom.* **2014**, *49* (8), 665–673. <https://doi.org/10.1002/jms.3411>.
- (14) Thomas, A.; Charbonneau, J. L.; Fournaise, E.; Chaurand, P. Sublimation of New Matrix Candidates for High Spatial Resolution Imaging Mass Spectrometry of Lipids: Enhanced Information in Both Positive and Negative Polarities after 1,5-Diaminonaphthalene Deposition. *Anal. Chem.* **2012**, *84* (4), 2048–2054. <https://doi.org/10.1021/ac2033547>.
- (15) Sparvero, L. J.; Amoscato, A. A.; Kochanek, P. M.; Pitt, B. R.; Kagan, V. E.; Bayär, H. Mass-Spectrometry Based Oxidative Lipidomics and Lipid Imaging: Applications in Traumatic Brain Injury. *Journal of Neurochemistry*. NIH Public Access December 2010, pp 1322–1336. <https://doi.org/10.1111/j.1471-4159.2010.07055.x>.
- (16) Cornett, D. S.; Frappier, S. L.; Caprioli, R. M. MALDI-FTICR Imaging Mass Spectrometry of Drugs and Metabolites in Tissue. *Anal. Chem.* **2008**, *80* (14), 5648–5653. <https://doi.org/10.1021/ac800617s>.
- (17) Heikkinen, E. M.; Auriola, S.; Ranta, V. P.; Demarais, N. J.; Grey, A. C.; Del Amo, E. M.; Toropainen, E.; Vellonen, K. S.; Urtti, A.; Ruponen, M. Distribution of Small

- Molecular Weight Drugs into the Porcine Lens: Studies on Imaging Mass Spectrometry, Partition Coefficients, and Implications in Ocular Pharmacokinetics. *Mol. Pharm.* **2019**, *16* (9), 3968–3976.  
<https://doi.org/10.1021/acs.molpharmaceut.9b00585>.
- (18) Everest-Dass, A. V.; Briggs, M. T.; Kaur, G.; Oehler, M. K.; Hoffmann, P.; Packer, N. H. N-Glycan MALDI Imaging Mass Spectrometry on Formalin-Fixed Paraffin-Embedded Tissue Enables the Delineation of Ovarian Cancer Tissues. *Mol. Cell. Proteomics* **2016**, *15* (9), 3003–3016. <https://doi.org/10.1074/mcp.M116.059816>.
- (19) Drake, R. R.; Powers, T. W.; Norris-Caneda, K.; Mehta, A. S.; Angel, P. M. In Situ Imaging of N-Glycans by MALDI Imaging Mass Spectrometry of Fresh or Formalin-Fixed Paraffin-Embedded Tissue. *Curr. Protoc. Protein Sci.* **2018**, *94* (1). <https://doi.org/10.1002/cpps.68>.
- (20) Hanrieder, J.; Zetterberg, H.; Blennow, K. MALDI Imaging Mass Spectrometry: Neurochemical Imaging of Proteins and Peptides. In *Neuromethods*; Humana Press Inc., 2019; Vol. 146, pp 179–197. [https://doi.org/10.1007/978-1-4939-9662-9\\_15](https://doi.org/10.1007/978-1-4939-9662-9_15).
- (21) Judd, A. M.; Gutierrez, D. B.; Moore, J. L.; Patterson, N. H.; Yang, J.; Romer, C. E.; Norris, J. L.; Caprioli, R. M. A Recommended and Verified Procedure for in Situ Tryptic Digestion of Formalin-Fixed Paraffin-Embedded Tissues for Analysis by Matrix-Assisted Laser Desorption/Ionization Imaging Mass Spectrometry. **2019**. <https://doi.org/10.1002/jms.4384>.
- (22) Dilillo, M.; Ait-Belkacem, R.; Esteve, C.; Pellegrini, D.; Nicolardi, S.; Costa, M.; Vannini, E.; De Graaf, E. L.; Caleo, M.; McDonnell, L. A. Ultra-High Mass

- Resolution MALDI Imaging Mass Spectrometry of Proteins and Metabolites in a Mouse Model of Glioblastoma. *Sci. Rep.* **2017**, *7* (1), 1–11.  
<https://doi.org/10.1038/s41598-017-00703-w>.
- (23) Spraggins, J. M.; Rizzo, D. G.; Moore, J. L.; Noto, M. J.; Skaar, E. P.; Caprioli, R. M. Next-Generation Technologies for Spatial Proteomics: Integrating Ultra-High Speed MALDI-TOF and High Mass Resolution MALDI FTICR Imaging Mass Spectrometry for Protein Analysis. *Proteomics* **2016**, *16* (11–12), 1678–1689.  
<https://doi.org/10.1002/pmic.201600003>.
- (24) Karas, M.; Bachmann, D.; Bahr, U.; Hillenkamp, F. Matrix-Assisted Ultraviolet Laser Desorption of Non-Volatile Compounds. *Int. J. Mass Spectrom. Ion Process.* **1987**, *78* (C), 53–68. [https://doi.org/10.1016/0168-1176\(87\)87041-6](https://doi.org/10.1016/0168-1176(87)87041-6).
- (25) Gessel, M. M.; Norris, J. L.; Caprioli, R. M. MALDI Imaging Mass Spectrometry: Spatial Molecular Analysis to Enable a New Age of Discovery. *J. Proteomics* **2014**, *0*, 71. <https://doi.org/10.1016/J.JPROT.2014.03.021>.
- (26) Fernandez-Lima, F. A.; Kaplan, D. A.; Park, M. A. Note: Integration of Trapped Ion Mobility Spectrometry with Mass Spectrometry. *Rev. Sci. Instrum.* **2011**, *82* (12), 126106. <https://doi.org/10.1063/1.3665933>.
- (27) Rivera, E. S.; Djambazova, K. V.; Neumann, E. K.; Caprioli, R. M.; Spraggins, J. M. Integrating Ion Mobility and Imaging Mass Spectrometry for Comprehensive Analysis of Biological Tissues: A Brief Review and Perspective. *J. Mass Spectrom.* **2020**, *55* (12), e4614. <https://doi.org/10.1002/jms.4614>.
- (28) Tang, W.; Chen, J.; Zhou, J.; Ge, J.; Zhang, Y.; Li, P.; Li, B. Quantitative MALDI Imaging of Spatial Distributions and Dynamic Changes of Tetrandrine in Multiple



- Organs of Rats. *Theranostics* **2019**, *9* (4), 932–944.  
<https://doi.org/10.7150/THNO.30408>.
- (29) Rubakhin, S. S.; Romanova, E. V.; Sweedler, J. V. High-Throughput Image-Guided Microprobe Mass Spectrometric Analysis of Single Cells. **2022**, 115–163.  
[https://doi.org/10.1007/978-1-0716-2525-5\\_6](https://doi.org/10.1007/978-1-0716-2525-5_6).
- (30) Cao, T.; Sweedler, J. V.; Bohn, P. W.; Shrout, J. D. Spatiotemporal Distribution of *Pseudomonas Aeruginosa* Alkyl Quinolones under Metabolic and Competitive Stress. *mSphere* **2020**, *5* (4). [https://doi.org/10.1128/MSPHERE.00426-20/SUPPL\\_FILE/MSPHERE.00426-20-SF008.TIF](https://doi.org/10.1128/MSPHERE.00426-20/SUPPL_FILE/MSPHERE.00426-20-SF008.TIF).
- (31) Bleich, R.; Watrous, J. D.; Dorrestein, P. C.; Bowers, A. A.; Shank, E. A. Thiopeptide Antibiotics Stimulate Biofilm Formation in *Bacillus Subtilis*. *Proc. Natl. Acad. Sci. U. S. A.* **2015**, *112* (10), 3086–3091.  
[https://doi.org/10.1073/PNAS.1414272112/SUPPL\\_FILE/PNAS.201414272SI.PDF](https://doi.org/10.1073/PNAS.1414272112/SUPPL_FILE/PNAS.201414272SI.PDF).
- (32) Wakeman, C. A.; Moore, J. L.; Noto, M. J.; Zhang, Y.; Singleton, M. D.; Prentice, B. M.; Gilston, B. A.; Doster, R. S.; Gaddy, J. A.; Chazin, W. J.; et al. The Innate Immune Protein Calprotectin Promotes *Pseudomonas Aeruginosa* and *Staphylococcus Aureus* Interaction. *Nat. Commun.* **2016**, *7* (1), 1–12.  
<https://doi.org/10.1038/ncomms11951>.
- (33) Periasamy, S.; Joo, H. S.; Duong, A. C.; Bach, T. H. L.; Tan, V. Y.; Chatterjee, S. S.; Cheung, G. Y. C.; Otto, M. How *Staphylococcus Aureus* Biofilms Develop Their Characteristic Structure. *Proc. Natl. Acad. Sci. U. S. A.* **2012**, *109* (4), 1281–1286. <https://doi.org/10.1073/pnas.1115006109>.

- (34) Yannarell, S. M.; Veličković, D.; Anderton, C. R.; Shank, E. A. Direct Visualization of Chemical Cues and Cellular Phenotypes throughout *Bacillus Subtilis* Biofilms. *mSystems* **2021**, *6* (6). [https://doi.org/10.1128/MSYSTEMS.01038-21/SUPPL\\_FILE/MSYSTEMS.01038-21-SF002.PDF](https://doi.org/10.1128/MSYSTEMS.01038-21/SUPPL_FILE/MSYSTEMS.01038-21-SF002.PDF).
- (35) Gonzalez, D. J.; Haste, N. M.; Hollands, A.; Fleming, T. C.; Hamby, M.; Pogliano, K.; Nizet, V.; Dorrestein, P. C. Microbial Competition between *Bacillus Subtilis* and *Staphylococcus Aureus* Monitored by Imaging Mass Spectrometry. *Microbiology* **2011**, *157* (9), 2485–2492. <https://doi.org/10.1099/MIC.0.048736-0/CITE/REFWORKS>.
- (36) Brockmann, E. U.; Steil, D.; Bauwens, A.; Soltwisch, J.; Dreisewerd, K. Advanced Methods for MALDI-MS Imaging of the Chemical Communication in Microbial Communities. *Anal. Chem.* **2019**, *91* (23), 15081–15089. <https://doi.org/10.1021/acs.analchem.9b03772>.
- (37) Watrous, J. D.; Phelan, V. V.; Hsu, C. C.; Moree, W. J.; Duggan, B. M.; Alexandrov, T.; Dorrestein, P. C. Microbial Metabolic Exchange in 3D. *ISME J.* **2013**, *7* (4), 770–780. <https://doi.org/10.1038/ismej.2012.155>.
- (38) Amstalden van Hove, E. R.; Smith, D. F.; Heeren, R. M. A. A Concise Review of Mass Spectrometry Imaging. *J. Chromatogr. A* **2010**, *1217* (25), 3946–3954. <https://doi.org/10.1016/J.CHROMA.2010.01.033>.
- (39) Wenzel, R. J.; Matter, U.; Schultheis, L.; Zenobi, R. Analysis of Megadalton Ions Using Cryodetection MALDI Time-of-Flight Mass Spectrometry. *Anal. Chem.* **2005**, *77* (14), 4329–4337. <https://doi.org/10.1021/AC0482054/ASSET/IMAGES/LARGE/AC0482054F00006>.

JPEG.

- (40) Guilhaus, M.; Mlynski, V.; Selby, D. Perfect Timing: Time-of-Flight Mass Spectrometry †. *Rapid. Commun. Mass Spectrom* **1996**, *11*, 951–962.  
[https://doi.org/10.1002/\(SICI\)1097-0231\(19970615\)11:9](https://doi.org/10.1002/(SICI)1097-0231(19970615)11:9).
- (41) Radionova, A.; Filippov, I.; Derrick, P. J. In Pursuit of Resolution in Time-of-Flight Mass Spectrometry: A Historical Perspective. *Mass Spectrom. Rev.* **2016**, *35* (6), 738–757. <https://doi.org/10.1002/MAS.21470>.
- (42) Mamyrin, B. A.; Karataev, V. I.; Shmikk, D. V.; Zagulin, V. A. The Mass-Reflectron, a New Nonmagnetic Time-of-Flight Mass Spectrometer with High Resolution. **1973**.
- (43) Bowman, A. P.; Blakney, G. T.; Hendrickson, C. L.; Ellis, S. R.; Heeren, R. M. A.; Smith, D. F. Ultra-High Mass Resolving Power, Mass Accuracy, and Dynamic Range MALDI Mass Spectrometry Imaging by 21-T FT-ICR MS. *Anal. Chem* **2020**, *92*, 3133–3142. <https://doi.org/10.1021/acs.analchem.9b04768>.
- (44) Comisarow, M. B.; Marshall, A. G. Fourier Transform Ion Cyclotron Resonance Spectroscopy. *Chem. Phys. Lett.* **1974**, *25* (2), 282–283.  
[https://doi.org/10.1016/0009-2614\(74\)89137-2](https://doi.org/10.1016/0009-2614(74)89137-2).
- (45) Valeja, S. G.; Kaiser, N. K.; Xian, F.; Hendrickson, C. L.; Rouse, J. C.; Marshall, A. G. Unit Mass Baseline Resolution for an Intact 148 KDa Therapeutic Monoclonal Antibody by Fourier Transform Ion Cyclotron Resonance Mass Spectrometry. *Anal. Chem.* **2011**, *83* (22), 8391–8395.  
[https://doi.org/10.1021/AC202429C/SUPPL\\_FILE/AC202429C\\_SI\\_001.PDF](https://doi.org/10.1021/AC202429C/SUPPL_FILE/AC202429C_SI_001.PDF).
- (46) Glish, G. L.; Goeringer, D. E. Tandem Quadrupole/Time-of-Flight Instrument for

- Mass Spectrometry/Mass Spectrometry. *Anal. Chem* **1984**, *56*, 2291–2295.
- (47) Allen, D. R.; McWhinney, B. C. Quadrupole Time-of-Flight Mass Spectrometry: A Paradigm Shift in Toxicology Screening Applications. *Clin. Biochem. Rev.* **2019**, *40* (3), 135. <https://doi.org/10.33176/AACB-19-00023>.
- (48) Cheng, K.; Brunius, C.; Fristedt, R.; Landberg, R. An LC-QToF MS Based Method for Untargeted Metabolomics of Human Fecal Samples. *Metabolomics* **2020**, *16* (4), 1–8. <https://doi.org/10.1007/S11306-020-01669-Z/FIGURES/2>.
- (49) Dong, F.; Deng, D.; Chen, H.; Cheng, W.; Li, Q.; Luo, R.; Ding, S. Serum Metabolomics Study of Polycystic Ovary Syndrome Based on UPLC-QTOF-MS Coupled with a Pattern Recognition Approach. *Anal. Bioanal. Chem.* **2015**, *407* (16), 4683–4695. <https://doi.org/10.1007/S00216-015-8670-X/TABLES/3>.
- (50) Godzien, J.; Ciborowski, M.; Martínez-Alcázar, M. P.; Samczuk, P.; Kretowski, A.; Barbas, C. Rapid and Reliable Identification of Phospholipids for Untargeted Metabolomics with LC-ESI-QTOF-MS/MS. *J. Proteome Res.* **2015**, *14* (8), 3204–3216.  
[https://doi.org/10.1021/ACS.JPROTEOME.5B00169/SUPPL\\_FILE/PR5B00169\\_SI\\_002.PDF](https://doi.org/10.1021/ACS.JPROTEOME.5B00169/SUPPL_FILE/PR5B00169_SI_002.PDF).
- (51) Guan, S.; Jia, B.; Chao, K.; Zhu, X.; Tang, J.; Li, M.; Wu, L.; Xing, L.; Liu, K.; Zhang, L.; et al. UPLC-QTOF-MS-Based Plasma Lipidomic Profiling Reveals Biomarkers for Inflammatory Bowel Disease Diagnosis. *J. Proteome Res.* **2020**, *19* (2), 600–609.  
[https://doi.org/10.1021/ACS.JPROTEOME.9B00440/ASSET/IMAGES/LARGE/PR9B00440\\_0004.JPEG](https://doi.org/10.1021/ACS.JPROTEOME.9B00440/ASSET/IMAGES/LARGE/PR9B00440_0004.JPEG).

- (52) Lesur, A.; Schmit, P. O.; Bernardin, F.; Letellier, E.; Brehmer, S.; Decker, J.; Dittmar, G. Highly Multiplexed Targeted Proteomics Acquisition on a TIMS-QTOF. *Anal. Chem.* **2021**, *93* (3), 1383–1392.  
[https://doi.org/10.1021/ACS.ANALCHEM.0C03180/ASSET/IMAGES/LARGE/AC0C03180\\_0007.JPEG](https://doi.org/10.1021/ACS.ANALCHEM.0C03180/ASSET/IMAGES/LARGE/AC0C03180_0007.JPEG).
- (53) Meier, F.; Park, M. A.; Mann, M. Trapped Ion Mobility Spectrometry and Parallel Accumulation–Serial Fragmentation in Proteomics. *Mol. Cell. Proteomics* **2021**, *20*, 100138.  
<https://doi.org/10.1016/J.MCPRO.2021.100138/ATTACHMENT/BB37F05F-F2B9-4BC6-B008-BA9CAFA136FB/MMC2.ZIP>.
- (54) Towers, M. W.; Karancsi, T.; Jones, E. A.; Pringle, S. D.; Claude, E. Optimised Desorption Electrospray Ionisation Mass Spectrometry Imaging (DESI-MSI) for the Analysis of Proteins/Peptides Directly from Tissue Sections on a Travelling Wave Ion Mobility Q-ToF. *J. Am. Soc. Mass Spectrom.* **2018**, *29* (12), 2456–2466.  
<https://doi.org/10.1007/s13361-018-2049-0>.
- (55) Spraggins, J. M.; Djambazova, K. V.; Rivera, E. S.; Migas, L. G.; Neumann, E. K.; Fuetterer, A.; Suetering, J.; Goedecke, N.; Ly, A.; Van De Plas, R.; et al. High-Performance Molecular Imaging with MALDI Trapped Ion-Mobility Time-of-Flight (TimsTOF) Mass Spectrometry. *Anal. Chem.* **2019**, *91* (22), 14552–14560.  
<https://doi.org/10.1021/acs.analchem.9b03612>.
- (56) Ruotolo, B. T.; Gillig, K. J.; Stone, E. G.; Russell, D. H. Peak Capacity of Ion Mobility Mass Spectrometry: Separation of Peptides in Helium Buffer Gas. *J. Chromatogr. B Anal. Technol. Biomed. Life Sci.* **2002**, *782* (1–2), 385–392.

- [https://doi.org/10.1016/S1570-0232\(02\)00566-4](https://doi.org/10.1016/S1570-0232(02)00566-4).
- (57) Fernandez-Lima, F.; Kaplan, D. A.; Suetering, J.; Park, M. A. Gas-Phase Separation Using a Trapped Ion Mobility Spectrometer. *Int. J. Ion Mobil. Spectrom.* **2011**, *14* (2), 93–98. <https://doi.org/10.1007/s12127-011-0067-8>.
- (58) Wyttenbach, T.; Kemper, P. R.; Bowers, M. T. Design of a New Electrospray Ion Mobility Mass Spectrometer. *Int. J. Mass Spectrom.* **2001**, *212* (1–3), 13–23. [https://doi.org/10.1016/S1387-3806\(01\)00517-6](https://doi.org/10.1016/S1387-3806(01)00517-6).
- (59) Hofmann, J.; Hahm, H. S.; Seeberger, P. H.; Pagel, K. Identification of Carbohydrate Anomers Using Ion Mobility-Mass Spectrometry. *Nature* **2015**, *526* (7572), 241–244. <https://doi.org/10.1038/nature15388>.
- (60) Bush, M. F.; Hall, Z.; Giles, K.; Hoyes, J.; Robinson, C. V.; Ruotolo, B. T. Collision Cross Sections of Proteins and Their Complexes: A Calibration Framework and Database for Gas-Phase Structural Biology. *Anal. Chem.* **2010**, *82* (22), 9557–9565. <https://doi.org/10.1021/ac1022953>.
- (61) Dodds, J. N.; May, J. C.; McLean, J. A. Correlating Resolving Power, Resolution, and Collision Cross Section: Unifying Cross-Platform Assessment of Separation Efficiency in Ion Mobility Spectrometry. *Anal. Chem.* **2017**, *89* (22), 12176–12184. <https://doi.org/10.1021/acs.analchem.7b02827>.
- (62) Stow, S. M.; Causon, T. J.; Zheng, X.; Kurulugama, R. T.; Mairinger, T.; May, J. C.; Rennie, E. E.; Baker, E. S.; Smith, R. D.; McLean, J. A.; et al. An Interlaboratory Evaluation of Drift Tube Ion Mobility-Mass Spectrometry Collision Cross Section Measurements. *Anal. Chem.* **2017**, *89* (17), 9048–9055. <https://doi.org/10.1021/acs.analchem.7b01729>.

- (63) Zhao, Y.; Singh, A.; Li, L.; Linhardt, R. J.; Xu, Y.; Liu, J.; Woods, R. J.; Amster, I. J. Investigating Changes in the Gas-Phase Conformation of Antithrombin III upon Binding of Arixtra Using Traveling Wave Ion Mobility Spectrometry (TWIMS). *Analyst* **2015**, *140* (20), 6980–6989. <https://doi.org/10.1039/c5an00908a>.
- (64) Guntner, A. S.; Thalhamer, B.; Klampfl, C.; Buchberger, W. Collision Cross Sections Obtained with Ion Mobility Mass Spectrometry as New Descriptor to Predict Blood-Brain Barrier Permeation by Drugs. *Sci. Rep.* **2019**, *9* (1), 1–10. <https://doi.org/10.1038/s41598-019-55856-7>.
- (65) Gomez, J. D.; Ridgeway, M. E.; Park, M. A.; Fritz, K. S. Utilizing Ion Mobility to Identify Isobaric Post-Translational Modifications: Resolving Acrolein and Propionyl Lysine Adducts by TIMS Mass Spectrometry. *Int. J. Ion Mobil. Spectrom.* **2018**, *21* (3), 65–69. <https://doi.org/10.1007/s12127-018-0237-z>.
- (66) Barré, F.; Rocha, B.; Dewez, F.; Towers, M.; Murray, P.; Claude, E.; Cillero-Pastor, B.; Heeren, R.; Porta Siegel, T. Faster Raster Matrix-Assisted Laser Desorption/Ionization Mass Spectrometry Imaging of Lipids at High Lateral Resolution. *Int. J. Mass Spectrom.* **2019**, *437*, 38–48. <https://doi.org/10.1016/j.ijms.2018.09.015>.
- (67) Spraggins, J. M.; Djambazova, K. V.; Rivera, E. S.; Migas, L. G.; Neumann, E. K.; Fuetterer, A.; Suetering, J.; Goedecke, N.; Ly, A.; Van de Plas, R.; et al. High-Performance Molecular Imaging with MALDI Trapped Ion-Mobility Time-of-Flight (TimsTOF) Mass Spectrometry. *Anal. Chem.* **2019**, *91* (22), 14552–14560. <https://doi.org/10.1021/acs.analchem.9b03612>.
- (68) Williams, J. P.; Bugarcic, T.; Habtemariam, A.; Giles, K.; Campuzano, I.; Rodger,

- P. M.; Sadler, P. J. Isomer Separation and Gas-Phase Configurations of Organoruthenium Anticancer Complexes: Ion Mobility Mass Spectrometry and Modeling. *J. Am. Soc. Mass Spectrom.* **2009**, *20* (6), 1119–1122.  
<https://doi.org/10.1016/j.jasms.2009.02.016>.
- (69) Adams, K. J.; Ramirez, C. E.; Smith, N. F.; Muñoz-Muñoz, A. C.; Andrade, L.; Fernandez-Lima, F. Analysis of Isomeric Opioids in Urine Using LC-TIMS-TOF MS. *Talanta* **2018**, *183*, 177–183. <https://doi.org/10.1016/j.talanta.2018.02.077>.
- (70) Fu, T.; Oetjen, J.; Chapelle, M.; Verdu, A.; Szesny, M.; Chaumot, A.; Degli-Esposti, D.; Geffard, O.; Clément, Y.; Salvador, A.; et al. In Situ Isobaric Lipid Mapping by MALDI-Ion Mobility Separation-Mass Spectrometry Imaging. *J. Mass Spectrom.* **2020**, e4531. <https://doi.org/10.1002/jms.4531>.
- (71) Hale, O. J.; Sisley, E. K.; Griffiths, R. L.; Styles, I. B.; Cooper, H. J. Native LESA TWIMS-MSI: Spatial, Conformational, and Mass Analysis of Proteins and Protein Complexes. *J. Am. Soc. Mass Spectrom.* **2020**, *31* (4), 873–879.  
<https://doi.org/10.1021/jasms.9b00122>.
- (72) Giles, K.; Pringle, S. D.; Worthington, K. R.; Little, D.; Wildgoose, J. L.; Bateman, R. H. Applications of a Travelling Wave-Based Radio-Frequency-Only Stacked Ring Ion Guide. *Rapid Commun. Mass Spectrom.* **2004**, *18* (20), 2401–2414.  
<https://doi.org/10.1002/rcm.1641>.
- (73) Pringle, S. D.; Giles, K.; Wildgoose, J. L.; Williams, J. P.; Slade, S. E.; Thalassinou, K.; Bateman, R. H.; Bowers, M. T.; Scrivens, J. H. An Investigation of the Mobility Separation of Some Peptide and Protein Ions Using a New Hybrid Quadrupole/Travelling Wave IMS/Oa-ToF Instrument. *Int. J. Mass Spectrom.*



- 2007**, 261 (1), 1–12. <https://doi.org/10.1016/j.ijms.2006.07.021>.
- (74) May, J. C.; McLean, J. A. Ion Mobility-Mass Spectrometry: Time-Dispersive Instrumentation. *Analytical Chemistry*. American Chemical Society February 3, 2015, pp 1422–1436. <https://doi.org/10.1021/ac504720m>.
- (75) Stauber, J.; MacAleese, L.; Franck, J.; Claude, E.; Snel, M.; Kaletas, B. K.; Wiel, I. M. V. D.; Wisztorski, M.; Fournier, I.; Heeren, R. M. A. On-Tissue Protein Identification and Imaging by MALDI-Ion Mobility Mass Spectrometry. *J. Am. Soc. Mass Spectrom.* **2010**, 21 (3), 338–347. <https://doi.org/10.1016/j.jasms.2009.09.016>.
- (76) Ahonen, L.; Fasciotti, M.; Gennäs, G. B. af; Kotiaho, T.; Daroda, R. J.; Eberlin, M.; Kostianen, R. Separation of Steroid Isomers by Ion Mobility Mass Spectrometry. *J. Chromatogr. A* **2013**, 1310, 133–137. <https://doi.org/10.1016/j.chroma.2013.08.056>.
- (77) Groessl, M.; Graf, S.; Knochenmuss, R. High Resolution Ion Mobility-Mass Spectrometry for Separation and Identification of Isomeric Lipids. *Analyst* **2015**, 140 (20), 6904–6911. <https://doi.org/10.1039/c5an00838g>.
- (78) Rister, A. L.; Martin, T. L.; Dodds, E. D. Formation of Multimeric Steroid Metal Adducts and Implications for Isomer Mixture Separation by Traveling Wave Ion Mobility Spectrometry. *J. Mass Spectrom.* **2019**, 54 (5), 429–436. <https://doi.org/10.1002/jms.4350>.
- (79) Hernández-Mesa, M.; Le Bizec, B.; Monteau, F.; García-Campaña, A. M.; Dervilly-Pinel, G. Collision Cross Section (CCS) Database: An Additional Measure to Characterize Steroids. *Anal. Chem.* **2018**, 90 (7), 4616–4625.

- <https://doi.org/10.1021/acs.analchem.7b05117>.
- (80) Ellis, B. M.; Fischer, C. N.; Martin, L. B.; Bachmann, B. O.; McLean, J. A. Spatiochemically Profiling Microbial Interactions with Membrane Scaffolded Desorption Electrospray Ionization-Ion Mobility-Imaging Mass Spectrometry and Unsupervised Segmentation. *Anal. Chem.* **2019**, *91* (21), 13703–13711. <https://doi.org/10.1021/acs.analchem.9b02992>.
- (81) Trim, P. J.; Henson, C. M.; Avery, J. L.; McEwen, A.; Snel, M. F.; Claude, E.; Marshall, P. S.; West, A.; Princivalle, A. P.; Clench, M. R. Matrix-Assisted Laser Desorption/Ionization-Ion Mobility Separation-Mass Spectrometry Imaging of Vinblastine in Whole Body Tissue Sections. *Anal. Chem.* **2008**, *80* (22), 8628–8634. <https://doi.org/10.1021/ac8015467>.
- (82) Xu, L.; Kliman, M.; Forsythe, J. G.; Korade, Z.; Hmelo, A. B.; Porter, N. A.; Mclean, J. A. Profiling and Imaging Ion Mobility-Mass Spectrometry Analysis of Cholesterol and 7-Dehydrocholesterol in Cells Via Sputtered Silver MALDI. <https://doi.org/10.1007/s13361-015-1131-0>.
- (83) Trimpin, S.; Herath, T. N.; Inutan, E. D.; Wager-Miller, J.; Kowalski, P.; Claude, E.; Michael Walker, J.; Mackie, K. Automated Solvent-Free Matrix Deposition for Tissue Imaging by Mass Spectrometry. *Anal. Chem.* **2010**, *82* (1), 359–367. <https://doi.org/10.1021/ac902065u>.
- (84) Harvey, D. J.; Scarff, C. A.; Crispin, M.; Scanlan, C. N.; Bonomelli, C.; Scrivens, J. H. MALDI-MS/MS with Traveling Wave Ion Mobility for the Structural Analysis of N-Linked Glycans. *J. Am. Soc. Mass Spectrom.* **2012**, *23* (11), 1955–1966. <https://doi.org/10.1007/s13361-012-0425-8>.

- (85) Ridenour, W. B.; Kliman, M.; McLean, J. A.; Caprioli, R. M. Structural Characterization of Phospholipids and Peptides Directly from Tissue Sections by MALDI Traveling-Wave Ion Mobility-Mass Spectrometry. *Anal. Chem.* **2010**, *82* (5), 1881–1889. <https://doi.org/10.1021/ac9026115>.
- (86) Škrášková, K.; Claude, E.; Jones, E. A.; Towers, M.; Ellis, S. R.; Heeren, R. M. A. Enhanced Capabilities for Imaging Gangliosides in Murine Brain with Matrix-Assisted Laser Desorption/Ionization and Desorption Electrospray Ionization Mass Spectrometry Coupled to Ion Mobility Separation. *Methods* **2016**, *104*, 69–78. <https://doi.org/10.1016/j.ymeth.2016.02.014>.
- (87) Langridge, J. I.; Claude, E. Matrix-Assisted Laser Desorption and Desorption Electrospray Ionization Mass Spectrometry Coupled to Ion Mobility. In *Methods in Molecular Biology*; Humana Press Inc., 2020; Vol. 2084, pp 245–265. [https://doi.org/10.1007/978-1-0716-0030-6\\_16](https://doi.org/10.1007/978-1-0716-0030-6_16).
- (88) Li, H.; Smith, B. K.; Márk, L.; Nemes, P.; Nazarian, J.; Vertes, A. Ambient Molecular Imaging by Laser Ablation Electrospray Ionization Mass Spectrometry with Ion Mobility Separation. *Int. J. Mass Spectrom.* **2015**, *377* (1), 681–689. <https://doi.org/10.1016/j.ijms.2014.06.025>.
- (89) Stopka, S. A.; Vertes, A. Metabolomic Profiling of Adherent Mammalian Cells In Situ by LAESI-MS with Ion Mobility Separation. In *Methods in Molecular Biology*; Humana Press Inc., 2020; Vol. 2084, pp 235–244. [https://doi.org/10.1007/978-1-0716-0030-6\\_15](https://doi.org/10.1007/978-1-0716-0030-6_15).
- (90) Griffiths, R. L.; Sisley, E. K.; Lopez-Clavijo, A. F.; Simmonds, A. L.; Styles, I. B.; Cooper, H. J. Native Mass Spectrometry Imaging of Intact Proteins and Protein

- Complexes in Thin Tissue Sections. *Int. J. Mass Spectrom.* **2019**, *437*, 23–29.  
<https://doi.org/10.1016/j.ijms.2017.10.009>.
- (91) Sisley, E. K.; Ujma, J.; Palmer, M.; Giles, K.; Fernandez-Lima, F. A.; Cooper, H. J. LESA Cyclic Ion Mobility Mass Spectrometry of Intact Proteins from Thin Tissue Sections. **2020**. <https://doi.org/10.1021/acs.analchem.9b05169>.
- (92) Illes-Toth, E.; Cooper, H. J. Probing the Fundamentals of Native Liquid Extraction Surface Analysis Mass Spectrometry of Proteins: Can Proteins Refold during Extraction? *Anal. Chem.* **2019**, *91* (19), 12246–12254.  
<https://doi.org/10.1021/acs.analchem.9b02075>.
- (93) Bodzon-Kulakowska, A.; Suder, P. Imaging Mass Spectrometry: Instrumentation, Applications, and Combination with Other Visualization Techniques. *Mass Spectrom. Rev.* **2016**, *35* (1), 147–169. <https://doi.org/10.1002/mas.21468>.
- (94) Spraker, J. E.; Luu, G. T.; Sanchez, L. M. Imaging Mass Spectrometry for Natural Products Discovery: A Review of Ionization Methods. *Natural Product Reports*. Royal Society of Chemistry February 1, 2020, pp 150–162.  
<https://doi.org/10.1039/c9np00038k>.
- (95) Perez, C. J.; Bagga, A. K.; Prova, S. S.; Yousefi Taemeh, M.; Ifa, D. R. Review and Perspectives on the Applications of Mass Spectrometry Imaging under Ambient Conditions. *Rapid Commun. Mass Spectrom.* **2019**, *33* (S3), 27–53.  
<https://doi.org/10.1002/rcm.8145>.
- (96) Kolakowski, B. M.; Mester, Z. Review of Applications of High-Field Asymmetric Waveform Ion Mobility Spectrometry (FAIMS) and Differential Mobility Spectrometry (DMS). *Analyst*. Royal Society of Chemistry August 20, 2007, pp

- 842–864. <https://doi.org/10.1039/b706039d>.
- (97) Guevremont, R. High-Field Asymmetric Waveform Ion Mobility Spectrometry: A New Tool for Mass Spectrometry. *Journal of Chromatography A*. Elsevier November 26, 2004, pp 3–19. <https://doi.org/10.1016/j.chroma.2004.08.119>.
- (98) Purves, R. W.; Guevremont, R. Electrospray Ionization High-Field Asymmetric Waveform Ion Mobility Spectrometry-Mass Spectrometry. *Anal. Chem.* **1999**, *71* (13), 2346–2357. <https://doi.org/10.1021/ac981380y>.
- (99) Ibrahim, Y. M.; Baker, E. S.; Danielson, W. F.; Norheim, R. V.; Prior, D. C.; Anderson, G. A.; Belov, M. E.; Smith, R. D. Development of a New Ion Mobility (Quadrupole) Time-of-Flight Mass Spectrometer. *Int. J. Mass Spectrom.* **2015**, *377* (1), 655–662. <https://doi.org/10.1016/j.ijms.2014.07.034>.
- (100) Baker, E. S.; Livesay, E. A.; Orton, D. J.; Moore, R. J.; Danielson, W. F.; Prior, D. C.; Ibrahim, Y. M.; LaMarche, B. L.; Mayampurath, A. M.; Schepmoes, A. A.; et al. An LC-IMS-MS Platform Providing Increased Dynamic Range for High-Throughput Proteomic Studies. *J. Proteome Res.* **2010**, *9* (2), 997–1006. <https://doi.org/10.1021/pr900888b>.
- (101) Morris, C. B.; May, J. C.; Leaptrot, K. L.; McLean, J. A. Evaluating Separation Selectivity and Collision Cross Section Measurement Reproducibility in Helium, Nitrogen, Argon, and Carbon Dioxide Drift Gases for Drift Tube Ion Mobility–Mass Spectrometry. *J. Am. Soc. Mass Spectrom.* **2019**, *30* (6), 1059–1068. <https://doi.org/10.1021/jasms.8b06014>.
- (102) Hinz, C.; Liggi, S.; Griffin, J. L. The Potential of Ion Mobility Mass Spectrometry for High-Throughput and High-Resolution Lipidomics. *Current Opinion in*

*Chemical Biology*. Elsevier Ltd February 1, 2018, pp 42–50.

<https://doi.org/10.1016/j.cbpa.2017.10.018>.

- (103) Lanucara, F.; Holman, S. W.; Gray, C. J.; Eyers, C. E. The Power of Ion Mobility-Mass Spectrometry for Structural Characterization and the Study of Conformational Dynamics. *Nature Chemistry*. Nature Publishing Group March 21, 2014, pp 281–294. <https://doi.org/10.1038/nchem.1889>.
- (104) Dilger, J. M.; Valentine, S. J.; Glover, M. S.; Clemmer, D. E. A Database of Alkaline-Earth-Coordinated Peptide Cross Sections: Insight into General Aspects of Structure. *J. Am. Soc. Mass Spectrom* **2013**. <https://doi.org/10.1007/s13361-013-0579-z>.
- (105) Dilger, J. M.; Glover, M. S.; Clemmer, D. E. A Database of Transition-Metal-Coordinated Peptide Cross-Sections: Selective Interaction with Specific Amino Acid Residues. *J. Am. Soc. Mass Spectrom*. **2017**, *28* (7), 1293–1303. <https://doi.org/10.1007/s13361-016-1592-9>.
- (106) Valentine, S. J.; Counterman, A. E.; Clemmer, D. E. A Database of 660 Peptide Ion Cross Sections: Use of Intrinsic Size Parameters for Bona Fide Predictions of Cross Sections. *J. Am. Soc. Mass Spectrom*. **1999**, *10* (11), 1188–1211. [https://doi.org/10.1016/S1044-0305\(99\)00079-3](https://doi.org/10.1016/S1044-0305(99)00079-3).
- (107) Picache, J. A.; Rose, B. S.; Balinski, A.; Leaptrot, K. L.; Sherrod, S. D.; May, J. C.; McLean, J. A. Collision Cross Section Compendium to Annotate and Predict Multi-Omic Compound Identities. *Chem. Sci*. **2019**, *10* (4), 983–993. <https://doi.org/10.1039/c8sc04396e>.
- (108) Ekelöf, M.; Dodds, J.; Khodjaniazova, S.; Garrard, K. P.; Baker, E. S.;

- Muddiman, D. C. Coupling IR-MALDESI with Drift Tube Ion Mobility-Mass Spectrometry for High-Throughput Screening and Imaging Applications. *J. Am. Soc. Mass Spectrom.* **2020**, *31* (3), 642–650.  
<https://doi.org/10.1021/jasms.9b00081>.
- (109) Michelmann, K.; Silveira, J. A.; Ridgeway, M. E.; Park, M. A. Fundamentals of Trapped Ion Mobility Spectrometry. *J. Am. Soc. Mass Spectrom.* **2014**, *26* (1), 14–24. <https://doi.org/10.1007/s13361-014-0999-4>.
- (110) Neumann, E.; Migas, L.; Allen, J. L.; Caprioli, R.; Van de Plas, R.; Spraggins, J. Spatial Metabolomics of the Human Kidney Using MALDI Trapped Ion Mobility Imaging Mass Spectrometry. **2020**.  
<https://doi.org/10.26434/CHEMRXIV.12118644.V2>.
- (111) Cintron-Diaz, Y. L.; De La Rocha, A. M. A.; Castellanos, A.; Chambers, J. M.; Fernandez-Lima, F. Mapping Chemotherapeutic Drug Distribution in Cancer Cell Spheroids Using 2D-TOF-SIMS and LESA-TIMS-MS. *Analyst* **2020**, *145* (21), 7056–7062. <https://doi.org/10.1039/C9AN02245G>.
- (112) Cintron-Diaz, Y. L.; Gomez-Hernandez, M. E.; Verhaert, M. M. H. A.; Verhaert, P. D. E. M.; Fernandez-Lima, F. Spatially Resolved Neuropeptide Characterization from Neuropathological Formalin-Fixed, Paraffin-Embedded Tissue Sections by a Combination of Imaging MALDI FT-ICR Mass Spectrometry Histochemistry and Liquid Extraction Surface Analysis-Trapped Ion Mobility Spectrometry-Tandem Mass Spectrometry. *J. Am. Soc. Mass Spectrom.* **2022**, *33* (4), 681–687.  
[https://doi.org/10.1021/JASMS.1C00376/ASSET/IMAGES/LARGE/JS1C00376\\_0005.JPEG](https://doi.org/10.1021/JASMS.1C00376/ASSET/IMAGES/LARGE/JS1C00376_0005.JPEG).

- (113) Centers for Disease Control, U. Antibiotic Resistance Threats in the United States, 2019. **2019**. <https://doi.org/10.15620/CDC:82532>.
- (114) Kumar, N.; David, M. Z.; Boyle-Vavra, S.; Sieth, J.; Daum, R. S. High Staphylococcus Aureus Colonization Prevalence among Patients with Skin and Soft Tissue Infections and Controls in an Urban Emergency Department. *J. Clin. Microbiol.* **2015**, *53* (3), 810. <https://doi.org/10.1128/JCM.03221-14>.
- (115) Wertheim, H. F. L.; Melles, D. C.; Vos, M. C.; Van Leeuwen, W.; Van Belkum, A.; Verbrugh, H. A.; Nouwen, J. L. The Role of Nasal Carriage in Staphylococcus Aureus Infections. *Lancet Infect. Dis.* **2005**, *5* (12), 751–762. [https://doi.org/10.1016/S1473-3099\(05\)70295-4](https://doi.org/10.1016/S1473-3099(05)70295-4).
- (116) Giraudy, C.; Hausmann, S.; Lemeille, S.; Prados, J.; Redder, P.; Linder, P. The C-Terminal Region of the RNA Helicase CshA Is Required for the Interaction with the Degradosome and Turnover of Bulk RNA in the Opportunistic Pathogen Staphylococcus Aureus. *RNA Biol.* **2015**, *12* (6), 658–674. <https://doi.org/10.1080/15476286.2015.1035505>.
- (117) Kourtis, A. P.; Hatfield, K.; Baggs, J.; Mu, Y.; See, I.; Epton, E.; Nadle, J.; Kainer, M. A.; Dumyati, G.; Petit, S.; et al. *Vital Signs*: Epidemiology and Recent Trends in Methicillin-Resistant and in Methicillin-Susceptible *Staphylococcus Aureus* Bloodstream Infections — United States. *MMWR. Morb. Mortal. Wkly. Rep.* **2019**, *68* (9), 214–219. <https://doi.org/10.15585/mmwr.mm6809e1>.
- (118) Fluckiger, U.; Widmer, A. F. Epidemiology of Methicillin-Resistant Staphylococcus Aureus. *Chemotherapy* **1999**, *45* (2), 121–134. <https://doi.org/10.1159/000007173>.



- (119) Spellberg, B.; Gilbert, D. N. The Future of Antibiotics and Resistance: A Tribute to a Career of Leadership by John Bartlett. *Clin. Infect. Dis.* **2014**, *59* (suppl\_2), S71–S75. <https://doi.org/10.1093/CID/CIU392>.
- (120) Heidary, M.; Khosravi, A. D.; Khoshnood, S.; Nasiri, M. J.; Soleimani, S.; Goudarzi, M. Daptomycin. *J. Antimicrob. Chemother.* **2018**, *73* (1), 1–11. <https://doi.org/10.1093/JAC/DKX349>.
- (121) Stefani, S.; Campanile, F.; Santagati, M.; Mezzatesta, M. L.; Cafiso, V.; Pacini, G. Insights and Clinical Perspectives of Daptomycin Resistance in *Staphylococcus Aureus*: A Review of the Available Evidence. *Int. J. Antimicrob. Agents* **2015**, *46* (3), 278–289. <https://doi.org/10.1016/J.IJANTIMICAG.2015.05.008>.
- (122) Ji, S.; Jiang, S.; Wei, X.; Sun, L.; Wang, H.; Zhao, F.; Chen, Y.; Yu, Y. In-Host Evolution of Daptomycin Resistance and Heteroresistance in Methicillin-Resistant *Staphylococcus Aureus* Strains From Three Endocarditis Patients. *J. Infect. Dis.* **2020**, *221* (Supplement\_2), S243–S252. <https://doi.org/10.1093/INFDIS/JIZ571>.
- (123) Van Meer, G.; Voelker, D. R.; Feigenson, G. W. Membrane Lipids: Where They Are and How They Behave. *Nat. Rev. Mol. Cell Biol.* **2008**, *9* (2), 112–124. <https://doi.org/10.1038/nrm2330>.
- (124) Fahy, E.; Cotter, D.; Sud, M.; Subramaniam, S. Lipid Classification, Structures and Tools. *Biochim. Biophys. Acta* **2011**, *1811* (11), 637. <https://doi.org/10.1016/J.BBALIP.2011.06.009>.
- (125) Slavetinsky, C. J.; Peschel, A.; Ernst, C. M. Alanyl-Phosphatidylglycerol and Lysyl-Phosphatidylglycerol Are Translocated by the Same MprF Flippases and Have Similar Capacities to Protect against the Antibiotic Daptomycin in

- Staphylococcus Aureus. *Antimicrob. Agents Chemother.* **2012**, *56* (7), 3492–3497. <https://doi.org/10.1128/AAC.00370-12>.
- (126) Kilelee, E.; Pokorny, A.; Yeaman, M. R.; Bayer, A. S. Lysyl-Phosphatidylglycerol Attenuates Membrane Perturbation Rather than Surface Association of the Cationic Antimicrobial Peptide 6W-RP-1 in a Model Membrane System: Implications for Daptomycin Resistance. *Antimicrob. Agents Chemother.* **2010**, *54* (10), 4476–4479. <https://doi.org/10.1128/AAC.00191-10>.
- (127) Jiang, J.-H.; Bhuiyan, S.; Shen, H.-H.; Cameron, D. R.; Rupasinghe, T. W. T.; Wu, C.-M.; Le Brun, A. P.; Kostoulas, X.; Domene, C.; Fulcher, A. J.; et al. Antibiotic Resistance and Host Immune Evasion in Staphylococcus Aureus Mediated by a Metabolic Adaptation. <https://doi.org/10.1073/pnas.1812066116>.
- (128) Kuhn, S.; Slavetinsky, C. J.; Peschel, A. Synthesis and Function of Phospholipids in Staphylococcus Aureus. *International Journal of Medical Microbiology*. Elsevier GmbH February 1, 2015, pp 196–202. <https://doi.org/10.1016/j.ijmm.2014.12.016>.
- (129) Tsai, M.; Ohniwa, R. L.; Kato, Y.; Takeshita, S. L.; Ohta, T.; Saito, S.; Hayashi, H.; Morikawa, K. Staphylococcus Aureus Requires Cardiolipin for Survival under Conditions of High Salinity. *BMC Microbiol.* **2011**, *11* (1), 1–12. <https://doi.org/10.1186/1471-2180-11-13>.
- (130) Hines, K. M.; Waalkes, A.; Penewit, K.; Holmes, E. A.; Salipante, S. J.; Werth, B. J.; Xu, L. Characterization of the Mechanisms of Daptomycin Resistance among Gram-Positive Bacterial Pathogens by Multidimensional Lipidomics. *mSphere* **2017**, *2* (6). <https://doi.org/10.1128/msphere.00492-17>.
- (131) Bisignano, C.; Ginestra, G.; Smeriglio, A.; Camera, E. La; Crisafi, G.; Franchina,

- F. A.; Tranchida, P. Q.; Alibrandi, A.; Trombetta, D.; Mondello, L.; et al. Study of the Lipid Profile of ATCC and Clinical Strains of Staphylococcus Aureus in Relation to Their Antibiotic Resistance. *Mol.* 2019, Vol. 24, Page 1276 **2019**, 24 (7), 1276. <https://doi.org/10.3390/MOLECULES24071276>.
- (132) Jones, T.; Yeaman, M. R.; Sakoulas, G.; Yang, S. J.; Proctor, R. A.; Sahl, H. G.; Schrenzel, J.; Xiong, Y. Q.; Bayer, A. S. Failures in Clinical Treatment of Staphylococcus Aureus Infection with Daptomycin Are Associated with Alterations in Surface Charge, Membrane Phospholipid Asymmetry, and Drug Binding. *Antimicrob. Agents Chemother.* **2008**, 52 (1), 269–278. <https://doi.org/10.1128/AAC.00719-07>.
- (133) Mishra, N. N.; Bayer, A. S. Correlation of Cell Membrane Lipid Profiles with Daptomycin Resistance in Methicillin-Resistant Staphylococcus Aureus. *Antimicrob. Agents Chemother.* **2013**, 57 (2), 1082–1085. <https://doi.org/10.1128/AAC.02182-12>.
- (134) Sohlenkamp, C.; Geiger, O. Bacterial Membrane Lipids: Diversity in Structures and Pathways. *FEMS Microbiol. Rev.* **2016**, 40 (1), 133–159. <https://doi.org/10.1093/FEMSRE/FUV008>.
- (135) Hines, K. M.; Alvarado, G.; Chen, X.; Gatto, C.; Pokorny, A.; Iii, F. A.; Wilkinson, B. J.; Xu, L.; Ellermeier, C. D. Lipidomic and Ultrastructural Characterization of the Cell Envelope of Staphylococcus Aureus Grown in the Presence of Human Serum. **2020**. <https://doi.org/10.1128/mSphere.00339-20>.
- (136) Rubio, A.; Moore, J.; Varoglu, M.; Conrad, M.; Chu, M.; Shaw, W.; Silverman, J. A. LC-MS/MS Characterization of Phospholipid Content in Daptomycin-

- Susceptible and -Resistant Isolates of Staphylococcus Aureus with Mutations in MprF. <http://dx.doi.org/10.3109/09687688.2011.640948> **2012**, 29 (1), 1–8.  
<https://doi.org/10.3109/09687688.2011.640948>.
- (137) Peschel, A.; Jack, R. W.; Otto, M.; Collins, L. V.; Staubitz, P.; Nicholson, G.; Kalbacher, H.; Nieuwenhuizen, W. F.; Jung, G.; Tarkowski, A.; et al. Staphylococcus Aureus Resistance to Human Defensins and Evasion of Neutrophil Killing via the Novel Virulence Factor Mprf Is Based on Modification of Membrane Lipids with L-Lysine. *J. Exp. Med.* **2001**, 193 (9), 1067–1076.  
<https://doi.org/10.1084/JEM.193.9.1067>.
- (138) Bayer, A. S.; Mishra, N. N.; Sakoulas, G.; Nonejuie, P.; Nast, C. C.; Pogliano, J.; Chen, K. T.; Ellison, S. N.; Yeaman, M. R.; Yanga, S. J. Heterogeneity of MprF Sequences in Methicillin-Resistant Staphylococcus Aureus Clinical Isolates: Role in Cross-Resistance between Daptomycin and Host Defense Antimicrobial Peptides. *Antimicrob. Agents Chemother.* **2014**, 58 (12), 7462–7467.  
[https://doi.org/10.1128/AAC.03422-14/SUPPL\\_FILE/ZAC012143533SO1.PDF](https://doi.org/10.1128/AAC.03422-14/SUPPL_FILE/ZAC012143533SO1.PDF).
- (139) Shen, T.; Hines, K. M.; Ashford, N. K.; Werth, B. J.; Xu, L. Varied Contribution of Phospholipid Shedding From Membrane to Daptomycin Tolerance in Staphylococcus Aureus. *Front. Mol. Biosci.* **2021**, 8, 526.  
<https://doi.org/10.3389/FMOLB.2021.679949/BIBTEX>.
- (140) Otto, M. Staphylococcal Biofilms. *Current Topics in Microbiology and Immunology*. *Curr Top Microbiol Immunol* 2008, pp 207–228.  
[https://doi.org/10.1007/978-3-540-75418-3\\_10](https://doi.org/10.1007/978-3-540-75418-3_10).
- (141) Crick, F. Central Dogma of Molecular Biology. *Nat.* 1970 2275258 **1970**, 227

- (5258), 561–563. <https://doi.org/10.1038/227561a0>.
- (142) Kunkel, T. A. DNA Replication Fidelity. *J. Biol. Chem.* **2004**, *279* (17), 16895–16898. <https://doi.org/10.1074/jbc.R400006200>.
- (143) DeLeo, F. R.; Diep, B. A.; Otto, M. Host Defense and Pathogenesis in Staphylococcus Aureus Infections. *Infect. Dis. Clin. North Am.* **2009**, *23* (1), 17–34. <https://doi.org/10.1016/J.IDC.2008.10.003>.
- (144) Benveniste, R.; Davies, J. Mechanisms of Antibiotic Resistance in Bacteria. *Annu. Rev. Biochem.* **1973**, *42*, 471–506. <https://doi.org/10.1146/ANNUREV.BI.42.070173.002351>.
- (145) Dever, L. A.; Dermody, T. S. Mechanisms of Bacterial Resistance to Antibiotics. *Arch. Intern. Med.* **1991**, *151* (5), 886–895. <https://doi.org/10.1001/ARCHINTE.1991.00400050040010>.
- (146) Ode, H.; Matsuyama, S.; Hata, M.; Neya, S.; Kakizawa, J.; Sugiura, W.; Hoshino, T. Computational Characterization of Structural Role of the Non-Active Site Mutation M36I of Human Immunodeficiency Virus Type 1 Protease. *J. Mol. Biol.* **2007**, *370* (3), 598–607. <https://doi.org/10.1016/J.JMB.2007.04.081>.
- (147) Lorch, M.; Mason, J. M.; Sessions, R. B.; Clarke, A. R. Effects of Mutations on the Thermodynamics of a Protein Folding Reaction: Implications for the Mechanism of Formation of the Intermediate and Transition States. *Biochemistry* **2000**, *39* (12), 3480–3485. [https://doi.org/10.1021/BI9923510/SUPPL\\_FILE/BI9923510\\_S.PDF](https://doi.org/10.1021/BI9923510/SUPPL_FILE/BI9923510_S.PDF).
- (148) Gingras, H.; Patron, K.; Bhattacharya, A.; Leprohon, P.; Ouellette, M. Gain- and Loss-of-Function Screens Coupled to Next-Generation Sequencing for Antibiotic Mode of Action and Resistance Studies in Streptococcus Pneumoniae.

- Antimicrob. Agents Chemother.* **2019**, 63 (5). <https://doi.org/10.1128/AAC.02381-18>.
- (149) Yang, B.; Yao, H.; Li, D.; Liu, Z. The Phosphatidylglycerol Phosphate Synthase PgsA Utilizes a Trifurcated Amphipathic Cavity for Catalysis at the Membrane-Cytosol Interface. *Curr. Res. Struct. Biol.* **2021**, 3, 312–323.  
<https://doi.org/10.1016/J.CRSTBI.2021.11.005>.
- (150) Peleg, A. Y.; Miyakis, S.; Ward, D. V.; Earl, A. M.; Rubio, A.; Cameron, D. R.; Pillai, S.; Moellering, R. C.; Eliopoulos, G. M. Whole Genome Characterization of the Mechanisms of Daptomycin Resistance in Clinical and Laboratory Derived Isolates of Staphylococcus Aureus. *PLoS One* **2012**, 7 (1), e28316.  
<https://doi.org/10.1371/journal.pone.0028316>.
- (151) Aebersold, R.; Mann, M. Mass Spectrometry-Based Proteomics. *Nat.* **2003** 422 (6928), 198–207. <https://doi.org/10.1038/nature01511>.
- (152) Zhang, Y.; Fonslow, B. R.; Shan, B.; Baek, M. C.; Yates, J. R. Protein Analysis by Shotgun/Bottom-up Proteomics. *Chem. Rev.* **2013**, 113 (4), 2343–2394.  
[https://doi.org/10.1021/CR3003533/ASSET/IMAGES/MEDIUM/CR-2012-003533\\_0002.GIF](https://doi.org/10.1021/CR3003533/ASSET/IMAGES/MEDIUM/CR-2012-003533_0002.GIF).
- (153) Archer, N. K.; Mazaitis, M. J.; William Costerton, J.; Leid, J. G.; Powers, M. E.; Shirtliff, M. E. Staphylococcus Aureus Biofilms: Properties, Regulation and Roles in Human Disease. *Virulence* **2011**, 2 (5), 445.  
<https://doi.org/10.4161/VIRU.2.5.17724>.
- (154) Römling, U.; Balsalobre, C. Biofilm Infections, Their Resilience to Therapy and Innovative Treatment Strategies. *J. Intern. Med.* **2012**, 272 (6), 541–561.

<https://doi.org/10.1111/JOIM.12004>.

- (155) Bernier, S. P.; Lebeaux, D.; DeFrancesco, A. S.; Valomon, A.; Soubigou, G.; Coppée, J.-Y.; Ghigo, J.-M.; Beloin, C. Starvation, Together with the SOS Response, Mediates High Biofilm-Specific Tolerance to the Fluoroquinolone Ofloxacin. *PLoS Genet.* **2013**, *9* (1), e1003144.

<https://doi.org/10.1371/JOURNAL.PGEN.1003144>.

- (156) Resch, A.; Rosenstein, R.; Nerz, C.; Götz, F. Differential Gene Expression Profiling of *Staphylococcus Aureus* Cultivated under Biofilm and Planktonic Conditions. *Appl. Environ. Microbiol.* **2005**, *71* (5), 2663–2676.

<https://doi.org/10.1128/AEM.71.5.2663-2676.2005>.

- (157) Perez-Lopez, M. I.; Mendez-Reina, R.; Trier, S.; Herrfurth, C.; Feussner, I.; Bernal, A.; Forero-Shelton, M.; Leidy, C. Variations in Carotenoid Content and Acyl Chain Composition in Exponential, Stationary and Biofilm States of *Staphylococcus Aureus*, and Their Influence on Membrane Biophysical Properties. *Biochim. Biophys. Acta - Biomembr.* **2019**, *1861* (5), 978–987.

<https://doi.org/10.1016/J.BBAMEM.2019.02.001>.

- (158) Rohde, H.; Burandt, E. C.; Siemssen, N.; Frommelt, L.; Burdelski, C.; Wurster, S.; Scherpe, S.; Davies, A. P.; Harris, L. G.; Horstkotte, M. A.; et al. Polysaccharide Intercellular Adhesin or Protein Factors in Biofilm Accumulation of *Staphylococcus Epidermidis* and *Staphylococcus Aureus* Isolated from Prosthetic Hip and Knee Joint Infections. *Biomaterials* **2007**, *28* (9), 1711–1720.

<https://doi.org/10.1016/J.BIOMATERIALS.2006.11.046>.

- (159) Balaban, N.; Cirioni, O.; Giacometti, A.; Ghiselli, R.; Braunstein, J. B.; Silvestri, C.;

- Mocchegiani, F.; Saba, V.; Scalise, G. Treatment of Staphylococcus Aureus Biofilm Infection by the Quorum-Sensing Inhibitor RIP. *Antimicrob. Agents Chemother.* **2007**, *51* (6), 2226–2229. <https://doi.org/10.1128/AAC.01097-06>.
- (160) Flemming, H. C.; Wingender, J. The Biofilm Matrix. *Nat. Rev. Microbiol.* **2010**, *8* (9), 623–633. <https://doi.org/10.1038/nrmicro2415>.
- (161) Cramton, S. E.; Gerke, C.; Schnell, N. F.; Nichols, W. W.; Götz, F. The Intercellular Adhesion (Ica) Locus Is Present in Staphylococcus Aureus and Is Required for Biofilm Formation. *Infect. Immun.* **1999**, *67* (10), 5427–5433. <https://doi.org/10.1128/IAI.67.10.5427-5433.1999/ASSET/49C29213-27FB-4143-B6E7-25108262062D/ASSETS/GRAPHIC/II1090404005.JPEG>.
- (162) Stewart, P. S.; Costerton, J. W. Antibiotic Resistance of Bacteria in Biofilms. *Lancet* **2001**, *358* (9276), 135–138. [https://doi.org/10.1016/S0140-6736\(01\)05321-1](https://doi.org/10.1016/S0140-6736(01)05321-1).
- (163) Hindy, J.-R.; Quintero-Martinez, J. A.; Lahr, B. D.; Palraj, R.; Go, J. R.; Fida, M.; Abu Saleh, O. M.; Arshad, V.; Talha, K. M.; DeSimone, D. C.; et al. Incidence of Monomicrobial Staphylococcus Aureus Bacteremia: A Population-Based Study in Olmsted County, Minnesota—2006 to 2020. *Open Forum Infect. Dis.* **2022**, *9* (7). <https://doi.org/10.1093/OFID/OFAC190>.
- (164) Moormeier, D. E.; Bayles, K. W. Staphylococcus Aureus Biofilm: A Complex Developmental Organism. *Mol. Microbiol.* **2017**, *104* (3), 365–376. <https://doi.org/10.1111/MMI.13634>.
- (165) Bayer, A. S.; Prasad, R.; Chandra, J.; Koul, A.; Smriti, M.; Varma, A.; Skurray, R. A.; Firth, N.; Brown, M. H.; Koo, S. U. P.; et al. In Vitro Resistance of



- Staphylococcus Aureus to Thrombin-Induced Platelet Microbicidal Protein Is Associated with Alterations in Cytoplasmic Membrane Fluidity. *Infect. Immun.* **2000**, 68 (6), 3548–3553. <https://doi.org/10.1128/IAI.68.6.3548-3553.2000>.
- (166) Li, M.; Rigby, K.; Lai, Y.; Nair, V.; Peschel, A.; Schitteck, B.; Otto, M. Staphylococcus Aureus Mutant Screen Reveals Interaction of the Human Antimicrobial Peptide Dermcidin with Membrane Phospholipids. *Antimicrob. Agents Chemother.* **2009**, 53 (10), 4200–4210. <https://doi.org/10.1128/AAC.00428-09>.
- (167) Gonzalez, D. J.; Okumura, C. Y.; Hollands, A.; Kersten, R.; Akong-Moore, K.; Pence, M. A.; Malone, C. L.; Derieux, J.; Moore, B. S.; Horswill, A. R.; et al. Novel Phenol-Soluble Modulin Derivatives in Community-Associated Methicillin-Resistant Staphylococcus Aureus Identified through Imaging Mass Spectrometry. *J. Biol. Chem.* **2012**, 287 (17), 13889–13898. <https://doi.org/10.1074/JBC.M112.349860>.
- (168) Gonzalez, D. J.; Vuong, L.; Gonzalez, I. S.; Keller, N.; McGrosso, D.; Hwang, J. H.; Hung, J.; Zinkernagel, A.; Dixon, J. E.; Dorrestein, P. C.; et al. Phenol Soluble Modulin (PSM) Variants of Community-Associated Methicillin-Resistant Staphylococcus Aureus (MRSA) Captured Using Mass Spectrometry-Based Molecular Networking. *Mol. Cell. Proteomics* **2014**, 13 (5), 1262–1272. <https://doi.org/10.1074/MCP.M113.031336>.
- (169) Moree, W. J.; Phelan, V. V.; Wu, C. H.; Bandeira, N.; Cornett, D. S.; Duggan, B. M.; Dorrestein, P. C. Interkingdom Metabolic Transformations Captured by Microbial Imaging Mass Spectrometry. *Proc. Natl. Acad. Sci. U. S. A.* **2012**, 109

(34), 13811–13816.

[https://doi.org/10.1073/PNAS.1206855109/SUPPL\\_FILE/SAPP.PDF](https://doi.org/10.1073/PNAS.1206855109/SUPPL_FILE/SAPP.PDF).

- (170) Michelsen, C. F.; Khademi, S. M. H.; Johansen, H. K.; Ingmer, H.; Dorrestein, P. C.; Jelsbak, L. Evolution of Metabolic Divergence in *Pseudomonas Aeruginosa* during Long-Term Infection Facilitates a Proto-Cooperative Interspecies Interaction. *ISME J. 2015 106* **2015**, *10* (6), 1323–1336.  
<https://doi.org/10.1038/ismej.2015.220>.
- (171) Si, T.; Li, B.; Zhang, K.; Xu, Y.; Zhao, H.; Sweedler, J. V. Characterization of *Bacillus Subtilis* Colony Biofilms via Mass Spectrometry and Fluorescence Imaging. *J. Proteome Res.* **2016**, *15* (6), 1955–1962.  
<https://doi.org/10.1021/ACS.JPROTEOME.6B00127>.
- (172) Phelan, V. V.; Fang, J.; Dorrestein, P. C. Mass Spectrometry Analysis of *Pseudomonas Aeruginosa* Treated with Azithromycin. *J. Am. Soc. Mass Spectrom.* **2015**, *26* (6), 873–877. [https://doi.org/10.1007/S13361-015-1101-6/ASSET/IMAGES/LARGE/JS8B05035\\_0002.JPEG](https://doi.org/10.1007/S13361-015-1101-6/ASSET/IMAGES/LARGE/JS8B05035_0002.JPEG).
- (173) Garg, N.; Zeng, Y.; Edlund, A.; Melnik, A. V.; Sanchez, L. M.; Mohimani, H.; Gurevich, A.; Miao, V.; Schiffler, S.; Lim, Y. W.; et al. Spatial Molecular Architecture of the Microbial Community of a *Peltigera* Lichen . *mSystems* **2016**, *1* (6). <https://doi.org/10.1128/MSYSTEMS.00139-16/ASSET/E213F968-EAE8-4373-8686-29846ACBF1BC/ASSETS/GRAPHIC/SYS0061620740008.JPEG>.
- (174) McCaughey, C. S.; Trebino, M. A.; Yildiz, F. H.; Sanchez, L. M. Utilizing Imaging Mass Spectrometry to Analyze Microbial Biofilm Chemical Responses to Exogenous Compounds. *Methods Enzymol.* **2021**, *665*, 281–304.

<https://doi.org/10.1016/BS.MIE.2021.11.014>.

- (175) Li, B.; Dunham, S. J. B.; Ellis, J. F.; Lange, J. D.; Smith, J. R.; Yang, N.; King, T. L.; Amaya, K. R.; Arnett, C. M.; Sweedler, J. V. A Versatile Strategy for Characterization and Imaging of Drip Flow Microbial Biofilms. *Anal. Chem.* **2018**, *90* (11), 6725–6734.  
[https://doi.org/10.1021/ACS.ANALCHEM.8B00560/ASSET/IMAGES/LARGE/AC-2018-00560J\\_0005.JPEG](https://doi.org/10.1021/ACS.ANALCHEM.8B00560/ASSET/IMAGES/LARGE/AC-2018-00560J_0005.JPEG).
- (176) Wakeman, C. A.; Moore, J. L.; Noto, M. J.; Zhang, Y.; Singleton, M. D.; Prentice, B. M.; Gilston, B. A.; Doster, R. S.; Gaddy, J. A.; Chazin, W. J.; et al. The Innate Immune Protein Calprotectin Promotes *Pseudomonas Aeruginosa* and *Staphylococcus Aureus* Interaction. *Nat. Commun.* **2016**, *7* (1), 1–12.  
<https://doi.org/10.1038/ncomms11951>.
- (177) Garg, N.; Zeng, Y.; Edlund, A.; Melnik, A. V.; Sanchez, L. M.; Mohimani, H.; Gurevich, A.; Miao, V.; Schiffler, S.; Lim, Y. W.; et al. Spatial Molecular Architecture of the Microbial Community of a *Peltigera* Lichen. *mSystems* **2016**, *1* (6). <https://doi.org/10.1128/MSYSTEMS.00139-16/ASSET/E213F968-EAE8-4373-8686-29846ACBF1BC/ASSETS/GRAPHIC/SYS0061620740008.JPEG>.
- (178) Girolamo, F. Di; Lante, I.; Muraca, M.; Putignani, L. The Role of Mass Spectrometry in the “Omics” Era. *Curr. Org. Chem.* **2013**, *17* (23), 2891.  
<https://doi.org/10.2174/1385272817888131118162725>.
- (179) Bligh, E. G.; Dyer, W. J. *A RAPID METHOD OF TOTAL LIPID EXTRACTION AND PURIFICATION*1.
- (180) Cajka, T.; Fiehn, O. Toward Merging Untargeted and Targeted Methods in Mass

- Spectrometry-Based Metabolomics and Lipidomics. *Anal. Chem.* **2016**, *88* (1), 524–545.  
[https://doi.org/10.1021/ACS.ANALCHEM.5B04491/ASSET/IMAGES/LARGE/AC-2015-04491V\\_0008.JPEG](https://doi.org/10.1021/ACS.ANALCHEM.5B04491/ASSET/IMAGES/LARGE/AC-2015-04491V_0008.JPEG).
- (181) Cassat, J. E.; Lee, C. Y.; Smeltzer, M. S. Investigation of Biofilm Formation in Clinical Isolates Of. **2007**, 127–144. [https://doi.org/10.1007/978-1-59745-468-1\\_10](https://doi.org/10.1007/978-1-59745-468-1_10).
- (182) Nelson, K. A.; Daniels, G. J.; Fournie, J. W.; Hemmer, M. J. Optimization of Whole-Body Zebrafish Sectioning Methods for Mass Spectrometry Imaging. *J. Biomol. Tech.* **2013**, *24* (3), 119. <https://doi.org/10.7171/JBT.13-2403-002>.
- (183) Shi, S. R.; Cote, R. J.; Taylor, C. R. Antigen Retrieval Immunohistochemistry: Past, Present, and Future. *J. Histochem. Cytochem.* **1997**, *45* (3), 327–343. <https://doi.org/10.1177/002215549704500301>.
- (184) Cattoretti, G.; Pileri, S.; Parravicini, C.; Becker, M. H. G.; Poggi, S.; Bifulco, C.; Key, G.; D'Amato, L.; Sabattini, E.; Feudale, E.; et al. Antigen Unmasking on Formalin-Fixed, Paraffin-Embedded Tissue Sections. *J. Pathol.* **1993**, *171* (2), 83–98. <https://doi.org/10.1002/PATH.1711710205>.
- (185) Yang, J.; Norris, J. L.; Caprioli, R. Novel Vacuum Stable Ketone-Based Matrices for High Spatial Resolution MALDI Imaging Mass Spectrometry. *J. Mass Spectrom.* **2018**, *53* (10), 1005–1012. <https://doi.org/10.1002/jms.4277>.
- (186) Vasilopoulou, C. G.; Sulek, K.; Brunner, A. D.; Meitei, N. S.; Schweiger-Hufnagel, U.; Meyer, S. W.; Barsch, A.; Mann, M.; Meier, F. Trapped Ion Mobility Spectrometry and PASEF Enable In-Depth Lipidomics from Minimal Sample

- Amounts. *Nat. Commun.* **2020**, *11* (1), 1–11. <https://doi.org/10.1038/s41467-019-14044-x>.
- (187) Labeit, S.; Gautel, M.; Lakey, A.; Trinick, J. Towards a Molecular Understanding of Titin. *EMBO J.* **1992**, *11* (5), 1711–1716. <https://doi.org/10.1002/J.1460-2075.1992.TB05222.X>.
- (188) Prentice, B. M.; Ryan, D. J.; Van De Plas, R.; Caprioli, R. M.; Spraggins, J. M. Enhanced Ion Transmission Efficiency up to  $m/z$  24 000 for MALDI Protein Imaging Mass Spectrometry. *Anal. Chem.* **2018**, *90* (8), 5090–5099. <https://doi.org/10.1021/acs.analchem.7b05105>.
- (189) Welte, M. A.; Gould, A. P. Lipid Droplet Functions beyond Energy Storage. *Biochim. Biophys. Acta - Mol. Cell Biol. Lipids* **2017**, *1862* (10), 1260–1272. <https://doi.org/10.1016/J.BBALIP.2017.07.006>.
- (190) Meijer, H. J. G.; Munnik, T. Phospholipid-Based Signaling in Plants. *Artic. Annu. Rev. Plant Biol.* **2003**. <https://doi.org/10.1146/annurev.arplant.54.031902.134748>.
- (191) Garabedian, A.; Benigni, P.; Ramirez, C. E.; Baker, E. S.; Liu, T.; Smith, R. D.; Fernandez-Lima, F. Towards Discovery and Targeted Peptide Biomarker Detection Using NanoESI-TIMS-TOF MS. *J. Am. Soc. Mass Spectrom.* **2018**, *29* (5), 817–826. [https://doi.org/10.1007/S13361-017-1787-8/SUPPL\\_FILE/JS8B05799\\_SI\\_001.DOCX](https://doi.org/10.1007/S13361-017-1787-8/SUPPL_FILE/JS8B05799_SI_001.DOCX).
- (192) Meier, F.; Beck, S.; Grassl, N.; Lubeck, M.; Park, M. A.; Raether, O.; Mann, M. Parallel Accumulation-Serial Fragmentation (PASEF): Multiplying Sequencing Speed and Sensitivity by Synchronized Scans in a Trapped Ion Mobility Device. *J. Proteome Res.* **2015**, *14* (12), 5378–5387.

<https://doi.org/10.1021/acs.jproteome.5b00932>.

- (193) Wölk, C.; Youssef, H.; Guttenberg, T.; Marbach, H.; Vizcay-Barrena, G.; Shen, C.; Brezesinski, G.; Harvey, R. D. Phase Diagram for a Lysyl-Phosphatidylglycerol Analogue in Biomimetic Mixed Monolayers with Phosphatidylglycerol: Insights into the Tunable Properties of Bacterial Membranes. *Chemphyschem* **2020**, *21* (8), 702. <https://doi.org/10.1002/CPHC.202000026>.
- (194) Koprivnjak, T.; Zhang, D.; Ernst, C. M.; Pesche, A.; Nauseef, W. M.; Weiss, J. P. Characterization of Staphylococcus Aureus Cardiolipin Synthases 1 and 2 and Their Contribution to Accumulation of Cardiolipin in Stationary Phase and within Phagocytes. *J. Bacteriol.* **2011**, *193* (16), 4134–4142. <https://doi.org/10.1128/JB.00288-11>.
- (195) Butler, A. E.; Janson, J.; Bonner-Weir, S.; Ritzel, R.; Rizza, R. A.; Butler, P. C. Beta-Cell Deficit and Increased Beta-Cell Apoptosis in Humans with Type 2 Diabetes. *Diabetes* **2003**, *52* (1), 102–110. <https://doi.org/10.2337/DIABETES.52.1.102>.
- (196) Prentice, B. M.; Hart, N. J.; Phillips, N.; Haliyur, R.; Judd, A.; Armandala, R.; Spraggins, J. M.; Lowe, C. L.; Boyd, K. L.; Stein, R. W.; et al. Imaging Mass Spectrometry Enables Molecular Profiling of Mouse and Human Pancreatic Tissue. *Diabetologia* **2019**, *62* (6), 1036–1047. <https://doi.org/10.1007/S00125-019-4855-8/FIGURES/5>.
- (197) Ryan, D. J.; Patterson, N. H.; Putnam, N. E.; Wilde, A. D.; Weiss, A.; Perry, W. J.; Cassat, J. E.; Skaar, E. P.; Caprioli, R. M.; Spraggins, J. M. MicroLESA: Integrating Autofluorescence Microscopy, in Situ Micro-Digestions, and Liquid

- Extraction Surface Analysis for High Spatial Resolution Targeted Proteomic Studies. *Anal. Chem.* **2019**, *91* (12), 7578–7585.  
[https://doi.org/10.1021/ACS.ANALCHEM.8B05889/ASSET/IMAGES/LARGE/AC-2018-058898\\_0004.JPEG](https://doi.org/10.1021/ACS.ANALCHEM.8B05889/ASSET/IMAGES/LARGE/AC-2018-058898_0004.JPEG).
- (198) Bittremieux, W.; Tabb, D. L.; Impens, F.; Staes, A.; Timmerman, E.; Martens, L.; Laukens, K. Quality Control in Mass Spectrometry-Based Proteomics. *Mass Spectrom. Rev.* **2018**, *37* (5), 697–711. <https://doi.org/10.1002/MAS.21544>.
- (199) Kovatchev, B. A Century of Diabetes Technology: Signals, Models, and Artificial Pancreas Control. *Trends Endocrinol. Metab.* **2019**, *30* (7), 432–444.  
<https://doi.org/10.1016/J.TEM.2019.04.008>.
- (200) Bosco, D.; Armanet, M.; Morel, P.; Niclauss, N.; Sgroi, A.; Muller, Y. D.; Giovannoni, L.; Parnaud, G.; Berney, T. Unique Arrangement of  $\alpha$ - and  $\beta$ -Cells in Human Islets of Langerhans. *Diabetes* **2010**, *59* (5), 1202.  
<https://doi.org/10.2337/DB09-1177>.
- (201) Thiede, B.; Höhenwarter, W.; Krah, A.; Mattow, J.; Schmid, M.; Schmidt, F.; Jungblut, P. R. Peptide Mass Fingerprinting. *Methods* **2005**, *35* (3), 237–247.  
<https://doi.org/10.1016/J.YMETH.2004.08.015>.
- (202) Cillero-Pastor, B.; Heeren, R. M. A. Matrix-Assisted Laser Desorption Ionization Mass Spectrometry Imaging for Peptide and Protein Analyses: A Critical Review of on-Tissue Digestion. *J. Proteome Res.* **2014**, *13* (2), 325–335.  
<https://doi.org/10.1021/pr400743a>.
- (203) Spengler, B. Mass Spectrometry Imaging of Biomolecular Information. *Anal. Chem.* **2015**, *87* (1), 64–82. <https://doi.org/10.1021/ac504543v>.

- (204) Han, J.; Permentier, H.; Bischoff, R.; Groothuis, G.; Casini, A.; Horvatovich, P. Imaging of Protein Distribution in Tissues Using Mass Spectrometry: An Interdisciplinary Challenge. *TrAC - Trends in Analytical Chemistry*. Elsevier B.V. March 1, 2019, pp 13–28. <https://doi.org/10.1016/j.trac.2018.12.016>.
- (205) Spraggins, J. M.; Rizzo, D. G.; Moore, J. L.; Rose, K. L.; Hammer, N. D.; Skaar, E. P.; Caprioli, R. M. MALDI FTICR IMS of Intact Proteins: Using Mass Accuracy to Link Protein Images with Proteomics Data. *J. Am. Soc. Mass Spectrom.* **2015**, *26* (6), 947–985. <https://doi.org/10.1007/s13361-015-1147-5>.
- (206) Gregorich, Z. R.; Ge, Y. Top-down Proteomics in Health and Disease: Challenges and Opportunities. *Proteomics* **2014**, *14* (10), 1195–1210. <https://doi.org/10.1002/pmic.201300432>.
- (207) van Remoortere, A.; Zeijl, J. M. Van; Oever, V. Den. MALDI Imaging and Profiling MS of Higher Mass Proteins from Tissue. *J. Am. Soc. Mass Spectrom.* **2010**, *21* (11), 62–66.
- (208) Mainini, V.; Bovo, G.; Chinello, C.; Gianazza, E.; Grasso, M.; Cattoretti, G.; Magni, F. Detection of High Molecular Weight Proteins by MALDI Imaging Mass Spectrometry. *Mol. Biosyst.* **2013**, *9* (6), 1101–1107. <https://doi.org/10.1039/c2mb25296a>.
- (209) Liu, H.; Han, M.; Li, J.; Qin, L.; Chen, L.; Hao, Q.; Jiang, D.; Chen, D.; Ji, Y.; Han, H.; et al. A Caffeic Acid Matrix Improves In Situ Detection and Imaging of Proteins with High Molecular Weight Close to 200,000 Da in Tissues by Matrix-Assisted Laser Desorption/Ionization Mass Spectrometry Imaging. *Anal. Chem.* **2021**, *93* (35), 11920–11928. <https://doi.org/10.1021/acs.analchem.0c05480>.



- (210) Spraggins, J. M.; Caprioli, R. M. High-Speed MALDI-TOF Imaging Mass Spectrometry: Rapid Ion Image Acquisition and Considerations for next Generation Instrumentation. *J. Am. Soc. Mass Spectrom.* **2011**, *22* (6), 1022–1031. <https://doi.org/10.1007/s13361-011-0121-0>.
- (211) Ogrinc Potočnik, N.; Porta, T.; Becker, M.; Heeren, R. M. A.; Ellis, S. R. Use of Advantageous, Volatile Matrices Enabled by next-Generation High-Speed Matrix-Assisted Laser Desorption/Ionization Time-of-Flight Imaging Employing a Scanning Laser Beam. *Rapid Commun. Mass Spectrom.* **2015**, *29* (23), 2195–2203. <https://doi.org/10.1002/rcm.7379>.
- (212) Dilillo, M.; De Graaf, E. L.; Yadav, A.; Belov, M. E.; McDonnell, L. A. Ultraviolet Photodissociation of ESI- and MALDI-Generated Protein Ions on a Q-Exactive Mass Spectrometer. *J. Proteome Res.* **2019**, *18* (1), 557–564. <https://doi.org/10.1021/acs.jproteome.8b00896>.
- (213) Nicolardi, S.; Switzar, L.; Deelder, A. M.; Palmblad, M.; Van Der Burgt, Y. E. M. Top-Down MALDI-In-Source Decay-FTICR Mass Spectrometry of Isotopically Resolved Proteins. *Anal. Chem.* **2015**, *87* (6), 3429–3437. <https://doi.org/10.1021/ac504708y>.
- (214) Chen, B.; Lietz, C. B.; Li, L. In Situ Characterization of Proteins Using Laserspray Ionization on a High-Performance MALDI-LTQ-Orbitrap Mass Spectrometer. *J. Am. Soc. Mass Spectrom.* **2014**, *25* (12), 2177–2180. <https://doi.org/10.1007/s13361-014-0986-9>.
- (215) Fort, K. L.; Van De Waterbeemd, M.; Boll, D.; Reinhardt-Szyba, M.; Belov, M. E.; Sasaki, E.; Zschoche, R.; Hilvert, D.; Makarov, A. A.; Heck, A. J. R. Expanding

- the Structural Analysis Capabilities on an Orbitrap-Based Mass Spectrometer for Large Macromolecular Complexes. *Analyst* **2018**, *143* (1), 100–105.  
<https://doi.org/10.1039/c7an01629h>.
- (216) Zemaitis, K.; Veličković, D.; Kew, W.; Fort, K. L.; Reinhardt-Szyba, M.; Pamreddy, A.; Ding, Y.; Kaushik, D.; Sharma, K.; Makarov, A. A.; et al. Enhanced Spatial Mapping of Histone Proteoforms in Human Kidney Through MALDI-MSI by High-Field UHMR Orbitrap Detection. *ChemRxiv* **2022**, No. This content is a preprint and has not been peer-reviewed. <https://doi.org/10.26434/chemrxiv-2022-mq46m-v2>.
- (217) Zubarev, R. A.; Makarov, A. Orbitrap Mass Spectrometry. *Anal. Chem.* **2013**, *85* (11), 5288–5296. <https://doi.org/10.1021/ac4001223>.
- (218) Spraggins, J. M.; Van de Plas, R.; Moore, J. L.; Ryan, D. J.; Caprioli, R. M. Maximizing Performance of Spatial Proteomics through the Fusion of Ultra-High Speed MALDI-TOF and High Mass Resolution MALDI FTICR IMS. In *Proceedings of the 64th ASMS Conference on Mass Spectrometry and Allied Topics*; San Antonio, 2016.
- (219) Djambazova, K. V.; Klein, D. R.; Migas, L. G.; Neumann, E. K.; Rivera, E. S.; Van de Plas, R.; Caprioli, R. M.; Spraggins, J. M. Resolving the Complexity of Spatial Lipidomics Using MALDI TIMS Imaging Mass Spectrometry. *Anal. Chem.* **2020**. <https://doi.org/10.1021/acs.analchem.0c02520>.
- (220) McDowell, C. T.; Klamer, Z.; Hall, J.; West, C. A.; Wisniewski, L.; Powers, T. W.; Angel, P. M.; Mehta, A. S.; Lewin, D. N.; Haab, B. B.; et al. Imaging Mass Spectrometry and Lectin Analysis of N-Linked Glycans in Carbohydrate Antigen-

- Defined Pancreatic Cancer Tissues. *Mol. Cell. Proteomics* **2021**, *20*, 100012.  
<https://doi.org/10.1074/MCP.RA120.002256>.
- (221) Jeanne Dit Fouque, K.; Garabedian, A.; Leng, F.; Tse-Dinh, Y. C.; Ridgeway, M. E.; Park, M. A.; Fernandez-Lima, F. Trapped Ion Mobility Spectrometry of Native Macromolecular Assemblies. *Anal. Chem.* **2021**, *93* (5), 2933–2941.  
<https://doi.org/10.1021/acs.analchem.0c04556>.
- (222) Short, S. A.; White, D. C. Metabolism of Phosphatidylglycerol, Lysylphosphatidylglycerol, and Cardiolipin of *Staphylococcus Aureus*. *J. Bacteriol.* **1971**, *108* (1), 219.
- (223) Missiakas, D. M.; Schneewind, O. Growth and Laboratory Maintenance of *Staphylococcus Aureus*. *Curr. Protoc. Microbiol.* **2013**, *28* (1), 9C.1.1-9C.1.9.  
<https://doi.org/10.1002/9780471729259.MC09C01S28>.
- (224) Kohler, C.; Proctor, R. A.; Bayer, A. S.; Yeaman, M. R.; Lalk, M.; Engelmann, S.; Mishra, N. N. Proteomic and Membrane Lipid Correlates of Reduced Host Defense Peptide Susceptibility in a *SnoD* Mutant of *Staphylococcus Aureus*. *Antibiotics* **2019**, *8* (4). <https://doi.org/10.3390/ANTIBIOTICS8040169>.
- (225) Yarwood, J. M.; Bartels, D. J.; Volper, E. M.; Greenberg, E. P. Quorum Sensing in *Staphylococcus Aureus* Biofilms. *J. Bacteriol.* **2004**, *186* (6), 1838–1850.  
<https://doi.org/10.1128/JB.186.6.1838-1850.2004>.
- (226) Hanson, R. W.; Owen, O. E. Gluconeogenesis. *Encycl. Biol. Chem.* **2004**, 197–203. <https://doi.org/10.1016/B0-12-443710-9/00268-4>.
- (227) Mallett, T. C.; Wallen, J. R.; Karplus, P. A.; Sakai, H.; Tsukihara, T.; Claiborne, A. STRUCTURE OF COENZYME A-DISULFIDE REDUCTASE FROM

- Staphylococcus Aureus AT 1.54 Å RESOLUTION. *Biochemistry* **2006**, *45* (38), 11278. <https://doi.org/10.1021/BI061139A>.
- (228) Harris, D. R.; Ward, D. E.; Feasel, J. M.; Lancaster, K. M.; Murphy, R. D.; Mallet, T. C.; Crane, E. J. Discovery and Characterization of a Coenzyme A Disulfide Reductase from *Pyrococcus Horikoshii*. *FEBS J.* **2005**, *272* (5), 1189–1200. <https://doi.org/10.1111/J.1742-4658.2005.04555.X>.
- (229) Cassat, J. E.; Moore, J. L.; Wilson, K. J.; Stark, Z.; Prentice, B. M.; Van De Plas, R.; Perry, W. J.; Zhang, Y.; Virostko, J.; Colvin, D. C.; et al. Integrated Molecular Imaging Reveals Tissue Heterogeneity Driving Host-Pathogen Interactions. *Sci. Transl. Med.* **2018**, *10* (432), 6361. [https://doi.org/10.1126/SCITRANSLMED.AAN6361/SUPPL\\_FILE/AAN6361\\_SM.PDF](https://doi.org/10.1126/SCITRANSLMED.AAN6361/SUPPL_FILE/AAN6361_SM.PDF).
- (230) Akbar, S.; Lee, S. Y.; Boylan, S. A.; Price, C. W. Two Genes from *Bacillus Subtilis* under the Sole Control of the General Stress Transcription Factor  $\sigma(B)$ . *Microbiology* **1999**, *145* (5), 1069–1078. <https://doi.org/10.1099/13500872-145-5-1069/CITE/REFWORKS>.
- (231) Prágai, Z.; Harwood, C. R. Regulatory Interactions between the Pho and  $\Sigma B$ -Dependent General Stress Regulons of *Bacillus Subtilis*. *Microbiology* **2002**, *148* (5), 1593–1602. <https://doi.org/10.1099/00221287-148-5-1593/CITE/REFWORKS>.
- (232) Wang, R.; Braughton, K. R.; Kretschmer, D.; Bach, T. H. L.; Queck, S. Y.; Li, M.; Kennedy, A. D.; Dorward, D. W.; Klebanoff, S. J.; Peschel, A.; et al. Identification of Novel Cytolytic Peptides as Key Virulence Determinants for Community-

- Associated MRSA. *Nat. Med.* 2007 1312 **2007**, 13 (12), 1510–1514.  
<https://doi.org/10.1038/nm1656>.
- (233) Kennedy, A. D.; Otto, M.; Braughton, K. R.; Whitney, A. R.; Chen, L.; Mathema, B.; Mediavilla, J. R.; Byrne, K. A.; Parkins, L. D.; Tenover, F. C.; et al. Epidemic Community-Associated Methicillin-Resistant *Staphylococcus Aureus*: Recent Clonal Expansion and Diversification. *Proc. Natl. Acad. Sci. U. S. A.* **2008**, 105 (4), 1327–1332.  
[https://doi.org/10.1073/PNAS.0710217105/SUPPL\\_FILE/10217TABLE7.PDF](https://doi.org/10.1073/PNAS.0710217105/SUPPL_FILE/10217TABLE7.PDF).
- (234) Fahy, E.; Sud, M.; Cotter, D.; Subramaniam, S. LIPID MAPS Online Tools for Lipid Research. *Nucleic Acids Res.* **2007**, 35 (suppl\_2), W606–W612.  
<https://doi.org/10.1093/NAR/GKM324>.
- (235) Fahy, E.; Subramaniam, S.; Murphy, R. C.; Nishijima, M.; Raetz, C. R. H.; Shimizu, T.; Spener, F.; Van Meer, G.; Wakelam, M. J. O.; Dennis, E. A. Update of the LIPID MAPS Comprehensive Classification System for Lipids. *J. Lipid Res.* **2009**, 50 (SUPPL.), S9–S14. <https://doi.org/10.1194/JLR.R800095-JLR200>.
- (236) Azhar, A.; Rasool, S.; Haque, A.; Shan, S.; Saeed, M.; Ehsan, B.; Haque, A. Detection of High Levels of Resistance to Linezolid and Vancomycin in *Staphylococcus Aureus*. *J. Med. Microbiol.* **2017**, 66 (9), 1328–1331.  
<https://doi.org/10.1099/JMM.0.000566>.
- (237) Nannini, E.; Murray, B. E.; Arias, C. A. Resistance or Decreased Susceptibility to Glycopeptides, Daptomycin, and Linezolid in Methicillin-Resistant *Staphylococcus Aureus*. *Curr. Opin. Pharmacol.* **2010**, 10 (5), 516–521.  
<https://doi.org/10.1016/J.COPH.2010.06.006>.

- (238) Eisenstein, B. I.; Oleson, F. B.; Baltz, R. H. Daptomycin: From the Mountain to the Clinic, with Essential Help from Francis Tally, MD. *Clin. Infect. Dis.* **2010**, *50* (Supplement\_1), S10–S15. <https://doi.org/10.1086/647938>.
- (239) Muraih, J. K.; Pearson, A.; Silverman, J.; Palmer, M. Oligomerization of Daptomycin on Membranes. *Biochim. Biophys. Acta - Biomembr.* **2011**, *1808* (4), 1154–1160. <https://doi.org/10.1016/J.BBAMEM.2011.01.001>.
- (240) Nakhate, P. H.; Yadav, V. K.; Pathak, A. N. Correspondence: A Review on Daptomycin; the First US-FDA Approved Lipopeptide Antibiotics. *J. Sci. Innov. Res.* **2013**, *2* (5), 970–980.
- (241) Pokorny, A.; Almeida, P. F. The Antibiotic Peptide Daptomycin Functions by Reorganizing the Membrane. *J. Membr. Biol.* **2021**, *254* (1), 97–108. <https://doi.org/10.1007/S00232-021-00175-0/FIGURES/7>.
- (242) Staubitz, P.; Neumann, H.; Schneider, T.; Wiedemann, I.; Peschel, A. MprF-Mediated Biosynthesis of Lysylphosphatidylglycerol, an Important Determinant in Staphylococcal Defensin Resistance. *FEMS Microbiol. Lett.* **2004**, *231* (1), 67–71. [https://doi.org/10.1016/S0378-1097\(03\)00921-2](https://doi.org/10.1016/S0378-1097(03)00921-2).
- (243) Ernst, C. M.; Staubitz, P.; Mishra, N. N.; Yang, S. J.; Hornig, G.; Kalbacher, H.; Bayer, A. S.; Kraus, D.; Peschel, A. The Bacterial Defensin Resistance Protein MprF Consists of Separable Domains for Lipid Lysinylation and Antimicrobial Peptide Repulsion. *PLOS Pathog.* **2009**, *5* (11), e1000660. <https://doi.org/10.1371/JOURNAL.PPAT.1000660>.
- (244) Ernst, C. M.; Peschel, A. Broad-Spectrum Antimicrobial Peptide Resistance by MprF-Mediated Aminoacylation and Flipping of Phospholipids. *Mol. Microbiol.*

- 2011**, 80 (2), 290–299. <https://doi.org/10.1111/J.1365-2958.2011.07576.X>.
- (245) Humphries, R. M.; Pollett, S.; Sakoulas, G. A Current Perspective on Daptomycin for the Clinical Microbiologist. *Clinical Microbiology Reviews*. American Society for Microbiology (ASM) October 2013, pp 759–780.  
<https://doi.org/10.1128/CMR.00030-13>.
- (246) Mishra, N. N.; Bayer, A. S.; Weidenmaier, C.; Grau, T.; Wanner, S.; Stefani, S.; Cafiso, V.; Bertuccio, T.; Yeaman, M. R.; Nast, C. C.; et al. Phenotypic and Genotypic Characterization of Daptomycin-Resistant Methicillin-Resistant Staphylococcus Aureus Strains: Relative Roles of MprF and Dlt Operons. *PLoS One* **2014**, 9 (9), e107426. <https://doi.org/10.1371/journal.pone.0107426>.
- (247) Jenson, R. E.; Baines, S. L.; Howden, B. P.; Mishra, N. N.; Farah, S.; Lew, C.; Berti, A. D.; Shukla, S. K.; Bayer, A. S.; Rose, W. E. Prolonged Exposure to  $\beta$ -Lactam Antibiotics Reestablishes Susceptibility of Daptomycin-Nonsusceptible Staphylococcus Aureus to Daptomycin. *Antimicrob. Agents Chemother.* **2020**, 64 (9). [https://doi.org/10.1128/AAC.00890-20/SUPPL\\_FILE/AAC.00890-20-S0001.PDF](https://doi.org/10.1128/AAC.00890-20/SUPPL_FILE/AAC.00890-20-S0001.PDF).
- (248) Gregoire, N.; Chauzy, A.; Buyck, J.; Rammaert, B.; Couet, W.; Marchand, S. Clinical Pharmacokinetics of Daptomycin. *Clinical Pharmacokinetics*. Adis December 14, 2020, pp 1–11. <https://doi.org/10.1007/s40262-020-00968-x>.
- (249) Wenisch, J. M.; Meyer, B.; Fuhrmann, V.; Saria, K.; Zuba, C.; Dittrich, P.; Thalhammer, F. Multiple-Dose Pharmacokinetics of Daptomycin during Continuous Venovenous Haemodiafiltration. *J. Antimicrob. Chemother.* **2012**, 67 (4), 977–983. <https://doi.org/10.1093/jac/dkr551>.

- (250) Elmore, S. Apoptosis: A Review of Programmed Cell Death. *Toxicol. Pathol.* **2007**, 35 (4), 495. <https://doi.org/10.1080/01926230701320337>.
- (251) Jones, R. N.; Barry, A. L. Antimicrobial Activity and Spectrum of LY146032, a Lipopeptide Antibiotic, Including Susceptibility Testing Recommendations. *Antimicrob. Agents Chemother.* **1987**, 31 (4), 625–629. <https://doi.org/10.1128/AAC.31.4.625>.
- (252) Kang, J.; David, L.; Li, Y.; Cang, J.; Chen, S. Three-in-One Simultaneous Extraction of Proteins, Metabolites and Lipids for Multi-Omics. *Front. Genet.* **2021**, 12, 313. <https://doi.org/10.3389/FGENE.2021.635971/BIBTEX>.
- (253) Boudjemaa, R.; Briandet, R.; Revest, M.; Jacqueline, C.; Caillon, J.; Fontaine-Aupart, M. P.; Steenkeste, K. New Insight into Daptomycin Bioavailability and Localization in Staphylococcus Aureus Biofilms by Dynamic Fluorescence Imaging. *Antimicrob. Agents Chemother.* **2016**, 60 (8), 4983–4990. [https://doi.org/10.1128/AAC.00735-16/SUPPL\\_FILE/ZAC008165439SO1.PDF](https://doi.org/10.1128/AAC.00735-16/SUPPL_FILE/ZAC008165439SO1.PDF).
- (254) Li, Z.; Nair, S. K. Quorum Sensing: How Bacteria Can Coordinate Activity and Synchronize Their Response to External Signals? *Protein Sci.* **2012**, 21 (10), 1403–1417. <https://doi.org/10.1002/PRO.2132>.
- (255) Fuqua, W. C.; Winans, S. C.; Peter Greenberg<sup>2</sup>, E. Quorum Sensing in Bacteria: The LuxR-LuxI Family of Cell Density-Responsive Transcriptional Regulators. *J. Bacteriol.* **1994**, 176 (2), 269–275.
- (256) Zhu, J.; Miller, M. B.; Vance, R. E.; Dziejman, M.; Bassler, B. L.; Mekalanos, J. J. Quorum-Sensing Regulators Control Virulence Gene Expression in *Vibrio Cholerae*. *Proc. Natl. Acad. Sci.* **2002**, 99 (5), 3129–3134.



<https://doi.org/10.1073/PNAS.052694299>.

- (257) Haque, S.; Ahmad, F.; Dar, S. A.; Jawed, A.; Mandal, R. K.; Wahid, M.; Lohani, M.; Khan, S.; Singh, V.; Akhter, N. Developments in Strategies for Quorum Sensing Virulence Factor Inhibition to Combat Bacterial Drug Resistance. *Microb. Pathog.* **2018**, *121*, 293–302. <https://doi.org/10.1016/J.MICPATH.2018.05.046>.
- (258) Pader, V.; Hakim, S.; Painter, K. L.; Wigneshweraraj, S.; Clarke, T. B.; Edwards, A. M. Staphylococcus Aureus Inactivates Daptomycin by Releasing Membrane Phospholipids. *Nat. Microbiol.* **2016**, *2* (1), 1–8. <https://doi.org/10.1038/nmicrobiol.2016.194>.
- (259) Poppert, S.; Riecker, M.; Wellinghausen, N.; Frickmann, H.; Essig, A. Accelerated Identification of Staphylococcus Aureus from Blood Cultures by a Modified Fluorescence in Situ Hybridization Procedure. *J. Med. Microbiol.* **2010**, *59* (1), 65–68. <https://doi.org/10.1099/JMM.0.015503-0/CITE/REFWORKS>.
- (260) Foster, T. Staphylococcus. *Mol. Detect. Hum. Bact. Pathog.* **1996**, 307–322. [https://doi.org/10.5005/jp/books/12697\\_25](https://doi.org/10.5005/jp/books/12697_25).
- (261) Niehaus, M.; Soltwisch, J.; Belov, M. E.; Dreisewerd, K. Transmission-Mode MALDI-2 Mass Spectrometry Imaging of Cells and Tissues at Subcellular Resolution. *Nat. Methods* **2019**, *16* (9), 925–931. <https://doi.org/10.1038/s41592-019-0536-2>.
- (262) Spivey, E. C.; McMillen, J. C.; Ryan, D. J.; Spraggins, J. M.; Caprioli, R. M. Combining MALDI-2 and Transmission Geometry Laser Optics to Achieve High Sensitivity for Ultra-High Spatial Resolution Surface Analysis. *J. Mass Spectrom.* **2019**, *54* (4), 366–370. <https://doi.org/10.1002/jms.4335>.

- (263) Djambazova, K.; Klein, D. R.; Migas, L.; Neumann, E.; Rivera, E.; Van de Plas, R.; Caprioli, R. M.; Spraggins, J. Resolving the Complexity of Spatial Lipidomics with MALDI Trapped Ion Mobility Spectrometry. **2020**.  
<https://doi.org/10.26434/CHEMRXIV.12331652.V1>.
- (264) Jeanne Dit Fouque, K.; Fernandez-Lima, F. Recent Advances in Biological Separations Using Trapped Ion Mobility Spectrometry – Mass Spectrometry. *TrAC Trends Anal. Chem.* **2019**, *116*, 308–315.  
<https://doi.org/10.1016/J.TRAC.2019.04.010>.
- (265) Naylor, C. N.; Reinecke, T.; Ridgeway, M. E.; Park, M. A.; Clowers, B. H. Validation of Calibration Parameters for Trapped Ion Mobility Spectrometry. *J. Am. Soc. Mass Spectrom.* **2019**, *30* (10), 2152–2162.  
[https://doi.org/10.1007/S13361-019-02289-1/SUPPL\\_FILE/JS8B06234\\_SI\\_001.DOCX](https://doi.org/10.1007/S13361-019-02289-1/SUPPL_FILE/JS8B06234_SI_001.DOCX).
- (266) Guo, R.; Zhou, L.; Chen, X. Desorption Electrospray Ionization (DESI) Source Coupling Ion Mobility Mass Spectrometry for Imaging Fluoropezil (DC20) Distribution in Rat Brain. *Anal. Bioanal. Chem.* **2021**, *413* (23), 5835–5847.  
<https://doi.org/10.1007/S00216-021-03563-6/FIGURES/8>.
- (267) Struwe, W. B.; Pagel, K.; Benesch, J. L. P.; Harvey, D. J.; Campbell, M. P. GlycoMob: An Ion Mobility-Mass Spectrometry Collision Cross Section Database for Glycomics. *Glycoconj. J.* **2016**, *33* (3), 399–404.  
<https://doi.org/10.1007/S10719-015-9613-7/FIGURES/3>.
- (268) Zheng, X.; Aly, N. A.; Zhou, Y.; Dupuis, K. T.; Bilbao, A.; Paurus, V. L.; Orton, D. J.; Wilson, R.; Payne, S. H.; Smith, R. D.; et al. A Structural Examination and

- Collision Cross Section Database for over 500 Metabolites and Xenobiotics Using Drift Tube Ion Mobility Spectrometry. *Chem. Sci.* **2017**, 8 (11), 7724–7736.  
<https://doi.org/10.1039/c7sc03464d>.
- (269) Prentice, B. M.; Chumbley, C. W.; Caprioli, R. M. High-Speed MALDI MS/MS Imaging Mass Spectrometry Using Continuous Raster Sampling. *J. Mass Spectrom.* **2015**, 50 (4), 703–710. <https://doi.org/10.1002/JMS.3579>.
- (270) Lanekoff, I.; Burnum-Johnson, K.; Thomas, M.; Short, J.; Carson, J. P.; Cha, J.; Dey, S. K.; Yang, P.; Prieto Conaway, M. C.; Laskin, J. High-Speed Tandem Mass Spectrometric in Situ Imaging by Nanospray Desorption Electrospray Ionization Mass Spectrometry. *Anal. Chem.* **2013**, 85 (20), 9596–9603.  
[https://doi.org/10.1021/AC401760S/SUPPL\\_FILE/AC401760S\\_SI\\_001.PDF](https://doi.org/10.1021/AC401760S/SUPPL_FILE/AC401760S_SI_001.PDF).
- (271) Colley, M.; Djambazova, Katerina V. Neumann, E. K. N.; Fuetterer, A.; Krause, M.; Caprioli, R. M.; Spraggins, J. M. PASEF Imaging Mass Spectrometry: High Spatial Resolution In Situ Molecular Mapping And Identification. In *American Society for Mass Spectrometry*; 2022.
- (272) Miller, S. A.; Kevin, #; Fouque, J. D.; Ridgeway, M. E.; Park, M. A.; Fernandez-Lima, F. Trapped Ion Mobility Spectrometry, Ultraviolet Photodissociation, and Time-of-Flight Mass Spectrometry for Gas-Phase Peptide Isobars/Isomers/Conformers Discrimination. *J. Am. Soc. Mass Spectrom* **2022**, 33, 7. <https://doi.org/10.1021/jasms.2c00091>.